Selective Catalytic Oxidation over Metal Oxides for the Valorization of Biomass Derived Feedstocks and Propane

by

Prabu K

AcSIR Registration No: 10CC17J26022

A thesis submitted to the
Academy of Scientific & Innovative Research
for the award of the degree of

Doctor of Philosophy

in

Science

Under the Supervision of

Dr. Thirumalaiswamy Raja

CSIR-National Chemical Laboratory

Pune

Academy of Scientific and Innovative Research

AcSIR Headquarters, CSIR-HRDC campus

Sector 19, Kamla Nehru Nagar,

Ghaziabad, U.P. – 201 002, India

October 2021

Certificate

This is to certify that the work incorporated in this Ph.D. thesis entitled, *"Selective catalytic oxidation over metal oxides for the valorization of biomass derived feedstocks and Propane"*, submitted by *Mr. Prabu K* to the Academy of Scientific and Innovative Research (AcSIR), in partial fulfillment of the requirements for the award of the Degree of *Doctor of Philosophy in Science*, embodies original research work carried out by the student. We, further certify that this work has not been submitted to any other University or Institution in part or full for the award of any degree or diploma. Research materials obtained from other sources and used in this research work has been duly acknowledged in the thesis. Image (s), illustration (s), figure (s), table (s) etc., used in the thesis from other source (s), have also been duly cited and acknowledged.

Signature of Student

Mr. Prabu K

Date: 22-10-2021

Signature of Supervisor

Dr. Thirumalaiswamy Raja

Date: 22-10-2021

Statements of Academic Integrity

I, Prabu K , a Ph.D. student of the Academy of Scientific and Innovative Research (AcSIR) with Registration No.10CC17J26022 hereby undertake that, the thesis entitled "Selective catalytic oxidation over metal oxides for the valorization of biomass derived feedstocks and Propane" has been prepared by me and that the document reports original work carried out by me and is free of any plagiarism in compliance with the UGC Regulations on *"Promotion of Academic Integrity and Prevention of Plagiarism in Higher Educational Institutions (2018)" and the CSIR Guidelines for "Ethics in Research and in Governance (2020)".*

Signature of the Student

Date : 22-10-2021

Place : Pune

It is hereby certified that the work done by the student, under my supervision, is plagiarism free in accordance with the UGC Regulations on "*Promotion of Academic Integrity and Prevention of Plagiarism in Higher Educational Institutions (2018)" and the CSIR Guidelines for "Ethics in Research and in Governance (2020)".*

Signature of the Supervisor

Name: **Dr. Thirumalaiswamy Raja**

Date : 22-10-2021

Place : Pune

Dedicated to my beloved family members and friends…

"The only true wisdom is in knowing
you know nothing"

~Socrates

Acknowledgements…

This thesis has been seen through to completion with the support and encouragement of numerous people including my well wishers, friends and colleagues. At this point of accomplishment I like to thank all those people who made this possible, which is an unforgettable experience for me.

Foremost, I would like to express my heartfelt and deepest gratitude to my advisor, Dr. T. Raja, who introduced me to a fascinating realm of chemistry. I am deeply indebted to him for his invaluable guidance and unconditional support. His tireless attitude has been an impetus for me throughout the course of study. I take this opportunity to express my deepest sense of gratitude and reverence towards him for guiding me in the right direction throughout the course of this work. Besides my advisor, I would like to express my deepest appreciation to my doctoral advisory committee: Dr. S. Dhanasekaran, Dr. Sakya S Sen and Dr. M. Banu for their unfailing support and continuous encouragement during the course of this study.

I extend my sincere thanks to the Director of CSIR-NCL Dr. Ashish Lele, Prof. Ashwini Kumar Nangia (former Director); Dr. C.S. Gopinath (former Chairman) and Dr. Shubhangi B Umbarkar (Chairman, Catalysis and Inorganic Chemistry Division) for providing me the opportunity to carry out my research work in this prestigious and well-equipped laboratory. My heartfelt thanks to Dr. C.V.V. Satyanarayana, Dr. D. Srinivas, Dr. C.P. Vinod, Dr. Nandini Devi, Dr. Paresh L. Dhepe, Dr. Kushal Bhatte, and Dr. Sudarsanam Putla. I also like to thank Mr. Jha, Ms. Violet Samuel, Mr. Madhu, Mr. Purushothaman, Mr. Nayak and all other scientific and non-scientific staff for their help and support during my tenure as a research student.

Words fail me when I intend to express my thanks and gratitude to my senior colleagues Dr. Aswathy T V, Dr. Pranjal Gogoi and Dr. Ashok Kumar V for their tremendous support and hope they had given to me. Without that hope, this thesis would not have been possible. I would like to say a special thanks to Mr. Periyasamy K, my ex-labmate and forever friend; who introduced me to NCL and that I am today. I would also like to acknowledge my present and past labmates Sheetal, Manikandan, Sana, Prabu M, Sruthy, Divya, Fahima, Gayathri, Asamsa, Aditya, Athul, Sivaprasad, Vipul, Karthik, Sampath, Amrin, Akash, Kiran, Snehal, Eeswar, Saravanan, Samridhi, Archana, Anshu, Aaron, Shwetha, Gourab, Priyanshu and Mayuri. I would also like to extend my regards to my seniors Dr. Mohan, Dr. Shibin, Dr. Lenin, Dr. Sreedala, Dr. Anju, and Dr. Lakshmiprasad.

I sincerely thank all my institute friends especially, Sudhakar, Chaithanya, Suman, Sathish, Vedikuyil, Maya, Pawan, Sourik, Yogita, Preethi, Betsy, Sreejith, Arunima, Susmita, Chinnu, Sema, Lavanya, Zinoy, Kumar, Amrutha, Sibo, Ravi, Mahindra, Subramani, Siva kumar, Sangeetha, Namitha, Arun, Jeyavani, Manoj, Nittan and Pavan

Kalbande. Special thanks to Dr. Sathiyakamatchi, Dr. G. Raja, Dr. Raj Kumar, Dr. Divagar, Dr. Bharathi, Dr. Madhu, Dr. Niveditha, Dr. Sakthivel, Tharchanaa, Ananthan, Saravana Kumar, Neethu, Poovarasan, Dr. CVVS group, Dr. CPV group, Dr. CSG group, Dr. RND group and well wishers in NCL for their timely help.

I extend my sincere thanks to Student Academic Office and Catalysis and Inorganic Chemistry Division at CSIR-NCL for their help and support at crucial times. I am grateful to CSIR, New Delhi, for awarding the research fellowship, AcSIR for PhD registration and Director, CSIR-National Chemical Laboratory for extending all infrastructural facilities. I would also like to thank my M.Sc., B.Sc., and school friends for their support and encouragement.

Last, but not the least, I am grateful for my parents Ranjitham and Kandasamy whose constant love, blessings and support keep me motivated and confident. My accomplishments and success are because they believed in me. I would like to pay high regards to my brother Dr. Praveen, my sister Tamila; love to Sanju and Nandhu for their unconditional love and affection. I would extend my respect and indeed indebted to my uncle Manoharan because of whom I was able to do Ph.D. I would extend my thanks to my cousins and their family for their love and encouragement.

Above all, I owe it all to Almighty God for giving me the wisdom, health and belief to undertake research work of my thesis and enabling me to its completion.

Prabu K

Table of contents

Chapter 4: Effective and selective oxidation of 2-Butanol over Mn supported catalyst systems

Chapter 5A: A Highly efficient and reusable Ru-NaY catalyst for the base free oxidation of 5-hydroxymethylfurfural to 2,5-furandicarboxylic acid

Chapter 5B: An enhanced catalytic performance of Ru nanoparticles supported NMC catalyst for the oxidation of HMF to FDCA

List of figures

Schemes

Tables

List of Abbreviations

ODHP	Oxidative dehydrogenation propane
DH	Dehydrogenation
PXRD	Powder X-ray diffraction
FE-SEM	Field emission scanning electron microscopy
TEM	Transmission electron microscopy
XPS	X-ray photoelectron spectroscopy
TPD	Temperature programmed desorption
GC	Gas chromatography
FID	Flame ionization detector
TCD	Thermal conductivity detector
HPLC	High performance liquid chromatography
BET	Brunauer-Emmett-Teller
TPR	Temperature programmed reduction
DRS	Diffuse reflectance spectroscopy
UV	Ultra violet
TGA	Thermogravimetric analysis
DTA	Differential thermal analysis
FWHM	Full width at half maximum
FCC	Fluid catalytic cracking
FBR	Fixed bed reactor
GHSV	Gas hourly space velocity
LHSV	Liquid hourly space velocity
BN	Boron nitride
h	Hour
HRTEM	High resolution transmission electron microscopy
ICP-OES	Inductively coupled plasma-optical emission spectroscopy
IUPAC	International Union of Pure and Applied Chemistry
JCPDS	Joint committee on Powder Diffraction Standards
MvK	Mars van Krevelen
SAED	Selected area electron diffraction

T_{max}	Temperature of the first maxima in the profile
TOS	Time on stream
Vp	Pore volume
FTIR	Fourier transform infrared spectroscopy
atm. Pressure	Atmospheric pressure
MEK	Methyl ethyl ketone
HT	Hydrotalcite
C	Carbon
AC	Activated carbon
HAP	Hydroxyapatite
CNT	Carbon nanotube
PVP	Polyvinylpyrrolidone
MC	Mesoporous carbon
NMC	Nitrogen doped mesoporous carbon
HMF	5-hydroxymethylfurfural
FDCA	2,5-furandicarboxylic acid
DFF	2,5-diformylfuran
FFCA	5-formyl-2-furancarboxylic acid
HMFCA	5-hydroxymethyl-2-furancarboxylic acid
PET	Polyethylene furanote
DRIFTS	Diffuse reflectance infrared fourier transform spectroscopy
TOF	Turnover frequency
L/B	Lewis and Brønsted acid sites
HAADF	High-angle annular dark-field imaging
STEM	Scanning transmission electron microscope

Chapter-1

Introduction

1.1. Catalysis

Catalysis is a known phenomenon from very long ago until today. Life would not exist without catalysis as it plays an important role in energy demand and production in our modern society. Catalysis is ubiquitous in the chemical industry for the synthesis of value-added products, renewable energy production, and environmental pollution control by reducing the emission of hazardous gases from automotive. In the 19th century, the development of catalysts was initiated by Kirchhoff, H. Davy, E. Davy, and Faraday. The chemical reactions were aided in the presence of other materials, which are not consumed in the process. According to the International Union of Pure and Applied Chemistry (IUPAC), a catalyst is simply a substance that increases the rate of chemical reactions without modifying overall standard Gibbs free energy in the reaction [1]. The term catalyst was first described by Swedish chemist J.J. Berzelius in 1836 [2], which was coined from Greek words *kata* meaning down and *lyein* meaning loosen. Afterwards in 1895, Ostwald initiated and claimed in terms of thermodynamics, catalyst is a material that accelerates a chemical reaction without changing the equilibrium of the reaction [3]. Currently, more than 90 % of chemicals and fuel processes are operated by catalysts for our everyday lives and are play a crucial role in the wellbeing of people.

Typically catalysis was distinguished into homogeneous and heterogeneous catalysis. In homogeneous catalysis, reactant and catalyst are present in a single fluid phase. Most of the homogeneous processes take place in the liquid phase and are widely used in reactions involving organometallic complexes, metal ions, and the synthesis of organic molecules. However, a major challenge in the homogeneous process is the recovery of catalysts from product/substrate. In heterogeneous catalysis, reactant and catalyst are present in different phases. A heterogeneous catalytic process occurs by the adsorption of reactant onto solid active surface sites and desorption of products. Heterogeneous catalysis provides several advantages over homogeneous methods, such as easy separation of catalyst from product and recovery of the catalyst for reuse. This process has been employed in many industrial processes for the production of value-added products and fuels. In the early 1800s Ambrogio Fusinieri, and Michael Faraday have explored the ability of platinum (Pt) to facilitate oxidation reactions [4, 5]. Later, numerous catalytic processes have been started and

developed which facilitated isomerization, polymerization, oxidation, hydrogenation and dehydrogenation. The above-stated catalytic reactions contribute in the development of the industrial rebellion.

1.2. Selective oxidation

Selective oxidation transformation is the most prominent process for manufacturing aldehydes/ketones, carboxylic acids, and lower olefins; which are important processes in the chemical industry for the production of fine and specialty chemicals. Nowadays, there is an extensive need for olefins particularly, propylene which is the major chemical building block for the production of polypropylene, acrylonitrile, propylene oxide, etc. Also, selective conversion of 2-Butanol is a crucial reaction where the product methyl ethyl ketone (MEK), is considered the main commodity chemicals in the chemical industry. 5-hydroxymethylfurfural (HMF) is one of the most significant platform molecules. The selective oxidation of HMF to commodity chemical 2,5-furandicarboxylic acid (FDCA) is an important process where FDCA serves as a substitution for terephthalic acid in the polymer industries for the production of bio-based polymer polyethylene furanoate (PEF), which is used in PEF bottles, films, fibers for apparel and furniture. This would contribute to a more active, sustainable green process for producing aldehyde/ketones and carboxylic acids.

1.3. Oxidative dehydrogenation of propane

Oxidative dehydrogenation of propane (ODHP) seems to be one of the most attractive alternatives to dehydrogenation routes for the production of lower olefins [6-8]. In this method, an oxidative gas (O_2) is co-feed with the alkane. This process has several advantages, such as exothermicity (ΔH_{298K} = -117 kJ/mol^{-1}) that is not thermodynamically limited **(Eq. 1.1)** and can be operated at a much low temperature which minimizes coke deposition on the catalyst surface ensuring the long-term stability and catalytic activity of the catalyst. However, using molecular oxygen as an oxidant in propane activation suffers from over-oxidation due to the high energy required for C-H bond activation in propane compared with propene molecule. In addition, flammability limitation of the reaction mixture, elimination of reaction heat (hotspots), and reaction lead to thermal runaway. Therefore, to develop a selective catalyst for ODHP and to enhance the selectivity/productivity of propene to reduce the deep oxidation is a must.

$$\mathbf{C_3H_8 + ½\ O_2 \longrightarrow C_3H_6 + H_2O} \qquad \mathbf{(1.1)}$$

1.3.1. Catalytic dehydrogenation of propane

There is a huge increase in the worldwide demand for lower olefins particularly propylene which is the basic feedstocks in the petrochemical industry for the production of a variety of polymers [9-11]. Conventionally, lower olefins are produced by steam cracking of naphtha, fluid catalytic cracking (FCC) of light diesel, and dehydrogenation of alkanes [12-14]. These methods need a huge amount of energy, which is not sufficient to attain the propylene demand, which is expected to increase to 130 million metric tons by 2023 [15, 16]. In the present scenario, shale gas development would have a significant impact on the world economy for at least several decades and possibly as long as a century more for the production of propylene. To date, various propane dehydrogenation technologies (ABB Lummus-Catofin, UOP Oleflex, Philips STAR, Linde BASF PDH, China university of petroleum ADHO, Snamprogetti Yarsintez FBD-4, Dow chemical company FCDh, and KBR K-PRO^{TM}) have been unfold, which are listed in **Table 1**. However, the most extensively used process for propylene production is the dehydrogenation of propane using CrO_x/Al_2O_3 (Catofin process) and $Pt\text{-}Sn/Al_2O_3$ (Oleflex process), and these processes are highly endothermic (ΔH_{298}= +124.3 kJ mol^{-1}) in nature with a limitation over the thermodynamic equilibrium [17-21].

Table 1.1 Catalytic dehydrogenation process technology [22]

Technology	FBD-4	Catofin	Oleflex	PDH	STAR	ADHO	FCDh	K-PRO
Invertor	Snamprogetti-Yarsintez	ABB Lummus	Honeywell UOP	Linde-BASF	Phillips	China University of Petroleum	Dow Chemical Company	KBR
Year	1964	1986	1990	1995	1999	2016	2016	2018
Reactor	Fluidized bed	Adiabatic fixed bed reactor	Moving bed	Tubular fixed bed	Tubular fixed bed	Fluidized bed	Up-flow Fluidized bed	Fluidized bed (riser)
Catalyst	CrO_x/Al_2O_3	K(Na)-CrO_x/Al_2O_3	Pt-Sn/Al_2O_3	Pt-Sn/ZrO_2	Pt-$Sn/ZnAl_2O_3$/ $CaO\text{-}Al_2O_3$	Refractory mixed oxides	Pt-Ga-$K/Si\text{-}Al_2O_3$	Non-Pt and Non-Cr
Temperature (°C)	550-600	560-650	525-705	550-650	480-620	500-650	600	600
Conversion (%)	45-50	45-50	30-40	40-45	~35	~ 50	~ 45	~ 45
Selectivity (%)	80-85	82-87	85-88	~ 95	80-90	~ 90	~ 93	87-90
Catalyst life/years	-	2-3	1-3	>2	>5	-	-	4-6

1.3.1.1. Catofin Process

The Catofin process was developed by ABB Lummus Company for the dehydrogenation of C_3-C_5 paraffins. **Fig.1.1** shows a typical Catofin propane dehydrogenation unit. An adiabatic fixed-bed reactor was designed and developed for the dehydrogenation process with four different zones: catalytic reaction of propane dehydrogenation to propylene, reactor on purge, regeneration, product compressor, and refining units. Before entering the catalyst bed, the hydrocarbon (propane) is preheated with hot air. The chromium oxide (CrO_x) supported alumina (Al_2O_3) catalysts were loaded, and the reaction was performed at 650 °C and 0.5 bar. The Catofin process achieved >92 mol % propylene selectivity with high propane conversion. Nevertheless, this process is highly endothermic with lower efficiency and huge energy consumption. Besides this, the plant needs to shut down periodically under high reaction temperature conditions, which may damage the hardware and reaction systems. However, in addition to this, the high toxicity of Cr-based catalyst causes environmental antagonism, the acute side reactions and instigates catalyst deactivation and frequent regeneration of the catalyst [23].

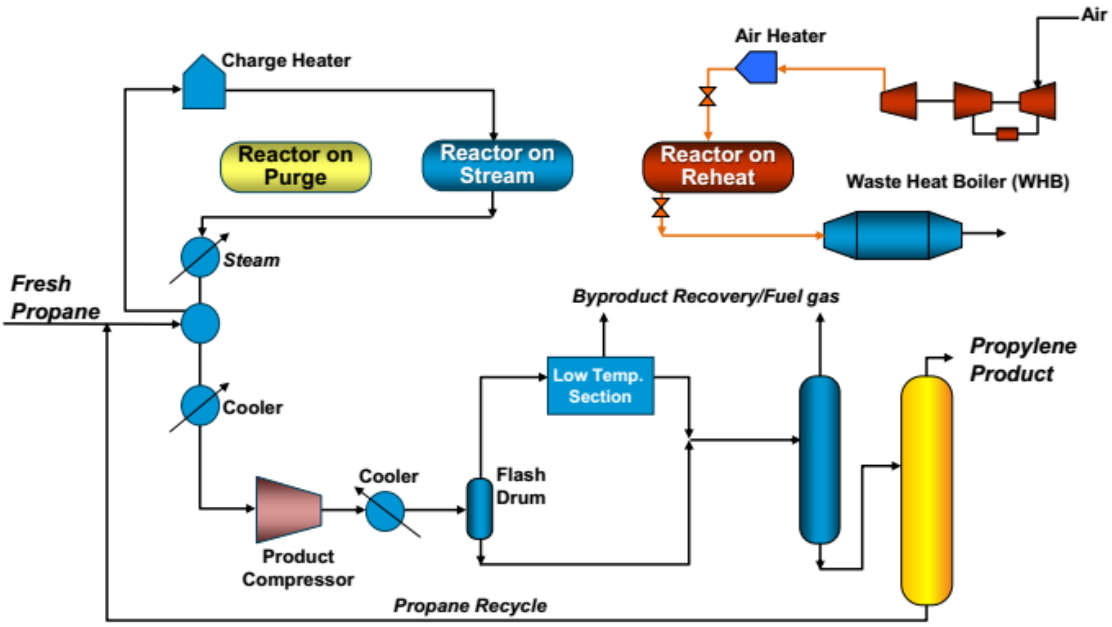

Fig.1.1 A schematic representation of Catofin® dehydrogenation process [24].

1.3.1.2. Oleflex process

The UOP Oleflex process technology was developed by Honeywell in 1990. Catalytic dehydrogenation of propane to propylene is performed in a moving bed reactor. The reaction is carried out using a Pt-Sn based catalyst at a temperature from 525 to 700 ºC and pressure between 1 to 3 bar. The Pt-based catalyst exhibits high propane dehydrogenation activity due

to the affinity for paraffinic C-H bonds. However, Pt-based catalysts exhibit a high tendency to sintering as well as coke formation, which block the active sites and is also not cost-effective. The UOP Oleflex™ propane dehydrogenation process has three or four different segments such as; reactor sector, product recovery, and regeneration sector as shown in **Fig. 1.2.** The preheated C_3 hydrocarbons feed is initiated into the reactor, and each reactor section contains interstage heaters; and a feed-effluent gas-gas exchanger. The last reactor is connected to continuous catalyst regeneration (CCR) to regenerate the catalyst. In the product recuperation unit, the cooling of reactor effluents is conducted which is compressed and finally hydrogen and olefins are separated by cryogenic systems.

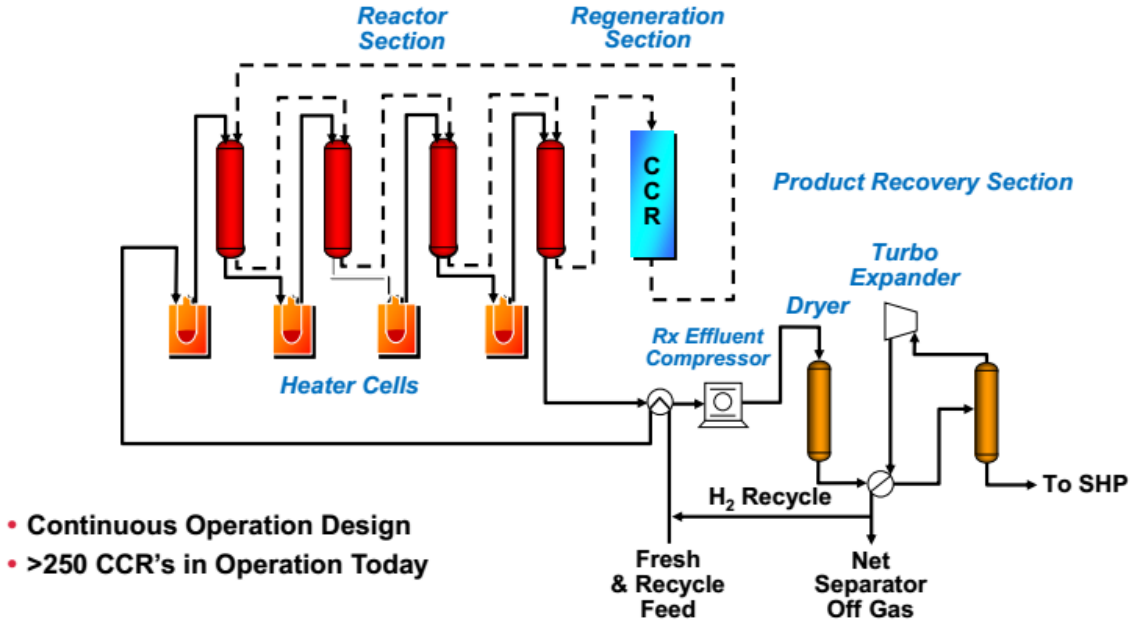

Fig.1.2 A schematic representation of UOP Oleflex™ dehydrogenation process [25].

1.3.2. Thermodynamics of alkane dehydrogenation

Dehydrogenation of lower hydrocarbons is highly endothermic **(Eq. 1.2)** and thermodynamically unfavorable. According to Le Chatelier's principle, activation of alkanes at higher reaction temperature and low partial pressure help to achieve higher conversion. **Fig. 1.3** shows the reaction temperature within the range 570-750 °C is required for propane dehydrogenation at atmospheric pressure. Upon increasing the temperature, the rates of both C-H cleavage and C-C bond cleavage side reactions will be amplified. Due to this, increased cracking products such as methane and ethylene **(Eq. 1.3)** are formed. Besides, three different side reactions can occur: the addition of hydrogen in propane which leads to the formation of hydrogenolysis products ethane as well as methane **(Eq. 1.4)**, cracking of propane molecule

(Eq. 1.3), and coke formation on metal surfaces **(Eq. 1.5)**. A plausible reaction pathway is illustrated below for the dehydrogenation of propane to propylene.

$$C_3H_8 \longleftrightarrow C_3H_6 + H_2 \ (\Delta H_{298} = 124.3 \text{ kJ mol}^{-1}) \qquad (1.2)$$

$$C_3H_8 \longleftrightarrow CH_4 + C_2H_4 \ (\Delta H_{298} = 98.9 \text{ kJ mol}^{-1}) \qquad (1.3)$$

$$C_3H_8 + H_2 \longleftrightarrow C_2H_6 + CH_4 \ (\Delta H_{298} = 37.7 \text{ kJ mol}^{-1}) \qquad (1.4)$$

$$C_3H_8 \longleftrightarrow 3C + 4H_2 \ (\Delta H_{298} = 119.5 \text{ kJ mol}^{-1}) \qquad (1.5)$$

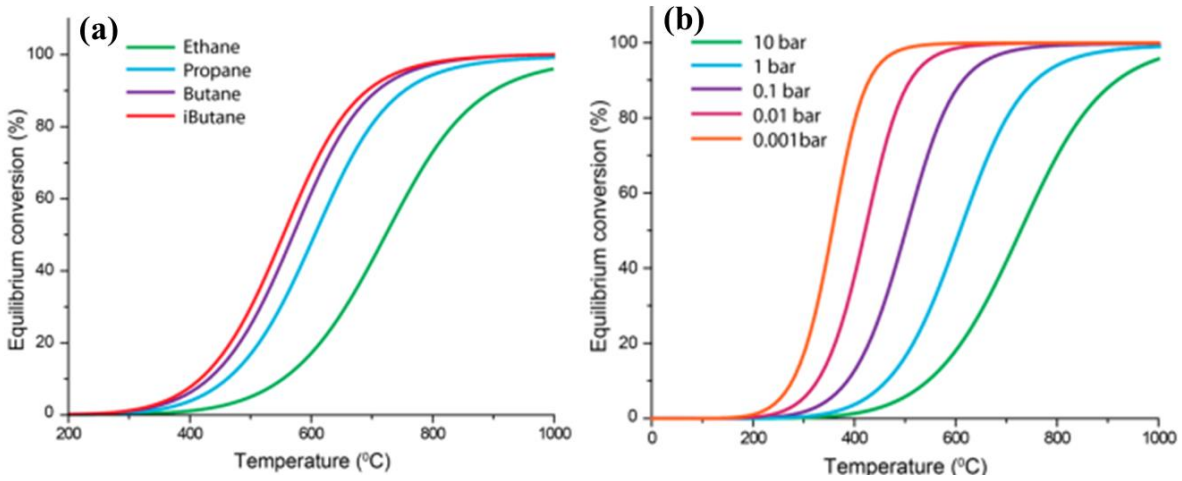

Fig. 1.3 (a) Equilibrium conversion of C_2-C_4 alkanes to olefins versus temperature at 1 bar (b) pressure dependence of the dehydrogenation of propane versus temperature [26].

1.3.3. Oxidants

Enhancing the selectivity and productivity of the value-added chemicals (aldehydes/ketones, dicarboxylic acids, olefins) through selective oxidation using oxidants such as CO_2, Air and N_2O is a great challenge [27, 28]. Using CO_2 as a mild oxidant to oxidize propane to propene (Eq. 1.6) decreases the over-oxidation and reduces surface can be re-oxidized. Furthermore, employing and mitigating CO_2 levels in the atmosphere could reduce global warming. However, employing CO_2 in ODHP is highly endothermic (ΔH_{298K} = +166.6 kJ mol^{-1}), and it is difficult to activate the thermodynamically stable CO_2 molecule. Hence, the introduction of O_2 along with CO_2 will make the reaction exothermic and increase the oxidizing capability of CO_2. The addition of a small quantity of O_2 reduces catalyst deactivation rate; however, the selectivity of propene will be declined. Thus, designing an appropriate catalyst, promoters, and suitable supports would enhance the oxidizing ability of CO_2 and maintain a stable selectivity of propene.

$$C_3H_8 + CO_2 \longrightarrow C_3H_6 + CO + H_2O \qquad (1.6)$$

Other oxidants like N_2O has been employed as the oxidant for ODH of lower hydrocarbons and exhibited higher catalytic activity when compared to oxygen due to the least catalytic combustion.

1.3.4. Kinetics of ODHP

The effect of reaction rates on different reactant concentrations (C_3H_8 & O_2) and temperature is recognized by chemical kinetics. The kinetic study was initiated by S.L.T Andersson, on $V/AlPO_4$ supported catalyst with varying vanadium loading (0.2-15 wt %) at different temperatures and partial pressure of propane as well as oxygen [29]. **Table 1.2** described activation energy and rate constant for lower alkanes. Later, many researchers have studied many kinetic models for ODH of light paraffins; such as the Langmuir-Hinshelwood model, Eley-Ridel model, Power-law model [30-32], and Mars-van Krevelen (MvK) model. The MvK model is the most appropriate method of ODHP [33-37]. Thus, vanadia-supported catalysts have been found zero-order with reference to the partial pressure of oxygen and first-order with respect to the partial pressure of propane, which propounds that the activation of C-H bond in propane is a rate-determining step [38].

Table 1.2 Bond dissociation energies for lower hydrocarbons [39]

Bond type	**Energy kJ mol^{-1}**
C-C	376
Primary C-H	420
Secondary C-H	401
Tertiary C-H	390
Allylic C-H	361
Vinylic C-H	445

1.3.5. Alkane activation mechanism

The most acceptable mechanism for selective oxidation and ODH is Mars-van Krevelen (MvK) or redox mechanism [40]. In this mechanism, the activation of C-H bond in propane molecule is achieved by homolytic scission [41]. It is well known that the C-H bond in the methylene group is weaker than the methyl group (primary carbon) and a recent report suggested that C-H bond activation is the rate-determining step. Initially, lattice oxygen participates in the C-H bond activation of secondary carbon (methylene group) with the formation of propyl radical and O-H bond via paired electron mechanism. In the second step,

C-H bond breaks in the methyl group to form propene. Then, the reduced oxide surface can be re-oxidized by an external supply of oxygen, and this cycle continues throughout the reaction. Two different oxygen species are present on the catalyst surface, namely electrophilic and nucleophilic. **Scheme. 1.1** shows that the electron-deficient electrophilic oxygen species like O_2^-, O_2^{2-}, and O^- are responsible for complete oxidation [42]. The saturated surface nucleophilic O^{2-} species are highly selective towards propene.

$$CH_3CH_2CH_3 + O^{2-} \longrightarrow CH_3CH{=}CH_2 + H_2O + 2e^- \quad (1.7)$$

$$O_2 + e^- \longrightarrow O_2^- \quad (1.8)$$

$$O_2^- + e^- \longrightarrow O_2^{2-} \longrightarrow 2O^- \quad (1.9)$$

$$2O^- + 2e^- \longrightarrow 2O^{2-} \quad (2.0)$$

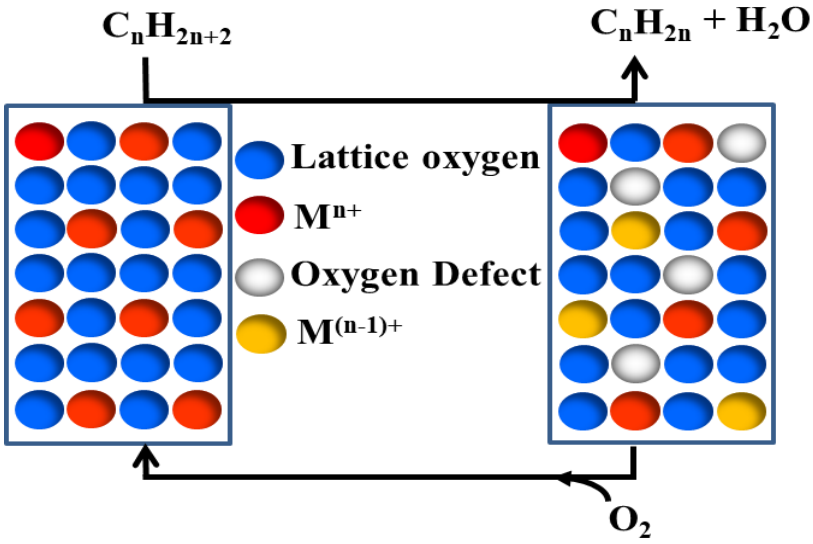

Fig. 1.4 MvK mechanism.

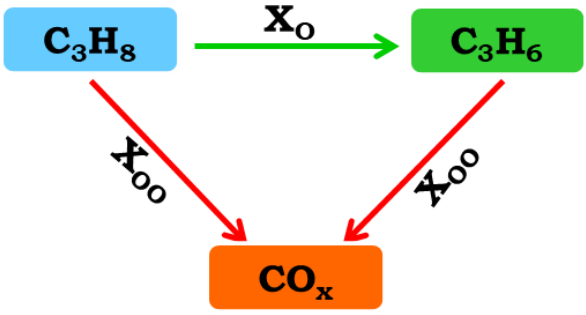

Scheme. 1.1 X_O represents nucleophilic oxygen and X_{OO} represents electrophilic oxygen.

1.3.6. Catalyst design for ODH of propane: A literature review

A great number of catalysts have been investigated for ODHP [43-46]. The most prominent key properties of an ODH catalyst are oxide supports interaction, oxygen vacancy, acid-base

properties, nature of supports, surface oxide reducibility, reactant feed ratio and resistant to coke formation. Furthermore, the catalyst should have superior thermal stability and retain the structural integrity for long-term reaction. Although many reports deal with ODH of propane, vanadium oxide-based catalysts show high catalytic activity and selectivity towards the desired products [35, 37, 47-52].

1.3.6.1. Acid-base properties

Acid-base property has a dominant role in heterogeneous catalysts, particularly in the ODH of lower alkanes [53]. The surface metal oxide catalyst contains metal cations (acidic centers), oxygen and hydroxyl groups (basic centers). The addition of an admissible amount of additives (K, P, Ca, Ni, Mg, Zn, Nb, and Mo) to vanadium oxide supported catalyst modifies the acid-base properties and redox nature [54, 55]. Thus, modification of surface properties increases the concentration of acid sites (increase in the electronegativity of additive ions) and enhances catalytic activity. A small amount of alkali and alkaline earth dopants into the oxide surface can increase the basicity M-O bond energy and increase the selectivity of propene. P. Concepcion and co-workers reported that selectivity of propene is correlated to the nucleophilicity of surface oxygen species [56].

1.3.6.2. Role of oxide supports

Oxidative dehydrogenation of propane has been widely studied using a different catalyst, supports, and reaction conditions. Among all, vanadium oxide (VO_x) supported catalysts are studied effectively for the ODH of propane to propene. The crucial part of VO_x is the variable oxidation state (+3, +4, and +5), and also vanadium oxide has been examined over numerous supports, including Al_2O_3, SiO_2, TiO_2, CeO_2, MgO, ZrO_2, Nb_2O_5 and zeolites [37, 57]. These supports play a crucial role in ODH of propane. Typically, oxide supports (Al_2O_3, SiO_2, TiO_2) poses high surface area, durability, high thermal stability, and strong metal-support interaction (SMSI). The supported VO_x catalysts contain isolated monomeric vanadia, and this molecularly dispersed species has been investigated by several authors. High surface area alumina has been employed for ODH of propane due to its acid properties, high metal dispersion, and uniform pore size distribution. Nevertheless, alumina supports are acidic in nature, and therefore, alkaline metals are used as promoters to suppress the coke formation on the surface and reduce side reactions.

1.3.6.3. Supported VO_x catalysts

Highly dispersed oxide-supported catalysts have been extensively studied for the oxidative dehydrogenation of propane and used for numerous other industrial catalytic processes [58]. The structural complexing and binding strength of lattice oxygen in the surface VO_x species has a crucial role that presides over the selectivity of propene, and a few reports for ODH of propane are listed in **Table. 1.3.** Different types of VO_x species can be found such as monomeric (isolated VO_x), dimeric, polymeric, and crystalline V_2O_5 which depends on the loading of vanadia, synthesis method, calcination temperature, and the nature of oxide supports [37, 59].

It is reported that three types of oxygen atoms are present in surface VO_4 species, such as (i) terminal V=O sites, (ii) oxygen atom bridging to vanadia atom (V-O-V), and (iii) oxygen atom bridging to vanadia atom and oxide supports sites (V-O-supports) [60]. The selectivity of olefins is achieved over a catalyst containing a high density of surface vanadia oxide and isolated monovanadate species on the surface. Moreover, theoretical studies have been confirmed that terminal and bridging lattice oxygen provide the active sites for C-H activation in propane, which is in good accordance with the DFT calculations [61].

Table 1.3 Performance of some transition metal oxide catalyst for ODH of propane

Catalyst	Reaction Temperature (°C)	Conversion of propane (%)	Selectivity of propene (%)	References
VO_x-Al_2O_3	488	33	38	62
$CeVO_4$	550	41	69	63
Nb-CeO_2	500	14	25	64
CoMgAlO-LDH	600	15	67	65
V-MCM 41	550	11	61	66
VO_x-SBA-15	450	13	57	67
VO_x-KIT-6	600	55	64	68
CMK-3	450	13	48	69
VO_x-SiO_2	520	3	78	70

1.3.6.4. Boron based catalyst for ODH of propane

Recently hexagonal-boron nitride (h-BN) and boron-containing catalysts are found highly active for ODHP, and it has a greater tendency to cleave only the C-C bond of propane than

over the vanadium-based catalysts [71]. The h-BN catalyst gave high selectivity of propene (71.8 %) with the low conversion of propane (11.3 %) at 560 ºC [72]. However, the catalyst was reported to give low selectivity for CO_x and relatively higher selectivity for C_2 products. Currently, boron nitride (BN) based catalyst is synthesized with high thermal stability and conductivity. Chaturbedy *et al*, reported that high surface area boron nitride (BN) catalyst is achieved 70 % selectivity of propene and 52 % conversion of propane at 525 ºC with high O_2/C_3 ratio. However, the catalyst needs regeneration every five hours to regain the original catalytic activity [73]. Hermans and co-workers reported that boron nitride (BN) and boron-containing materials (NiB, WB, B4C, and TiB2) are highly active for ODH of propane [74]. Nevertheless, the stability of the catalyst needs to improve, and the role of nitrogen species present in the BN catalyst has yet to confirm from operando techniques. So far, no unusual kinetic aspects of the ODH reaction have been discovered, nor has a mechanism been uncovered to explain the unprecedented activity.

1.3.6.5. Carbon based catalytic systems for ODH of propane

Carbon-based catalysts acquired numerous attention due to their large volume, tunable pore size, as well as high surface area, and they have been extensively studied for several catalytic applications. Schlogl *et al*. reported metal-free carbon nanomaterial (nanotube, onion-like carbons and carbon nanofilaments) for ODH of ethylbenzene to styrene [75]. In agreement with this, oxygen containing functional groups and quinoidic groups are observed active for ODH of propane [76].

1.3.6.6. Reactor type and operation system

The selection of a suitable reactor is pivotal to executing the oxidative dehydrogenation process. A fixed bed reactor (FBR) has been used for selective catalytic oxidation reactions. However, due to the hot spots, catalyst deactivation is a major drawback related to FBR. It is difficult to run the reaction under isothermal conditions. The fluidized bed reactor has many advantages like; (i) uniform residence time distribution, (ii) mass transfer, and (iii) periodic regeneration of the catalyst [77]. Additionally, a twin reactor provides catalyst regeneration for ODH reactions, which can be an appealing alternative route for commercial implementation [78]. Later, a fluidized (CREC: Chemical Reactor Engineering Centre) riser simulator reactor was designed to understand the reaction kinetics and mechanism for ODH of propane under oxygen-free conditions [79].

1.4. Selective oxidation of 2-Butanol

1.4.1. Introduction

Selective oxidation of alcohols to aldehydes/ketones plays an important role in the chemical industry and academia for the production of fine chemicals and fuels [80, 81]. Conventionally, aldehydes/ketones were prepared by the oxidation of alcohols using a stoichiometric amount of oxidants, such as salts of permanganates [82], chromates 83, 84], and bromates [85]. Due to the generation of an enormous quantity of metal wastes, conventional methods are replaced by a catalytic method for the production of aldehydes/ketones. In the homogeneous catalytic method, high catalytic activity towards the desired product was achieved; however, it has a major drawback in the separation and reuse of the catalysts. To overcome these difficulties, the heterogeneous catalytic method was used. It plays a vital role in the separation and reuse of the catalysts; but the challenging task was the synthesis of catalysts with high selectivity towards desired products.

Lower alcohols such as methanol, ethanol, propanol and butanol are the main raw materials for the production of many value-added chemicals using sustainable catalysis [86]. Among them, methanol, as well as ethanol, has been established for H_2 production through steam reforming and partial oxidation. Moreover, methanol is widely studied for formaldehyde production too. The 2-Butanol has several advantages over methanol and ethanol due to the higher hydrogen content, less hygroscopic nature, and low vapor pressure [87]. 2-Butanol can be selectively oxidized to methyl ethyl ketone (MEK) which is a main commodity chemical in the industry [88, 90]. The estimated market size of MEK was over 1.4 MMT in 2014, and to be expected to 1.9 MMT by 2022, which are depicted in Fig. 1.5. Commercially, MEK is produced by the dehydrogenation of 2-Butanol using copper and zinc-based catalyst [91, 92]. The mesoporous Cu-Zn-Al_2O_3 catalyst is active and highly selective for MEK with lower by-products compared with catalyst prepared by normal co-precipitation method [93]. Keuler *et al*. synthesized copper-based catalyst on different supports such as SiO_2 and MgO for 2-Butanol dehydrogenation. The high surface area SiO_2 supported Cu (15 wt %) showed a higher yield than MgO supported catalyst [94]. Lambert *et al.* reported Cu/SiO_2 xerogel catalysts for the dehydrogenation, and interesting observation was observed. The bigger metallic Cu particles located outside silica were more active and responsible for 2-Butanol dehydrogenation [95]. The highly dispersed 3 nm Cu nanoparticle showed the least activity than bigger (15-30 nm) particles.

When compared to conventional process selective catalytic oxidation of 2-Butanol to MEK has conceptual advantages like high conversion of 2-Butanol and exothermicity (Eq. 4.1). Hence, the process is thermodynamically favorable, which helps to provide a workable reaction temperature between 200 and 400 °C. Even though it has numerous advantages over traditional processes, tailoring a highly active catalyst is challenging and selective towards desired products with sustainability, which is an interesting area of research in heterogeneous catalysis.

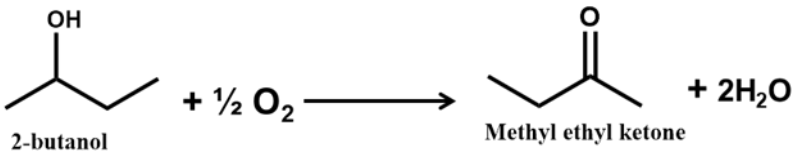

(2.1)

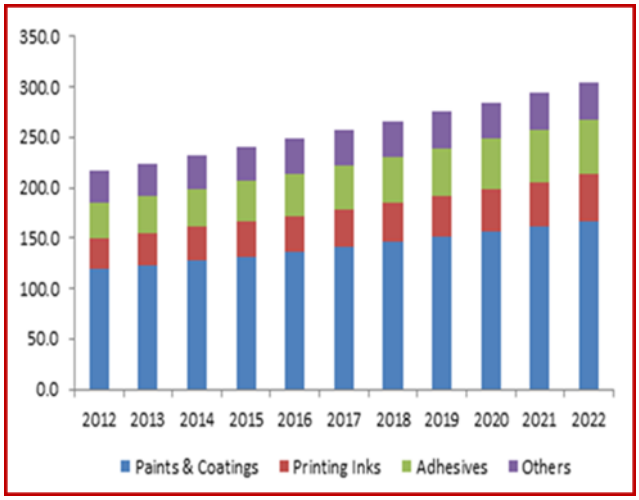

Fig.1.5 Commercially important products from Methyl ethyl ketone [96].

In the past 2-3 decades, researchers started to investigate noble metal-based catalysts for the selective oxidation of 2-Butanol to MEK. **Table 1.4** shows the list of catalysts employed for the 2-Butanol oxidation. The bimetallic AuPd nanoparticle stabilized by polyvinylpyrrolidone (PVP) was utilized for various oxidation reactions of molecules such as benzyl alcohol, 1-Butanol, and 2-Butanol. The 1:3 Au:Pd nanoparticles displayed high activity than the single site Au, Pd, and other bimetallic nanoparticles [97]. Yan and co-workers synthesized Au (111) surface, which can boost the selective oxidation of 2-Butanol with 100 % selectivity of 2-Butanone [98]. Mistry *et al*. investigated shape-dependent Pt nanoparticle (1 nm) supported on γ-Al_2O_3 and achieved high catalytic activity even at low temperature [99]. This study emphasizes the importance of catalysts structure and their catalytic performance.

Table 1.4 Oxidation of 2-Butanol to MEK over different catalyst systems

Catalyst	Reaction Temperature (°C)	Conversion of 2-Butanol (%)	Selectivity of MEK (%)	References
$(Zn_{1-z}In_z)(O_{1-x}N_x)$	400	100	75 (Yield)	100
Cu/SiO_2 xerogel	260	50	100	95
ReO_x/SBA-15	105	100	--	101
Au:Pd NPs	60	65	100	97
Au/Pd (100) alloys	--	18	100	102

1.4.2. Proposed mechanism for the selective oxidation of alcohols over noble metal-based catalysts

Several mechanisms have been proposed for the selective oxidation of alcohols based on the active centers and surface property of the catalysts. There are mainly three important key factors of noble metal catalyst for alcohol oxidation.

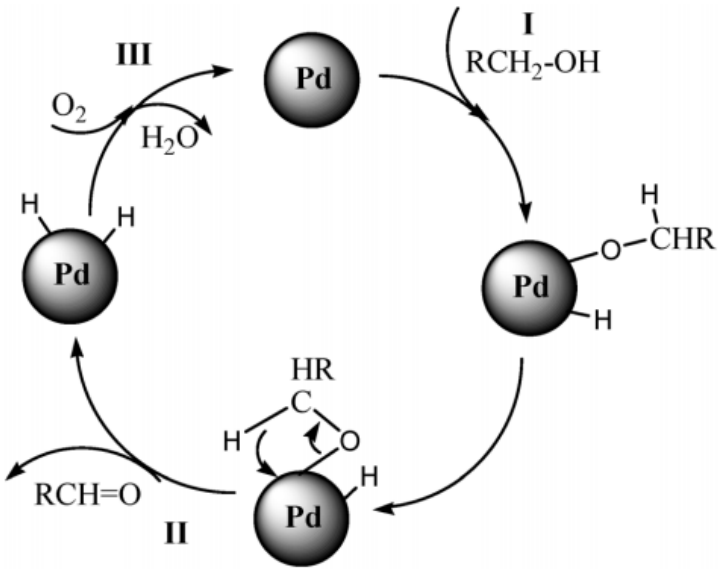

Scheme. 1.2 Mechanism for the selective oxidation of alcohol to represent aldehyde/ketones over noble metal catalysts [103].

The first step is the formation of a metal alkoxide and metal hydride through the insertion of a metal atom in between the O-H bond of alcohol [103]. The second step is proton abstraction by the surface Pd atoms through β-hydride elimination process and finally ends up with aldehyde/ketones as the product [104]. Later, Pd active sites can be regenerated by dioxygen via oxidation of adsorbed hydrogen.

1.4.3. Mechanism for non-noble metal oxide catalysts

So far, the most acceptable mechanism for the selective oxidation of alcohol using non-noble metal oxide catalysts is MvK mechanism [40]. **Scheme 1.3** shows the mechanism where initially lattice oxygen participates in the oxidation process to form aldehydes/ketones. Further, the reduced metal oxide surface of the catalyst is re-oxidized by replenishing with molecular oxygen. The cycle continues until the reaction is complete. A similar mechanism is followed for the gas phase oxidation reactions [105]. This is felicitous for the liquid phase oxidation reactions [106].

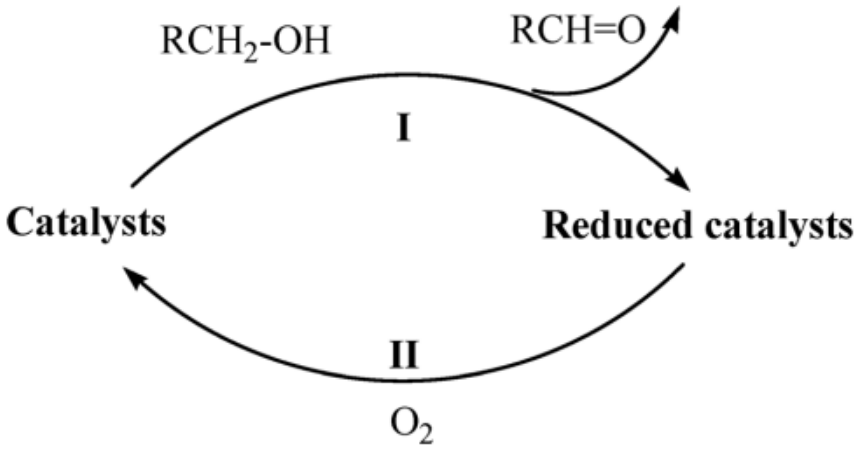

Scheme. 1.3 MvK mechanism for selective oxidation of alcohols to aldehydes over non-noble metal-based catalysts [40].

1.5. Selective oxidation of HMF to FDCA

1.5.1. Introduction

The majority of energy and fuels are currently produced from non-renewable resources, including natural gas, petroleum oil and coal. [107]. However, the global CO_2 level is increasing drastically with the continuous use of fossil-based feedstocks [108, 109]. This causes global climate change and serious environmental pollution. Hence, it is an urgent need to solve the ecological problems. Biomass is an alternative option and the fourth largest source of energy. The demand for the transformation of biomass into value-added products and clean energy fuels is increasing in our day today life due to the sustainability of this process [110, 111]. Biomass can be derived from various sources like lignocellulose, starch, crops, and lipids. The chemical composition of lignocellulose biomass includes cellulose (40-50 %), lignin (20-30 %) and hemicellulose (20-40 %) [112]. Hydrolysis of cellulose to glucose using metal-based catalysts is extensively studied [113]. The transformation of glucose to various value-added products is given in the **Scheme. 1.4**.

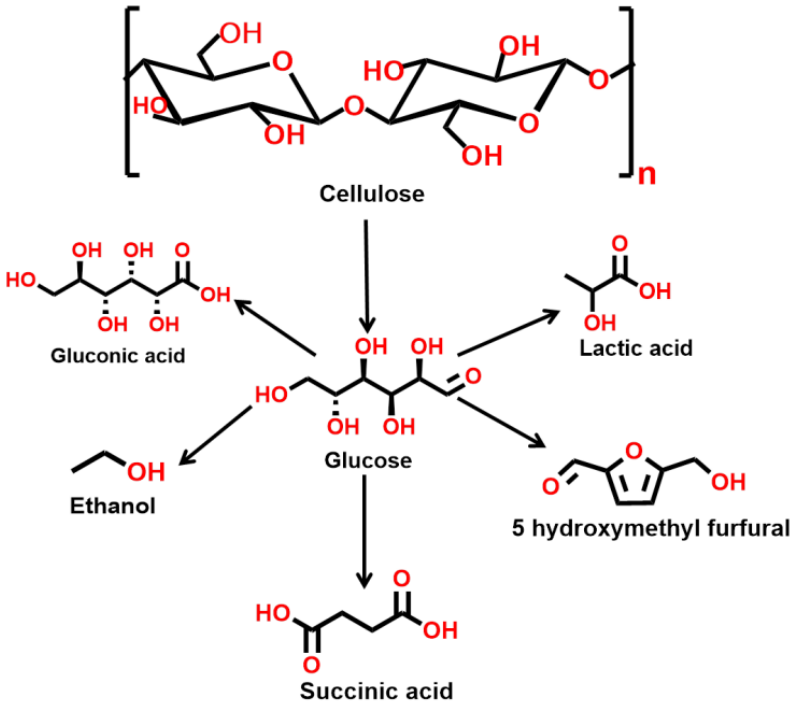

Scheme.1.4 Cellulose hydrolysis and glucose derived products.

In this thesis work, we concentrate on 5-hydroxymethyl furfural (HMF) oxidation, the most important platform molecule which undergoes oxidation, hydrogenation, decarbonylation, hydration, and etherification to produce monomers, platform chemicals, and fuels.

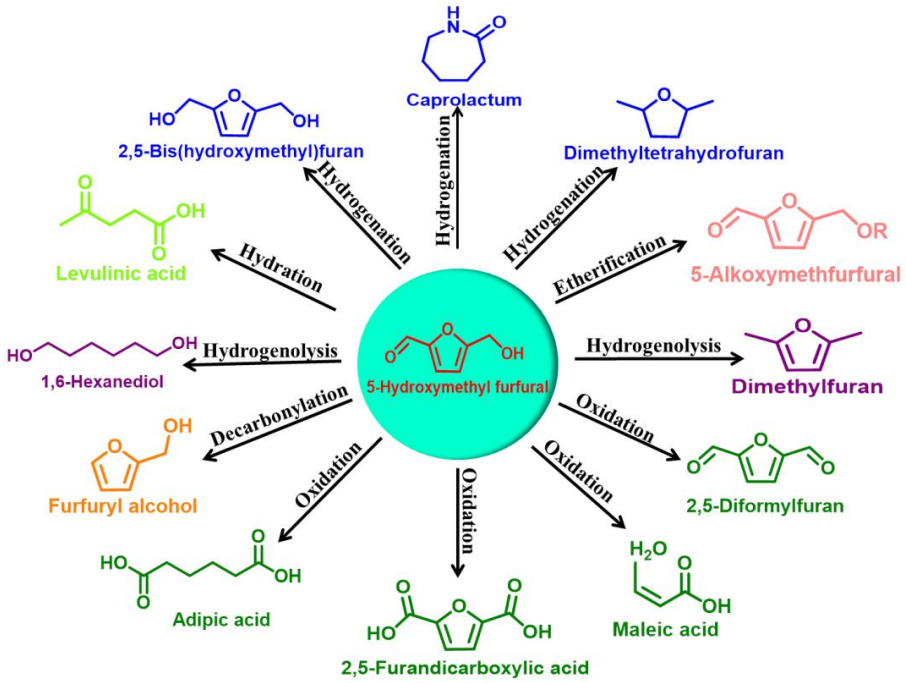

Scheme. 1.5 Valorization of HMF to various value-added products.

The oxidation of HMF can produce several value-added products such as 2,5-diformylfuran (DFF), 5-hydroxymethyl-2-furancarboxylic acid (HMFCA), and furandicarboxylic acid

(FDCA). Among them, FDCA has attracted much attention in academic as well as industry. FDCA is used as the monomer for the production of polyethylene furanoate (PEF), which is used in fiber products, soft drink bottles, and packing materials [114]. FDCA is an alternative to the conventional petroleum-based polyethylene terephthalate (PET) [115].

1.5.2. Homogeneous process

In the past decades, the homogeneous catalyst containing Co/Mn/Zr/Br was used for HMF oxidation using acetic acid as solvent [116]. However, it has several drawbacks, including separation of catalyst from the solvent and reusability of the catalyst. The other two major drawbacks in homogeneous catalysis are the lower yield of FDCA and the formation of by-products.

1.5.3. Heterogeneous process

Increasing demand for FDCA insists on overcoming the difficulties of a homogeneous process. Researchers have been started exploring heterogeneous catalysts using various metals (Au, Pt, Pd, and Ru) and oxides (Mn, Ce) on different supports [117].

1.5.4. Literature review

1.5.4.1. Au supported catalytic systems

Supported noble metal catalysts are highly active and selective for selective oxidation reactions. Generally, noble metal catalysts are supported over high surface area supports to achieve maximum metal dispersion and more active sites. Recently, supported gold catalyst is found more stable and active for HMF oxidation [118]. Au nanoparticles supported on CeO_2 and TiO_2 are more active for this reaction under mild reaction conditions (65-130 ºC, and 10 bar pressure). Interestingly, an increase in Ce^{3+} amount improves catalytic activity. However, most of the Au-supported catalysts require alkali (external base) for the oxidation of HMF to FDCA, which may cause environmental issues. The base free oxidation of Au-supported hydrotalcite (HT) catalyst showed high activity. However, the leaching of Mg^{2+} from HT support could effect catalyst recyclability [119]. **Table. 1.5** represents some of the previous reports available in the literature.

Table 1.5 Selective oxidation of HMF to FDCA over Au supported catalysts

Catalyst	Base	Reaction Temperature (ºC)	Yield of FDCA (%)	References
Au/CeO_2	2 equiv. NaOH	130	96	120
Au/TiO_2	4 equiv. NaOH	130	84	121
Au/C	2 equiv. NaOH	23	7	122
Au-Pd/CNT	Base free	100	96	123

1.5.4.2. Pt and Pd supported catalysts

Platinum (Pt) supported catalysts are very active for HMF oxidation than other noble metal catalysts [124]. Carbon-supported Pt catalyst showed 81 % FDCA yield at 1 bar oxygen [125]. However, Pt supported Al_2O_3, ZrO_2, and CeO_2 require a highly concentrated alkaline medium while the activity is lower than carbon supported catalysts. Other active catalysts for the base-free oxidation of HMF are Pt/PVP and Pt/IP. Palladium (Pd) catalysts are also studied for HMF oxidation and demonstrated reasonable activity. **Table. 1.6** depicts the reported Pt and Pd supported catalysts for HMF oxidation.

Table 1.6 Selective oxidation of HMF to FDCA over Pt and Pd supported catalysts

Catalyst	Base	Reaction Temperature (ºC)	Yield of FDCA (%)	References
Pt/TiO_2	2 equiv. Na_2CO_3	100	84	126
Pt/Al_2O_3	pH = 9	60	99	127
Pt/PVP	Base free	80	94	128
Pd/C	2 equiv. NaOH	23	71	122
Pd/Al_2O_3	1.25 equiv. NaOH	90	78	129
Pd/HT	Base free	100	99	130

1.5.4.3. Ru supported catalysts

Ruthenium (Ru) based catalysts are also studied for HMF oxidation owing to the similarity in properties with Pt and Pd [131]. Presently, Ru supported catalyst are highly active for HMF oxidation to FDCA and **Table. 1.7** shows some of the reported catalysts. Mishra *et al.* studied the oxidation of HMF using air as the oxidant with Ru nanoparticles supported on $MnCo_2O_4$

spinel catalyst with tunable acidic sites, which were crucial for the high yield of FDCA [132]. Later, ZrO_2 support with the high surface area was prepared from silanol-rich SiO_2 aerogel template and 97 % yield of FDCA was achieved after 16 h of reaction [133]. However, many reported systems use high pressure and longer reaction time (16 and 24 h) which are the major problems of this method.

Table 1.7 Selective oxidation of HMF to FDCA over Ru and non-noble metal supported catalysts

Catalyst	**Base**	**Reaction Temperature (°C)**	**Yield of FDCA (%)**	**References**
Ru/C	1 equiv. NaOH	120	69	134
Ru/HAP	Base free	120	99.9	135
MnO_x-CeO_2	$KHCO_3$	110	88.7	136
Co-Mn-0.25	$NaHCO_3$	120	95	137
Fe_xZr_1-O_2	Base free	160	61	138

1.5.4.4. Non-noble metal catalysts

Noble-metal supported catalysts are highly active and have good recyclability. However, they are not economically viable for large-scale production. Researchers started working to attain economic feasibility of the process to carry out the HMF oxidation using non-precious metal oxide catalysts with different oxidants shown in **Table. 1.7**. Commercially available MnO_2 can oxidize HMF to FDCA in the presence of an external base and achieve 91 % FDCA yield at 10 bar O_2 [139]. The enhanced catalytic activity of the catalyst was attributed to high oxygen mobility, and Mn^{4+} is more favorable for HMF oxidation.

1.6. Scope and objective of the thesis

The present thesis deals with the rational designing of efficient catalysts and tuning the catalytic activity in terms of stability and improving catalytic performance for selective oxidation of propane, 2-Butanol, and biomass-derived feedstocks. The developed catalysts were characterized for various chemical and physical properties. The structure-activity-selectivity correlations were examined for tailored catalysts.

1.7. Thesis framework

The thesis is widely split into six chapters.

Chapter 1: Introduction

Chapter 1 describes a general introduction to catalysis and briefly explains commercial dehydrogenation processes and their thermodynamic limitations. The advantages and importance of ODH process over traditional DH methods will be discussed. A brief description of existing catalyst systems for ODH of propane is also given. This chapter also includes a discussion on the valorization of biomass-derived feedstocks to renewable bio-based polymers and the literature overview.

Chapter 2: Synthesis methodology and characterization techniques

This chapter adopted various catalyst synthesis methodologies and their physicochemical properties. The structural activity relationship has been studied by powder XRD, XPS, BET surface area, UV-DRS, TPR, TEM, TGA, ICP-OES, and FTIR etc. The details of the instrumentation techniques have been represented.

Chapter 3: New insights into the composition and catalytic performance of VO_x-Ga/γ-Al_2O_3 for the oxidative dehydrogenation of propane to propene

In chapter 3 brief introduction of oxidative dehydrogenation of propane and its importance are discussed. The designed metal oxide (VO_x-Ga) supported γ-Al_2O_3 catalyst has been studied for the reaction. The optimized catalyst was stable up to 24 h of reaction, and spent catalysts were analyzed to understand more about the surface.

Chapter 4: Effective and selective oxidation of 2-Butanol over Mn supported catalyst systems

A brief introduction of selective oxidation of 2-Butanol to methyl ethyl ketone (MEK) is explained. Metal oxide (Mn_xO_y) with various supports is used for the oxidation of 2-Butanol. The various analysis is done to understand the role of the Mn_3O_4 phase, oxidation state, and metal-support interactions and to improve the selectivity of MEK.

Chapter 5: Selective oxidation of 5-Hydroxymethyl furfural to 2,5-Furandicarboxylic acid

Chapter 5 describes the detailed introduction of HMF oxidation to FDCA and this chapter is divided into two parts.

A. A highly efficient and reusable Ru-NaY catalyst for the base free oxidation of 5-Hydroxymethylfurfural to 2,5-Furandicarboxylic acid

Ruthenium exchanged NaY catalyst shows superior catalytic activity in the selective oxidation of HMF to FDCA using an O_2 oxidant. High metal dispersion, smaller Ru nanoparticles and high availability of metallic Ru play a vital role in obtaining a high yield of FDCA. The influence of surface acidic hydroxyl groups was characterized using different techniques.

B. An enhanced catalytic performance of Ru nanoparticles supported NMC catalyst for the oxidation of HMF to FDCA

Nitrogen-doped mesoporous carbon (NMC) supported catalysts were synthesized using the silica-assisted sol-gel process. The nitrogen content contributed to an increase in the percentage of Ru^0 on the catalysts, resulting in an increase in the number of active catalytic sites.

Chapter 6: summary and conclusions

This chapter discusses and summarizes the many state-of-the-art catalysts that were developed and applied for oxidative dehydrogenation of propane as well as selective oxidation of biomass-derived components. The conclusions of the present study are also associated with some suggestions for future prospects to improve these catalysts and their catalytic performance for selective oxidation.

References

1. A.D. Mc Naught, A. Wilkinson, IUPAC Compendium of Chemical Terminology, 2nd edition, British Royal Society of Chemistry, Cambridge, UK, 1997.
2. J. Berzelius, Ann. Chim. Phys. 61 (1836) 146–151.
3. G.M. Schwab, J.R. Anderson, M. Boudart (Eds.), Catalysis Science and Technology, Vol. 2, Springer, New York, 1981.
4. A. Fusinieri, G. Fisica 7 (1824) 371.
5. M. Faraday, Quart. J. Sci. 16 (1823) 179.
6. F. Cavani, F. Trifiro, Catal. Today 24 (1995) 307–313.
7. M.D. Argyle, K. Chen, A.T. Bell, E. Iglesia, J. Catal. 208 (2002) 139-149.
8. A.K. Venugopal, A.T. Venugopalan, P. Kaliyappan, T. Raja, Green Chem. 15 (2013) 3259–3267.
9. Derouane, E. Parmon,V. Lemos, F. Ribeiro, F. Sustainable Strategies for the Upgradinof Natural Gas: Fundamentals, Challenges, and Oppportunities; Springer: Netherlands, 2003.
10. J.S. Plotkin, Catal. Today 106 (2005) 10−14.
11. J.D. Burrington, C.T. Kartisek, R.K. Grasselli, J. Catal. 87 (1984) 363−380.
12. Appl Petrochem Res. 5 (2015) 377–392.
13. B. Hu, N.M. Schweitzer, G. Zhang, S.J. Kraft, D.J. Childers, M.P. Lanci, J.T. Miller, A.S. Hock, ACS Catal. 5 (2015) 3494–3503.
14. S. Tan, B. Hu, W. Kim, S.H. Pang, J.S. Moore, Y. Liu, R.S. Dixit, J.G. Pendergast, D.S. Sholl, S. Nair, C.W. Jones, ACS Catal. 6 (2016) 5673–5683.
15. Brookes T (2012) new technology developments in the petrochemical industry-refinery integration with petrochemicals to achieve higher value uplift. In: Egypt petrochemicals conference, Cairo-Egypt.
16. Hyde B (2012) Light olefins market review. In: Foro Pemex Petroquimica Mexico, 2012.
17. Propylene from Propane via Dehydrogenation (similar to UOP Oleflex), http://base.intratec.us/home/chemical-processes/propylene/propylene-from-propane-via-dehydrogenation.

18. Propylene from Propane via Dehydrogenation (similar to Lummus CATOFIN), http://base.intratec.us/home/chemicalprocesses/propylene/propylene-from-propane-via-dehydrogenation.
19. O.A. Barias, A. Holmen, E.A. Blekkan, J. Catal. 158 (1996) 1–12.
20. L. Deng, H. Miura, T. Shishido, S. Hosokawa, K. Teramura, T. Tanaka, ChemCatChem 6 (2014) 2680–2691.
21. A. Iglesias, A.M. Beale, K. Maaijen, C.W. Tsu, P. Glatzel, B.M. Weckhuysen, J. Catal. 276 (2010) 268-279.
22. S. Chen, X. Chang, G. Sun, T. Zhang, Y. Xu, Y. Wang, C. Pei, J. Gong, Chem. Soc. Rev. 50 (2021) 3315-3354.
23. C. Li, G. Wang, Chem. Soc. Rev. 50 (2021) 4359-4381.
24. https://www.lummustechnology.com/process-technologies/petrochemicals/propylene-production.
25. https://pdf4pro.com/view/take-the-profitable-path-to-olefins-using-uop-technologies-3984c7.html.
26. J.H.B. Sattler, J.R. Martinez, E.S. Jimenez, B.M. Weckhuysen, Chem. Rev. 114 (2014) 10613−10653.
27. E. Gomez, S. Kattel, B. Yan, S. Yao, P. Liu, J.G. Chen, Nature communications 9 (2018) 1398.
28. X. Wan, C. Zhou, J. Chen, W. Deng, Q. Zhang, Y. Yang, Y. Wang, ACS Catal. 4 (2014) 2175–2185.
29. S.L.T. Andersson, Appl. Catal. A: Gen. 112 (1994) 209-218.
30. Rideal, E. Proc. Cambridge Philos. Soc. 178 (1941) 428.
31. Eley, D. Rideal, E. Proc. R. Soc. London A. 178 (1941) 429−451.
32. Langmuir, I. Trans. Faraday. Soc. 17 (1921) 621−654.
33. A. Khodakov, J. Yang, S. Su, E. Iglesia, A.T. Bell, J. Catal. 177 (1998) 343−351.
34. Creaser, D. Andersson. B. Appl. Catal. A Gen. 141 (1996) 131−152.
35. K. Chen, A.T. Bell, E. Iglesia, J. Phys. Chem. B 104 (2000) 1292-1299.
36. A. Bottino, G. Capannelli, A. Comite, S. Storace, R.D. Felice, Chemi. Engi. Journal. 94 (2003) 11–18.
37. C.A. Carrero, R. Schloegl, I.E. Wachs, R. Schomaecker, ACS Catal. 4 (2014) 3357–3380.
38. Frank, B. Dinse, A. Ovsitser, O. Kondratenko, E. Schomacker. R, Appl. Catal. A. Gen. 323 (2007) 66−76.

39. D.R. Lide, Handbook of Chemistry and Physics, Ed. CRC press, 71st ed. (1990) 9–95.
40. Mars, P. Van Krevelen, D.W. Eng. Sci. 3 (1954) 41−57.
41. L. Leveles, K. Seshan, J.A. Lercher, L. Lefferts, J. Catal. 218 (2003) 296–306.
42. A.F. Carley, P.R. Davies, M.W. Roberts, Catal. Today 169 (2011) 118−124.
43. J. Pless, B. Bardin, H. Kim, D. Ko, M.T. Smith, R.R. Haammond, P.C. Stair, K.R. Poeppelmeier, J. Catal. 223 (2004) 419−431.
44. Z. Zhao, X. Gao, I.E. Wachs, J. Phys. Chem. B 107 (2003) 6333−6342.
45. L.Yuan, S. Bhatt, G. Beaucage, V.V. Guliants, S. Mamedov, R.S. Soman, J. Phys. Chem. B 109 (2005) 23250−23254.
46. B. Frank, J. Zhang, R. Blume, R. Schlogl, D.S. Su, Angew.Chem. Int. Ed. 48 (2009) 6913−6917.
47. M.D. Argyle, K. Chen, A.T. Bell, E. Iglesia, J. Catal. 208 (2002) 139−149.
48. R. Grabowski, Appl. Catal. A. Gen. 270 (2004) 37−47.
49. E.V. Kondratenko, M. Cherian, M. Baerns, R. Schloegl, X. Wang, I.E. Wachs, D. Su, J. Catal. 234 (2005) 131−142.
50. Hofmann, A.G. Pirovano, M.V. Sauer, J. Phys. Chem.C 113 (2009) 18191−18203.
51. X. Rozanska, R. Fortrie, J.J. Sauer, J. Am. Chem. Soc. 136 (2014) 7751−7761.
52. J.T. Grant, C.A. Carrero, A.M. Love, R. Verel, I. Hermans, ACS Catal. 5 (2015) 5787−5793.
53. N. Dimitratos, J.C. Vedrine, Catal. Today 81 (2003) 561-571.
54. M. Bismillah, Ansari, S.E. Park, Energy Environ. Sci. 5 (2012) 9419–9437.
55. I.A. Bakare, S. Adamu, M. Qamaruddin, S.A.A. Bogami, S. Al. Ghamdi, M.M. Hossain, Ind. Eng. Chem. Res. 58, 25 (2019) 10785–10792.
56. P. Concepcion, A. Galli, J.M.L. Nieto, A. Dejoz, M.I. Vazquez, Top. Catal. 3 (1996) 451–460.
57. X. Gao, I.E. Wachs, J. Phys. Chem. B 104 (2000) 1261-1268.
58. Rase, H. F. Handbook of Commercial Catalysis; CRC: New York, 2000.
59. C. Xiong, S. Chen, P. Yang, S. Zha, Z.J. Zhao, J. Gong, ACS Catal. 9 (2019) 5816–5827.
60. K. Alexopoulos, M.F. Reyniers, G.B. Marin, J. Catal. 289 (2012) 127–139.
61. Y. Wang, P. Hu, J. Yang, Y.A. Zhu, D. Chen, Chem. Soc. Rev. 50 (2021) 4299-4358.
62. M. Hoj, A.D. Jensen, J.D. Grunwaldt, Appl. Catal. A: Gen. 451 (2013) 207–215.
63. F. Luo, C.J. Jia, R.L.L. D. Sun, C.H Yan, Materials Research Bulletin 48 (2013) 1122–1127.

64. R. You, X. Zhang, L. Luo, Y. Pan, H. Pan, J. Yang, L. Wu, X. Zheng, Y. Jin, W. Huang, J. Catal. 348 (2017) 189–199.
65. G. Mitran, T. Cacciaguerra, S. Loridant, D. Tichit, I.C. Marcu, Appl. Catal. A Gen. 417-418 (2012) 153-162.
66. B. Solsona, T. Blasco, J.M.L. Nieto, M.L. Pena, Frey, A.V. Moya, J. Catal. 203 (2001) 443–452.
67. Y.M Liu, Y. Cao, K.K. Zhu, S.R. Yan, W.L. Dai, H.Y. He, K.N. Fan, Chem. Commun. (2002) 2832-2833.
68. Q. Liu, J. Li, Z. Zhao, M. Gao, L. Kong, J. Liu, Y. Wei, Catal. Sci. Technol. 6 (2016) 5927–5941.
69. A. Wegrzyniak, S. Jarczewski, P. Kustrowski, P. Michorczyk, J. Porous Mater 25 (2018) 687-696.
70. S.A. Karakoulia, K.S. Triantafyllidis, A.A. Lemonidou, Micro and Mesoporous materials, 110 (2008) 157-166.
71. J. Sheng, B. Yan, W.D. Lu, B. Qiu, X.Q. Gao, D. Wang, A.H. Lu, Chem. Soc. Rev. 50 (2021) 1438-1468.
72. J. Tian, J. Tan, M. Xu, Z. Zhang, S. Wan, S. Wang, J.D. Lin, Y. Wang. Sci. Adv. 5 (2019):eaav8063.
73. P. Chaturbedy, M. Ahamed, M. Eswaramoorthy, ACS Omega 3 (2018) 369−374.
74. J.T. Grant, W.P. McDermott, J.M. Venegas, S.P. Burt, J. Micka, S.P. Phivilay, C.A. Carrero, I. Hermans, ChemCatChem 9 (2017) 3623-3626.
75. X. Liu, D.S. Su, R. Schlogl, Carbon 46 (2008) 544 –561.
76. L. Liu, Q.F. Deng, B. Agula, T.Z. Ren, Y.P. Liu, B. Zhaorigetu, Z.Y. Yuan, Catal.Today 186 (2012) 35–41.
77. I.A. Bakare, M. Shamseldin, S.A. Razzak, S.A. Al-Ghamdi, M.M. Hossain, H.I. de Lasa, Chem. Eng. J. 278 (2015) 207–216.
78. S.A.A. Ghamdi, M. Volpe, M.M. Hossain, H.I. De Lasa, Appl.Catal. A. Gen. 450 (2013) 120–130.
79. A. Sameer. Al-Ghamdi, H.I. De Lasa, Fuel 128 (2014) 120–140.
80. W. Hou, N.A. Dehm, R.W.J. Scott, J. Catal. 253 (2008) 22−27.
81. T. Yan, J. Gong, C.B. Mullins, J. Am. Chem. Soc. 131 (2009) 16189−16194.
82. F.M. Menger, C. Lee, Tetrahedron Lett. 22 (1981) 1655–1656.
83. K.P.C. Vollhardt, N.E. Schore, Organic Chemistry: Structure and Function, Freeman, New York, 1999, p. 300.

84. D.G. Lee, U.A. Spitzer, J. Org. Chem. 35 (1970) 3589–3590.
85. C.K. Lee, B.S. Koo, Y.S. Lee, H.K. Cho, K.J. Lee, Bull. Korean Chem Soc. 23 (2002) 1667–1670.
86. J. Zhang, L. Wei, X. Man, X. Jiang, Y. Zhang, E. Hu, Z. Huang, Energy Fuels. 26 (2012) 3368–3380.
87. G.A. Nahar, S.S. Madhani, Int. J. Hydrogen Energy 35 (2010) 98−109.
88. P. Dagaut, S.M. Sarathy, M. Thomson, J. Proc. Combust. Inst. 32 (2009) 229−237.
89. A.V. Tran, R.P. Chambers, Biotechnol. Bioeng. 29 (1987) 343−351.
90. A. Multer, N. McGraw, K. Hohn, P. Vadlani, Ind. Eng. Chem. Res. 52 (2013) 56−60.
91. L. Zhenhua, H.U.O. Wenzhou, M.A. Hao, Q. Kai, Chin. J. Chem. Eng. 14, 5 (2006) 676–684.
92. G. Ertl, H. Knozinger, J. Weitkamp, Handbook of Heterogeneous Catalysis, vol.5, VCH, Weinheim, Germany, 1997, pp. p2140.
93. D. Fang, W. Ren, Z. Liu, X. F. Xu, L. Xu, H. Lu, W. Liao, H. Zhang, J. Nat. Gas Chem.18 (2009) 179.
94. J.N. Keuler, L. Lorenzen, S. Miachon, Appl. Catal. A: Gen. 218 (2001) 171.
95. S. Lambert, C. Cellier, F. Ferauche, E.M. Gaigneaux, B. Heinrichs, Catal. Com. 8 (2007) 2032–2036.
96. https://www.gminsights.com/industry-analysis/methyl-ethyl-ketoneMEK-market (accessed Oct 04, 2020).
97. W. Hou, N.A. Dehm, R.W.J. Scott, J. Catal. 253 (2008) 22–27.
98. T. Yan, J. Gong, C.B. Mullins, J. Am. Chem. Soc. 131 (2009) 16189−16194.
99. H. Mistry, F. Behafarid, E. Zhou, L.K. Ono, L. Zhang, B.R. Cuenya, ACS Catal. 4, 1 (2013) 109–115.
100. M. Maitri, S. Kumarsrinivasan, D.S. Bhange, B. Saha, P. Chakraborty, A.K. Viswanath, C.S. Gopinath, Chem. Mater. 22 (2010) 565–578.
101. X. She, J.H. Kwak, J. Sun, J. Hu, M.Y. Hu, C. Wang, C.H.F. Peden, Yong Wang, ACS Catal. 2 (2012) 1020−1026.
102. Z. Li, W.T. Tysoe, Surface Science 694 (2020) 121556.
103. Z. Guo, B. Liu, Q. Zhang, W. Deng, Y. Wang, Y. Yang, Chem. Soc. Rev. 43 (2014) , 3480-3524.
104. K. Mori, T. Hara, T. Mizugaki, K. Ebitani, K. Kaneda, J. Am. Chem. Soc. 126 (2004) 10657–10666.

105. I.W.C.E. Arends, R.A. Sheldon, M. Wallau, U. Schuchardt, Angew. Chem. Int. Ed. Engl. 36 (1997) 1144–1163.
106. V.D. Makwana, Y.C. Son, A.R. Howell, S.L. Suib, J. Catal. 210 (2002) 46–52.
107. A. Corma, A.S. Iborra, A. Velty, Chem. Rev. 107, 6 (2007) 2411–2502.
108. B. Kahn, Earth's CO_2 Passes the 400 PPM Threshold—Maybe Permanently, Climate Central, 2016.
109. M.R. Lloret, G. Rothenberg, N.R. Shiju, ChemSusChem 12 (2019) 3896–3914.
110. J.N. Chheda, G.W. Huber, J.A. Dumesic, Angew. Chem. 119 (2007) 7298.
111. S.R.A. Kersten, W.P.M.V. Swaaij, L. Lefferts, K. Seshan, Catalysis for Renewables: From Feedstock to Energy Production (Eds.: G. Centi, R. A. van Santen), Wiley-VCH, Weinheim, 2007; in particular, chap. 6, p. 119.
112. Y. Sun, J. Cheng, Bioresour. Technol. 83 (2002) 1–11.
113. M. Besson, P. Gallezot, C. Pinel, Chem. Rev. 114 (2014) 1827–1870.
114. E. De Jong, M.A. Dam, L. Sipos, G.J. M. Gruter, ACS Symp. Ser. 1105 (2012) 1–13.
115. A. Gandini, A.J.D. Silvestre, C.P. Neto, A. F. Sousa, M.J.J. Gomes, Polym. Sci., Part A: Polym. Chem. 47 (2009) 295–298.
116. W. Partenheimer, V.V. Grushin, Adv. Synth. Catal. 343 (2001) 102–111.
117. M. Sajid, X. Zhao, D. Liu, Green Chem. 20 (2018) 5427-5453.
118. M. Pan, A.J. Brush, Z.D. Pozun, H.C. Ham, W.Y. Yu, G. Henkelman, G.S. Hwang, C.B. Mullins, Chem. Soc.Rev. 42 (2013) 5002-5013.
119. N.K. Gupta, S. Nishimura, A. Takagaki, K. Ebitani, Green Chem. 13 (2011) 824.
120. O. Casanova, S. Iborra, A. Corma, ChemSusChem, 2 (2009) 1138–1144.
121. S. Albonetti, A. Lolli, V. Morandi, A. Migliori, C. Lucarelli, F. Cavani, Appl. Catal. B 163 (2015) 520–530.
122. S.E. Davis, L.R. Houk, E.C. Tamargo, A.K. Datye, R.J. Davis, Catal. Today, 160 (2011) 55–60.
123. X. Wan, C. Zhou, J. Chen, W. Deng, Q. Zhang, Y. Yang, Y. Wang, ACS Catal. 4 (2014) 2175–2185.
124. Z. Zhang, K. Deng, ACS Catal. 5 (2015) 6529–6544.
125. P. Verdeguer, N. Merat, A. Gaset, J. Mol. Catal. 85 (1993) 327–344.
126. H.A. Rass, N. Essayem, M. Besson, ChemSusChem 8 (2015) 1206–1217.
127. R. Sahu, P.L. Dhepe, React. Kinet. Mech. Catal. 112 (2014) 173–187.
128. S. Siankevich, G. Savoglidis, Z. Fei, G. Laurenczy, D.T.L. Alexander, N. Yan, P.J. Dyson, J. Catal. 315 (2014) 67–74.

129. B. Siyo, M. Schneider, J.J. Radnik, M.M.M. Pohl, P. Langer, N. Steinfeldt, Appl. Catal. A.Gen. 478 (2014)107–116.
130. Y. Wang, K. Yu, D. Lei, W. Si, Y. Feng, L.-L. Lou, S. Liu, ACS Sustainable Chem. Eng. 4 (2016) 4752–4761.
131. M.E. Zakrzewska, E.B. Lukasik, R.B. Lukasik, Chem. Rev. 111 (2011) 397–417.
132. D.K. Mishra, H.J. Lee, J. Kim, H.S. Lee, J.K. Cho, Y.W. Suh, Y. Yi, Y.J. Kim, Green Chem. 19 (2017) 1619–1623.
133. C.M. Pichler, M.G.A. Shaal, H. Joshi, W. Ciptonugroho, F. Schuth, ChemSusChem 11 (2018) 2083–2090.
134. K.R. Vuyyuru, P. Strasser, Catal. Today 195 (2012) 144–154.
135. T. Gao, Y. Yin, W. Fang, Q. Cao, Mol. Catal. 450 (2018) 55–64.
136. X. Han, C. Li, X. Liu, Q. Xia, Y. Wang, Green Chem. 19 (2017) 996-1004.
137. K.T.V. Rao, J.L. Rogers, S. Souzanchi, L. Dessbesell, M.B. Ray, C. Charles Xu, ChemSusChem 11 (2018) 3323–3334.
138. D. Yan, J. Xin, Q. Zhao, K. Gao, X. Lu, G. Wang, S. Zhang, Catal. Sci. Technol. 8 (2018) 164.
139. E. Hayashi, T. Komanoya, K. Kamata, M. Hara, ChemSusChem 10 (2017) 654-658.

Chapter-2

Synthesis methodology and characterization techniques

2.1. Introduction

This chapter describes the design of various catalysts and characterization techniques for better understanding the structure-activity relationship and tailoring the catalysts accordingly to improve the desired yield of the products. The suitable catalyst and method of preparation play a vital role in attaining high selectivity and stable activity. The Physico-chemical properties of materials were extensively studied to understand the nature of the catalysts. The structural characterization of all the synthesized catalysts was executed using powder XRD, electron microscopy, and N_2-sorption. These techniques confer information about crystallinity, particle size, structural morphology, and textural properties. The structural integrity of the catalysts was carried out using X-ray photoelectron spectroscopy (XPS), Fourier-transform infrared spectroscopy (FTIR), Raman spectroscopy, UV-visible spectroscopy, Inductively coupled plasma-optical emission spectroscopy (ICP-OES), Temperature programmed desorption (TPD), Temperature programmed reduction (TPR) and Thermogravimetric analysis (TGA).

2.2. Description of chemicals and gases used for this work

Table 2.1 List of chemicals used for the synthesis

Chemicals name	**Formula**	**Purity and Make**
Ammonium metavanadate	NH_4VO_3	99 %, Sigma Aldrich
Gallium nitrate	$Ga(NO_3)_3 \cdot xH_2O$	99.9 %, Sigma Aldrich
Oxalic acid	$C_2H_2O_4$	98 %, Merck
Aluminum oxide	γ-Al_2O_3	99.9 %, Alfa Aesar
Manganese nitrate	$Mn(NO_3)_2 \cdot 4H_2O$	98 %, Alfa Aesar
Aluminium nitrate	$Al(NO_3)_3 \cdot 9H_2O$	95 %, Alfa Aesar
Cerium nitrate	$Ce(NO_3)_3 \cdot 6H_2O$	99.9 % , Sigma Aldrich
Zirconyl nitrate	$ZrO(NO_3)_2 \cdot H_2O$	99.5 %, Loba Chemie
TEOS	$Si(OC_2H_5)_2$	98 %, Sigma Aldrich

Sodium hydroxide	NaOH	98 %, Merck
Ethanol	C_2H_5OH	99.9, CSS
Hydrochloric acid	HCl	37 %, Merck
2-Butanol	$C_4H_{10}O$	99 %, Alfa Aesar
NaY Zeolite	CBV-100, Si/Al ratio = 2.5	Zeolite international, USA
Ruthenium chloride	$RuCl_3.xH_2O$	99.9 %, Sigma Aldrich
Phenol	C_6H_5OH	99.9 %, Loba Chemie
Melamine	$C_3H_6N_6$	99.9 %, Loba Chemie
Formaldehyde	CH_2O	99.9 %, Loba Chemie
Sodium Borohydride	$NaBH_4$	99.9 %, Sigma Aldrich
Ludox AS-40	SiO_2	40 wt. % SiO_2 in water, Sigma Aldrich
5-hydroxymethylfurfural	$C_6H_6O_3$	99 %, Sigma Aldrich
2,5-furandicarboxylic acid	$C_6H_4O_5$	97 %, Sigma Aldrich
2,5-diformylfuran	$C_6H_4O_3$	97 %, Sigma Aldrich
5-hydroxymethyl-2-furan carboxylic acid	$C_6H_6O_4$	97 %, Sigma Aldrich
5-formyl-2-furan carboxylic acid	$C_6H_4O_4$	97 %, Sigma Aldrich

Gases and calibration gas mixtures used for selective oxidation reaction and catalyst characterization techniques are listed in **Table 2.2**

Table 2.2 List and applications of the gases used

Gas	Purity	Application	Supplier
Propane	99.9 %	Reactant gas	USA
Oxygen	99.5 %	Reactant gas	Vadilal Chemicals Ltd, India
Nitrogen (N_2), Hydrogen (H_2), Argon (Ar)	99.9 % 99.9 % 99.9 %	GC GC GC	Vadilal Chemicals Ltd, India
Helium	99.9 %	N_2-sorption, TPR , TPD	Vadilal Chemicals Ltd, India
Zero Air	99.9 %	GC, TGA	Vadilal Chemicals Ltd, India
Calibration gas mixtures	99.9 %	GC	Chemtron Science Laboratories, India
10 % CO_2/He	99.9 %	TPD	Vadilal Chemicals Ltd, India
10 % NH_3/He	99.9 %	TPD	Vadilal Chemicals Ltd, India
5 % H_2/Ar	99.9 %	TPR	Vadilal Chemicals Ltd, India
10 % O_2/He	99.9 %	TPR	Vadilal Chemicals Ltd, India

2.3. Catalyst synthesis

2.3.1. Synthesis of vanadium and gallium oxide supported on γ-Al_2O_3

The catalysts were prepared by an incipient wetness impregnation method. The amount of support; commercial γ-Al_2O_3 was suspended in 30 ml of distilled water, and the solution was sonicated for 45 min to get uniform dispersion. To this, the desired amount of ammonium metavanadate and gallium nitrate dissolved in an aqueous oxalic acid solution was added dropwise. After impregnation, the resulting mixture was stirred at 80 ºC for 3 h. The resulting material was dried at 120 °C for overnight followed by calcination at 560 °C for 4 h. A series of catalysts were prepared with different ratios of VO_x and Ga supported γ-Al_2O_3 and are denoted in **Table 2.3**.

Table 2.3 Catalyst compositions and sample codes

S.No.	Molar ratio	Sample code
1	10 % VO_x/γ-Al_2O_3	VO_x/γ-Al_2O_3
2	V_8Ga_2/γ-Al_2O_3	VGA-1
3	V_7Ga_3/γ-Al_2O_3	VGA-2
4	V_6Ga_4/γ-Al_2O_3	VGA-3
5	V_5Ga_5/γ-Al_2O_3	VGA-4
6	V_3Ga_7/γ-Al_2O_3	VGA-5
7	10 % Ga/γ-Al_2O_3	Ga/γ-Al_2O_3

2.3.2. Preparation of manganese oxide supported catalysts

2.3.2.1. Hydrothermal method

Mn-supported catalysts were synthesized by co-precipitation followed by the hydrothermal method [1]. The procedure is as follows: the metal nitrate precursors $Mn(NO_3)_2{\cdot}4H_2O$ and $Al(NO_3)_3{\cdot}9H_2O$ taken in a 1:1 molar ratio were dissolved in deionized water. The precipitating agent (NaOH) was added dropwise at constant pH (9.5 ± 0.2) to a 500 ml beaker, which was stirred. The solution was transferred into a Teflon-lined autoclave for hydrothermal synthesis and kept at 150 ºC for 12 h. Further, the precipitate was filtered, washed with distilled water, and dried at 110 ºC overnight; this catalyst was calcined at 450 ºC at 2 ºC min^{-1} for 6 h (Mn_xO_y-Al_2O_3). Similarly, Mn_xO_y-CeO_2 and Mn_xO_y-ZrO_2 catalysts were also prepared by the same procedure. The above-calcined catalysts are denoted as MA (Mn_xO_y-Al_2O_3), MC (Mn_xO_y-CeO_2), and MZ (Mn_xO_y-ZrO_2).

2.3.2.2. Sol-gel method

Mn-supported SiO_2 catalyst was synthesized by sol-gel method [2]. $Mn(NO_3)_2{\cdot}4H_2O$ and TEOS (1:1 molar ratio) was diluted using ethanol, and the solution was stirred at room temperature to get a clear homogeneous solution. Half of the alcohol was used for this, and another half was used to dilute water and acid. The mixed solution of EtOH-H_2O-HCl was added dropwise to the above Mn-TEOS-EtOH solution with constant stirring. After complete incorporation, the solution was stirred at 40 ºC for 12 h. Then the solution was dried at 110 ºC for overnight and calcined at 450 ºC for 6 h. Finally, the calcined Mn_xO_y-SiO_2 catalyst was labeled as MS.

2.3.3. Synthesis of Ru-NaY nanoparticles by ion-exchange method

The Synthesis of Ru nanoparticles by the ion-exchange method has been described in **Scheme 2.1**. Briefly, an appropriate amount of NaY zeolite was suspended in 30 ml of deionized water. The above solution was sonicated for 0.5 h at room temperature to get well dispersion of the NaY zeolite. To this 12 ml of $RuCl_3$ solution was added dropwise (for 3 wt % Ru-NaY), and the mixture was stirred at 80 °C for 3 h. Later, the solution was cooled down to room temperature, and then an aqueous solution of $NaBH_4$ ($Ru/NaBH_4$, 1:4) was added dropwise to the resulting mixture in a closed system with constant stirring to obtain metallic Ru. The final mixture was filtered and washed thoroughly with 2-liter deionized water. Finally, the filtered sample was dried at 110 °C for 10 h and denoted as 3 wt % Ru-NaY. A similar synthesis procedure was followed for 1 %, 2 %, and 5 wt % Ru-NaY catalysts with a calculated amount of Ru precursor.

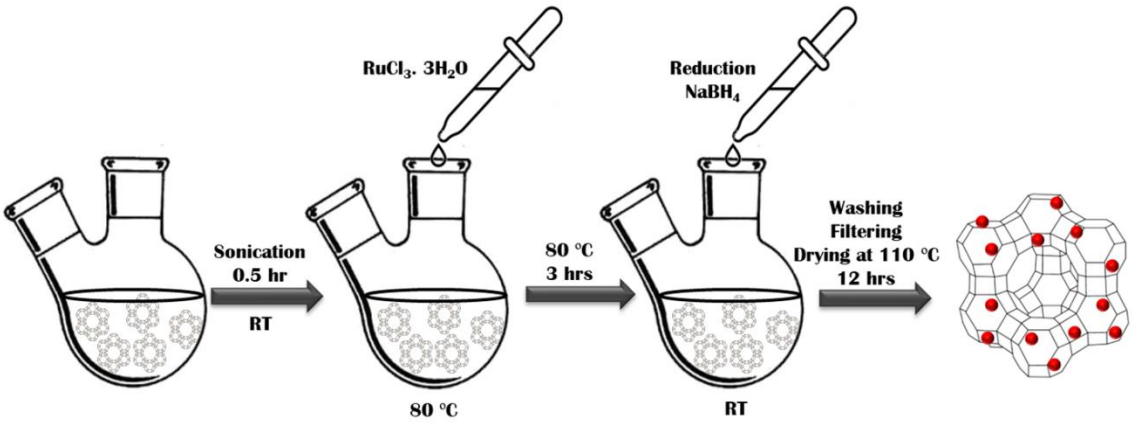

Scheme 2.1 Graphical representation of the synthesis technique for Ru exchanged NaY zeolite.

2.3.4. Synthesis of Ru nanoparticles supported on nitrogen-doped mesoporous carbon (NMCs) catalyst

2.3.4.1 Preparation of nitrogen-doped mesoporous carbon (NMC)

The synthesis procedure is shown in **scheme 2.2**, 39 mmol of phenol (carbon source) and 107 mmol of formaldehyde were dissolved in 0.2 M NaOH, and this solution was stirred at 70 °C for 45 min [3]. To this, 39 mmol of melamine (nitrogen source) and 107 mmol of formaldehyde were added and stirred at 70 °C for 1 h. To this, 37.5 g of Ludox AS-40 (40 % SiO_2) was added dropwise, and the solution was kept for aging for 1 hour. The final solution was transferred to a polypropylene bottle and kept in an oven at 80 °C for 5 days. The resulting colloidal mixture was dried at 80 °C for 2 days, ground to fine powders, and

carbonized at 800 °C under N_2 flow atmosphere for 3 h (heating rate 5 °C/min). The black residue was dissolved in 2 M NaOH at 80 °C for 12 h in order to remove silica from the polymer framework. The solution was washed with distilled water and dried at 110 °C for 12 h. The variation in nitrogen content was accomplished by changing the mole proportion of melamine to phenol (M/P), as given in **Table 5B.1**. Accordingly, the silica-free nitrogen-doped mesoporous carbon was named as NMC-x (x =1 and 2). The nitrogen-free mesoporous carbon (MC) was also combined, utilizing a similar procedure without melamine.

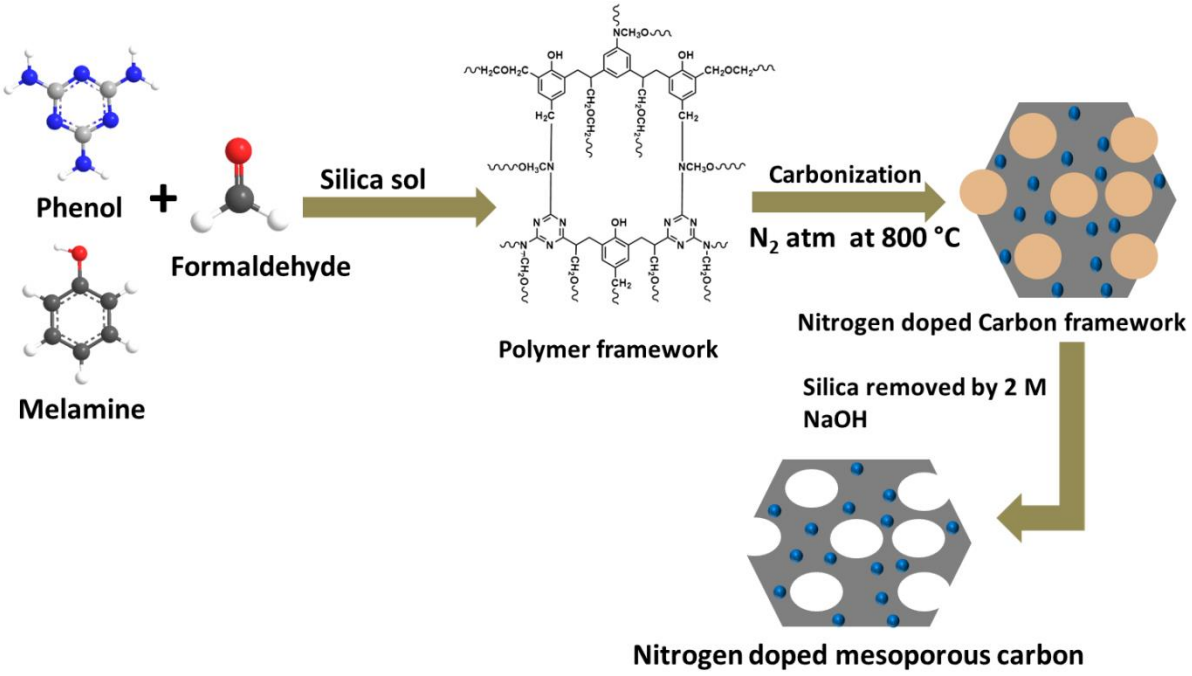

Scheme 2.2 Schematic diagram for the synthesis of nitrogen-doped mesoporous carbon.

2.3.4.2 Synthesis of Ru supported NMCs catalysts

The Ru-supported carbon catalyst (NMC) was prepared by the incipient wetness impregnation method [3]. Initially, an appropriate quantity of NMC was disseminated into 40 ml of distilled water and sonicated for 45 min. To this, the desired amount of Ru ($RuCl_3 \cdot xH_2O$, 4.6 mg/ml) was added slowly, and the solution was heated at 80 °C with continuous stirring for 6 h. Later, it was cooled down to room temperature and reduced by an aqueous solution of sodium borohydride (metal/$NaBH_4$ is 1:4). The catalyst was recovered by filtration and thoroughly washed with distilled water to remove chloride ions from the solution. The obtained resultant was dried at 110 °C for 12 h. Ru metal was loaded in different amounts employing the same synthesis procedure. The final catalysts were denoted as 3 wt % Ru-NMC-1, 2 wt % Ru-NMC-2, 3 wt % Ru-NMC-2, 4 wt % Ru-NMC-2, and 5 wt

% Ru-NMC-2 catalyst, which were used for HMF oxidation. The Ru-supported mesoporous carbon (MC) was also synthesized using above mentioned strategy.

2.4. Catalyst characterization

Catalyst development plays one of the major roles in heterogeneous catalysis to improve catalytic activity. Characterization of the synthesized catalyst is another important factor in understanding the active sites, reaction mechanism, and structure-activity-selectivity correlation for designing efficient catalysts to enhance activity and durability. A brief explanation and operating principle of several characterization techniques used in this present work are given below.

2.4.1. Powder X-ray diffraction (PXRD)

X-ray diffraction is one of the most significant and widely used techniques for catalyst characterization to study crystal structures and atomic spacing. It is based on the interference pattern of monochromatic X-rays and the crystalline nature of the sample [4]. This hypothesis was developed by W.H. Bragg and W.L. Bragg and was awarded by Nobel Prize in physics in 1915. The interaction of incident X-rays with the material produces constructive interference when stipulation satisfy Bragg's law [4, 5]. The mathematical expression of Bragg's law is,

$$n\lambda = 2d\sin\theta \qquad (2.1)$$

Where,

λ is the wavelength of the rays

n is the order of diffraction

d is the interplanar spacing

θ is the diffraction angle

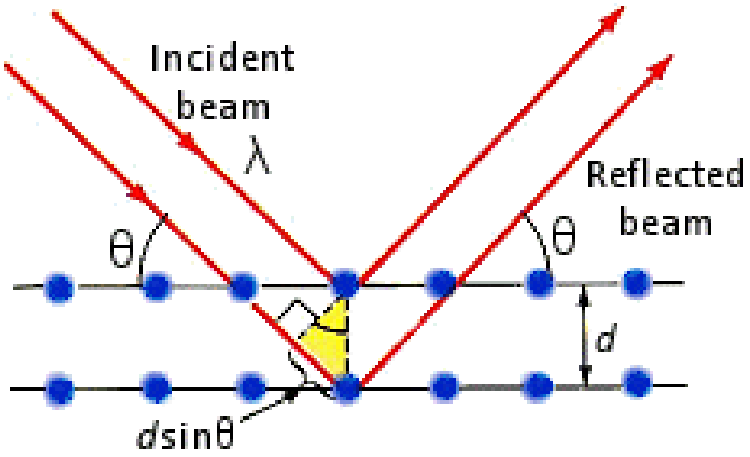

Fig. 2.1 Depiction of X-ray diffraction principle.

The powder X-ray diffraction furnished the details of lattice constant ionic radius and identifies crystalline phases. The average crystallite size can be calculated using the Debye-Scherrer formula by employing XRD line broadening [6].

$$t = 0.9\lambda / \beta Cos\theta \qquad (2.2)$$

Where, t- is the thickness of the crystallites (Å), λ- is the X-ray wavelength, β- is the structural broadening, and θ- is the Bragg angle. Powder X-ray diffraction (XRD) measurement of as-synthesized catalysts reported in this thesis was executed using Malvern PANalytical X pert pro dual goniometer with Ni as the filter and Cu Kα (λ =1.5418 Å) source with step size of 0.008° and a scan rate of 0.5° min^{-1} using a flat holder Bragg-Brentano geometry.

2.4.2. N_2 Physisorption

The N_2- physisorption is an important technique to identify the specific surface area and porosity of the materials. The multilayer adsorption was developed by Brunauer, Emmet, and Teller in 1938, by adsorbing N_2 gas on the catalyst surface at 77 K. The surface area was calculated by using the BET equation given below [7].

$$\frac{1}{V[(P_0/P)-1]} = \frac{C-1}{V_m c}\left(\frac{P}{P_0}\right) + \frac{1}{V_m c} \qquad (2.3)$$

Where,

P is the adsorption of equilibrium pressure

P_0 is the adsorption of saturation pressure

V_m is the volume of adsorbate required for monolayer coverage

C is the BET constant, and **V** is the volume of gas at STP

BET surface area of the catalyst is operated at constant temperature by the plotting volume of the gas adsorbed as a function of partial pressure. A linear relationship between $P/V(P_0/P)$ and P/P_0 is necessary to calculate the Nitrogen gas adsorbed. The limited portion of isotherm can be used in the relative pressure range from 0.05 to 0.3.

The Nitrogen sorption measurement was measured by (Quantachrome Autosorb IQ, USA) at -196 °C. The specific surface areas of the catalysts were determined by Brunauer-Emmett-Teller (BET) equation.

2.4.3. Transmission Electron Microscopy (TEM)

Transmission electron microscopy is a foremost technique that offers unique properties to gain more insights into the structure, composition of materials, topology, size, and shape of the particles. **Fig. 2.2** represents a typical TEM instrument. The working principle is a beam of electrons from an electron gun strikes on the materials using an objective lens. The beam of electrons is moderately transmitted through the materials depending upon the thickness and electron density of the materials. The transmitted electrons beam is viewing and focusing an image and recorded in a charge-coupled device (CCD) camera.

High-resolution transmission electron microscopy (HR-TEM) and high angle annular dark-field scanning TEM (HAADF-STEM) were collected on an FEI Technai TF-30 instrument operating at 300 k V. The powder samples were ultrasonically dispersed using isopropyl alcohol and deposited onto a carbon-coated copper grid.

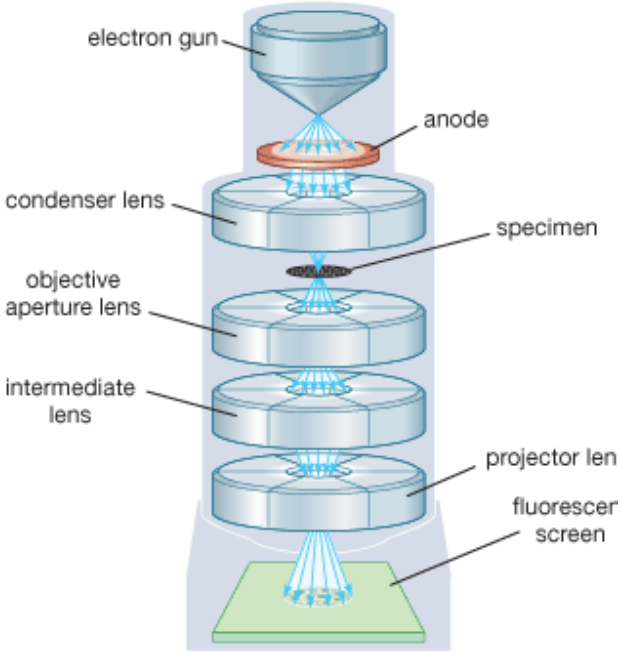

Fig. 2.2 Schematic representation of TEM.

2.4.4. Raman spectroscopy

Raman spectroscopy is the most powerful vibrational spectroscopy technique for the characterization of catalysts at the fundamental and molecular levels [8]. Raman spectroscopy is functioning on inelastic scattering of monochromatic light. In the course of the scattering process, the incident photons frequency is changed. Raman spectrum is emerging due to the inelastic collision between incident monochromatic laser beam and molecules of samples [9]. When monochromatic radiation strikes the sample surface, scattering occurs.

Raman spectra were collected by using Horiba JY LabRAMHR800 Raman spectrometer coupled with a microscope in reflectance mode with 635 nm excitation laser sources and a spectral resolution of 0.3 cm^{-1}.

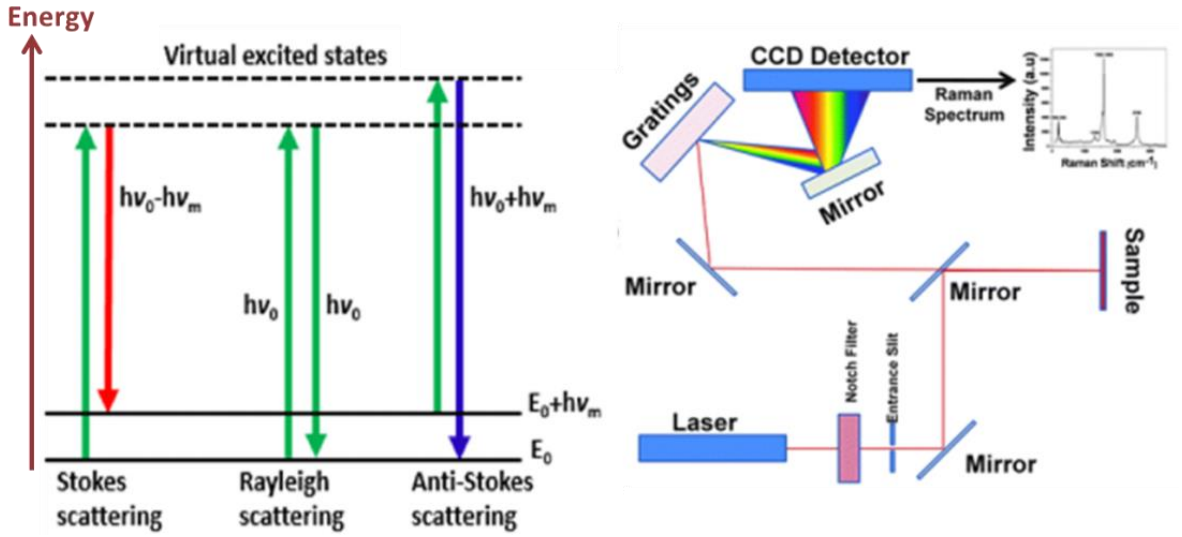

Fig. 2.3 Energy level diagram and schematic representation of Raman spectroscopy.

2.4.5. X-ray Photoelectron Spectroscopy (XPS)

X-ray photoelectron spectroscopy is the most important surface technique widely used to identify information about the electronic structure, oxidation state, and elemental composition on the surface. XPS working principle is based on Einstein's photoelectric effect: when shining monochromatic X-rays strike on a solid surface of the material, electrons are ejected and are measured by a detector.

The kinetic energy (K.E.) of the emitted electrons is manifested as [10]:

$$\mathbf{K.E. = h\nu - B.E. - \varphi} \qquad \mathbf{(2.4)}$$

Where,

hν is the energy of photons

B.E. is the binding energy of the photoelectron

Φ is the work function of the spectrometer

X-ray photoelectron spectroscopy (XPS) was performed for the present study on a ThermoKalpha+ spectrometer using monochromatic Al Kα radiation with an energy of 1486.6 eV. The pass energy for the spectral acquisition was kept at 50 eV for individual core levels. An electron flood gun was used to provide charge compensation during data acquisition.

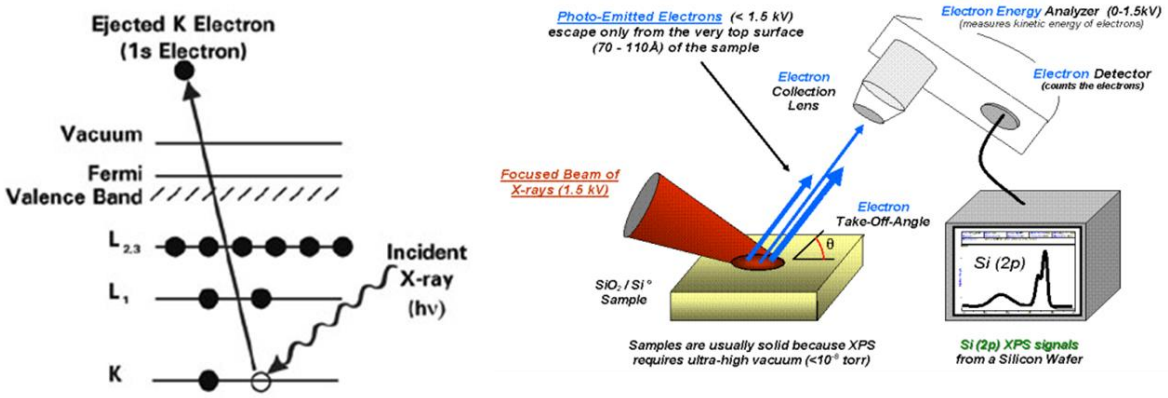

Fig.2.4 XPS Principle and instrument schematic.

2.4.6. Temperature Programmed Reduction (TPR)

TPR is the most widely used analysis technique to understand the number of reducible species available on the catalyst surface and metal-oxide support interaction. The reduction of metal oxides by H_2 is represented by the following reduction equation.

$$\mathbf{MO_x + xH_2 \rightarrow M + xH_2O} \qquad \mathbf{(2.5)}$$

TPR analysis was performed for the present study using Micromertics Autochem-2920 (USA) instrument (**Fig.2.5**). Before the TPR study, the catalyst was pre-treated at 300 °C for 60 min using 10 % O_2 in the He gas mixture. Subsequently, the reduction was performed under 5 % H_2 in Ar in the temperature range 50−600 °C at 5 °C min^{-1}. H_2 consumption was measured quantitatively by a thermal conductivity detector (TCD).

Fig. 2.5 Micromertics Autochem-2920 instrument.

2.4.7. Temperature Programmed Desorption (TPD)

Acid-base properties play a vital role in heterogeneous catalysis. The temperature programmed desorption (TPD) technique has been evolved to understand the interaction of gas with solid surfaces, thereby quantifying the total number of acid-base sites. In a typical TPD experiment, ammonia (NH_3) is used as a probe molecule to quantify the acid strength of the catalyst, and CO_2 is used for evaluating the basic sites of the catalyst.

The acidity of the catalyst was examined by NH_3-temperature programmed desorption using the Micromertics Autochem-2920 instrument (USA). Around 50 mg of the sample was taken and pre-treated under helium atmosphere at 300 °C with a constant flow rate (20 mL.min^{-1}) for 30 min, which was controlled by a mass flow controller (MFC Brooks). Then, the temperature was brought down to 50 °C, and NH_3 was adsorbed to the sample surface using 10 % NH_3 in He (20 mL.min^{-1}). Pure He (20 mL.min^{-1}) was flushed for 30 min at 100 °C to remove any physisorbed NH_3 from the sample surface. The desorption of NH_3 was performed in He flow (20 mL.min^{-1}) by raising the temperature 100−800 °C at 5 °C min^{-1}, and desorbed NH_3 was monitored by a thermal conductivity detector (TCD). The same procedure was followed to quantify basicity using CO_2 and helium mixture.

2.4.8. Fourier Transform Infrared Spectroscopy (FTIR)

IR spectroscopy is the most vital technique used to get an infrared spectrum of absorption in solid, liquid, and gas to recognize the functional groups present. FTIR was collected in the range 4000-400 cm^{-1} of mid-IR region wavelength. When Infrared radiation passes through the sample, some of the IR radiation is absorbed by the sample, and some are transmitted. The transmitted spectra were collected by the detector, representing the material's molecular fingerprint.

The *in situ* CO- FTIR spectra were collected using an FTIR spectrometer (Nicolet, iS50-Thermo Scientific) equipped with an MCT detector (cooled by liquid N_2) at a resolution of 8 cm^{-1} and 200 scans. Firstly, the sample was flushed with N_2 50 mL min^{-1} for 20 min^{-1} and was reduced at 250 °C for 1 h in 5 % H_2/Ar (20 ml/min^{-1}). Afterward, the sample was cooled to 50 °C, and the background spectrum was collected under N_2 atmosphere. Eventually, the CO gas mixture (1vol %/CO/N_2) was passed through MFC into the reaction chamber, and IR spectra were collected from room temperature to 250 °C.

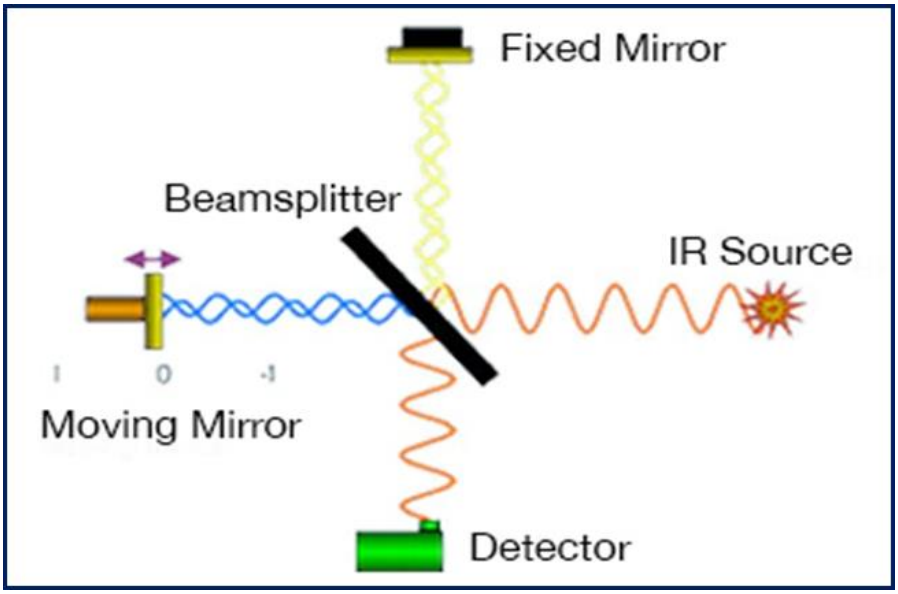

Fig. 2.6 Schematic diagram of FTIR.

The Brønsted and Lewis acidity was measured through a pyridine adsorption experiment. Before the analysis, the sample was preheated under N_2 atmosphere at 250 °C for 1 h. Subsequently, the pre-treated samples were cooled down to room temperature. Finally, pyridine vapors were (25 °C–200 °C) introduced into the samples, and FT-IR spectra were collected in the absorbance mode after pyridine treatment.

2.4.9. Inductively Coupled Plasma-Optical Emission Spectroscopy (ICP-OES)

ICP-OES is a widely used and one of the most versatile methods to analyze inorganic materials. The principle used in the ICP-OES is when the plasma energy is given to the analysis sample from outside, the elements are excited. The emission rays are released when the excited atoms return to a low energy position and emit the photons [11, 12]. The element is determined based on emitted photons intensity. **Fig. 2.7** shows a typical ICP-OES instrument.

The powder samples were digested in aqua regia and analyzed by using an ICP-OES (Spectro Arcos, FHS-12) instrument with Winlab software (FHS-12).

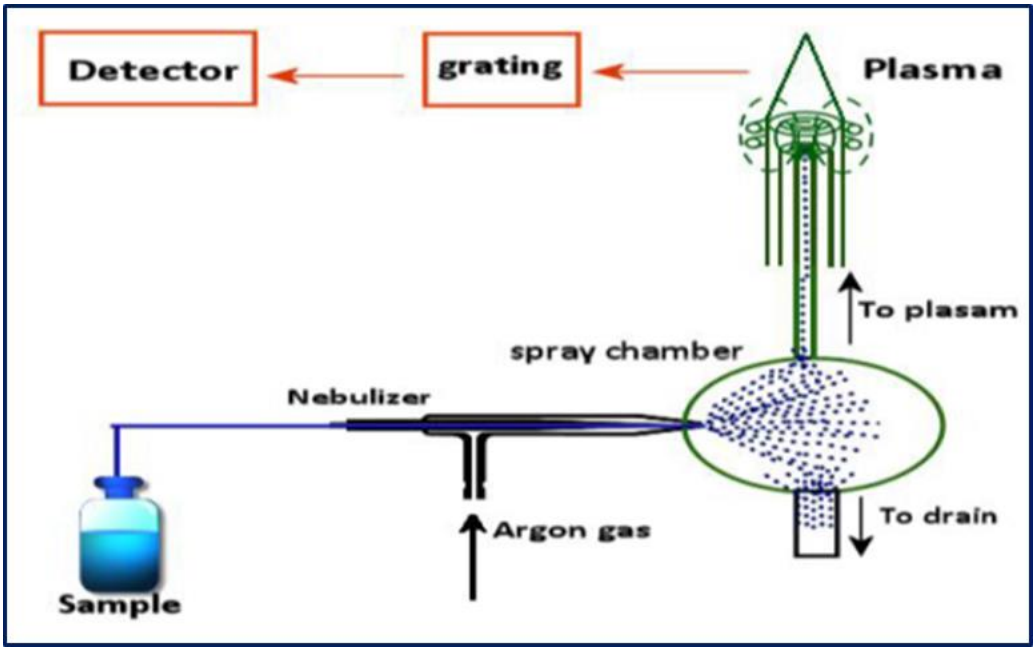

Fig. 2.7 Schematic diagram of ICP-OES instrument.

2.4.10. Ultra Violet (UV)-Visible Spectroscopy

Ultraviolet (UV) visible spectroscopy is an important tool, where ultraviolet radiation is absorbed in the material, which results in the transition of electrons from the ground state to a higher energy state. Commonly, molecules containing bonding and nonbonding electrons are excited to anti-bonding molecular orbitals. **Fig. 2.8** shows the absorption excitation of electrons and UV instrument. The Beer-Lambert law stated the quantitative method to determine the concentration of solute.

$$\mathbf{A = Log_{10}\,(I_0/I) = \varepsilon cL} \qquad \mathbf{(2.6)}$$

Where,

A is the absorbance measured

$\mathbf{I_0}$ is the intensity of the incident light

I is the transmitted intensity

L is the path length through the sample and **C** is the concentration of the absorbing species

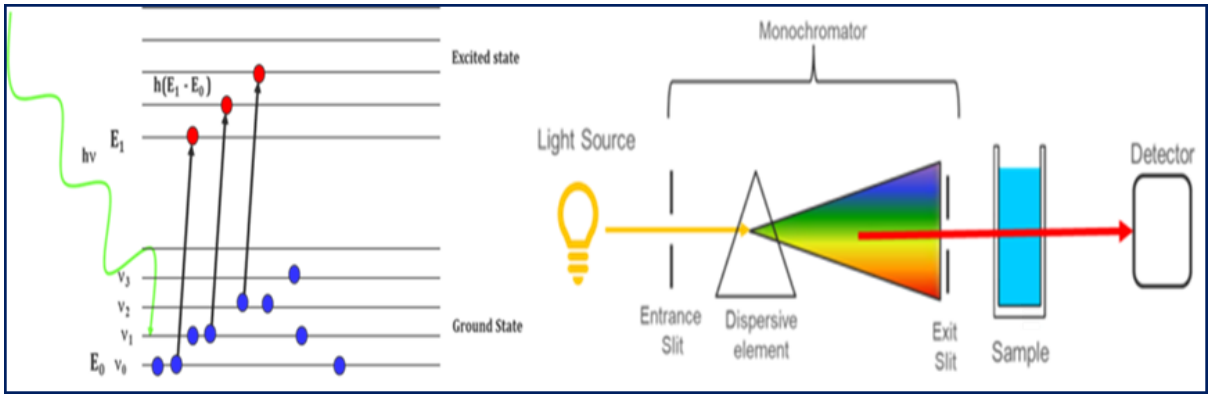

Fig. 2.8 Absorption excitation of electrons and UV-visible spectrometer.

Diffuse reflectance spectra were measured on all powder samples for this study using a Shimadzu UV-Vis-NIR spectrophotometer (Model UV-3600 plus), and reflectance data were converted to absorbance data using the Kubelka-Munk transformation. $BaSO_4$ powder was used as a reflectance reference sample.

2.4.11. Thermogravimetric Analysis (TGA)

Thermogravimetric analysis (TGA) is a valuable tool for understanding the thermal stability of materials. In this method, the mass of substances is observed as a function of time or temperature under a controlled gases atmosphere. The change in the mass of the sample is quantified as a function of temperature.

Thermal analysis of all the materials reported in the present thesis was analyzed by using a METTLER-TOLEDO TGA/SDTA851e instrument. Weight loss quantification analysis was performed under air atmosphere by increasing temperature to 800 °C, and the percentage weight loss of the catalysts was calculated.

2.4.12. Catalytic performances of ODH of propane and 2-Butanol oxidation

The catalytic activity of ODH propane was performed in a fixed bed reactor (FBR) system. The temperature was controlled by two zones furnace fitted with an Inconel HT reactor tube of 8 mm ID and 480 mm length. The catalyst bed temperature was measured by a K-type thermocouple, and the C_3/O_2/Ar gas feed was controlled by Brooks make mass flow controllers. In a single measurement, the calcined catalyst was pelletized, sieved to 1.2 to 1.7 mm grain-sized pellets; and 0.5 g of this catalyst was loaded at the center of the tube by using quartz wool. The ODHP reaction was carried out from 325-500 ºC with different GHSV and catalyst compositions. Gas hourly space velocity (GHSV) is described as the volume of feed

as gas per volume of the reactor or its content of the catalyst. The reaction products were analyzed by ThermoFisher Trace 1110 gas chromatograph coupled with TCD (Thermal conductivity detector) and FID (Flame ionization detector). The hydrocarbons were separated by Alumina plot-Q column (50 m length × 0.53 mm i.d. × 10 μm film thickness) and other permanent gases were eluted by Porapak-Q (3 m length ×1/8 in. o.d. × 2 mm i.d.) and Molecular sieve 5A column (2.7 m ×1/8 in dia.). Argon (99.9 %) was used as the carrier gas at a column flow of 20 mL min^{-1}. The column oven was held at 50 °C for 5 min, ramped up to 250 °C at 5 °C min^{-1}, and finally maintained at 250 °C for 10 min.

The conversion and selectivity of all the products were calculated using the following equations [13, 14].

$$\textbf{Conversion (mol \%)} = \frac{\mathbf{HC_{in} - HC_{out}}}{\mathbf{HC_{in}}} \times \mathbf{100} \qquad \textbf{(2.7)}$$

$$\textbf{Selectivity (\%)} = \frac{\mathbf{X_{out}}}{\mathbf{HC_{in} - HC_{out}}} \times \mathbf{100} \qquad \textbf{(2.8)}$$

(X= H_2, CO, CO_2, CH_4, C_2H_6, C_2H_4, C_3H_6, C_4H_8O, etc)

$$\textbf{Yield (\%)} = \frac{\textbf{Conversion} \times \textbf{Selectivity}}{\mathbf{100}} \qquad \textbf{(2.9)}$$

The catalytic performance for 2-Butanol oxidation was performed in downflow mode over the temperature range 200–350 °C at atmospheric pressure. 1 g of the catalyst was loaded at the center of an Inconel HT reactor tube (13 mm × 510 mm), packed with ceramic beads on either side of the catalyst bed. Temperatures of the catalyst bed were measured by a K-type thermocouple. 2-Butanol and oxygen feed flow was monitored by using the isocratic pump (Lab Alliance series II) and Brook's make mass flow controllers (5850 series), respectively. A gaseous product was measured by a wet gas flow meter (Ritter Drum-Type Wet Gas Meter). The liquid reaction products were condensed and analyzed by Agilent 6890N gas chromatography (FID) with HP-5 (5.5 % phenyl methyl siloxane) column (30 m length × 0.32 mm i.d. × 0.25 μm film thickness). Gaseous products were analyzed by customized

Thermo Fisher Trace 1110 GC coupled with (Molecular sieve 5A column 2.7 m ×1/8 in dia.) TCD detector.

Fig. 2.9 Fixed bed reactor system used for testing catalyst.

2.4.13. Catalytic performance of HMF oxidation

Catalytic activity was evaluated for HMF oxidation using Parr autoclave (USA) 4848 reactor controller with 5500 series compact reactor. In a 50 mL reactor vessel, catalyst (50−175 mg), water (30 mL), and HMF (0.5 mmol) were added and pressurized using O_2 gas. Subsequently, the reaction temperature (100−140 °C) was brought to the desired value, and the solution was stirred at 650 rpm. To maintain constant pressure (5−15 bar O_2 pressure), the reactor was connected to the O_2 cylinder with proper safety precautionary measurements. The sample was collected in 2 h of the time interval during the course of the reaction. The sample mixture was filtered using a 0.22 μm nylon filter and was analyzed by Agilent HPLC, equipped with RI detector using Rezex-organic acid H^+column (300 mm × 7.8 mm). A 5 mM H_2SO_4 was used as a mobile phase at 60 ºC with a flow rate of 0.6 mL min^{-1}, and analysis duration was made in 60 min. The yield of 2,5-furandicarboxylic acid (FDCA) and conversion of 5-hydroxymethylfurfural (HMF) was confirmed by HPLC using an external standard calibration method.

Fig. 2.10 Parr reactor setup.

References

1. A.K. Venugopal, A.T. Venugopalan, P. Kaliyappan, T. Raja, Green Chem. 15 (2013) 3259–3267.
2. K. Kamiya, T. Yoko, J. Mater. Sci. 21 (1986) 842–848.
3. P. Gogoi, N. Kanna, P. Begum, R.C. Deka, Satyanarayana C.V.V, T. Raja, ACS Catal. 10 (2020) 2489-2507.
4. A.A. Bunaciu, E.G. Udristioiu, H.Y. Aboulenein, Cri. Reviews in Anal. Chem. 45 (2015) 289–299.
5. N.F.M. Henry, J. Lipson, W.A. Wooster, The interpretation of X-ray diffraction photographs, Macmillan Co Ltd., London, 1951.
6. B.H. Toby, J. Appl. Crystallogr. 34 (2001) 210-213.
7. S. Brunauer, P.H. Emmett, E. Teller, J. Am. Chem. Soc. 60 (1938), 309-319.
8. C. Hess, Chem. Soc. Rev. 50 (2021) 3519 3564.
9. G.S. Bumbrah, R.M. Sharma, Egyptian Journal of Forensic Sciences 6 (2016) 209-215.
10. D. Briggs, M.P. Seah, Practical Surface Analysis, Vol. 1: Auger and X-ray Photoelectron Spectroscopy, 2nd ed. Wiley, New York, 1990.
11. K.F. Khan, The Pharma Innovation Journal 8 (11) (2019) 281-282.
12. S. Ghosh, V.L. Prasanna, B. Sowjanya1, P. Srivani, M. Alagaraja, D. Banji, Asian J. Pharm. Ana. 3 (1) (2013) 24-33.
13. F. Malherbe, C. Forano, B. Sharma, M.P Atkins, J.P. Besse, Appl. Clay Science, 13 (1998) 381-399.
14. S. Tan, L.B. Gil, N. Subramanian, D.S. Sholl, S. Nair, C.W. Jones, J.S. Moore, Y. Liu, R.S. Dixit , J.G. Pendergast, Appl.Catal. A Gen. 498 (2015) 167–175.

Chapter-3

New Insights into the Composition and Catalytic Performance of VO_x-Ga/γ-Al_2O_3 for the Oxidative Dehydrogenation of Propane to Propene

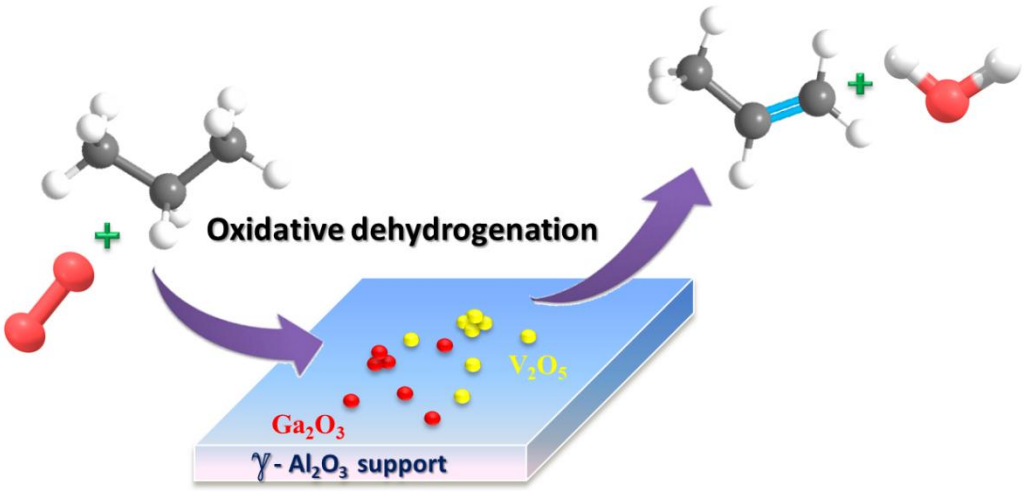

Synopsis

- Vanadium and gallium oxide supported on γ-Al_2O_3 are synthesized via incipient wetness impregnation method
- The catalysts were investigated for structure-activity relationship in ODH of propane
- The catalytic experiments revealed that the catalyst with 7 % vanadium and 3 % gallium demonstrated the highest catalytic activity and stability in the ODH of propane
- The redox nature of vanadium (V^{5+} and V^{4+}) oxide with higher surface V^{5+} in VGA-2 catalyst is more favorable for C-H activation
- H_2-TPR and UV-visible spectra showed the presence of highly dispersed monomeric VO_x species with tetrahedral coordination geometry, which influence the product selectivity

3.1. Oxidative dehydrogenation of propane

The world's demand for lower olefins is increasing significantly, particularly propylene, a primary feedstock in the petrochemical industries for producing polypropylene, propylene oxide, cumene, and acrylonitrile shown in **Fig. 3.1** [1-3]. A conventional process for producing lower olefins involves steam cracking, fluid catalytic cracking (FCC), and dehydrogenation of alkanes [4-6]. Steam and fluid cracking processes utilize a large amount of energy that is insufficient to attain the propylene demands [7, 8]. At present global scenario, it appears that shale gas exploration would have a significant impact on the world economy for at least several decades and possibly as long as shale gas is available, which is utilized more for the production of propylene in a more beneficial chemical process. As a result, researchers are focused on producing propylene via propane dehydrogenation using commercial catalysts like CrO_x/Al_2O_3 (Catofin process) and Pt-Sn/Al_2O_3 (Oleflex process). Since these processes are highly endothermic in nature **(Eq. 3.1)**, which results in the deactivation of the catalyst due to coke deposition over the active sites of the catalyst surface [9-11]. In addition, the search for new alternative catalysts is necessary due to the expensive Pt catalysts on the commercial level and environmentally unfriendly Cr-based catalysts.

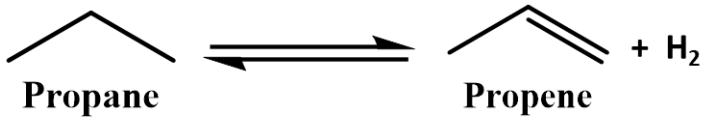

$(\Delta H^0_{298} = +124.3\ kJ\ mol^{-1})$ **(3.1)**

Oxidative dehydrogenation (ODH) of hydrocarbons is an attractive alternative route for the production of lower olefins [12-14]. In this scenario, an oxidative gas (O_2, CO_2, and N_2O) will be co-feed with alkane. One of the major advantages of this process could be that reaction occurs at a much lower temperature due to the exothermic nature **(Eq. 3.2).** As a result, coke deposition is minimized, thereby ensuring the long-term stability of the catalyst. The ODH of propane on the transitional metal oxides is believed to follow the Mars–van Krevelen (MvK) mechanism [15, 16]. Two types of oxygen species are formed during the process, namely electrophilic and nucleophilic species. The electrophilic oxygen species such as O_2^-, O_2^{2-}, and O^- are responsible for the total oxidation [17]. Nucleophilic lattice oxygen species (O^{2-}) are associated with selective oxidation [18, 19]. The ODH of propane has several limitations for scaling up for commercialization: (1) Undesirable over-oxidation reactions result in a low propene yield, (2) Activation energy of secondary C-H bond (401 kJ mol^{-1}) is higher than the allylic C-H bond in olefins (361 kJ mol^{-1}) [17]; and more CO_x

formation in the products (3) Catalyst deactivation during the reaction due to the hot spots is a major drawback related with FBR, and it is difficult to run the reaction under isothermal conditions. Therefore, designing an efficient and robust catalyst is of the utmost importance in order to increase the yield of propylene to reach the demand.

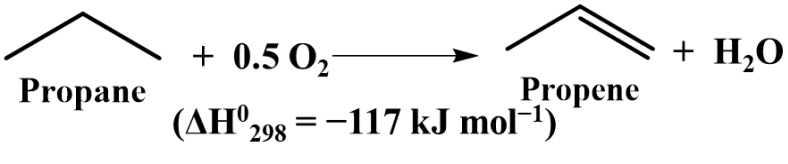

(3.2)

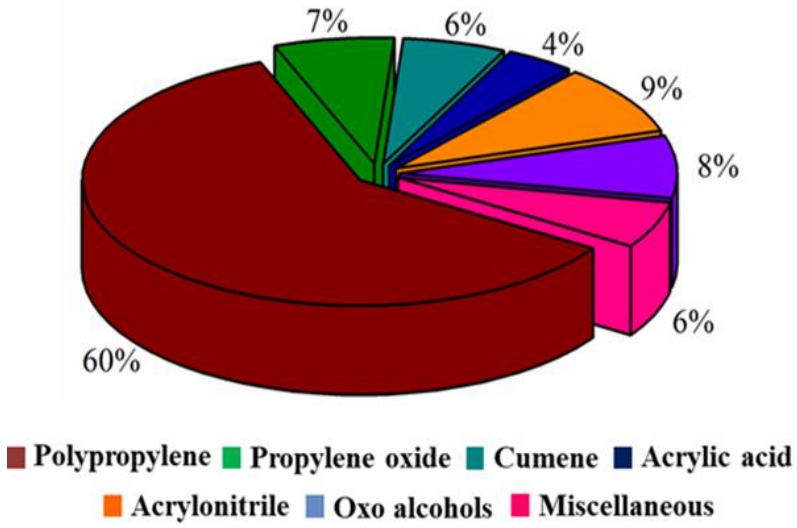

Fig. 3.1 Major propene derivatives.

3.2. Background of the work

In the last few decades, metal oxides (V, Cr, Mo, Ga) catalysts have been active for the activation of lower alkanes [20-24]. Mainly, vanadium oxide catalysts are widely used for DH and ODH of propane due to their unique properties like redox behavior and nature of active sites (monomeric, polymeric, and crystalline V_2O_5) present on the surface of the catalyst **Fig. 3.2** [20, 25-30]. However, the oxide supports such as Al_2O_3, SiO_2, Zr_2O_3, TiO_2, Nb_2O_5, SBA-15, and nano-porous materials play a crucial role in catalyst stability [31-36]. Additionally, the surface area, acid-base properties, and metal support interaction also induce catalytic activity. Hoj *et al.* reported that V/Al_2O_3 prepared by flame spray pyrolysis method could induce the space-time yield of 0.78 $g_{propene}/(g_{cat}.h)$, which showed a 12 % yield of propene at 488 ºC using 2 % of vanadium over alumina [37]. The intrinsic effect of support microstructures (B-Al_2O_3, F-Al_2O_3, and S-Al_2O_3) plays a crucial role in the catalytic activity of $5V/Al_2O_3$ for ODHP. The bulk morphology of alumina with monolithic particles shows that the intraparticle pores are beneficial to avoid the mass transfer disturbances, which in

turn increase the activity of ODH process [38]. Al_2O_3 with different nanostructures are the essential supports in catalysis due to their thermal stability and strong metal-support interaction [39]. Luo and co-workers developed nanorods assembled $CeVO_4$ hollow spheres by simple solution method. The catalyst was annealed at 500 ºC to obtain more Ce^{4+} species on the surface, and the catalyst shows high selectivity (70 %) of propene. However, the conversion of propane was low at the optimized reaction conditions [40]. Multivalent Ce^{4+}/Ce^{3+} have a good reduction potential with the ability to transport oxygen and create oxygen vacancies, particularly when nanostructured catalysts are employed. NbO_x introduced into CeO_2 rods, which suppress the surface reducibility and magnify the propene selectivity [41]. Chalupka *et al.* achieved vanadium incorporation into the SiBEA zeolite framework, which gave 12 % conversion of propane and 45 % of propene selectivity at 525 ºC [42]. The direct hydrothermal synthesis of vanadium incorporated mesoporous V/KIT-6 catalyst showed excellent catalytic activity for ODHP. This is due to the higher dispersion of VO_x species in tetrahedral coordination and 3D interconnected mesostructured systems [43].

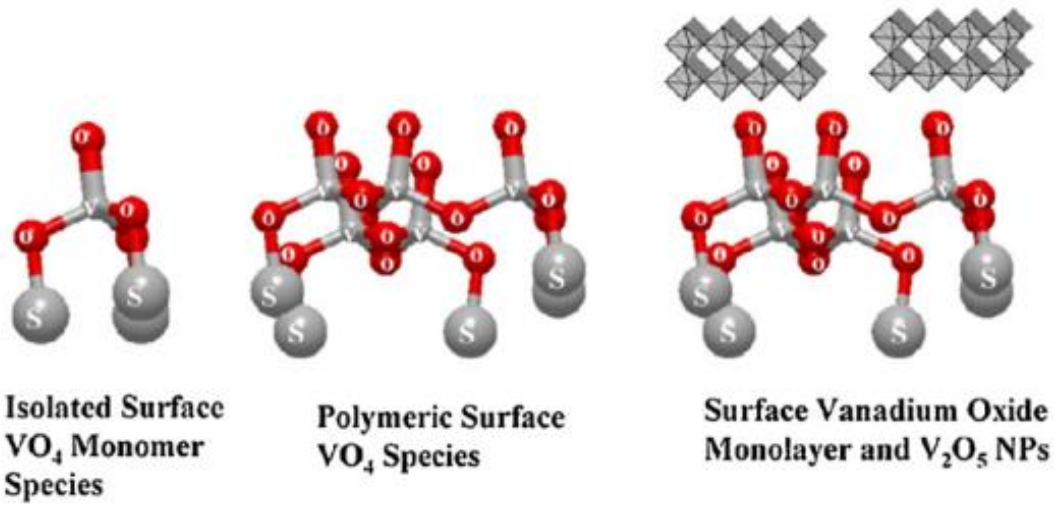

Fig. 3.2 Types of surface VO_x structure [44]

Recently, Ga-based catalysts were found highly active for the dehydrogenation of propane over TiO_2, Al_2O_3, and zeolite supports [45-47]. Choi *et al.* reported gallosilicate MFI zeolites synthesized using 3-mercaptopropyl-trimethoxysilane (MPS). With the addition of MPS to the zeolite framework, the Lewis acidic strength increased, and Brønsted acidity is reduced. The higher amount of strong Lewis acidity is more responsible for achieving high selectivity for propane dehydrogenation [48]. Tuning the synthesis method for designing hierarchical Ga-MFI zeolite catalysts showed superior activity than bulk Ga-MFI for PDH [49]. However, still debate is going on about the nature of active Ga sites and reaction mechanism for PDH.

Besides this, gallium is more responsible towards sintering; Lewis acid sites and four-coordinated $Ga^{3+}O_x$ species are active for propane activation [47, 50]. This chapter investigated the importance of catalyst designing to obtain a highly stable and selective VO_x-Ga/γ-Al_2O_3 catalyst for oxidative dehydrogenation of propane. To our best knowledge, VO_x and Ga_2O_3 mixed metal oxides supported high surface area γ-Al_2O_3 catalyst for ODH of propane have not been investigated yet. The structure-reactivity-selectivity correlation was investigated by various characterization techniques like X-ray photoelectron spectroscopy, temperature programmed reduction and UV-visible spectra, and DRIFTS study.

3.3. Results and discussion

3.3.1. Catalyst characterization

3.3.1.1. Structural analysis

In order to investigate the structural analysis of pure alumina and V, Ga metal oxide loaded catalysts, powder X-ray diffraction (PXRD) was performed (**Fig. 3.3).** All catalysts show the peaks around 37º, 46º, and 67º, which correspond to the 311, 400, and 440 planes of the γ-Al_2O_3 support. After metal loadings into support, it is observed that the overall structure remains intact. However, no characteristic peaks were observed for V_2O_5 and Ga_2O_3 crystalline phases, even at 10 wt % of vanadium loaded catalyst [51], which could be due to the high dispersion of VO_x and GaO_x on the amorphous alumina support. However, in Raman spectroscopy, V_2O_5 nanoparticles can be observed at 945 cm^{-1} **(Fig. 3.6)**.

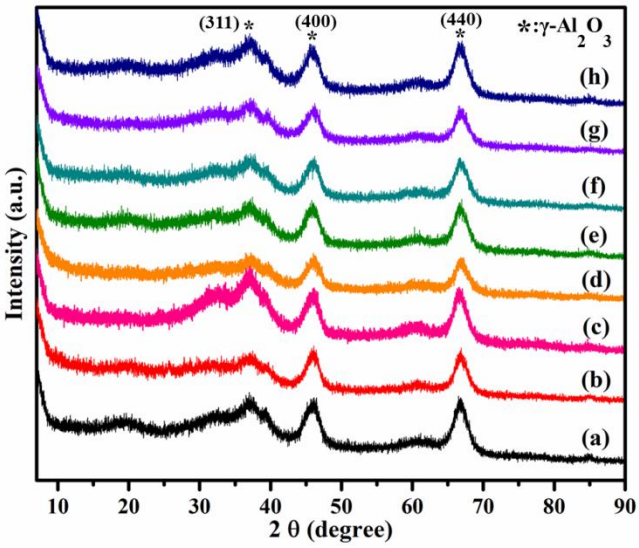

Fig. 3.3 PXRD patterns of as synthesized catalyst (a) γ-Al_2O_3, (b) VO_x/γ-Al_2O_3, (c) Ga/γ-Al_2O_3, (d) VGA-1, (e) VGA-2, (f) VGA-3, (g) VGA-4 and (h) VGA-5.

3.3.1.2. N_2- sorption analysis

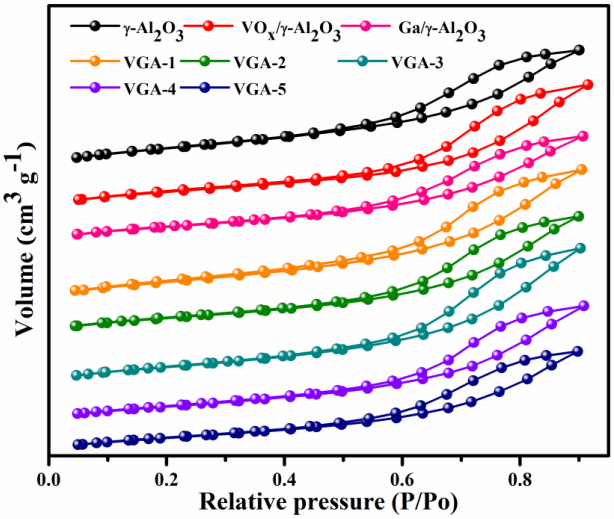

Fig. 3.4 N_2- sorption isotherms of the synthesized catalysts.

N_2-adsorption desorption isotherm of pure γ-Al_2O_3 and V, Ga metal oxide-loaded supported catalysts were recorded. **Fig. 3.4** represents all the calcined catalysts, which have a type IV isotherm and an H1 hysteresis loop, confirming the mesoporous nature of the materials. The surface area of the catalysts was calculated from the BET equation and shown in **Table 3.1**. The pure γ-Al_2O_3, which has a surface area of 268.33 m^2/g, and the surface area gradually decreases with the increase loading of vanadium and gallium. This implies that pores are partially blocked by vanadium and gallium oxide species. The surface acidity of all the calcined catalysts is depicted in **Table 3.1**.

Table 3.1 Physicochemical properties of pure alumina and V, Ga metal oxide loaded catalysts

Molar ratio	**Catalyst Code**	**BET Surface area [a] (m^2/g)**	**Acidity (mmol/g) [b]**	**H_2 consumption [c] (mmol g^{-1})**	**T_{max} [d] (°C)**	**Coke deposition (%) [e]**
γ-Al_2O_3	γ-Al_2O_3	268	1.87	-	-	-
10 % VO_x/γ-Al_2O_3	VO_x/γ-Al_2O_3	245	1.65	21	454	9
V_8Ga_2/γ-Al_2O_3	VGA-1	241	1.62	13	430	10
V_7Ga_3/γ-Al_2O_3	VGA-2	237	1.60	12	421	7
V_6Ga_4/γ-Al_2O_3	VGA-3	231	1.56	12	417	11
V_5Ga_5/γ-Al_2O_3	VGA-4	225	1.52	8.6	410	12
V_3Ga_7/γ-Al_2O_3	VGA-5	218.71	1.50	4.6	398	20
10 % Ga/γ-Al_2O_3	Ga/γ-Al_2O_3	221.71	1.67	-	-	15

(a) Data obtained from BET analysis.

(b) Acidity calculated from NH_3-TPD.

(c) Quantified from TPR data.

(d) The temperature of maxima in TPR analysis.

(e) Calculated from TG/DTA analysis.

3.3.1.3. H_2-Temperature programmed reduction and UV visible DRS spectroscopy

H_2-TPR was carried out to understand the structural aspect of the catalysts and their reducibility under TPR conditions. **Fig. 3.5a** show that only one reduction peak is appeared for all the catalyst at around 375-450 ºC, which can be ascribed to the reduction of V^{5+} and V^{3+} [52]. However, increasing the vanadium content from 3 to 10 wt %, the reduction peaks slowly shifted to higher temperature (400 to 450 ºC), and the intensity of peaks increased noticeably. On the other hand, 10 wt % VO_x/γ-Al_2O_3 shows a small shoulder peak around 547 ºC which is ascribed to the reduction of polymeric V_2O_5 like VO_x species [18, 43]. **Table 3.1** clearly shows that the hydrogen consumption gradually increases with the vanadium loading, and maximum consumption of 21 mmol g^{-1} is observed for VO_x/γ-Al_2O_3 catalyst. As per the recent report [38, 52] the shift in the reduction peak with an increase in the V content is mainly due to the presence of different types of VO_x species (monomeric, dimeric, and polymeric) present on the surface of the supported catalysts. Moreover, our result indicates that the VO_x species are started to reduce at low temperature (400 ºC), which hinted at the presence of highly dispersed monomeric vanadia with tetrahedral coordination geometries [43]. In contrast no reduction peaks pertaining to gallium oxide was appeared, inferring the difficulty to reduced gallium oxide in this temperature range.

Interestingly, the optimized reaction temperature and the observed reduction temperature are similar for 7 wt % vanadium loaded sample (VGA-2) and show higher catalytic activity around 400 ºC. Moreover, it is expected that at higher vanadium loading, the catalyst tends to form more polymeric VO_x species with octahedral coordination [53, 54], which would decrease the redox behaviour of V^{5+} as the redox behaviour of V in the catalyst is expected to promote good catalytic activity. UV-vis spectra of all synthesized catalysts were recorded to distinguish the degree of polymerization of VO_x species. The broad absorption bands have appeared for all the vanadium catalysts with respect to O→V charge transfer (CT) bands [55]. The absorption bands at 235 nm and 279 nm are allocated to tetrahedrally coordinated monomeric and oligomeric VO_x species [51]. Furthermore, no absorption bands were observed in the 400-500 nm range, which is ascribed to bulk-like vanadium species [56].

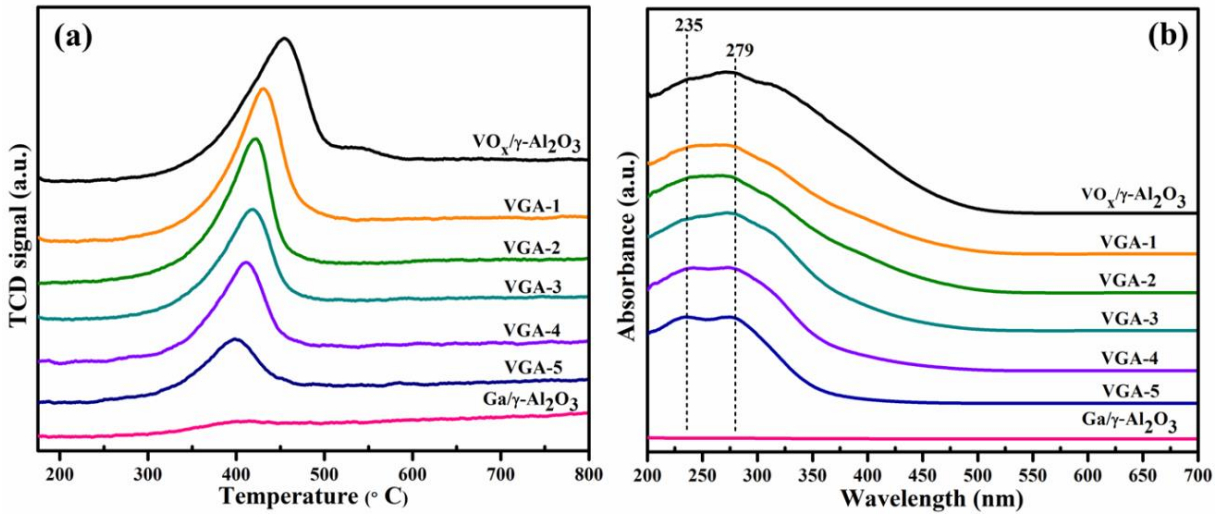

Fig. 3.5 (a) H_2-TPR profiles of the synthesized catalysts and (b) UV-visible DRS spectra of the catalysts.

3.3.1.4. Raman spectroscopy

Raman spectroscopy was carried out to understand various types of surface VO_x species in the catalyst. Typically, two peaks were observed for all vanadium-supported catalysts are shown in **Fig. 3.6**. The peak at 945 cm^{-1} (vanadyl V=O bonds) corresponds to crystalline V_2O_5 nanoparticles. The remaining bands, emerging at 300-400 cm^{-1} assigned to bulk V_2O_5 crystals [18]. A similar observation was observed in recent reports [20, 51, 57]. However, gallium oxide and bare alumina did not show any characteristic peak in Raman Spectroscopy.

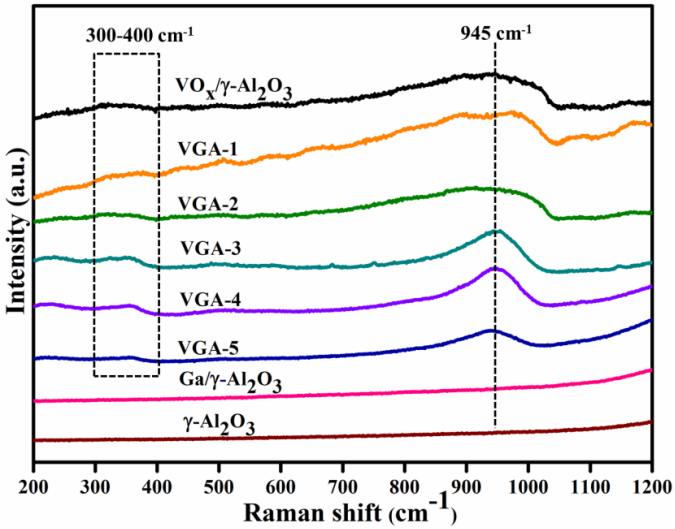

Fig. 3.6 Raman spectra of the synthesized catalysts.

3.3.2. Catalytic performance for ODH of propane

3.3.2.1. Effect of the catalyst composition

The catalytic activity of all the calcined catalysts was performed using a fixed bed continuous flow reactor, and the reaction products were evaluated by online gas chromatography (refer to

section **2.4.12**). The catalyst composition is an important parameter to affect the catalytic activity in oxidative dehydrogenation of propane, and the results are displayed in **Fig. 3.7**. The VO_x-supported γ-Al_2O_3 catalyst gave reasonable propene selectivity 39 % with 30 % propane conversion at 400 ºC. This indicates that VO_x is one of the best candidates for C-H activation at lower loadings of vanadia and the monolayer coverage of surface vanadium densities [30]. Kim *et al*. have examined that the catalysts exhibit a monolayer range of surface VO_x coverage which are highly active than bulk VO_x surfaces for selective oxidation reactions [44]. Interestingly, when Ga was added in combination with V, the catalytic performance of the catalysts was improved. Among all the catalysts, VGA-2 ($V_{7.0}Ga_{3.0}$/γ-Al_2O_3) showed relatively better catalytic performance with 19 % propane conversion and 66 % propene selectivity. The high activity is due to the monolayer coverage of vanadium, appropriate surface acidity, and oxygen mobility. Moreover, the presence of (confirmed from XPS) Ga^{3+} species in the catalyst may synergistically promote C-H activation. However, the selectivity and conversion decreased simultaneously on further increasing Ga content. This implies that the lower VO_x and higher Ga loading lead to the formation of cracked products. The bare Ga_2O_3 supported catalyst shows reasonable activity, but the conversion and selectivity are lower as compared to bare vanadium oxide. This emphasizes that the catalysts with optimum Ga and V content are essential to achieve an excellent catalytic performance. Therefore VGA-2 catalyst is found to be the optimized ratio for further study.

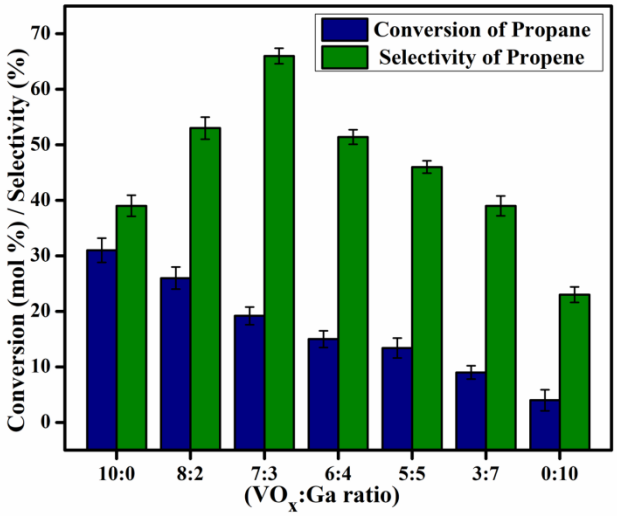

Fig. 3.7 Effect of catalyst composition for ODHP.

Reaction conditions: *0.5 g catalyst, total reactants flow (C_3H_8:O_2:Ar) GHSV 6000 h^{-1}, atm. pressure, 400 ºC.*

3.3.2.2. Effect of reaction temperature over VGA-2

Fig. 3.8 illustrated the catalytic performance and product distribution of $V_{7.0}Ga_{3.0}$/γ-Al_2O_3 (VGA-2) supported catalyst. ODHP was carried out within the 325-500 ºC temperature range. As VGA-2 showed the best catalytic performance among all the catalysts, it was further tested for different temperature studies to determine the optimum reaction conditions. Initially, the catalyst showed 60 % propene selectivity at 325 ºC with a lower conversion of propane (10 %). However, on increasing the reaction temperature, the conversion of propane increased gradually, and at 400 ºC, maximum propene selectivity (66 %) was achieved with 19 % conversion of propane. With a further increase in the temperature, the selectivity of propene dropped down, and the conversion of propane increased drastically. This implies that higher temperature C-C bond cracking is more favorable, which leads to more cracked products. This can be distinctly seen from **Fig 3.8b**, which causes lower propene yield due to the loss of some surface-active species and coke deposition over the active sites of the catalysts. Hence it may be inferred that V^{5+} is more active for ODHP owing to the redox nature and readily exchanging oxidation state under the reaction conditions from V^{4+} to V^{5+} [20]. Moreover, it is assumed that coordinatively unsaturated gallium oxide [47], acidity, and strong metal-support interaction (SMSI) play a vital role in achieving high selectivity of propene. Therefore, 400 ºC is the optimized temperature for further studies. The product distribution of VGA-2 catalyst is shown in **Fig. 3.8b**. At lower temperature, 40 % CO_2 is formed, and while increasing the reaction temperature H_2 and C_2 products are formed along with CO_2.

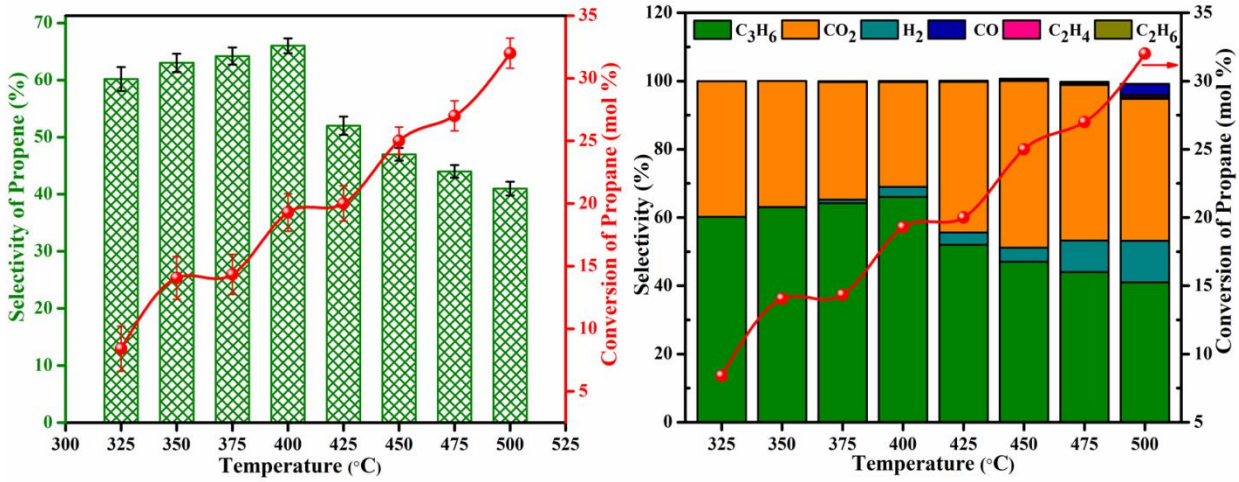

Fig. 3.8 (a) Effect of temperature over VGA-2 catalyst and (b) product distribution of VGA-2 catalyst. ***Reaction conditions:*** *0.5 g catalyst, total reactants flow (C_3H_8:O_2:Ar) GHSV 6000 h^{-1}, atm. pressure, temperature 325-500 ºC.*

3.3.2.3. Effect of C_3H_8 to O_2 ratio over VGA-2 catalyst

Gas hourly space velocity (GHSV) is one of the main parameters affecting catalytic activity. As per the previous reports, ODHP follows Mars van Krevelen mechanism [58, 59], where lattice oxygen (bridged oxygen) participates in the activation of the C-H bond of the methylene group, and the reduced surface can be re-oxidized by molecular oxygen. When the reaction was performed over VGA-2 catalyst with 1:1 ratio with respect to C_3H_8:O_2 at 400 ºC, 46 % conversion of propane and 28 % selectivity of propene was observed, which is also given in **Fig. 3.9**. On further increasing the oxygen flow rate, the conversion of propane increased drastically to 73 % with less selectivity of propene (10 %). As per the previous reports, molecular oxygen contains more electrophilic oxygen (O_2^-, O^- and O_2^{2-}), which is responsible for the total oxidation of propane. However, to attain high activity and enhance the surface-active species, we reduced the C_3H_8:O_2 to a 2:1 ratio. Surprisingly, the catalytic activity increased, and 66 % selectivity of propene and 19 % conversion of propane was achieved.

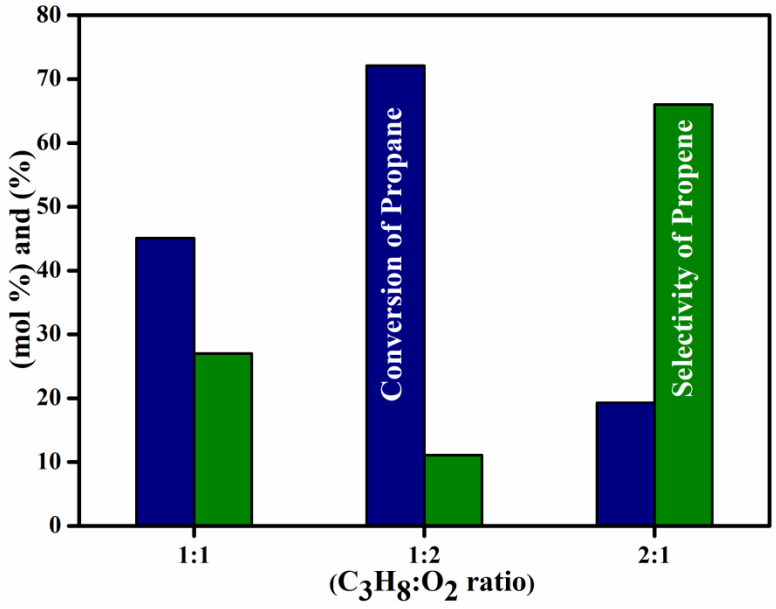

Fig. 3.9 Effect of C_3 to O_2 ratio over VGA-2.

Reaction conditions: *0.5 g catalyst, total reactants flow (C_3H_8:O_2:Ar) GHSV 6000 h^{-1}, atm. pressure, 400 ºC.*

3.3.2.4. Transmission electron microscopy

The surface morphology of the VGA-2 catalyst and the distribution of the supported metal oxides were confirmed by transmission electron microscopy. **Fig. 3.10** represents sheet-like morphology with small crystals of the metal oxides which are formed over the supported

mesoporous alumina. Further, STEM images revealed that vanadium and gallium are homogeneously distributed on the surface of the catalysts. However, lattice fringes of V and Ga oxides are not visible due to the amorphous nature of the alumina support.

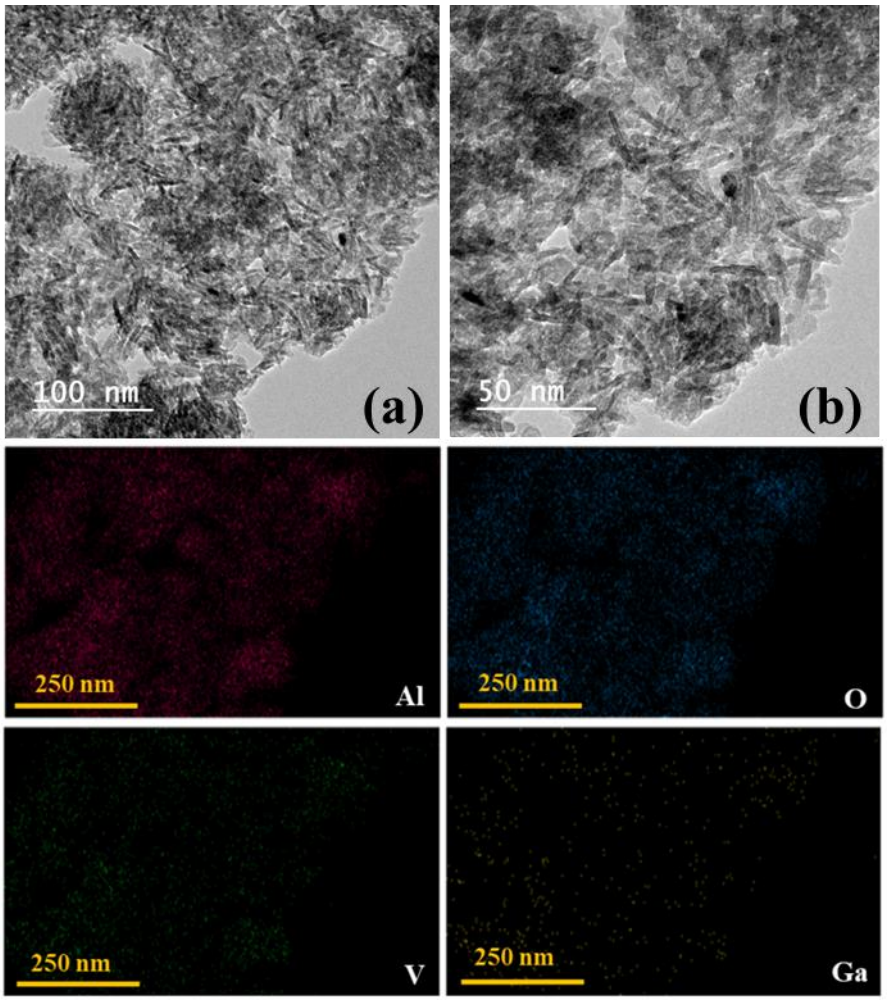

Fig. 3.10 (a-b**)** HR-TEM and elemental mapping images of fresh VGA-2 catalyst.

3.3.2.5. X-ray photoelectron spectroscopy

To investigate the oxidation state and surface composition of metal oxides, XPS analysis was carried out for VGA-2 catalyst, V 2p, Ga 3d, Ga 2p, Al 2p, and O 1s core levels as shown in **Fig. 3.11**. XPS spectrum of V2p shows two peaks at binding energy values of 516.2 and 517.4 eV, which corresponds to V^{4+} and V^{5+} respectively [51, 57]. In addition to this, the peak area of V^{4+} is 32.58, and V^{5+} is 67.42 %, respectively. Recent literature reports suggested that vanadium-based catalysts with higher V5+ species effectively affect C-H activation in propane. Therefore, the higher surface V^{5+} in the case of VGA-2 catalyst is expected to promote C-H activation in propane which in turn better catalytic activity in the catalyst. O 1s spectrum of VGA-2 catalyst was deconvoluted into two peaks as shown in **Fig.**

3.11f. The peaks at 531.2 and 533 eV correspond to lattice oxygen and surface hydroxyl species, respectively [14, 60]. The presence of lattice oxygen plays an important role in the initial activation of propane, and it will minimize the coke deposition during ODHP reaction. **Fig. 3.11c** represents XPS spectrum of Ga 3d core level of VGA-2 catalyst. The binding energy at 20.5 eV is assigned to Ga 3d band corresponds to $Ga^{3+,}$ and no peak was pertained for metallic Ga was observed [47, 61]. Moreover, it is anticipated that coordinatively unsaturated Ga^{3+} species are also active for ODH of propane [47]. Hence, the better catalytic activity in the case of VGA-2 catalysts may be due to the presence of Ga^{3+} species in the catalyst. The binding energy values at 23 and 25.8 eV are attributed to different oxygen species on the surface. **Fig. 3.11d** shows Ga 2p XPS spectra of VGA-2 catalyst. The spin-split peaks of the Ga 2p core-level spectrum were deconvoluted using XPS peak41 software into two peaks at around 1117.6 and 1144.5 eV. The binding energy value at 1117.4 and 1144.5 eV were assigned to Ga $2p_{3/2}$ and Ga $2p_{1/2,}$ respectively [62, 63]. **Fig. 3.11e** shows the deconvolution of the Al 2p core-level spectra, and binding energy values appear around 74.5 eV corresponds to the Al_2O_3. This is in good accordance with the BE reported for Al 2p in literature reports [64, 65].

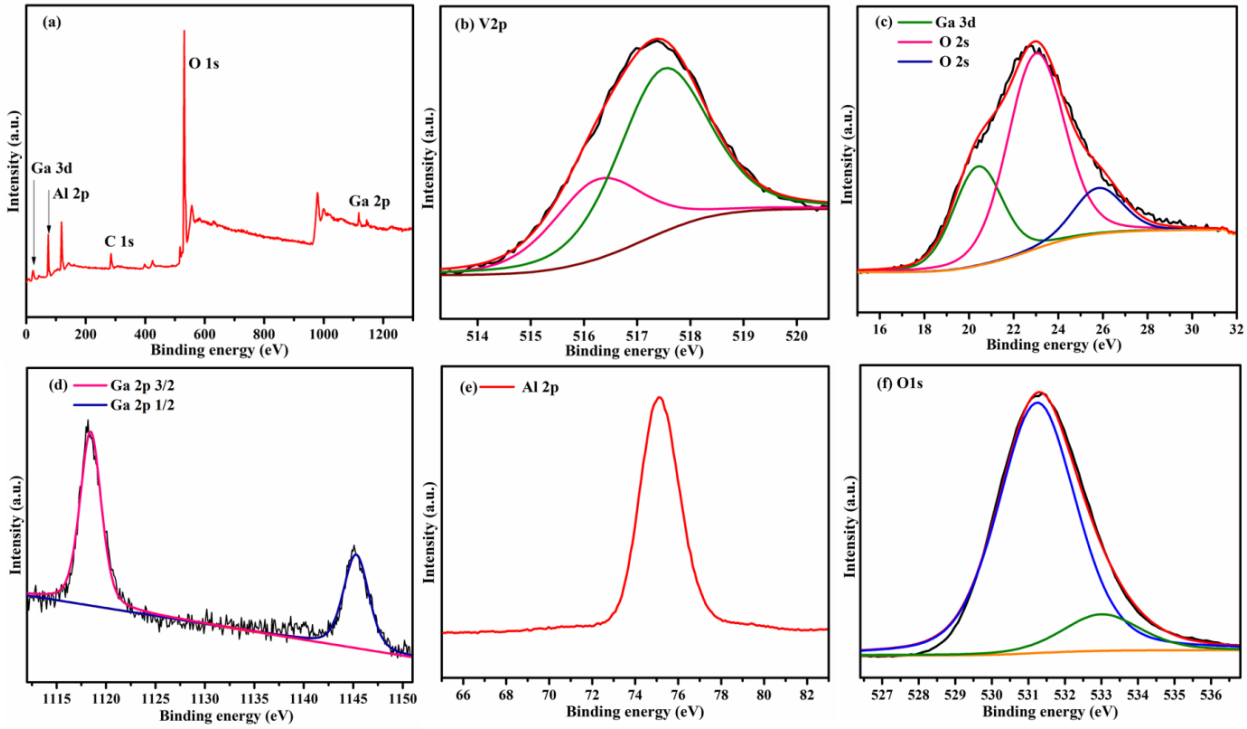

Fig. 3.11 XPS spectra of fresh VGA-2 catalyst (a) Full scan XPS, (b) V 2p, (c) Ga 3d, (d) Ga 2p, (e) Al 2p and (f) O 1s core level spectra.

3.3.2.6. *In-situ* DRIFTS study

In-situ DRIFTS studies were performed for all the catalysts to gain more insights into the ODHP reaction mechanism. **Fig. 3.12a** depicts DRIFT spectra of propane chemisorbed at ambient temperature and at 50 ºC for VGA-2 catalyst. The absorption bands at 1387 and 2800-3061 cm^{-1} were assigned to C-H stretching bands (likely $CH_{3\ ads}$ and $CH_{2\ ads}$ species) of physisorbed propane [38, 66-68]. Besides these peaks, the band at 1463 cm^{-1} is assigned to propoxide species, with the evolution of σ-bonds between most active hydrogen atoms in propane and surface lattice oxygen in the catalyst [69]. The above result clearly suggested that the surface lattice oxygen takes part in the adsorption process even at ambient temperature. This confirms that lattice oxygen has a predominant role in ODHP. The reaction follows the redox (MvK) mechanism. Further, the spectra were recorded at 325 ºC in C_3H_8:O_2:Ar atmosphere, which is depicted in **Fig. 3.12b**. The IR bands appeared at 2845-2920 and 2961 cm^{-1} attributed to stretching vibration of -C-H and =C-H bonds in propylene molecule [38]. Surprisingly, the new bond was observed at 1573 cm^{-1} corresponds to the vibration of C=C bond [57, 70]. However, at an elevated temperature (325 ºC), the peak intensity of 1463 cm^{-1} decreases due to the transformation of propoxide species. Upon, increasing the temperature to 350 ºC, no detectable absorption changes and no new bands were observed for all the catalysts.

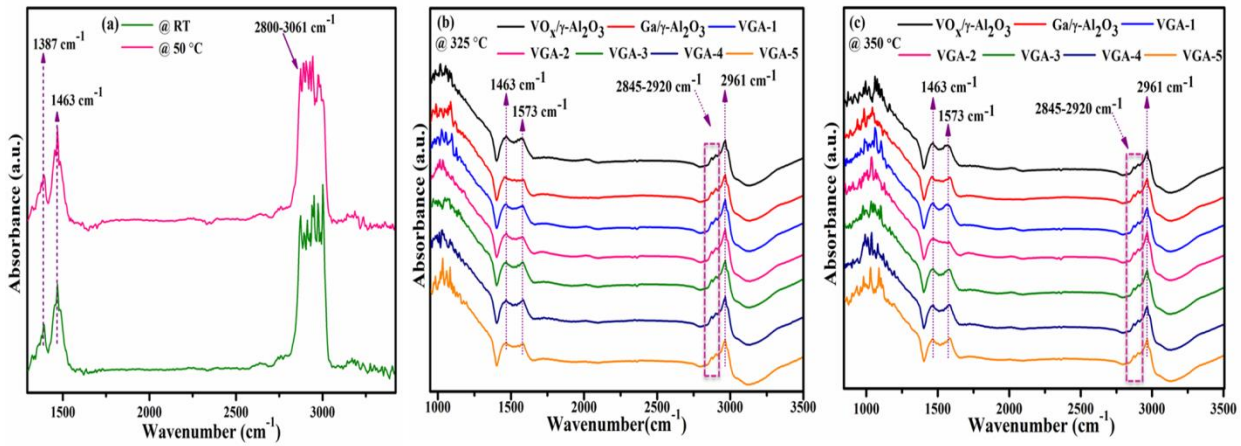

Fig. 3.12 In-situ DRIFT spectra (a) VGA-2 catalyst recorded for the propane chemisorbed at ambient temperature and 50 °C, (b) 325 ºC and (c) 350 ºC.

3.3.2.7. On stream study

Catalyst stability is the major problem in heterogeneous catalysis, especially in ODH reactions. **Fig. 3.13** illustrates that the optimized VGA-2 catalyst is used for TOS study at 400 ºC with 6000 h^{-1} GHSV with respect to C_3H_8:O_2:Ar. The catalyst initially showed 21 % propane conversion and after the fourth hour selectivity and conversion remains constant for

24 h of the reaction. This affirms that V^{5+} and V^{4+} are necessary species for ODHP. Moreover, a small quantity of Ga oxide on the support could enhance the selectivity of propene and impart stability to the catalyst. Therefore, 7 % V and 3 % Ga (VGA-2) supported on high surface area γ-Al_2O_3 is an active and stable catalyst for ODH of propane.

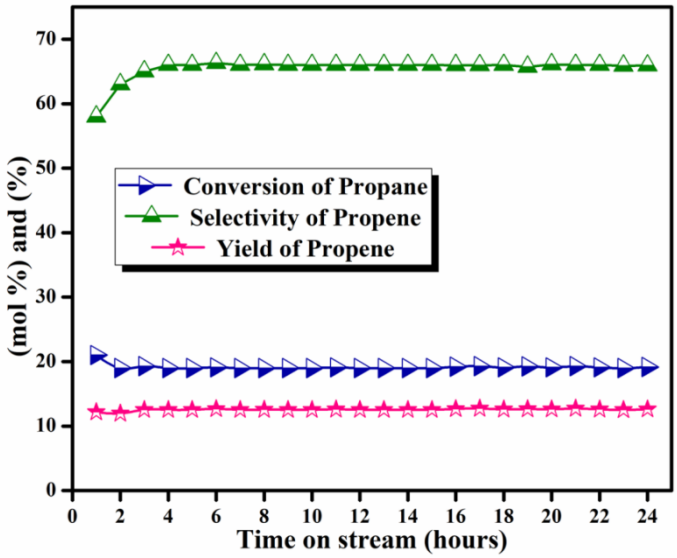

Fig. 3.13 Time on stream study over VGA-2 for 24 h.

Reaction conditions: *0.5 g catalyst, total reactants flow (C_3H_8:O_2:Ar) GHSV 6000 h^{-1}, atm. pressure,400 ºC.*

3.3.2.8. Spent catalyst analysis

Further, the spent catalyst was analyzed by various characterization techniques to understand the structural and morphological aspects. **Fig. 3.14** represents TEM and XPS spectra of spent VGA-2 catalyst which analyzed after 24 h of reaction. **Fig. 3.14a-b** clearly shows the agglomeration of metal particles (VO_x and GaO_x) on the catalyst surface after 24 h of ODH of propane reaction conditions, thereby decreasing the VO_x and GaO_x dispersion on the γ-Al_2O_3 support. However, due to the amorphous nature of the supported catalyst, the metal particles are not visible. **Fig. 3.14c-h** represents the XPS spectra of the spent VGA-2 catalyst. The V2p core level spectra were deconvoluted into two peaks assigned to V in +5, and +4 oxidation states The relative percentage of V4+ (47 %) is higher on the surface compared to the fresh catalyst. This result indicated that the peak intensity of V^{4+} is increased at the end of reaction due to the reducibility of V^{5+} or by the formation of polymerized VO_x species on the surface. No apparent changes are observed in Ga 3d, Ga 2p, and Al 2p core-level spectra. The O 1s core-level spectrum of spent vanadium catalyst exhibited two peaks at (1) 530.2 eV assigned to lattice oxygen and (2) 531.5 eV assigned to surface hydroxyl species.

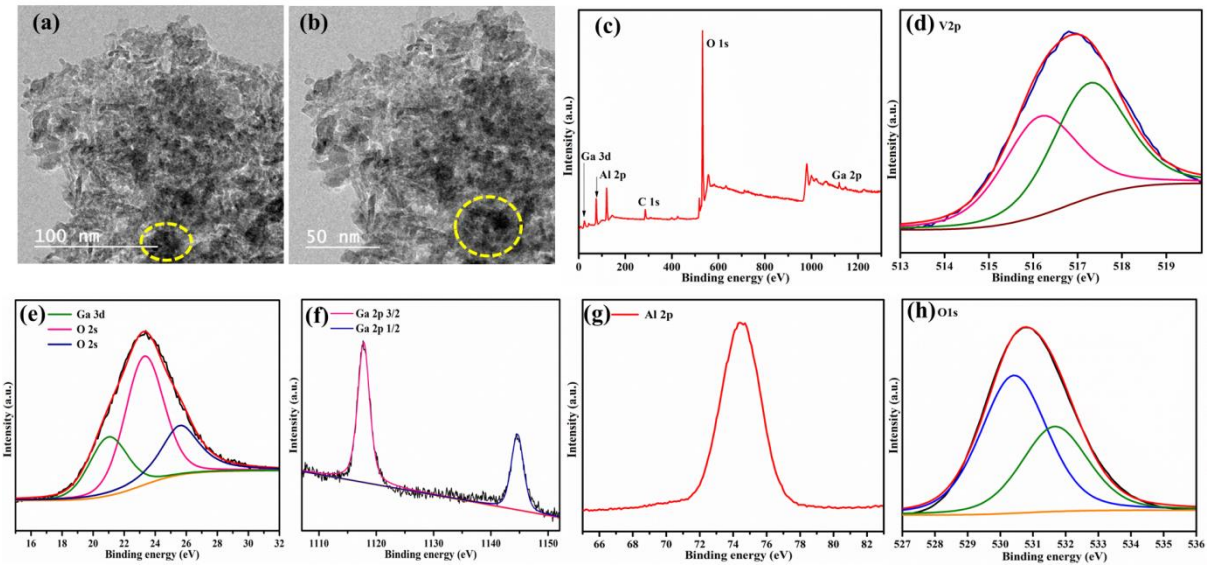

Fig. 3.14 TEM and XPS spectra of spent VGA-2 catalyst (a-b) HRTEM images; (c) Full scan XPS, (d) V 2p, (e) Ga 3d, (f) Ga 2p, (g) Al 2p and (h) O 1s core level spectra.

3.3.2.9. Thermogravimetric analysis

Coke deposition is the major drawback in catalysis, which can block the active sites of the catalyst surface. Thermogravimetric analysis was used to investigate the coke deposition after the reaction and values tabulated in **Table 3.1**. **Fig. 3.15** represents thermograms of the spent catalyst. The weight loss is quantified for all the spent catalysts at around 400 ºC. The Ga-supported catalyst showed the highest coke deposition due to high C-C bond cracking. However, vanadium-supported Al_2O_3 shows less coke deposition (9 %) than the Ga-supported catalyst, which implies that vanadium is a better candidate for C-H bond activation in comparison to Ga. Interestingly, the optimized VGA-2 catalyst shows the least coke deposition compared to all other compositions, which confirms the catalyst uniqueness and intriguing feature aid in driving the catalytic activity for a long time on stream study. This is well matched with spent TEM and XPS analysis. Moreover, the higher gallium loaded VGA-5 catalyst shows 20 % coke deposition due to higher C-C cracking reactions, and high gallium content leads to the formation of CO_x. Hence, the stable catalytic activity of VGA-2 can be attributed to the lower coke deposition during the reaction.

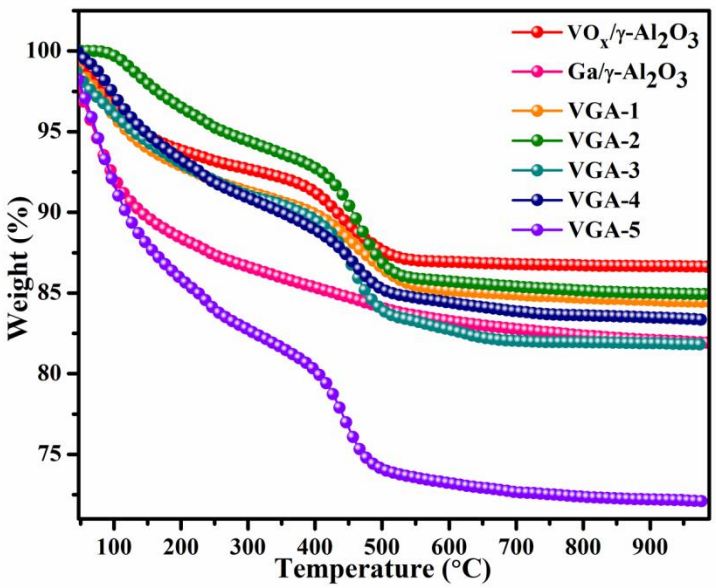

Fig. 3.15 Thermal stability of VO_x and Ga oxide supported spent catalysts.

3.4. Conclusions

In summary, a set of vanadium-gallium oxide-supported γ-Al_2O_3 catalysts has been synthesized by incipient wetness impregnation. The $V_{7.0}Ga_{3.0}$/γ-Al_2O_3 (VGA-2) catalyst showed excellent catalytic activity for the ODH of propane using O_2 as the oxidant. The highly dispersed isolated monomeric vanadia and unsaturated Ga^{3+} species are selective for propane activation. Textural and structural properties of the materials were analyzed by various techniques such as N_2-sorption, XRD, TEM, NH_3-TPD, TGA, and Raman analysis to gain more insights into the composite and catalytic performance. The increased catalytic activity of the VGA-2 catalyst was ascribed to the more nucleophilic lattice oxygen and higher VO_x density. Moreover, the *in-situ* DRIFTS study distinctly showed that the lattice oxygen plays a predominant role in alkane activation, and reaction follows the MvK mechanism.

References

1. J.S. Plotkin, Catal. Today. 106 (2005) 10-14.
2. M. Chen, J. Xu, Y. M. Liu, Y. Cao, H.Y. He, J.H. Zhuang, Appl. Catal. A 377 (2010) 35–41.
3. S.N. Koc, K. Dayioglu, H. Ozdemir, J. Chem. Sci. 128 (2016) 67.
4. Appl. Petrochem Res. 5 (2015) 377–392.
5. B. Hu, N.M. Schweitzer, G. Zhang, S.J. Kraft, D.J. Childers, M.P. Lanci, J.T. Miller, A.S. Hock, ACS Catal. 5 (2015) 3494–3503.
6. S. Tan, B. Hu, W. Kim, S.H. Pang, J.S. Moore, Y. Liu, R.S. Dixit, J.G. Pendergast, D.S. Sholl, S. Nair, C.W. Jones, ACS Catal. 6 (2016) 5673–5683.
7. Brookes T (2012) New technology developments in the petrochemical industry-refinery integration with petrochemicals to achieve higher value uplift. In: Egypt petrochemicals conference, Cairo-Egypt.
8. Hyde B (2012) Light olefins market review. In: Foro Pemex Petroquimica Mexico, 2012.
9. O.A. Barias, A. Holmen, E.A. Blekkan, J. Catal. 158 (1996) 1–12.
10. L. Deng, H. Miura, T. Shishido, S. Hosokawa, K. Teramura, T. Tanaka, ChemCatChem 6 (2014) 2680–2691.
11. A. Juez, A.M. Beale, K. Maaijen, T.C. Weng, P. Glatzel, B.M. Weckhuysen , Journal of Catal. 276 (2010) 268-279.
12. F. Cavani, F. Trifiro, Catal. Today. 24 (1995) 307–313.
13. M.D. Argyle, K. Chen, A.T. Bell, E. Iglesia, J. Catal. 208 (2002) 139.
14. A.K. Venugopal, A.T. Venugopalan, P. Kaliyappan, T. Raja, Green Chem. 15 (2013) 3259–3267.
15. R. Grabowski, Catalysis Reviews. 48 (2006) 199-268.
16. Special Supplement to Chemical Engineering Science, vol. 8, 1954 P. Mars and D. W. van Krevelen.
17. A.F. Carley, P.R. Davies, M.W. Roberts, Catal. Today. 169 (2011) 118−124.
18. S.A. Al-Ghamdi, H.I. de Lasa, Fuel. 128 (2014) 120-140.
19. Harold H. Kung advances in catalysis, volume 40.
20. C.A. Carrero, R. Schloegl, I.E. Wachs, R. Schomaecker, ACS Catal. 4 (2014) 3357−3380.
21. K. Chen, A.T. Bell, E. Iglesia, J. Phys. Chem. B. 104 (2000) 1292–1299.

22. M. Cherian, M.S. Rao, A.M. Hirt, I.E. Wachs, G. Deo, J. Catal. 211 (2002) 482–495.
23. K. Chen, S. Xie, A.T. Bell, E. Iglesia, J. Catal. 195 (2000) 244–252.
24. T. Davies, S.H. Taylor, J. Mole. Catal. A Chemi. 220 (2004) 77–84.
25. B. Frank, R. Fortrie, C. Hess, R. Schlogl, R. Schomacker, Appl. Catal. A, 353 (2009) 288–295.
26. A.A. Ayandiran, I.A. Bakare, H. Binous, S.A. Ghamdi, S.A. Razzaka, M.M. Hossain, Catal. Sci. Technol. 6 (2016) 5154.
27. S. Rostom, H.I.D. Lasa, Ind. Eng. Chem. Res. 56, 45 (2017) 13109–13124.
28. C. Heine, M. Havecker, M.S. Sanchez, A. Trunschke, R. Schloogl, M. Eichelbaum, J. Phys. Chem. C 117 (2013) 26988−26997.
29. B. Solsona, J.M. Lopez, M.L. Pena., F. Rey, V. Moya, T. Blasco, J. Catal. 203 (2001) 443–52.
30. K. Routray, K.R.S.K. Reddy, G. Deo, Appl Catal A Gen 265 (2004) 103–113.
31. K. Chen, A.T. Bell, E. Iglesia, J. Catal. 209 (2002) 35–42.
32. Comite, A. Sorrentino, G. Capannelli, M.D. Serio, R. Tesser, E. Santacesari, J. Mol. Catal. A Chem. 198 (2003) 151–165.
33. T.C. Watling, G. Deo, K. Seshan, I.E. Wachs, J.A. Lercher, Catal. Today 28 (1996) 139−145.
34. A.A. Lemonidou, L. Nalbandian, I.A. Vasalos, Catal. Today 61 (2000) 333−341.
35. Y.M. Liu, Y. Cao, S.R. Yan, W.L. Dai, K.N. Fan, Catalysis Letters, 88 (2003) 61–67.
36. E.V. Kondratenko, M. Cherian, M. Baerns, S. Dangsheng, R. Schlogl, X. Wang, I.E. Wachs. J. Catal. 234 (2005) 131–142.
37. M. Hoj, A.D. Jensen, J.D. Grunwaldt, Appl. Catal. A Gen. 451 (2013) 207–215.
38. Q.X. Luo, X.K. Zhang, B.L. Hou, J.G. Chen, C. Zhu, Z.W. Liu, Z.T. Liu, J. Lu, Catal. Sci. Technol. 8 (2018) 4864-4876.
39. M. Trueba, S.P. Trasatti, Eur. J. Inorg. Chem. (2005) 3393–3403.
40. F. Luo, C.J. Jia, R. Liu, L.D. Sun, C.H. Yan, Material. Res. Bull. 48 (2013) 1122–1127.
41. R. You, X. Zhang, L. Luo, Y. Pan, H. Pan, J. Yang, L. Wu, X. Zheng, Y. Jin, W. Huang, J. Catal. 348 (2017) 189–199.
42. K. Chalupka, C. Homas, Y. Millot, F. Averseng, S. Dzwigaj, J. Catal. 305 (2013) 46–55.
43. Q. Liu, J. Li, Z. Zhao, M. Gao, L. Kong, J. Liu, Y. Wei, Catal. Sci. Technol 6 (2016) 5927-5941.

44. T. Kim, I.E. Wachs, J. Catal. 255 (2008) 197−205.
45. S. Tan, S.J. Kim, J.S. Moore, Y. Liu, R.S. Dixit, J.G. Pendergast, D.S. Sholl, S. Nair, C.W. Jones, ChemCatChem. 7 (2016) 214–221.
46. M. Nakai, K. Miyake, R. Inoue, K. Ono, H.A. Jabri, Y. Hirota, Y. Uchida, S. Tanaka, M. Miyamoto, Y. Oumi, C.Y. Kong, N. Nishiyama, Catal. Sci. Technol. 9 (2019) 6234.
47. J.J.H.B. Sattler, I.D.G. Jimenez, L. Luo, B.A. Stears, A. Malek, D.G. Barton, B.A. Kilos, M.P. Kaminsky, T.W.G.M. Verhoeven, E.J. Koers, M. Baldus, B.M. Weckhuysen, Angew. Chem. Int. Ed. 53 (2014) 9251 –9256.
48. S.W. Choi, W.G. Kim, J.S. So, J.S. Moore, Y. Liu, R.S. Dixit, J.G. Pendergast, C. Sievers, D.S. Sholl, S. Nair, C.W. Jones, J. Catal. 345 (2017) 113–123.
49. W.G. Kim, J. So, S.W. Choi, Y. Liu, R.S. Dixit, C. Sievers, D.S. Sholl, S. Nair, C.W. Jones, Chem. Mater. 29 (2017) 7213–7222.
50. T. Otroshchenko, G. Jiang, V.A. Kondratenko, A.U. Rodemerck, E.V. Kondratenko, Chem. Soc. Rev. 50 (2021) 473.
51. Q.Q. Yang, P. Hu, N.Y. Xiu, W.Z. Lang, Y.J. Guo, Chemistry Select. 3 (2018) 10049 – 10055.
52. X.L. Xue, W.Z. Lang, X. Yan, Y.J. Guo, ACS Appl. Mater. Interfaces 9 (2017) 15408−15423.
53. H. Zhu, S.O. Chikh, H. Dong, I. Llorens, Y. Saih, D.H. Anjum, J.L. Hazemann, J.M. Basset, ChemCatChem 7 (2015) 3332 –3339.
54. B. Solsona, T. Blasco, J.M. Lopez Nieto, M.L. Pena, F. Rey, A.V. Moya, J. Catal. 203 (2001) 443 –452.
55. D.E. Keller, T. Visser, F. Soulimani, D.C. Koningsberger, B.M. Weckhuysen, Vib. Spectrosc. 43 (2007) 140–151.
56. X. Gao, S.R. Bare, M. Bert, X. Weckhuysen, I.E. Wachs, J. Phys. Chem. B. 102 (1998) 10842-10852.
57. G. Liu, Z.J. Zhao, T. Wu, L. Zeng, J. Gong, ACS Catal. 6 (2016) 5207−5214.
58. E. Nowicka, C. Reece, S.M. Althahban, K.M.H. Mohammed, S.A. Kondrat, D.J. Morgan, Q. He, D.J. Willock, S. Golunski, C.J. Kiely, G.J. Hutchings, ACS Catal. 8 (2018) 3454−3468.
59. D. Yun, Y. Wang, J.E. Herrera, ACS Catal. 8 (2018) 4681−4693.
60. G. Xie, X. Liu, Q. Li, H. Lin, Y. Li, M. Nie, L. Qin, J Mater Sci 52 (2017)10915–10926.

61. C.T. Shao, W.Z. Lang, X. Yan, Y.J. Guo, RSC Adv. 7 (2017) 4710.
62. L. Ding, H.Yi, W. Zhang, R. You, T. Cao, J. Yang, J. Lu, W. Huang, ACS Catal. 6 (2016) 3700−3707.
63. V. Thakur, S.M. Shivaprasad, Applied Surface Science 327 (2015) 389–39.
64. W. Jevasuwan, Y. Urabe, T. Maeda, N. Miyata, T. Yasuda, H. Yamada, M. Hata, N. Taoka, M. Takenaka , S. Takagi, Materials, 5 (2012) 404-414.
65. L. Shi, Y. Zhou, S. Qi, K.J. Smith, X. Tan, J. Yan, C. Yi, ACS Catal. 10 (2020) 10661−10671.
66. M. Schmal, M.M.V.M. Souza, V.V. Alegre, M.A.P Silva, D.V. Cesar, C.A.C. Perez, Catal. Today. 118 (2006) 392–401.
67. M.O. Guerrero, P. Alan, J. Mc Cu, J.A. Anderson, J. Catal. 390 (2020) 72−80.
68. M.A. Hasan, M.I. Zaki, L. Pasupulety, J. Phys. Chem. B. 106, 49 (2002) 12747–12756.
69. P.C. Redfern, P. Zapol, M. Sternberg, S.P. Adiga, S.A. Zygmunt, L.A. Curtiss, J. Phys. Chem. B, 110 (2006) 8363–8371.
70. A. Valcarcel, J.M. Ricart, A. Clotet, F. Illas, A. Markovits, C. Minot, J. Catal. 241 (2006) 115−122.

Chapter-4

Effective and Selective Oxidation of 2-Butanol over Mn Supported Catalyst Systems

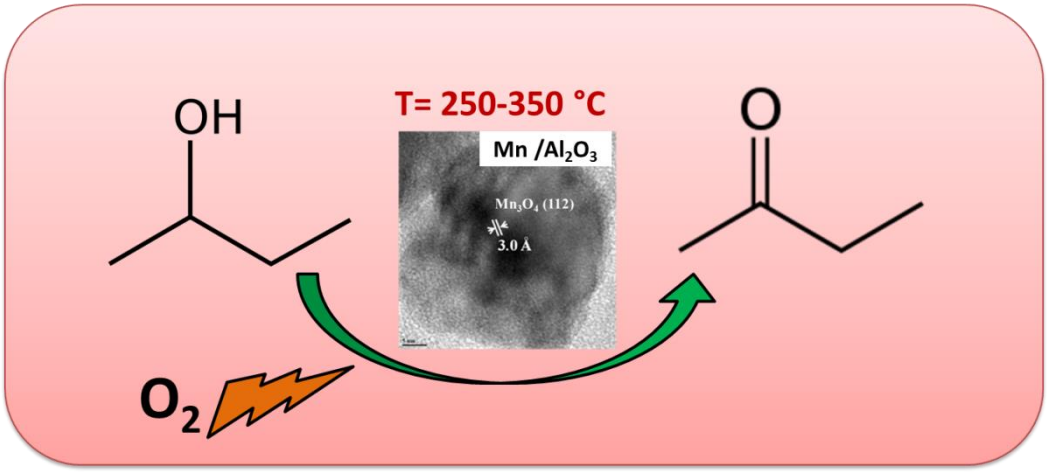

Synopsis

- A series of Mn_xO_y-Al_2O_3 (MA), Mn_xO_y-CeO_2 (MC), Mn_xO_y-ZrO_2 (MZ), and Mn_xO_y-SiO_2 (MS) catalysts were prepared by co-precipitation followed by the hydrothermal method

- Selective oxidation of 2-Butanol to MEK over Mn supported on different metal oxide supports was studied

- The presence of Mn_3O_4 species in MA catalysts is responsible for maximum catalytic activity towards 2-Butanol oxidation

- MA catalyst conferred a maximum 2-Butanol conversion of 51 % and selectivity of 88 % towards MEK

4.1. Background of the work

The nature of catalyst and support play a major role in oxidation catalysis. In oxidation reactions, two types of catalysts have been established, which are based on metal oxide (V, Cr, Fe, Co, and Mn), a redox and non-redox type catalyst like noble metals (Au, Pt, and Pd). There are only a few reports on the production of MEK using different oxidants. Mistry *et al*. reported that the catalytic activity of 2-Butanol oxidation depends upon the morphology of Pt nanoparticles supported on γ-Al_2O_3 [1]. Maitri *et al.* employed a solid solution of ZnO and InN for selective oxidation of 2-Butanol to MEK at higher temperatures between 350 and 450 $^{\circ}$C [2]. The low coverage of Au (111) surface facets are highly active for 2-Butanol oxidation to 2-Butanone, and higher oxygen coverage leads to both partial and total oxidation [3]. Later, Li *et al.* observed similar results, where the formation of 2-Butanone on oxygen-coverage of Pd (100) surfaces [4]. Hou and co-workers reported that liquid-phase oxidation of 2-Butanol using oxygen as an oxidant over Au:Pd bimetallic nanoparticles shows 100 % selectivity towards 2-Butanone at 60 °C [5]. Wang *et al.* have reported that the smaller Pt NPs (1.5-4.9 nm) showed the highest catalytic activity for aqueous phase oxidation [6]. Li *et al*. have studied the adsorption of 2-Butanol on both clean and oxygen covered Au/Pd (100) alloy surfaces; when alloy with gold coverage is less than ~ 0.4 mL, 2-Butanone is produced with activation energy of ~ 65 kJ /mol, and the yield of 2-Butanone increases linearly with palladium coverage in the alloy [7]. Sun *et al.* have utilized H_2O_2 as a green oxidant for 2-Butanol oxidation to MEK with tungsten-based polyoxometalate catalyst, and two different calorimetric techniques were used to identify thermal hazards associated with the 2-Butanol oxidation reaction system [8]. Several d-block metals like Pt, Ru, Rh, Au, Co, Ni, Ag, and Ir [6, 9] were tested as catalysts for oxidation of alcohols in liquid [6] as well as in the gas phase [9] reactions.

The present study demonstrates that selective oxidation of 2-Butanol over manganese oxide with various supported catalysts systems was studied for the first time. Over the few decades, manganese oxide catalysts have generated much interest due to their unique potentials, such as redox properties and a specific ratio of co-existence of different oxidation states (Mn^{2+}, Mn^{3+}, Mn^{4+}, Mn^{5+}, and Mn^{7+}), which enables the electron transfer to occur quickly [10-13]. Moreover, manganese oxides in the form of Mn_3O_4, MnO_2, and Mn_2O_3 are well-known for selective oxidation of VOCs [11, 14-17]. However, controlling an active oxidation state in Mn-based materials is challenging in heterogeneous catalysis. In this work, manganese oxide and supports like Al_2O_3, CeO_2, ZrO_2, and SiO_2 were prepared by traditional co-precipitation

and sol-gel methods (only SiO_2). Typically, two different manganese oxide structures (Mn_3O_4 and Mn_2O_3) were found by changing supports. Catalysts with a specific ratio of Mn^{+2}, Mn^{+3}, and Mn^{+4} show better catalytic activity towards the oxidation of 2-Butanol. This reaction was performed in a fixed bed reactor (FBR) continuous flow system, and the catalysts were subjected to several characterization techniques.

4.2. Results and discussion

4.2.1. Catalyst characterization

4.2.1.1. Powder X-ray diffraction

PXRD is one of the primary bulk techniques which offer detailed information about the nature and structural aspect of the catalysts. **Fig.4.1** shows the powder X-ray diffraction patterns of pristine supports and Mn with different oxide supported catalysts Mn_xO_y-Al_2O_3, Mn_xO_y-ZrO_2, Mn_xO_y-CeO_2, and Mn_xO_y-SiO_2. It is clearly seen from **Fig. 4.1b** Mn_xO_y-SiO_2 mixed oxide catalyst showed a broad diffraction peak at 2θ value 21° which is attributed to silica and the diffraction peaks observed at 2θ value 28°, 37°, 56° are assigned to Mn_2O_3 phase. This result is well-matched with JCPDS No.78-0390. In the case of Mn_xO_y-ZrO_2 mixed oxide catalyst, the diffraction peaks at 18°, 28°, 32°, 36°, 38°, 50°, and 60° correspond to Mn_3O_4 (JCPDS No.24-0734). In Mn_xO_y-CeO_2 mixed oxide catalyst, a high-intensity peak at around 28° (2θ) corresponds to ceria (JCPDS No. 75-0151) and the other peaks correspond to Mn_2O_3 phase (JCPDS No.78-0390).

The diffraction peaks for Mn_xO_y-Al_2O_3 catalysts at 2θ value 18°, 29°, 30°, 32°, 36°, 38°, 44°, 58°, 60°, and 64° are assigned to the Mn_3O_4 phase (JCPDS No. 24-0734). No additional peak pertaining to aluminum oxides was observed, suggesting the smaller crystallite size of alumina in the catalyst, or it may form a homogeneous solid solution with the Mn_3O_4 matrix.

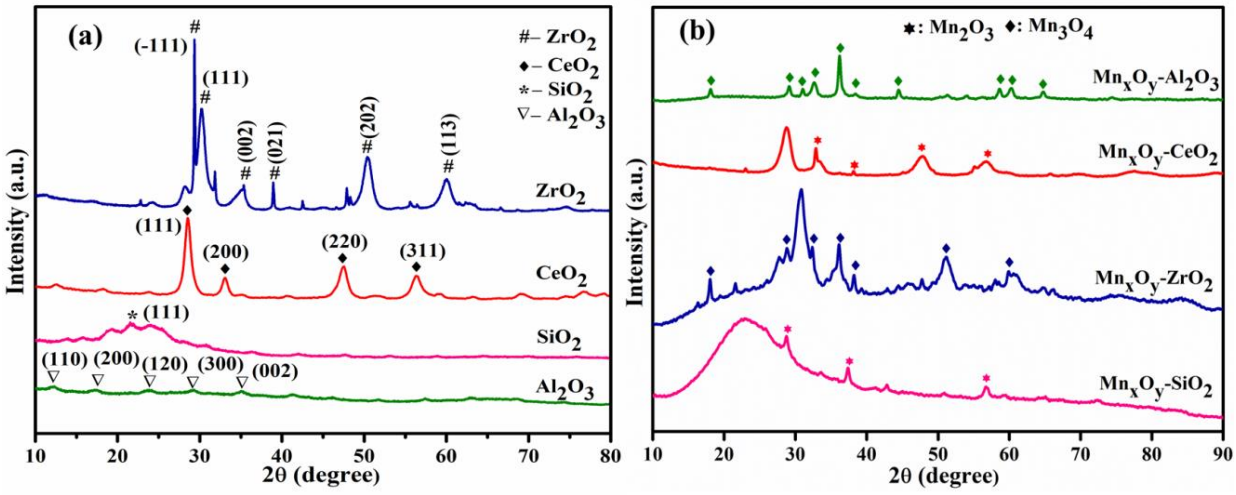

Fig.4.1 XRD profiles of (a) pure supports and (b) Mn supported catalysts.

4.2.1.2. N_2 physisorption

Table 4.1 provides the details about the textural properties of all the calcined catalysts. The surface area of catalysts increased in the order, (MA) Mn_xO_y-Al_2O_3< (MC) Mn_xO_y-CeO_2< (MZ) Mn_xO_y-ZrO_2< (MS) Mn_xO_y-SiO_2, respectively. Amongst all, Mn_xO_y-Al_2O_3 (MA) mixed oxide catalyst demonstrated the lowest surface area (84 m^2/g) compared to other catalysts due to the larger crystallite size [18]. In contrast, despite the larger crystallite size of Mn_xO_y-SiO_2 (MS), the catalyst offers the highest surface area (339 m^2/g) compared to the rest of the catalysts. This is due to the presence of porous silica in the catalyst. The Mn_xO_y-CeO_2 (MC) and Mn_xO_y-ZrO_2 (MZ) catalysts showed relatively higher surface area 89 and 103 m^2/g, respectively. Both the catalysts showed near 5±1.0 nm crystallite size, respectively.

Table 4.1 Textural properties of the catalysts calcined at 450 °C

S.No.	Catalysts	Catalyst Code	BET Surface area [a] (m^2/g)	Total pore volume [a] (cm^3/g)	Crystallite size [b] (nm)
1	Mn_xO_y- Al_2O_3	MA	84	0.32	24.7 ± 1.0
2	Mn_xO_y- CeO_2	MC	89	0.18	5.5 ± 1.0
3	Mn_xO_y- ZrO_2	MZ	103	1.20	4.6 ± 1.0
4	Mn_xO_y- SiO_2	MS	339	1.25	19.8 ± 1.0

(a) Calculated from BET surface area analysis.

(b) Average crystallite size calculated from the Scherer formula ($t = 0.9\lambda/ \beta Cos\theta$) using the (112) plane of Mn in MA, (400) plane of Mn in MC, (112) plane of Mn in MZ and (400) plane of Mn in MS in PXRD.

4.2.1.3. X-ray photoelectron spectroscopy

To understand the surface compositions and chemical state of various species present on the surface of the catalysts, the catalysts were subjected to XPS analysis. **Fig.4.2** shows the Mn 2p core-level XPS spectra of manganese oxide alone, freshly synthesized and spent (Mn_xO_y-Al_2O_3) MA catalysts. The XPS spectra were deconvoluted by peak fitting method with Shirley background removal in Mn 2p core-level spectrum, binding energy (BE) values at around 640.4, 641.7, and 643.3 eV were assigned to Mn^{2+}, Mn^{3+} and Mn^{4+} state respectively, which are in good accordance with the reported literature [19, 20]. In addition to this a broad peak (Satellite) was noticeable on the B.E. 645.5 eV of Mn $2p_{3/2}$ core-level in the XPS spectrum which is originated from the charge transfer from oxygen ligand to unfilled 3d orbital of Mn during the final state of the photoelectron emission process [21]. **Fig.4.2 b and**

c shows the Mn 2p core-level spectra for fresh and spent MA catalysts; three peaks were observed at B.E. value 640.4, 641.7, and 643.3 eV, which can be assigned to Mn in +2, +3, and +4 oxidation state respectively [19]. Infact, there is no significant change in the binding energy value of the spent MA catalyst proving that the catalyst poses a stable oxidation state even after 12 h of reaction under optimum reaction conditions.

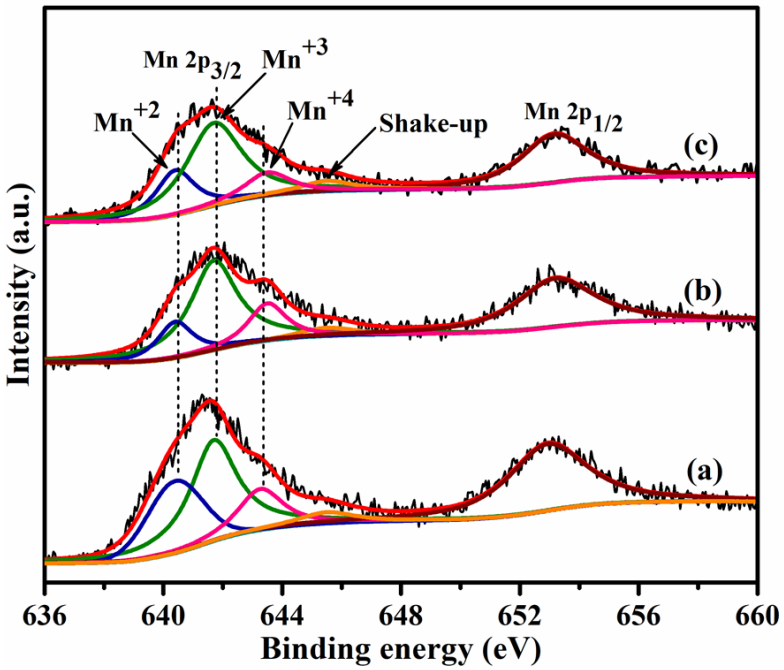

Fig.4.2 XPS spectra of Mn 2p core levels for (a) Manganese oxide (b) Fresh-Mn_xO_y-Al_2O_3 and (c) Spent-Mn_xO_y-Al_2O_3.

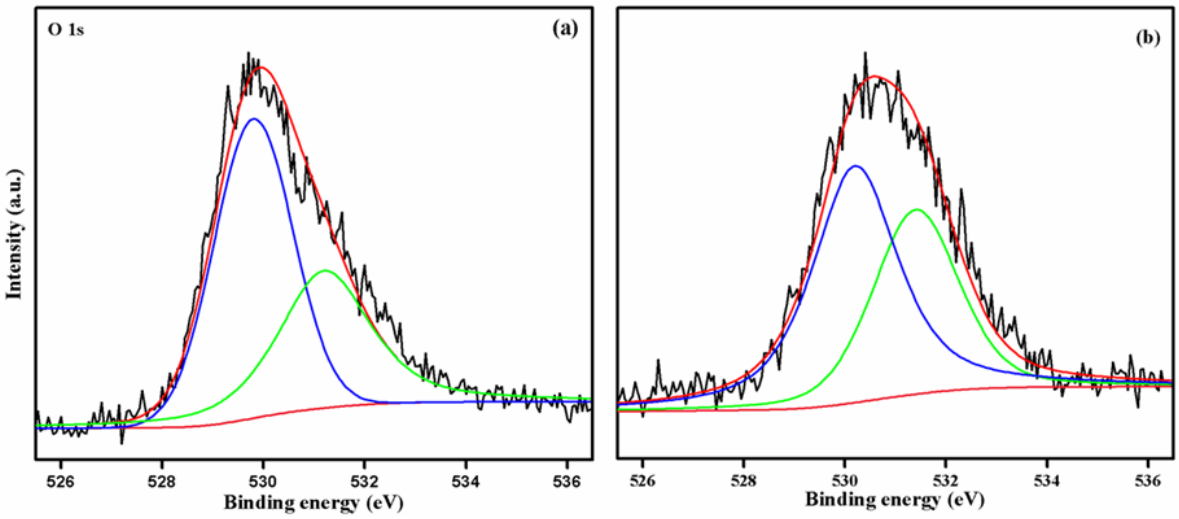

Fig. 4.3 XPS spectra of O 1s (a) Fresh-Mn_xO_y-Al_2O_3 and (b) Spent-Mn_xO_y-Al_2O_3.

The O1s spectra were deconvoluted into two peaks and shown in **Fig 4.3**. Both fresh and spent MA catalysts showed XPS peaks at around 530 and 531.5 eV, attributed to lattice oxygen and a surface hydroxyl group [22, 23]. Therefore, the superior catalytic activity of

Mn_xO_y-Al_2O_3 catalyst may be due to the presence of surface oxygen species that favors the selective oxidation of 2-Butanol. However, it should be worth mentioning that the peak intensity of lattice oxygen 530 eV was reduced after the reaction suggesting the participation of surface lattice oxygen in this oxidation reaction. After the regeneration in the presence of air, the catalyst shows the same performance.

4.2.1.4. Raman spectroscopy

Raman spectroscopy provides detailed information about the vibration modes of different metal oxide bonds in the catalysts. **Fig. 4.4** shows the Raman spectral data of Mn_xO_y-Al_2O_3, Mn_xO_y-CeO_2, Mn_xO_y-ZrO_2, and Mn_xO_y-SiO_2 catalysts. The spectra were measured between 200-1500 cm^{-1}. Except for the Mn_xO_y-SiO_2 catalyst, all the catalysts showed three distinct peaks at around 660, 317, and 372 cm^{-1} which are attributed to Mn_3O_4, Mn(III)-O, and Mn(IV)-O bond, respectively [24]. The typical Raman band at 630 and 680 cm^{-1} corresponds to Mn_2O_3 was not detectable due to the higher intensity of the Mn_3O_4 phase. In contrast, Mn_xO_y-CeO_2 catalyst showed an additional high-intensity peak at 457 cm^{-1} which can be assigned to the vibration mode (F_{2g}) of the cubic fluorite structure of the CeO_2 lattice [25, 26]. The result obtained from the Raman spectra is corroborated with the PXRD pattern of the catalysts.

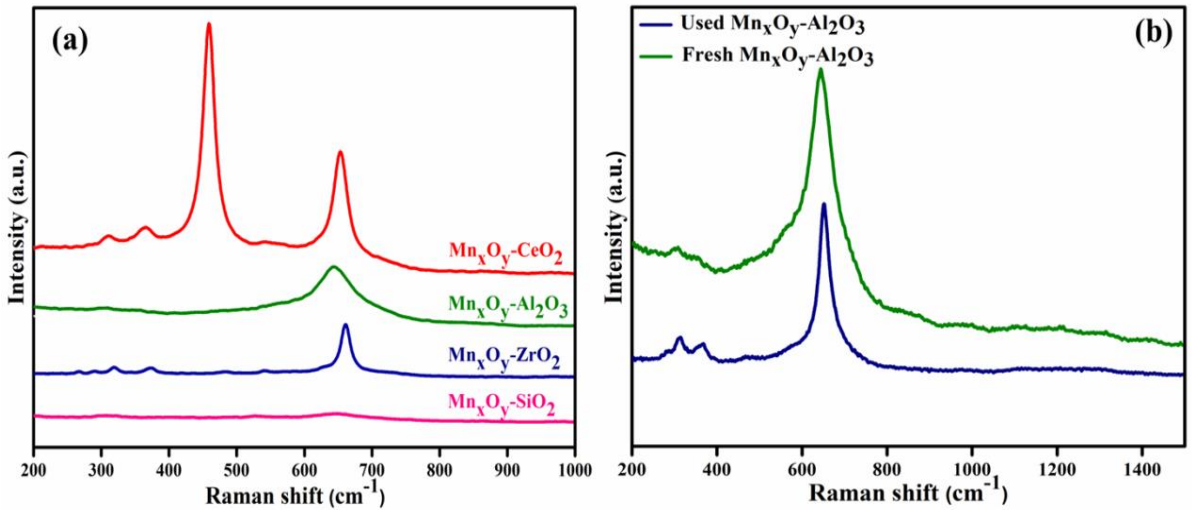

Fig. 4.4 (a) Raman spectra of all as-synthesized catalysts calcined at 450 °C (b) fresh and spent MA catalysts.

Further, the spent Mn_xO_y-Al_2O_3 catalyst was analyzed to elucidate any structural changes and the possible coke formation on the catalyst surface. **Fig. 4.4b** represents the Raman spectra of both fresh and spent catalysts. Raman spectra of the spent catalyst show hardly any structural change, pointing that the tailored catalyst is highly stable under the optimum reaction

conditions. Moreover, no peaks corresponding to D and G bands [27] were detected, suggesting no coke formation even after the reaction.

4.2.1.5. Temperature programmed desorption

Acidity is one of the key parameters which play an important role in the catalytic activity of 2-Butanol oxidation. To find the acidity of the catalysts, NH_3-TPD was carried out for all calcined catalysts, and the results are given in **Fig. 4.5**. Mn_xO_y-CeO_2 and Mn_xO_y-ZrO_2 catalysts showed no peaks, which confirmed that both the catalysts have no acidic sites. In Mn_xO_y-SiO_2 catalyst, the peak at 650 °C corresponds to strong acidic centers, and the broad peak in the temperature range between 200-300 °C was originated from the weak acidic site of the catalyst. Whereas, Mn_xO_y-Al_2O_3 catalyst showed two major peaks in which the peak observed at a lower temperature (~200 °C) and higher temperature (~650 °C) is due to weak and strong acidic sites, respectively. Thus, the NH_3-TPD results clearly suggest that MA catalyst exhibited the highest acidic site density, which helps enhance the catalytic activity of the catalyst and shows stable catalytic activity over 30 h.

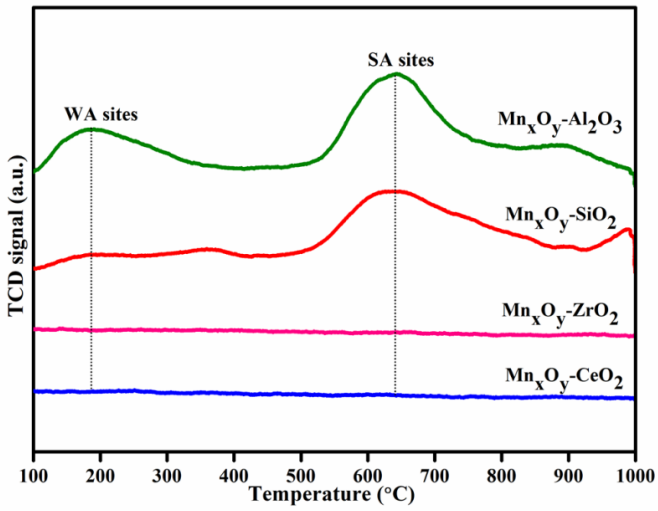

Fig. 4.5 NH_3-Temperature programmed desorption profile of calcined catalysts at 450 °C.

4.2.1.6. Transmission electron microscopy

Fig. 4.6 shows the TEM images of fresh and spent MA catalyst. TEM images reveal information about the morphology and lattice of the catalysts. **Fig. 4.6a–c** displays TEM images of fresh Mn_xO_y-Al_2O_3 catalyst in low and high resolutions. **Fig. 4.6(a)** and **(b)** TEM images clearly confirmed the uniform dispersion of manganese oxide on Al_2O_3. Indeed, the TEM results have directly demonstrated a nice decoration of alumina by nano Mn_xO_y. The d-spacing value of the Mn_xO_y-Al_2O_3 catalyst is 3.0 Å which is in agreement with the value obtained from PXRD results. TEM image of the spent Mn_xO_y-Al_2O_3 catalyst given in **Fig.**

4.6d shows no change in the morphology of the catalyst. This observation is in line with the Raman spectra of the spent MA catalyst.

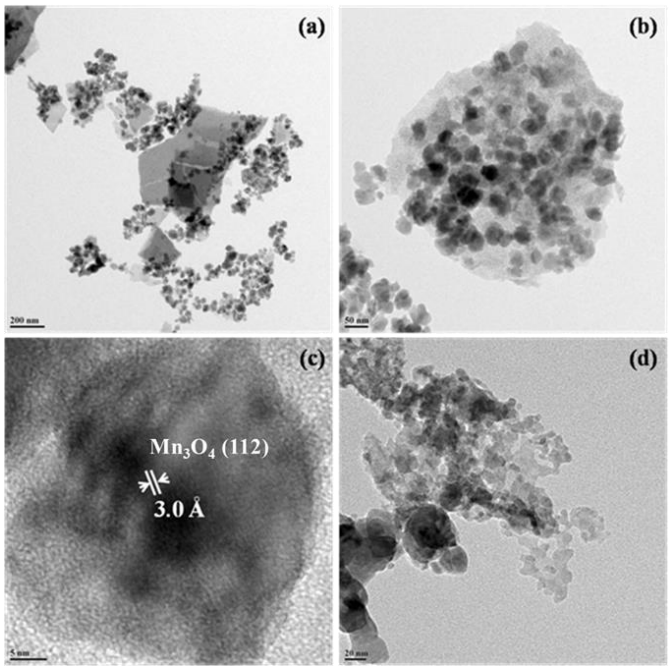

Fig. 4.6 TEM images of (a–c) fresh Mn_xO_y-Al_2O_3 and (d) spent Mn_xO_y-Al_2O_3.

4.2.2. Catalytic performance in selective oxidation of 2-Butanol

All the above-synthesized catalysts were evaluated for selective oxidation of 2-Butanol to methyl ethyl ketone (MEK) using a continuous flow fixed bed reactor as represented in **Section 2.4.12**. The developed catalysts were subjected to various reaction parameters like temperature, GHSV, and 2-Butanol flow to find optimum reaction conditions and unveil the best catalyst for the reaction. We found that these catalysts demonstrated admirable catalytic activity and stability under the optimum reaction conditions elaborated in the subsequent section.

4.2.2.1 Effect of supports

Support of a catalyst has an important role in any catalytic activity of a reaction. Choosing suitable support is a critical part of heterogeneous catalysis. To study the influence of the support for 2-Butanol to MEK reaction, manganese oxide catalyst was loaded on four different supports. Manganese oxide on Al_2O_3, CeO_2, ZrO_2, and SiO_2 catalysts were subjected to oxidation of 2-Butanol at 300 °C. The reaction was performed over 1 g catalyst with LHSV 1.8 h^{-1} with respect to 2-Butanol and GHSV 1200 h^{-1} of oxygen flow. The optimized reaction parameters and the results are depicted in **Fig. 4.7** and **Table 4.2**. MC catalyst shows maximum 2-Butanol conversion and MEK selectivity of 41 and 81 %, respectively. MS

catalyst shows better conversion (54 %), but selectivity towards MEK (33 %) was very low due to the complete oxidation of 2-Butanol to undesired products. MA and MZ catalysts show about 50 % conversion and 88 % selectivity towards MEK. MA and MZ catalysts show similar reaction trends on stream up to a certain time. However, after 12 h time on stream, MA catalyst shows slight increase in catalytic activity, but in MZ the catalyst activity decreases at the end of 12 h. This decrease in catalytic activity may be due to catalytic deactivation. Thus, MA catalysts show better activity than other tested catalysts.

Further, the reaction was performed with bare alumina support, and no conversion of 2-Butanol to MEK was observed, which confirms the dominating catalysis of manganese oxide in 2-Butanol oxidation. However, among all the catalysts MA catalyst demonstrated the highest 2-Butanol conversion (51 %) with maximum MEK yield (45 %), which may be due to the better synergistic effect between manganese oxide and alumina support. The enhanced catalytic activity of this catalyst can also be due to the presence of surface lattice oxygen which might help in the oxidation reaction. Hence, MA catalyst shows better catalytic activity of 2-Butanol and selectivity of MEK, which is further carried out to optimize the different reaction parameters.

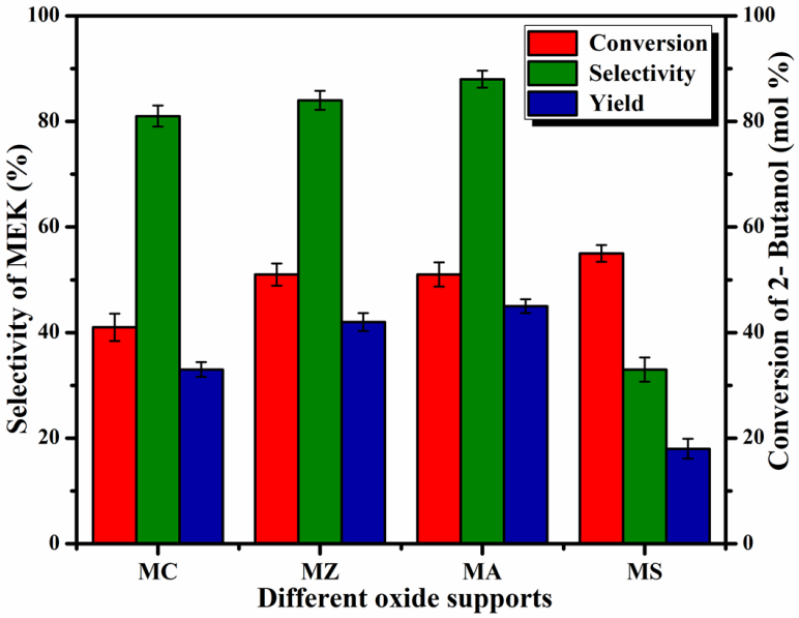

Fig.4.7 Conversion of 2-Butanol and selectivity of MEK over different Mn supported catalysts.

Reaction conditions: *300 °C, LHSV 1.8 h^{-1} with respect to 2-Butanol and GHSV 1200 h^{-1} with respect to oxygen at atm. pressure.*

Table 4.2 Catalytic activity of Mn_xO_y loaded on different supports

S. No.	Catalysts	Conversion of 2-Butanol (mol %)[a]	Selectivity (%)				Yield of MEK (%)
			MEK	Acetone	CH_3OH	CO_x[b]	
1	Mn_xO_y-CeO_2 (MC)	41	81	12	02	05	35
2	Mn_xO_y-ZrO_2 (MZ)	51	84	08	07	01	42
3	Mn_xO_y-Al_2O_3 (MA)	51	88	05	05	02	45
4	Mn_xO_y-SiO_2 (MS)	55	33	17	14	36	18

Reaction conditions: *300 °C, LHSV 1.8 h^{-1} with respect to 2-Butanol and GHSV 1200 h^{-1} with respect to oxygen at atmosphere pressure.*

(a) Conversion at steady state.
(b) CO and CO_2

4.2.2.2. Effect of temperature

Temperature is one of the main factors which influence the catalytic activity. To examine the effect of temperature, oxidation of 2-Butanol was carried out at a temperature range between 250-350 °C with MA catalyst, and the results are shown in **Fig. 4.8**. Oxidation of 2-Butanol was carried out at the contact time of 1.8 h^{-1} with respect to 2-Butanol, and GHSV 1200 h^{-1} with respect to oxygen at atmospheric pressure. At low temperature (250 °C), conversion towards 2-Butanol and selectivity of MEK were observed to be 30 and 80 %, respectively. Further increase in temperature to 300 °C, conversion and selectivity increased to 51 and 88 % respectively and remains constant for 30 h of time on stream. At higher temperature (325 and 350 °C), the initial conversion was increased, and after 7 h the conversion slowly decreased; this could be due to the deactivation at higher temperatures. Hence, 300 ºC is selected as the optimized temperature to achieve maximum conversion and selectivity of MEK.

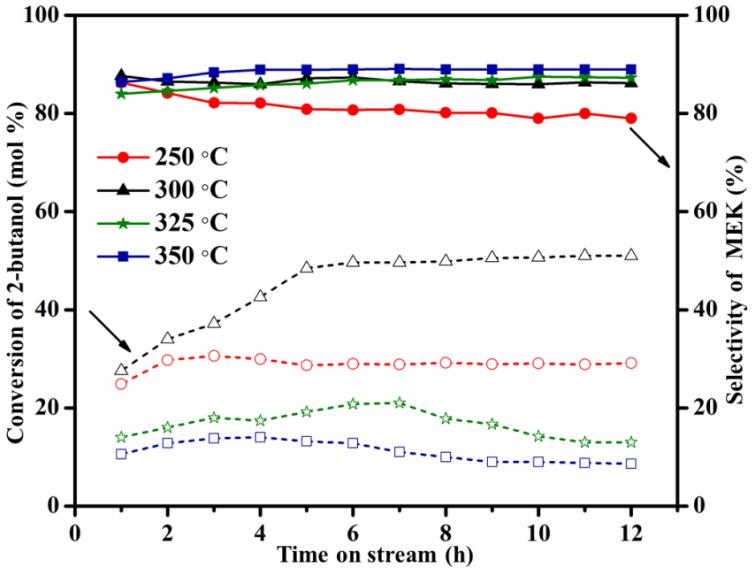

Fig. 4.8 Conversion of 2-Butanol and selectivity of MEK at various reaction temperatures over MA.

Reaction conditions: *LHSV 1.8 h^{-1} with respect to 2-Butanol and GHSV 1200 h^{-1} with respect to oxygen at atm. pressure.*

4.2.2.3 Effect of space velocity of 2-Butanol

In order to study the effect of contact time between reactants and catalytic active centres, a reaction was performed at different flow rates of 2-Butanol and the results are shown in **Fig. 4.9**. Oxidation was carried out at three different 2-Butanol flows (LHSV 1.8, 3.6 and 5.4 h^{-1}), at 300 °C, GHSV 1200 h^{-1} with respect to oxygen at atmospheric pressure. At LHSV 1.8 h^{-1}, a 51 % conversion of 2-Butanol was observed with maximum selectivity (88 %) of MEK. At this flow, 2-Butanol has optimum contact time to react with adsorbed oxygen on the surface of the catalyst. While increasing the 2-Butanol flow to LHSV 3.6 h^{-1}, conversion of 2-Butanol was decreased to 26 % but the selectivity of MEK was increased to 90 %. At LHSV 5.4 h^{-1} the conversion and selectivity decreased to 20 and 89 %, respectively. Due to the decreasing contact time between reactants and active centers, a trend in a decrease in conversion was observed at higher LHSV of 2-Butanol (3.6 and 5.4 h^{-1}). Therefore, LHSV 1.8 h^{-1} was the optimized flow rate of 2-Butanol for further studies.

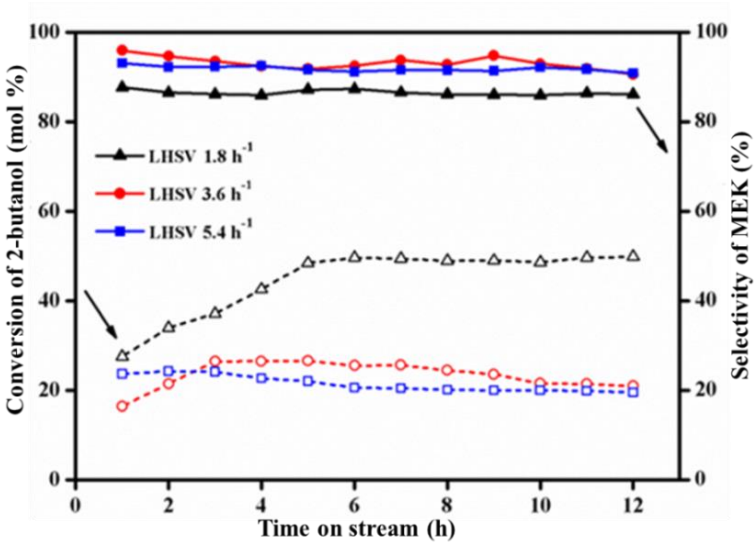

Fig. 4.9 Conversion of 2-Butanol and selectivity of MEK at various 2-Butanol flow rates over MA.

Reaction conditions: *300 °C, GHSV 1200 h^{-1} with respect to oxygen at atm. pressure.*

4.2.2.4. Effect of oxygen flow

In an oxidation reaction, the change in catalytic activity typically depends upon the flow of oxidants. To examine the effect of oxidant on the catalytic activity, the reaction was performed at three different molecular oxygen flows (GHSV 600, 1200 and 1800 h^{-1}) and the results are depicted in **Fig. 4.10**. The reaction was executed at GHSV 600 h^{-1} the maximum conversion of 2-Butanol was 35 %. Further increase in oxidant flow to GHSV 1200 h^{-1} conversion attained the maximum (51 %) and selectivity (88 %), favoring the partial oxidation of 2-Butanol to MEK. Upon increasing GHSV to 1800 h^{-1}, relatively low conversion and selectivity were obtained due to the complete oxidation of 2-Butanol to CO_x and undesired side products. Based on the above results, GHSV 1200 h^{-1} was optimized oxygen flow rate to attain maximum selectivity of MEK.

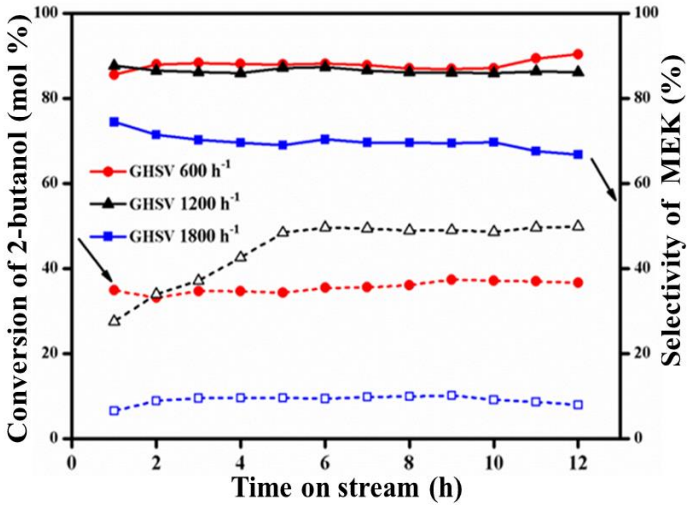

Fig. 4.10 Conversion of 2-Butanol and selectivity of MEK at different oxygen flow rates over MA.

Reaction conditions: *300 °C, LHSV 1.8 h^{-1} with respect to 2-Butanol at atm. pressure.*

4.2.2.5. Long term stability test

The stability of the optimized MA catalyst was determined for a long period of time on stream (TOS) with optimized reaction parameters: 300 ºC, GHSV 1.8 h^{-1} for 2-Butanol, and GHSV 1200 h^{-1} for molecular oxygen. The initial conversion of 2-Butanol was 27 % and the selectivity of MEK was 88 %. As reaction time increases, conversion of 2-Butanol increases gradually; after the fifth hour, the conversion and selectivity of MEK remain constant for 30 h. Catalytic performance of 51 % conversion of 2-Butanol and 88 % selectivity of MEK is observed under optimized reaction conditions.

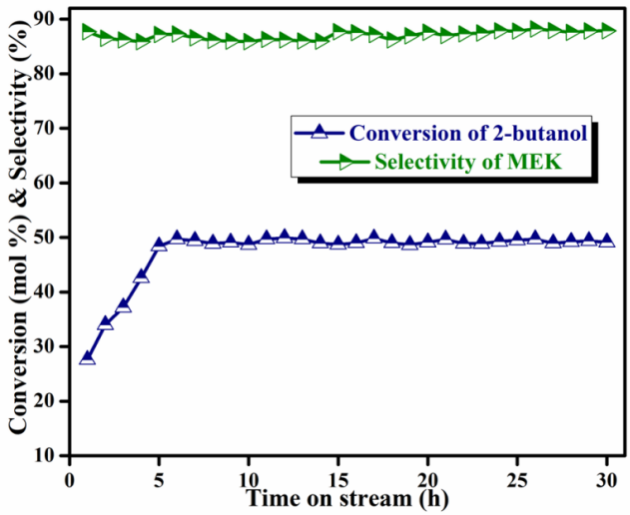

Fig. 4.11 Long term stability test of MA catalyst for oxidation of 2-Butanol over 30 h

Reaction conditions: *300 °C, LHSV 1.8 h^{-1} with respect to 2-Butanol and GHSV 1200 h^{-1} with respect to oxygen at atm. pressure.*

4.3. Conclusions

In this study, manganese oxides with different supported catalysts were prepared by the simple co-precipitation and sol-gel method. Their physicochemical characterization techniques like PXRD and Raman spectroscopy revealed Mn in Mn_3O_4 and Mn_2O_3 phases. Among all the catalysts, MA showed superior catalytic performance of 2-Butanol oxidation. The XPS study was evident that Mn in +2, +3, and +4 oxidation states is beneficial to enhance the activity in MA catalyst. In addition, surface acidity, Mn_3O_4 species, and synergetic effect play an essential role in achieving maximum selectivity of MEK. The optimization experiments proved that MA catalyst was highly active and stable activity up to 30 h of time on stream without any considerable loss in its catalytic activity; this emphasizes the durability of the catalyst. In summary, these results demonstrate a better activity than the other catalytic systems reported for oxidation of 2-Butanol to MEK.

References

1. H. Mistry, F. Behafarid, E. Zhou, L.K. Ono, L. Zhang, B.R. Cuenya, ACS Catal. 4 (1) (2013) 109–115.
2. M. Maitri, S. Kumarsrinivasan, D.S. Bhange, B. Saha, P. Chakraborty, A.K. Viswanath, C.S. Gopinath, Chem. Mater. 22 (2010) 565–578.
3. T. Yan, J. Gong, C.B. Mullins, J. Am. Chem. Soc. 2009, 131,16189−16194.
4. Z. Li, W.T. Tysoe, Surf. Sci. 604 (2010) 1377−1387.
5. W.B. Hou, N.A. Dehm, R.W.J. Scott, J. Catal. 253 (2008) 22–27.
6. T. Wang, H. Shou, Y. Kou, H.C. Liu, Green Chem. 11 (2009) 562–568.
7. Z. Li, W.T. Tysoe, Surface Science 694 (2020) 121556.
8. Y. Sun, L. Ni, M. Papadaki, Z. Jiao, W. Zhu, J. Jiang, C. Mashuga, S. Mannan, B. Wilhite, J. Loss Prev Process Ind. 66 (2020) 104177.
9. P. Papaefthimiou, T. Ioannides, X.E. Verykios, Appl. Catal. B 13 (1997) 175–184.
10. G. Deo, I.E. Wachs, J. of Catal. 146 (1994) 323-334.
11. A. Heidarnezhada, F. Zamani, Cat.Com. 60 (2014) 105-109.
12. J. Wang, H. Zhao, J. Song, T. Zhu, W. Xu, Catalysts 9 (2019) 726.
13. K. Zhang, X. Han, Z. Hu, X. Zhang, Z. Tao, J. Chen, Chem. Soc. Rev. 44 (2015) 699–728.
14. A.R. Gandhe, J.S. Rebello, J.L. Figueiredo, J.B. Fernandes, Appl. Catal. B 72 (2007) 129–135.
15. M.A. Peluso, L.A. Gambaro, E. Pronsato, D. Gazzoli, H.J. Thomas, J.E. Sambeth, Catal. Today 133 (2008) 487–492.
16. S.C. Kim, W.G. Shim, Appl. Catal. B 98 (2010) 180–185.
17. J.L. Wang, J.E. Li, C.J. Jiang, P. Zhou, P.Y. Zhang, J.G. Yu, Appl. Catal. B 204 (2017) 147–155.
18. P. Kaliyappan, A.T. Venugopalan, A.K. Venugopal , M. Marimuthu, R. Shukla, A.K. Tyagi, T. Raja, RSC Adv. 5 (2015) 3619.
19. M.C. Biesinger, B.P. Payne, A.P. Grosvenor, L.W.M. Lau, A.R. Gerson, R.S.C. Smart, Appl. Sur. Sci. 257 (2011) 2717–2730.
20. S. Bag, K. Roy, C.S. Gopinath, C.R. Raj, ACS Appl. Mater. Interfaces, 6 (2014) 2692-2699.
21. B. Murugan, D. Srinivas, C.S. Gopinath, V. Ramaswamy. A.V. Ramaswamy, Chem. Mater. 17 (2005) 3983-3993.
22. A.E. Nelson, K.H. Schulz, Appl. Surf. Sci. 210 (2003) 206–221.

23. C.S. Gopinath, S.G. Hedge, A.V. Ramasamy, S. Mahapatra, Mater. Res. Bull. 37 (2002) 1323–1332.
24. L. Li, Z. Go, A. Du, H. Liu, J. Matter. Chem. 22 (2012) 3600-3605.
25. E.S. Gnanakumar, C.J. Jino, T. Raja, C.S. Gopinath, J. Nanosci. Nanotech. 13 (2013) 2682–2688.
26. E.S. Gnanakumar, M. Naik, M. Manikandan, T. Raja, C.S. Gopinath, ChemCatChem 6 (2014) 3116-3124.
27. P.A. Bharad, K. Sivaranjani, C.S. Gopinath, Nanoscale 7 (2015) 11206-11215.

Chapter-5

Selective Oxidation of 5-Hydroxymethylfurfural to 2,5-Furandicarboxylic acid

5.1. Introduction

Identifying renewable energy resources for clean energy fuels and chemicals is one of the major challenges that humankind is confronting [1]. Today, 90 % of the energy and chemicals are obtained from petroleum derived feedstocks (natural gas, coal, and crude oil). However, the burning of fossil fuels is neither secure nor sustainable in the long run; it produces 30 billion tonnes of CO_2 per year there by increasing global warming which is one of the serious environmental issues humanity is witnessing [2-4]. These environmental issues triggered the use of renewable resources to produce chemicals and fuels [5].

5.1.1. Synthesis of HMF from biomass

Lignocellulosic biomass resources (LCB) are quite abundant plant based renewable and sustainable carbon resources. LCB is first foremost composed of cellulose (40-50 %), hemicelluloses (20-30) and lignin (10-25 %) [6]. Among the aforementioned, cellulose is a biopolymer obtained from β-1,4 glycosidic bonds of anhydrous glucose units [7]. Further cellulose hydrolysis to glucose, followed by dehydration which is, converted to HMF or through *in situ* isomerization of glucose to cellulose, finally cellulose undergoes dehydration to form the desired end product HMF **(Scheme 5.1)** [8, 9]. HMF is one of the foremost biomass-based platform chemicals draws significant attention these days owing to its wide applications in industries for various value-added chemicals and fuels. HMF can undergo a variety of chemical transformations such as hydrogenation, oxidation, and esterification, etc. which is shown in **section 1.5.1**.

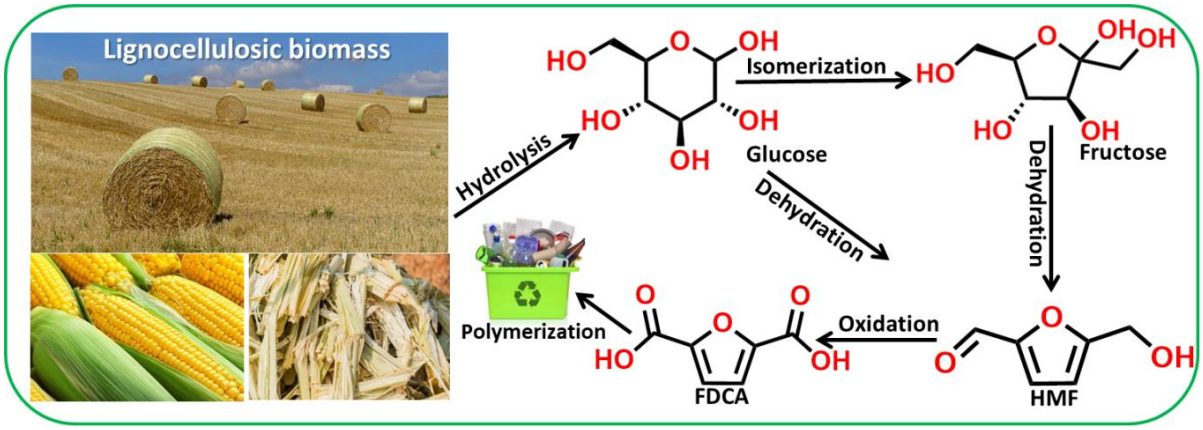

Scheme. 5.1 Upgradation of cellulose into value-added products.

5.1.2. FDCA as a polymer building block

The catalytic oxidation of HMF can produce key intermediates and value-added chemicals such as DFF, HMFCA, and FDCA. Among the oxidation products, the most important commodity chemical is FDCA which is substituted for petroleum-based terephthalic acid, as given in **Scheme 5.2**. In addition, it is used as a monomer in the production of plant-based polyethylene furanoate (PEF) [10] and could replace the conventional fossil-based polyethylene terephthalate (PET) [11-13]. Besides this, FDCA is also used as a monomer to produce polyesters, polyamides, and plasticizers [14, 15].

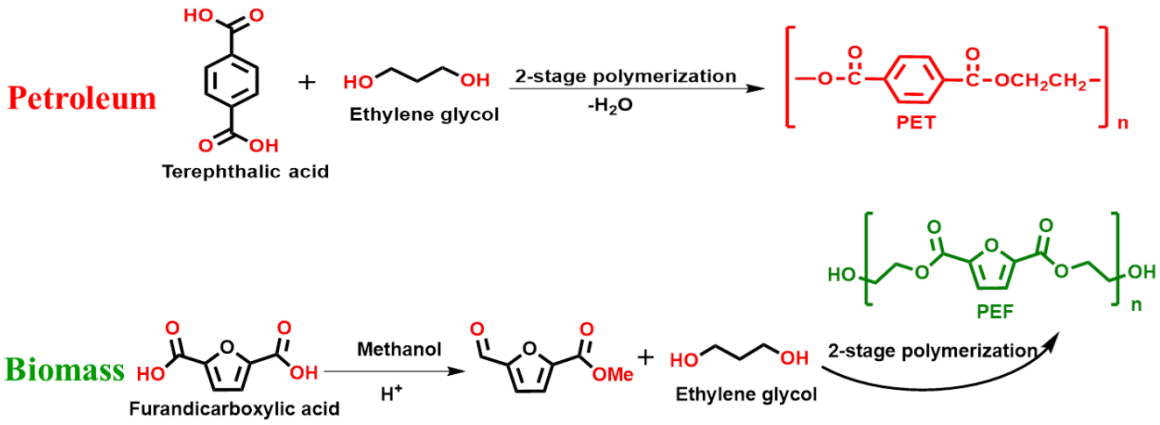

Scheme. 5.2 Comparison of PET and PEF production processes.

Additionally, FDCA also has prospective uses in medicine. The diethyl ester of FDCA has anaesthetic properties similar to cocaine [16]. Dicalcium 2,5-furandicarboxylate inhibits the growth of Bacillus megatorium [17, 18]. FDCA itself is a strong complexing agent, chelating with ions Ca^{2+}, Cu^{2+} and Pb^{2+} reportedly efficient of removing kidney stones [18, 19]. In 2011, Avantium was announced the first pilot-scale for FDCA production with a capacity of

40 tons per year [20]. **Fig. 5.1** shows the vast scope of market potential of FDCA.

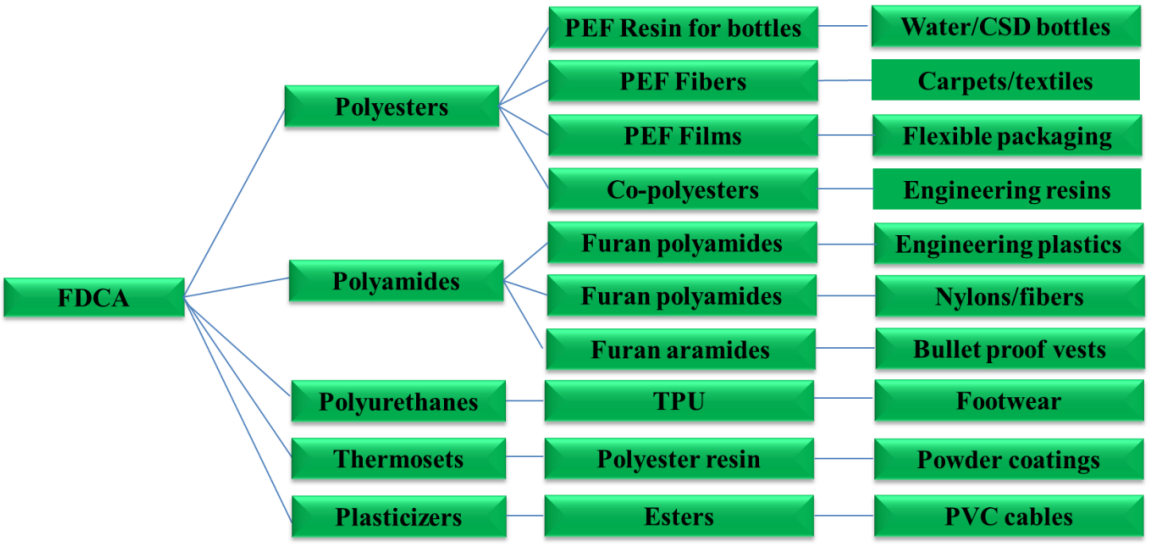

Fig. 5.1 Products of commercial importance derived from FDCA [21].

5.1.3. Background of the work

The selective oxidation of HMF to FDCA has been widely studied using different metal-supported heterogeneous noble metals such as Au, Pt, Pd, and Ru based catalysts for the higher and excellent catalytic activity of the reaction [22-26]. Very importantly, in most of the cases, the catalyst stability remains a significant issue because of excess usage of external bases like NaOH and Na_2CO_3 in the reaction medium. There is an interesting observation for the base free oxidation of HMF to FDCA using Au supported hydrotalcite catalyst using O_2 as oxidant, where the yield of FDCA was 92 %. However, this value was not stable [27]. Recently, Gao *et al.* reported the bimetallic Au-Pd nanoparticles over La doped LDH catalyst which gave 100 % yield of FDCA within 6 h of reaction time [28]. Haian *et al.* reported that reconstructed hydrotalcite supported Pd-Au bimetallic catalyst achieved a high yield of FDCA (90 %) at 60 °C over 6 h [29]. However, the commercial implementation of HMF conversion to FDCA will require a new catalytic material and novel approaches which minimize precious metal content in the catalyst. Therefore, from the commercial and economic viewpoint, using noble metals (Au, Pt, and Pd) based catalysts is not a cost-effective process. Also, this catalyst needs an external base, which is not environmentally benign.

Presently, Ru based catalyst is found to be highly active for HMF oxidation into FDCA without using any base. Guangshun *et al.* reported Ru/C catalyst under base free conditions with 88 % yield of FDCA which may be further improved. [30]. Mishra and co-workers

developed an efficient Ru supported on $MnCO_2O_4$ spinel catalyst with tunable Brønsted and Lewis acidic sites which plays an important role in the production of FDCA. The yield achieved was 99.1 % at 24 bar pressure [31]. However, the catalyst demonstrated the activity at high pressure, and the role of acidic sites was not explained thoroughly. Pichler *et al.* have reported 97 % selectivity of FDCA with smaller Ru nanoparticles supported on high surface area ZrO_2 [32]. Liu *et al.* studied CoO_x nanoparticles distributed mesoporous carbon giving 98 % conversion of HMF in 30 h [33]. It has been recently demonstrated that nitrogen-doped mesoporous carbon materials have attracted much interest and are more efficient for biomass conversion due to their excellent chemical stability, high porosity, high specific surface area, tunable pore size, and chemical inertness [34-40]. On the other hand, doping nitrogen into mesoporous carbon which can be chemically functionalized with metallic nanoparticles to confer or enhance catalytic activity [41, 42]. Zhu and co-workers employed nitrogen-doped carbon spheres with war wrinkled cages for HMF to FFCA using tert-butyl hydroperoxide (TBHP) as an oxidant *[43]*. Yang *et al.* studied the HMF oxidation to FDCA using Pt dispersed on nitrogen-doped porous carbon using an external base $NaHCO_3$ and showed 85 % yield of FDCA [44]. Guan *et al.* have reported 96.7 % yield of FDCA with hierarchical porous nitrogen-doped carbon supported bimetallic AuPd catalyst [45]. A view of the above reported work for the production of FDCA which can impose technical limitations like lack of recyclability, product recovery, metal leaching, and cost of production. To alleviate the above problems, we have developed a highly efficient, cost-effective, and reusable Ru based catalyst for oxidation of HMF to FDCA. Herein, we are reporting Ru nanoparticles supported on NaY zeolites and nitrogen doped mesoporous carbon (NMC) catalyst for the first time for base free oxidation of HMF to FDCA. A simple ion exchange method was adopted for the synthesis of Ru/NaY catalysts, and incipient wetness impregnation method used to incorporate of Ru nanoparticles into the NMC support. These materials were extensively characterized by various notable physicochemical characterization techniques to get more insights into the catalytic activity.

This chapter is divided into two parts depending on the catalyst system involved in this reaction.

A. A highly efficient and reusable Ru-NaY catalyst for the base free oxidation of 5-Hydroxymethylfurfural to 2,5-Furandicarboxylic acid

B. An enhanced catalytic performance of Ru nanoparticles supported NMC catalyst for the oxidation of HMF to FDCA

References

1. J.H. Clark, F.E.I. Deswarte, T.J. Farmer, Biofuels, Bioprod. Biorefin 3 (2009) 72.
2. B. Kahn, Earth's CO_2 passes the 400 PPM threshold-maybe permanently, Climate Central. (2016).
3. A. Goeppert, M. Czaun, J.P. Jones, G.K. Surya Prakash, G.A. Olah, Chem. Soc. Rev. 43 (2014) 7995-8048.
4. S.R. Goswami, M.J. Dumont, V. Raghavan, Starch 68 (2016) 274–286.
5. P. Gallezot, Chem. Soc. Rev. 41 (2012) 1538–1558.
6. H. Kobayashi, A. Fukuoka, Green Chem. 15 (2013) 1740.
7. S.V.D. Vyver, J. Geboers, P.A. Jacobs, B.F. Sels, ChemCatChem, 3 (2011) 82–94.
8. F. Delbecq, C. Len, Molecules, 23 (2018), Article 1973.
9. S. Zhu, J. Wang. W. Fan, Catal. Sci. Technol. 5 (2015) 3845–3858.
10. https://www.avantium.com/renewable-polymers, Amsterdam, The Netherlands.
11. A.R.C. Morais, A.M.D. Costa Lopes, R.B. Lukasik, Chem. Rev. 115 (2015) 3–27.
12. C.S. Lancefield, L.W. Teunissen, B.M. Weckhuysen, P.C.A. Bruijnincx, Green Chem. 20 (2018) 3214–3221.
13. A.F. Rogeri, S. Toma, J.C.M. Bordado, J.F.P. Gomes, Chem. Rev. 113 (2013) 7421–7469.
14. A. Gandini, A.J.D. Silvestre, C.P. Neto, A.F. Sousa, M. Gomes, J. Polym. Sci. Part A Polym. Chem. 47 (2009) 295–298.
15. R.J.I. Knoop, W. Vogelzang, J.V. Haveren, D.S.V. Es, J. Polym. Sci. Part A Polym. Chem. 51 (2013) 4191–4199.
16. J.C. Lewis, J. Biol. Chem. 274 (1972) 1861-1868.
17. M. Duennenberger, M. Schellenbaum, Swiss Patent, CH 532890, 1973; Chem. Abstr. 78 (1973) p159405t., n.d.
18. J. Lewkowski, ARKIVOC (2001), 17–54.
19. W. Fraefel, H.F. Lichti, M. Brunetti, US Patent, 4383832, 1983.
20. Biorefineries of FDCA, https://biorrefineria.blogspot.com/2017/06/biorrefinerias-de-fdca-acido-2-5-furanodicarboxilico-PEF.html (accessed 21 September 2018).
21. https://www.polyestertime.com/fdca-furandicarboxylic-acid-pef-polyamides.
22. Z. Zhang, K. Deng, ACS Catal. 5 (2015) 6529–6544.
23. J. Cai, H. Ma, J. Zhang, Q. Song, Z. Du, Y. Huang, J. Xu, Chem. Eur. J. 19 (2013) 14215–14223.

24. H.A. Rass, N. Essayem, M. Besson, Green Chem. 15 (2013) 2240.
25. N. Mei, B. Liu, J. Zheng, K. Lv, D. Tang, Z. Zhang, Catal. Sci. Technol. 5 (2015) 3194–3202.
26. S.E. Davis, B.N. Zope, R.J. Davis, Green Chem. 14 (2012) 143–147.
27. N.K. Gupta, S. Nishimura, A. Takagaki, K. Ebitani, Green Chem. 13 (2011) 824.
28. Z. Gao, X. Renfeng, G. Fan, L. Yang, F. Li, ACS Sustainable Chem. Eng. 5 (2017) 5852–5861.
29. X. Haian, A. Jiahuan, H. Mei, X. Siquan, L. Zhang, Z. Cailin, Catal. Today 319 (2019) 113–120.
30. Y. Guangshun, S.P. Teong, Y. Zhang, Green Chem. 18 (2016) 979–983.
31. D.K. Mishra, H.J. Lee, J. Kim, H.S. Lee, J.K. Cho, Y.W. Suh, Y. Yi, Y.J. Kim, Green Chem. 19 (2017) 1619–1623.
32. C.M. Pichler, M.G.A. Shaal, H. Joshi, W. Ciptonugroho, F. Schuth, ChemSusChem 11 (2018) 2083–2090.
33. X. Liu, M. Zhang, Z. Li, ACS Sustainable Chem. Eng. 8 (2020) 4801−4808.
34. M. Li, F. Xu, H. Li, Y. Wang, Catal. Sci. Technol. 6 (2016) 3670–3693.
35. H. Yu, K.A. Kim, M.J. Kang, S.Y. Hwang, H.G. Cha, ACS Sustainable Chem. Eng. 7 (2019) 3742−3748.
36. X. Fan, L. Zhang, G. Zhang, Z. Shu, J. Shi, Carbon 61 (2013) 423−430.
37. Y. S. Ren, Z. L. Yuan, K. L. Lv, J. Sun, Z. H. Zhang, Q. Chi, Green Chem. 20 (2018) 4946–4956.
38. C.V. Nguyen, Y. Liao, T. Kang, J.E. Chen, T. Yoshikawa, Y. Nakasaka, T. Masuda, K.C.W. Wu, Green Chem. 18 (2016) 5957–5961.
39. Y. Lin, D.S. Su, ACS Nano, 8 (2014) 7823–7833.
40. H. Watanabe, S. Asano, S.I. Fujita, H. Yoshida, M. Arai, ACS Catal. 5 (2015) 2886–2894.
41. Z. Yang, X.G. Duan, J. Wang, Y. Li, X. Fan, F. Zhang, G. Zhang, W. Peng, ACS Sustainable Chem. Eng. 8 (2020) 4236−4243.
42. K. Gong, F. Du, Z. Xia, M. Durstock, L. Dai, Science 323, 5915 (2009) 760−764.
43. J. Zhu, C. Yao, A. Maity, J. Xu, T. Zhan, W. Liu, M. Sun, S. Wang, V. Polshettiwar, H. Tan, Chem. Commun. 57 (2021) 2005-2008.
44. C. Yang, X. Li, Z. Zhang, L. Bohan, J. Li, Z. Liu, W. Zhu, F. Tao, G. Lv, Y. Yang, Fuel 278 (2020) 118361.

45. W. Guan, Y. Zhang, Y. Wei, B. Li, Y. Feng, C. Yan, P. Huo, Y. Yan, Fuel 278 (2020) 118362.

Chapter-5A

A Highly Efficient and Reusable Ru-NaY Catalyst for the base free Oxidation of 5-Hydroxymethylfurfural to 2,5-Furandicarboxylic acid

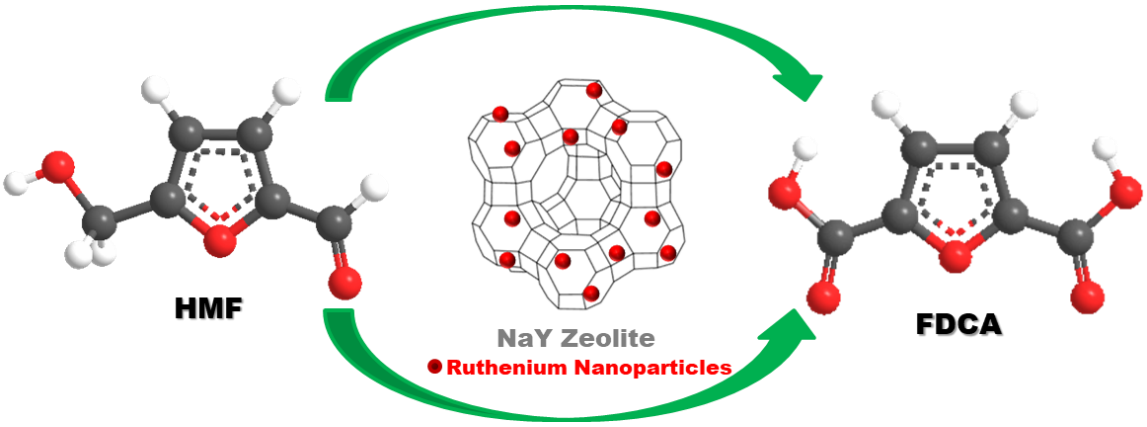

Synopsis

- A series of Ru exchanged NaY catalysts were synthesized by the ion-exchange method and applied for base free oxidation of HMF to FDCA
- 3 wt % Ru-NaY catalyst demonstrated 94 % of FDCA yield with complete conversion of HMF in a short span of time
- Small size Ru nanoparticles with desired acidic sites in the catalysts were responsible for the HMF oxidation
- A higher amount of metallic Ru plays a vital role in catalytic activity and productivity
- The catalyst was highly reusable for HMF oxidation

5A.1. Results and discussion

5A.1.1. Catalyst characterization

5A.1.1.1. Powder X-ray diffraction

To understand the structural features of the materials, PXRD analysis was conducted, and **Fig. 5A.1** shows the diffraction patterns of bare NaY cationic clay compared with different ruthenium metal loaded NaY zeolite. The PXRD pattern of pure NaY zeolite exhibits a highly crystalline nature of the zeolite framework (JCPDS No.43-0168) whose intensities did not change even after Ru exchange. No peak pertaining to metallic Ru or its oxides were observed, pointing to the homogeneous distribution of Ru nanoparticle on the zeolite support. The absence of any peak corresponds to Ru may also be due to the higher intensities of NaY zeolite support [1, 2].

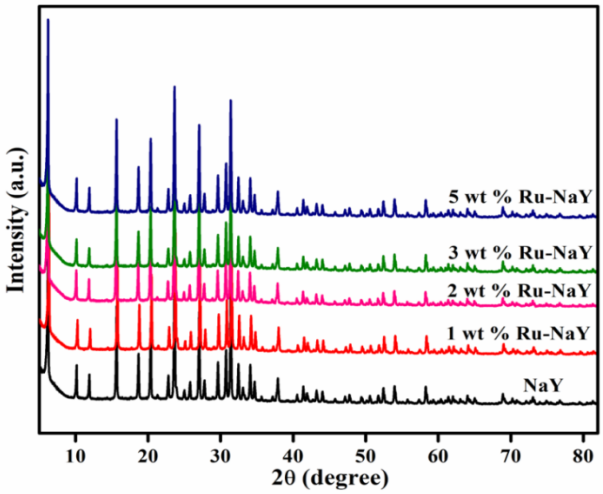

Fig. 5A.1 Powder XRD pattern of pristine NaY and Ru supported NaY catalysts.

5A.1.1.2. N_2 Physisorption and H_2 Chemisorption analysis

The textural properties of all the synthesized materials were studied by N_2 adsorption-desorption study. **Table 5A.1** shows BET surface area of NaY zeolite as 866 m^2/g, and the pore volume is 0.37 cm^3/g. However, with increasing the metal loading, surface area and pore volume of the catalyst are decreasing gradually. This decrease in the surface area was due to pore blockage by Ru nanoparticles in the cavities of zeolite. Most of the Ru particles were well dispersed on the surface of NaY support, which was confirmed by H_2 chemisorption study. It was noticed that at higher Ru loading, the crystallite size of Ru was large, leading to the lower dispersion of those nanoparticles on the support. At the lowest metal loading, the catalyst demonstrated the highest dispersion. Ru metal surface area was also calculated from the H_2-chemisorption study, and it was observed that 5 % Ru loaded

catalyst has least active surface area reflecting in the lowest activity of the catalyst. The actual Ru content was determined by ICP-OES analysis.

Table 5A.1 Textural properties of Ru-NaY catalysts

Samples	BET Surface area[a] (m^2/g)	Total pore volume[a] (cm^3/g)	BJH pore size (Å)	Ru content[b] (wt %)	Ru metal dispersion[c] (%)	Ru metal surface area[c] (m^2/g)	Average Ru crystallite size[c] (nm)
NaY	866	0.37	19.0	-	-	-	-
1 wt % Ru-NaY	842	0.36	18.7	0.91	53.2	4.7	1.8
2 wt % Ru-NaY	833	0.36	18.4	1.82	32.4	3.4	3.2
3 wt % Ru-NaY	820	0.34	18.1	2.91	22.6	3.2	3.4
5 wt % Ru-NaY	786	0.31	17.6	4.70	12.3	2.4	6.4

(a) Calculated from BET

(b) Amount of Ru calculated from ICP-OES

(c) Obtained by H_2-Chemisorption

5A.1.1.3 Field emission scanning electron microscopy

The surface morphology of the catalyst was examined by FE-SEM. **Fig. 5A.2(a)** shows pure NaY zeolite having a porous structure and crystalline nature. SEM micrograph clearly reveals that the morphology of the catalysts did not change after exchanging Ru in the zeolite framework. These results are in good agreement with the XRD results of the catalysts.

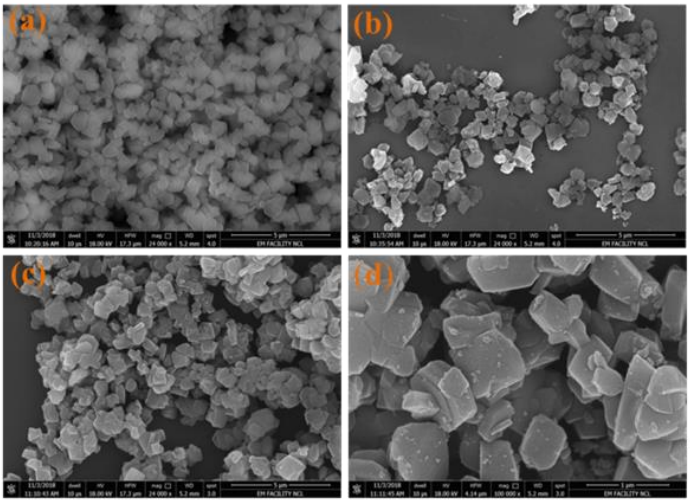

Fig. 5A.2 FE-SEM images of (a) NaY, (b) 2 wt % Ru-NaY and (c, d) 3 wt % Ru-NaY.

5A.1.1.4. Fourier transform infrared spectroscopy

Fig. 5A.3 shows the FTIR spectra of bare NaY and Ru supported NaY. A broad peak at 3428 cm^{-1} is attributed to the stretching vibration of hydroxyl group T-OH from the surface of NaY zeolites or in supercages, which was confirmed for all the samples [3]. The IR band appears at 1021 cm^{-1} is related to asymmetric stretching of $(Si/Al\text{-}O)_4$, and the bending vibration of water molecule appears at 1638 cm^{-1} [4, 5]. Therefore, proton abstraction is considered the first step for the conversion of HMF to FDCA. The acidic OH groups in sodalite cage and high frequency acidic OH groups located at supercage play an important role in the HMF conversion. However, internal hydroxyl groups within the supercage are Brønsted acids, and these can be detected by *in situ* pyridine FTIR.

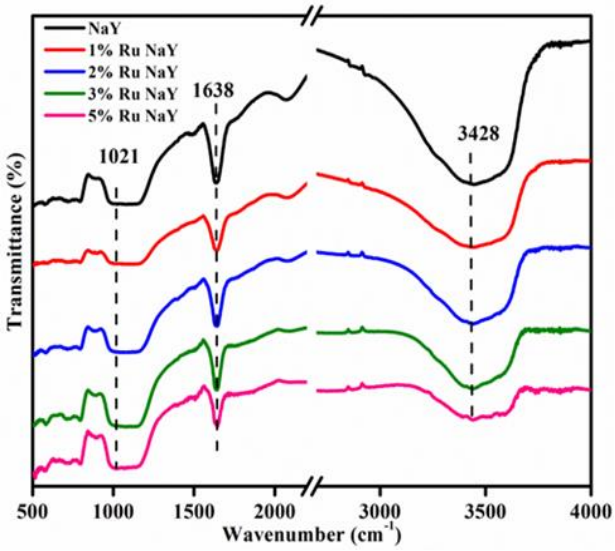

Fig. 5A.3 FTIR spectra of Ru supported NaY catalysts.

5A.1.1.5. Temperature programmed reduction

The reducibility of Ru supported NaY samples was investigated by H_2-TPR as shown in **Fig. 5A.4**. The main peak at 70 to 150 °C temperature region can be ascribed to the reduction of RuO_x species. However, with increasing metal loading from 1 % to 5 % the intensity of TPR peak is gradually increased [6] implying that hydrogen consumption is increased with the increase in Ru content of the catalysts.

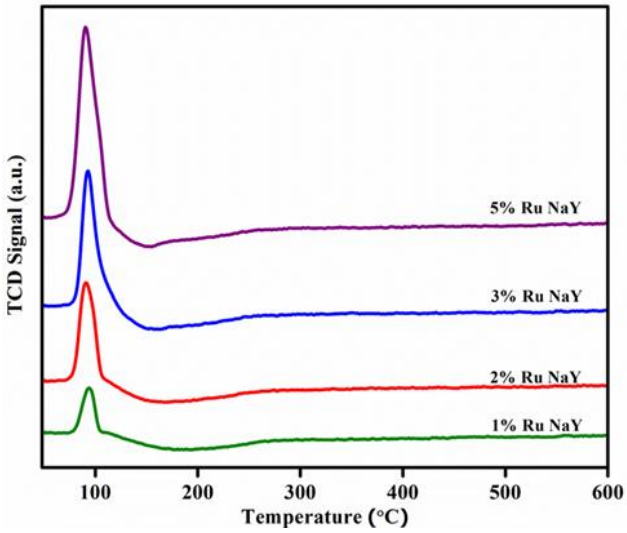

Fig. 5A.4 H_2-TPR profiles of the Ru supported NaY Catalysts.

5A.1.1.6. NH_3-temperature programmed desorption

The synthesized catalysts were subjected to NH_3-TPD to find out the exact quantity of the acidic sites in the catalysts. The results are shown in **Fig. 5A.5**. NH_3-TPD profiles clearly indicated that a single peak was observed for ammonia desorption around 240-300 °C corresponding to moderate acidity of the surface [7]. On increasing ruthenium loading, the acidity of the materials was also increased (5 wt % Ru-NaY: 1.43 mmol/g). However, the activity of the catalysts was not proportional to the acid strength. In fact, 5 wt % Ru-NaY demonstrated lowest yield of FDCA among all the catalysts. This abnormal catalytic activity trend may be due to the formation of intermediate FFCA products. 3 wt % Ru-NaY shows the highest yield of FDCA. The role of Brønsted and Lewis acidity on the catalytic activity will be discussed in *in-situ* pyridine FTIR.

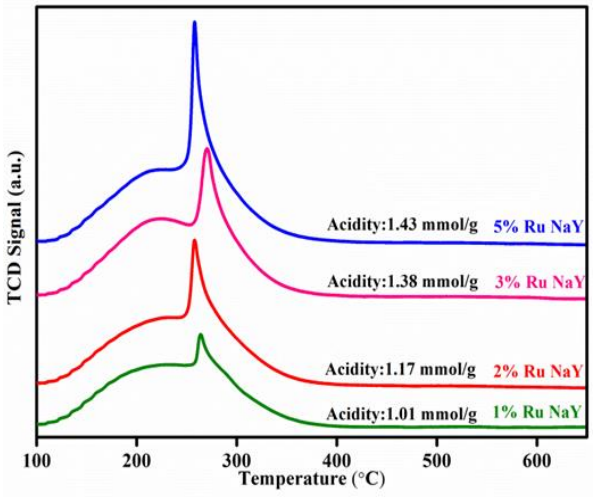

Fig. 5A.5 NH_3-TPD profiles of Ru supported NaY catalysts.

5A.1.1.7. *in situ*- Pyridine FTIR

To study the function of Brønsted, and Lewis acidity for NaY zeolite, metal ion-exchanged zeolites were subjected to *in situ*- FTIR spectroscopy of adsorbed pyridine. **Fig. 5A.6** shows absorption bands at 1507 cm^{-1} and 1540 cm^{-1}, which corresponds to pyridine adsorbed at Brønsted acidic sites [8]. The bands at 1455 and 1558 cm^{-1} specify the existence of coordinatively bonded pyridine from Lewis acid sites [9]. The peak at 1489 cm^{-1} is attributed to both Brønsted and Lewis acidity. The band at 1575 cm^{-1} could also be considered as quantification for Lewis acidic sites, but these bands are typically less intense than 1558 cm^{-1} band and have some degree of overlap. The pyridine FTIR spectra indicated that NaY and metal loaded NaY have both Lewis and Brønsted acidic sites while pure NaY shows less intense peaks than the metal loaded samples. It implies that Ru also plays an important role in improving the acidic strength of the samples, which could perform an important role in the oxidation of HMF to attain the maximum yield of FDCA. **Table 5A.2** depicted the L/B ratios for each catalyst calculated by peak deconvolution to get the amount of pyridine adsorbed on each type of sites [9].

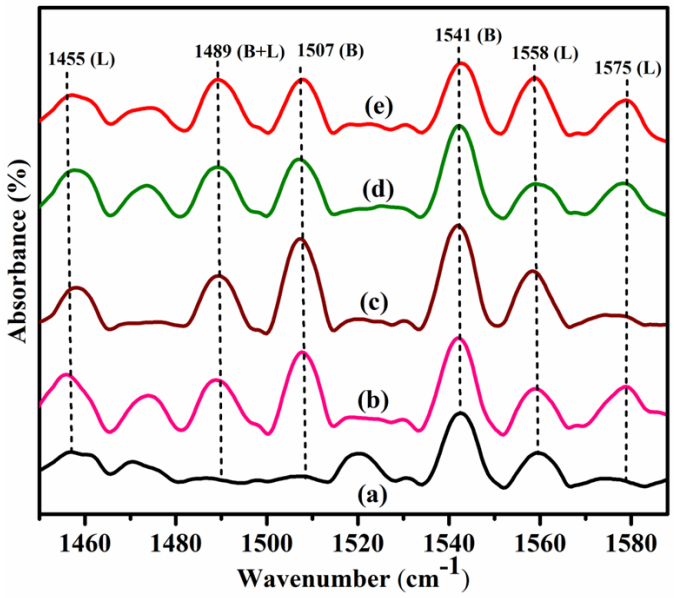

Fig. 5A.6 *In situ* pyridine FT-IR spectra of (a) NaY zeolite (b) 1 wt % Ru-NaY (c) 2 wt % Ru-NaY (d) 3 wt % Ru-NaY and (e) 5 wt % Ru-NaY.

5A.1.1.8. Transmission electron microscopy

The dispersion of Ru and their particle size in 3 wt % Ru-NaY catalyst were further confirmed by HRTEM analysis. It was observed that Ru metal nanoparticles were uniformly distributed over the surface of the NaY zeolites with a broad distribution of Ru particles

ranging from 1-12 nm. The diffraction pattern shows the uniform interplanar spacing of 0.2 nm corresponding to 101 plane of Ru nanoparticles, and interplanar spacing of 0.23 nm matches well with 100 plane. Ru particle size distribution was derived by TEM analysis, which is represented in **Fig. 5A.7**. The average particle size of Ru nanoparticles was 4 nm which is in accordance with the H_2 chemisorption results. However, Ru particle size (4 nm) is bigger than the pore size of NaY zeolite, therefore the majority of Ru particles are present on the external surface of the NaY zeolite. **Fig. 5A.8** shows HAADF-STEM and elemental mapping of 3 wt % Ru-NaY catalyst, which confirmed that Ru nanoparticles are homogeneously distributed over the NaY support.

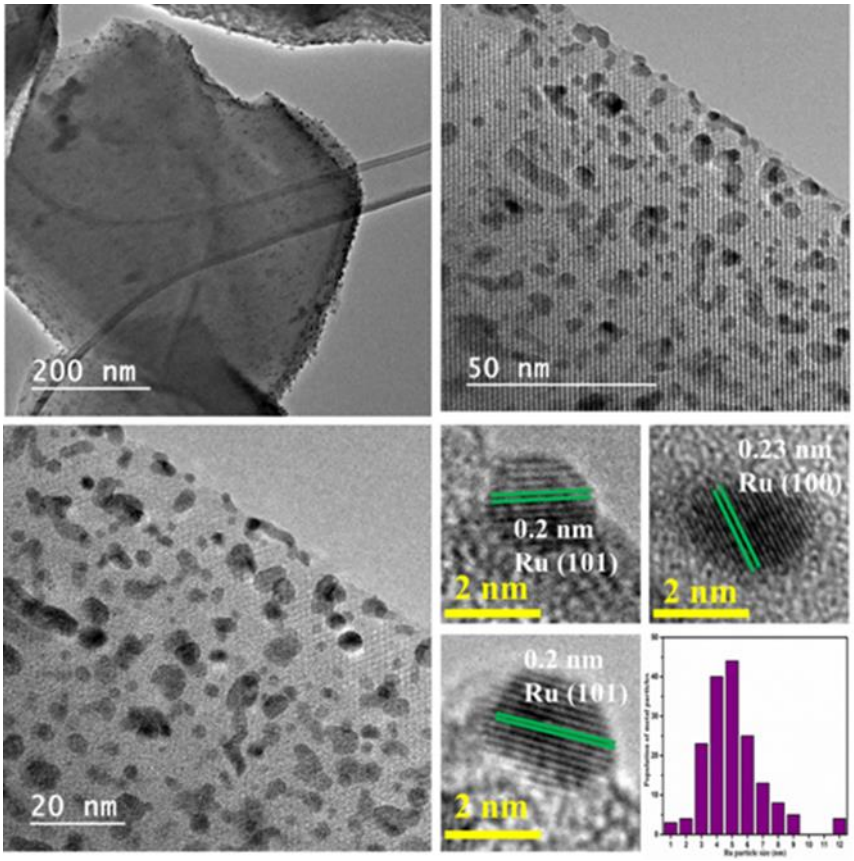

Fig. 5A.7 HRTEM images and Ru particle size distribution of 3 wt % Ru-NaY.

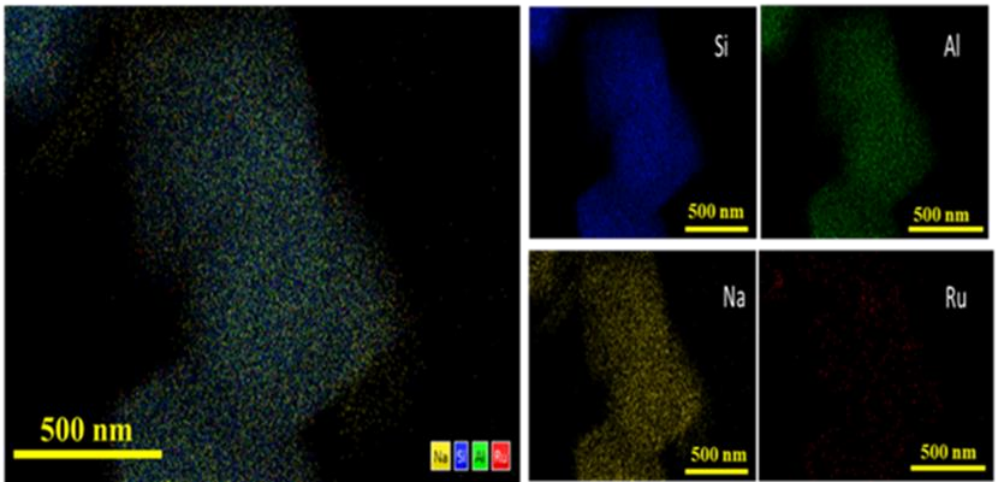

Fig. 5A.8 HAADF-STEM elemental mapping of 3 wt % Ru-NaY.

5A.1.1.9. X-ray photoelectron spectroscopy

To explore the chemical states and surface properties of active Ru species on the NaY supports, XPS analysis was performed. **Fig. 5A.9** depicts the Ru 3d core-level spectra of 3 wt % Ru-NaY which was deconvoluted by peak fitting method into three major peaks (Ru $3d_{5/2}$, Ru $3d_{3/2,}$ and C 1s). The peak at 284.7 eV corresponds to carbon contamination on the surface. The electronic structure of 3 wt % Ru-NaY catalyst confirms that Ru exists in two different oxidation states. The metallic ruthenium was observed at 280.6 and 284.5 eV which were allocated to Ru^0 $3d_{5/2}$ and Ru^0 $3d_{3/2}$ peaks, and the peaks at 281.7 and 286.6 eV were assigned to +4 oxidation state of Ru in RuO_2 [10]. According to XPS data, the surface composition of metallic ruthenium and ruthenium oxide was 70 % and 30 %, respectively.

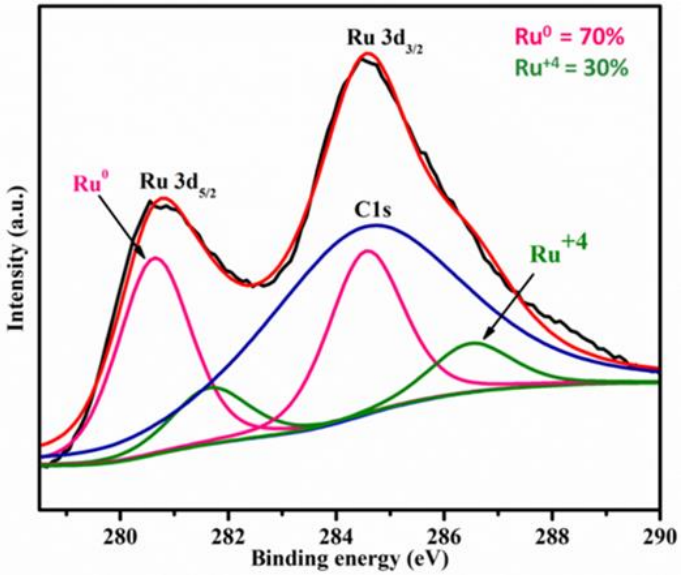

Fig. 5A.9 XPS spectra of 3 wt % Ru-NaY catalyst.

5A.1.2.10. *Insitu* CO-FTIR

Insitu CO-FTIR was carried out to understand the possible oxidation state of Ru in the synthesized catalysts. The spectra were collected at 120 °C and given in **Fig. 5A.10**. It was observed that IR bands appear in the range 2000-2500 cm^{-1} for all catalysts which can be attributed to the vibrational stretching mode of CO bound to different types of Ru present on the support. The bands emerging at 2117 and 2175 cm^{-1} region assigned to two different multicarbonyl species adsorbed on partially oxidized Ru species (Ru^{+n}) $(CO)_x$, x >1) [11]. However, still debates are going on about the precise oxidation of Ru (n) and the number of carbonyl groups adsorbed on Ru species. Whereas, IR band observed at 2053 cm^{-1} region can be correlated with the linearly bound CO with the metallic Ru species. Interestingly the intensity of this peak was more among all, which implies the higher abundancy of metallic Ru in the catalysts. The CO-FTIR results are in good agreement with the XPS results.

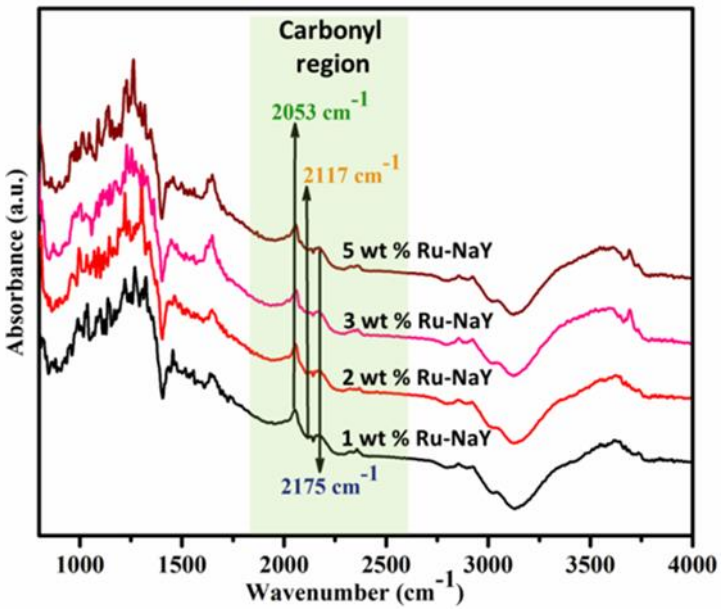

Fig. 5A.10 CO-FTIR spectra of Ru exchanged NaY catalysts.

5A.1.2. Catalytic performance of 5-HMF oxidation

5A.1.2.1. Base free oxidation of HMF to FDCA

Fig. 5A.11 represents the catalytic tests of HMF to FDCA over 3 wt % Ru-NaY catalyst. The reaction was performed at 120 ºC, and 10 bar initial oxygen pressure under base-free conditions [12, 13]. The catalyst demonstrated complete HMF conversion in 2 h with a yield of 58 % towards FDCA. Interestingly, the yield of FDCA increased gradually with the increase of the reaction time, and at the end of 8th h the yield of FDCA and FFCA was 94 %

and 6 %, respectively. Further studies on the relationship of the catalytic activity with Ru particle size and amount of acidic –OH groups inside the supercage have proved that they possess a crucial role in achieving the high yield of FDCA [14, 15].

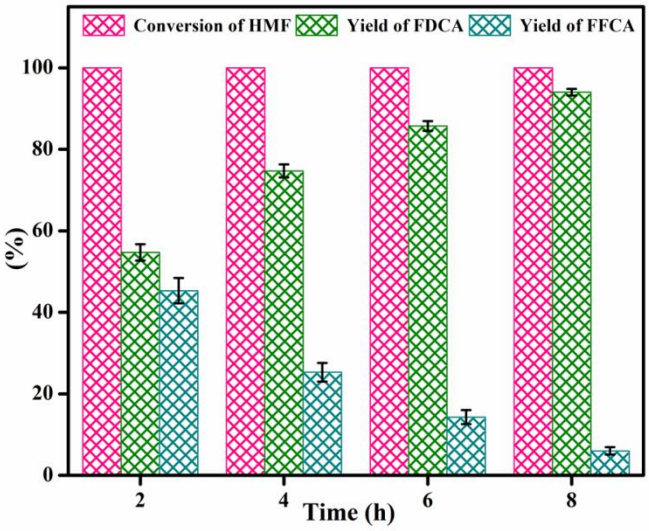

Fig. 5A.11 HMF conversion and the yield of FDCA with time over 3 wt % Ru-NaY. ***Reaction Conditions:*** *150 mg catalyst, HMF 0.5 mmol, Water 30 ml, O_2 10 bar, 120 ºC.*

Scheme 5A.1 exhibits a general reaction pathway for the selective oxidation of HMF to FDCA. Initially, HMF may be oxidized to DFF or HMFCA, important intermediates of this reaction while using molecular oxygen as an oxidant. These two intermediates further could be oxidized to FFCA. Finally, FFCA will be oxidized to FDCA.

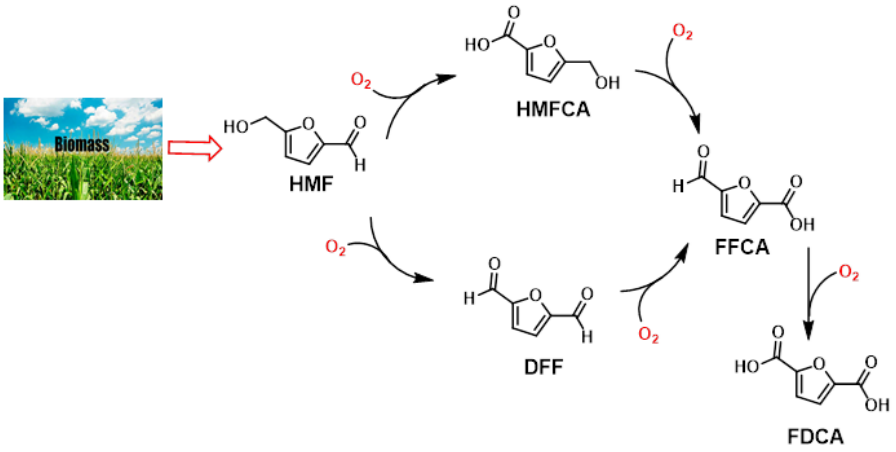

Scheme. 5A.1 Possible reaction pathway for selective oxidation of HMF to FDCA.

5A.1.2.2. Product distribution of HMF oxidation over Ru-NaY catalysts

To determine the optimal catalyst composition for the production of FDCA from HMF a series of Ru exchanged NaY catalysts with different metal loading were prepared by the ion-

exchange method, and their activity are shown in **Fig. 5A.12**. The catalytic performance of 3 wt % Ru-NaY catalyst was already discussed in the above section. Although a complete HMF conversion was observed for 3 wt % Ru-NaY catalysts within 2 h, the maximum yield of FDCA was achieved after 8 h. Therefore, reaction time also hold a crucial role for this reaction. The higher catalytic activity of this catalyst could be assigned to the optimum metal loading, better metal dispersion, higher availability of catalytic active sites, and desired acidic sites of the catalyst. Despite the higher metal dispersion, 1 wt % Ru-NaY shows only 31.04 % yield of FDCA after 8 h. This could be due to the lower metal loading and less acidic sites (1.01 mmol /g) of this material as confirmed by NH_3-TPD analysis. Recently Mishra *et al.* reported Brønsted and Lewis acidic sites have a major role in achieving higher yield of FDCA [13]. Upon increasing the metal loading up to 2 wt %, the yield of FDCA was further increased to 75.66 %. However, the catalytic activity was still inferior to 3 wt % Ru-NaY. On the other hand, 5 wt % Ru-NaY catalyst showed a decrease in FDCA yield (32.8 %) with the simultaneous increase in FFCA yield (67.2 %). This may be due to the larger crystallite size of Ru (6.4 nm) which reduces metal dispersion on the NaY support as confirmed from H_2-chemisorption results. A similar reaction was also performed over metal free NaY zeolite support under the optimized reaction conditions which showed 26 % of HMF conversion with DFF yield of 5.3 %. No FDCA formation was noticed during the reaction, proving the dominating catalysis of Ru nanoparticles over NaY support. The above results confirmed the superior catalytic activity of 3 wt % Ru on NaY support as a whole catalyst.

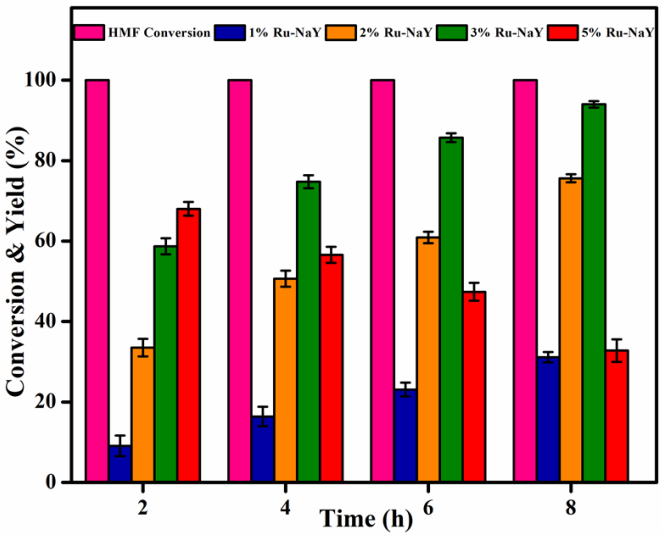

Fig. 5A.12 Effect of Ru loading on HMF conversion and FDCA yield with time.

***Reaction conditions**: 150 mg catalyst, HMF 0.5 mmol, Water 30 ml, O_2 10 bar, 120 ºC.*

Table 5A.2 Catalytic tests of HMF oxidation over various Ru supported catalysts

S. No.	Catalysts	HMF Conversion (%)	Yield of FFCA (%)	Yield of DFF (%)	Yield of FDCA (%)	TOF [a] (h^{-1})	L/B [b] ratio
1	1 wt % Ru-NaY	100	68.8	0	31.14	4.1×10^{-2}	0.93
2	2 wt % Ru-NaY	100	24.34	0	75.66	5.8×10^{-2}	1.06
3	3 wt % Ru-NaY	100	6.0	0	94.0	7.6×10^{-2}	1.04
4	5 wt % Ru-NaY	100	67.2	0	32.8	4.3×10^{-2}	0.98
5	NaY	26	0	5.3	0	0	0.76

(a) TOF= Turnover frequency (moles of HMF converted per mole of metal per hour).

(b) L/B= Lewis and Brønsted acid sites (L/B) ratio was calculated from pyridine FT-IR.

Reaction conditions: *150 mg catalyst, HMF 0.5 mmol, Water 30 ml, O_2 10 bar, 120 ºC, 8 h.*

5A.1.2.3. Effect of reaction temperature over 3 wt % Ru-NaY

Since 3 wt % Ru-NaY catalyst was found to be the best catalyst among all, this catalyst was further subjected to various temperatures for the best catalytic activity results. Temperature is a vital parameter, which can influence catalytic activity of 3 wt % Ru-NaY catalyst. **Fig. 5A.13** represents the catalytic activity of 3 wt % Ru-NaY at different temperatures. **Table 5A.2** shows the product distribution, and no HMFCA was observed under these reaction conditions. The oxidation of HMF mainly produced DFF, FFCA, and FDCA. Initially, the reaction was performed at 100 ºC where the conversion of HMF was 100 % with the yield of FDCA approximately equal to 47 %. Further, with increasing temperature up to 120 ºC; 94 % yield of FDCA was obtained with complete HMF conversion at 8 h. When the reaction was executed at 140 °C, initially the yield of FDCA was higher than the reaction performed at 120 ºC. However, an increase in the reaction time, activity was decreased gradually to 70 % at 8 h. This might be owing to the degradation of HMF at high temperatures [16]. Thus, 120 ºC is observed as the optimized temperature for HMF oxidation to FDCA.

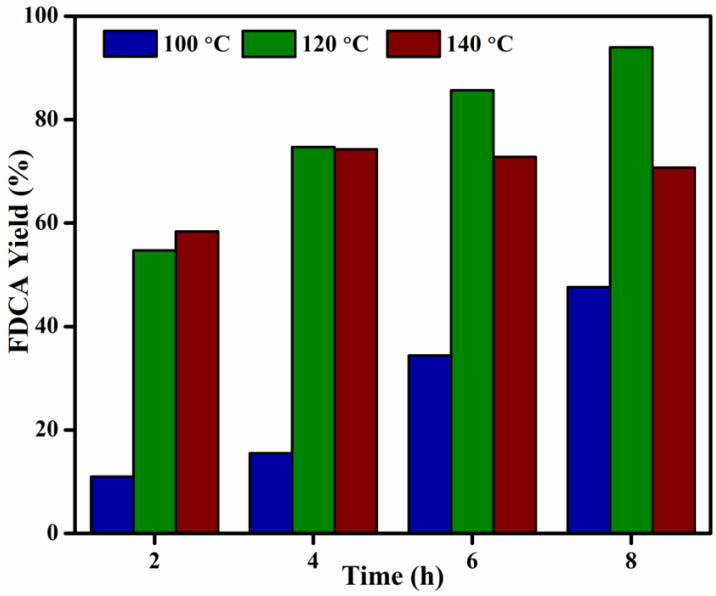

Fig. 5A.13 Effect of reaction temperature on FDCA yield over 3 wt % Ru-NaY.

Reaction conditions: *150 mg catalyst, HMF 0.5 mmol, Water 30 ml, O_2 10 bar.*

5A.1.2.4. Effects of pressure and catalyst loading

The effect of oxygen pressure was examined over 3 wt % Ru-NaY catalyst for HMF oxidation. The oxygen pressure was varied from 5-15 bar at a stable reaction temperature viz. 120 ºC. The results are shown in **Fig. 5A.14a** wherein 5 bar oxygen leads to increasing FDCA yield with the reaction time and the maximum yield achieved was 83 % with complete conversion of HMF at 8 h. On further increasing the pressure up to 8 bar, the yield of FDCA was gradually increased as reaction time prolonged. However, these pressures are still needed to be increased to achieve maximum yield. Further increasing the oxygen pressure to 10 bar, higher yield of FDCA (94 %) was achieved with 100 % conversion of HMF whereas high pressure did not fetch appreciable increase in the yield.

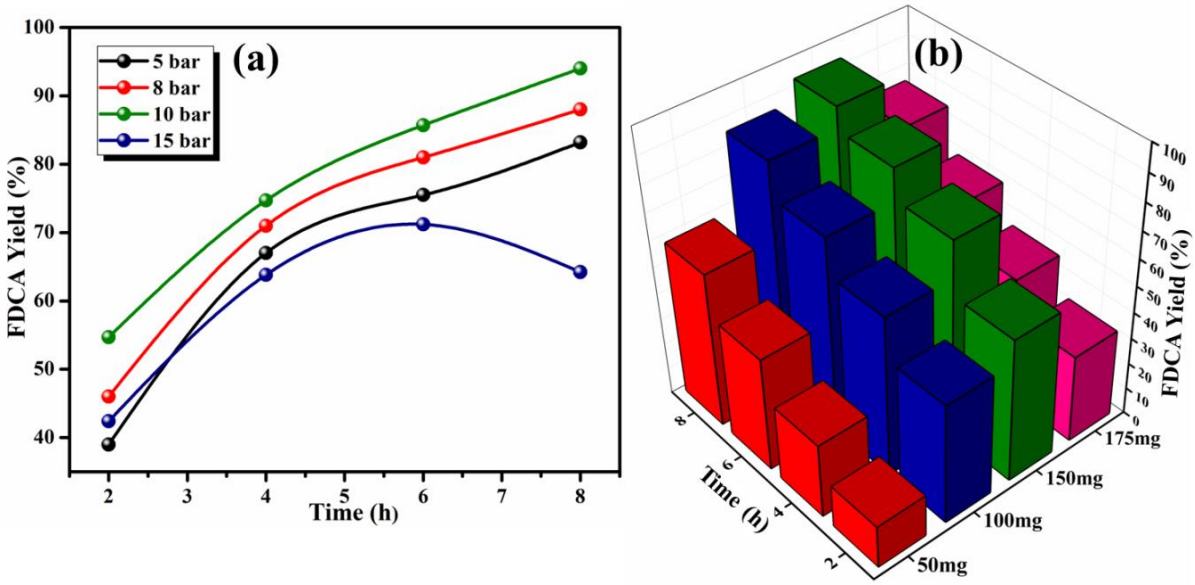

Fig. 5A.14 (a**)** Effect of reaction pressure and (b) catalysts amount on FDCA yield over 3 wt % Ru-NaY catalyst.

Reaction conditions: *120 ºC, HMF 0.5 mmol, Water 30 ml.*

Later, we have investigated the influence of catalyst amount on the selective oxidation of HMF to FDCA. **Fig. 5A.14b** shows the yield of FDCA at varying catalyst quantities. The study was started using 50 mg of 3 wt % Ru-NaY at optimized pressure and temperature. The yield of furandicarboxylic acid increases as reaction time prolonged to 8 h and a low yield of FDCA was observed as 59 %. It confirms that the number of Ru active sites is not sufficient for the oxidation of HMF to FDCA. We attempted to enhance the catalytic activity by using 100 mg and 150 mg of the catalyst and the yield of FDCA obtained was 86 % and 94 % respectively. Furthermore, increasing catalyst amount up to 175 mg, a decrease in the yield of FDCA (75.8%) was observed which may be due to the formation of other side products [17]. Finally, we optimized the catalyst amount as 150 mg which gave superior catalytic performance of converting HMF to FDCA.

5A.1.2.5. Reaction pathway for the base free oxidation of HMF to FDCA

The base free oxidation of HMF using 3 wt % Ru-NaY catalyst shows higher catalytic activity and productivity of FDCA. Based on the above results on HMF oxidation, the reaction mechanism follows an aldehyde group through DFF and FFCA by identifying the reaction profile of the products. A 100 % HMF conversion was attained in a shorter reaction time (2 h). Especially, complete conversion of DFF was observed at 2 h, for the yield of FFCA (45.3 %) and FDCA (54.7 %). When the reaction was prolonged to 8 h, 94 % yield of

FDCA was achieved while FFCA yield was 6 %. According to the catalyst characterizations and experimental part for HMF oxidation, acidic sites can favor the adsorption of an aldehyde group on the catalyst surface [18]. In addition, a high concentration of basic sites produces HMFCA via hemiacetal intermediates [19, 20].

5A.1.2.6. Recyclability test

Catalysts recyclability is one of the essential factors in industrial and economic viewpoints. As 3 wt % Ru-NaY was found to be the best catalyst. Hence it was further tested for recyclability study to understand the true performance of the catalyst. Initially 3 wt % Ru-NaY catalyst was filtered, washed several times with distilled water, and finally washed with ethanol, dried at 110 ºC for 10 h. The resulting catalyst was reused for HMF oxidation, and it was observed that 3 wt % Ru-NaY catalyst was truly recyclable even after 5th cycle with a minor drop in the FDCA yield, and the results are depicted in **Fig. 5A.15**. This drop in the product yield may be due to the loss of some of the active catalytic sites during the reaction or post-reaction process.

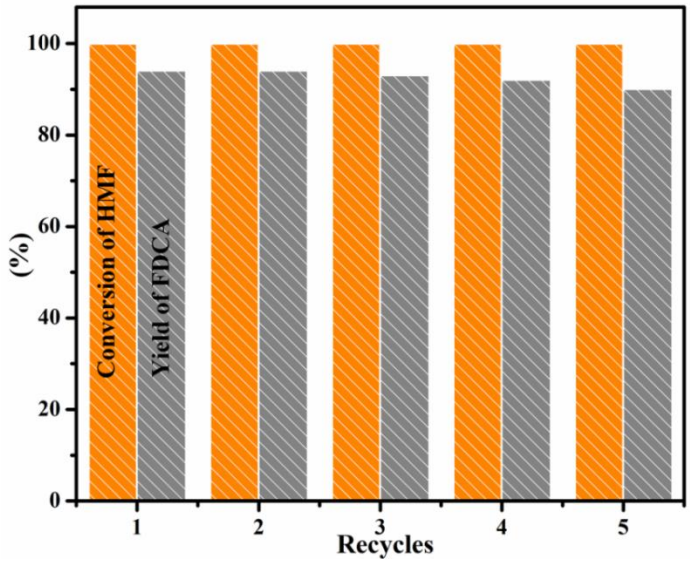

Fig. 5A.15 Recyclability of 3 wt % Ru-NaY catalyst.

Reaction conditions: *150 mg catalyst, HMF 0.5 mmol, Water 30 ml, O_2 10 bar, 120 ºC, 8 h.*

5A.1.2.7. Spent catalyst analysis

Fig. 5A.16 represents XRD pattern of spent 3 wt % Ru-NaY catalyst which is clearly indicating that the morphology of the catalyst did not get changed even after oxidation reaction. The absence of any Ru peak or its oxides points that these metal nanoparticles are well dispersed on the NaY support. Morphology of the catalyst was determined by TEM

Fig. 5A.17a where it is undoubtedly indicating that some of the Ru nanoparticles were agglomerated under the reaction conditions, and the XPS spectra of spent 3 wt % Ru-NaY catalyst **Fig. 5A.17b** specified that some active metallic ruthenium was oxidized into Ru oxide under the reaction conditions. Hence the slight drop in the FDCA yield may be due to the loss of catalytic active sites and agglomeration of Ru nanoparticles after the reaction.

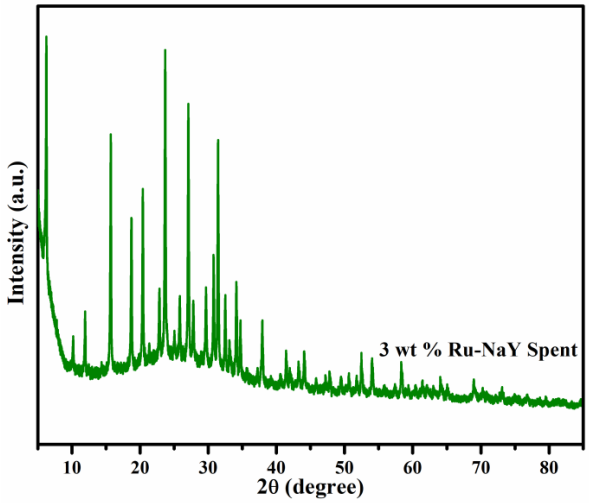

Fig. 5A.16 XRD pattern of Spent 3 wt % Ru-NaY catalyst.

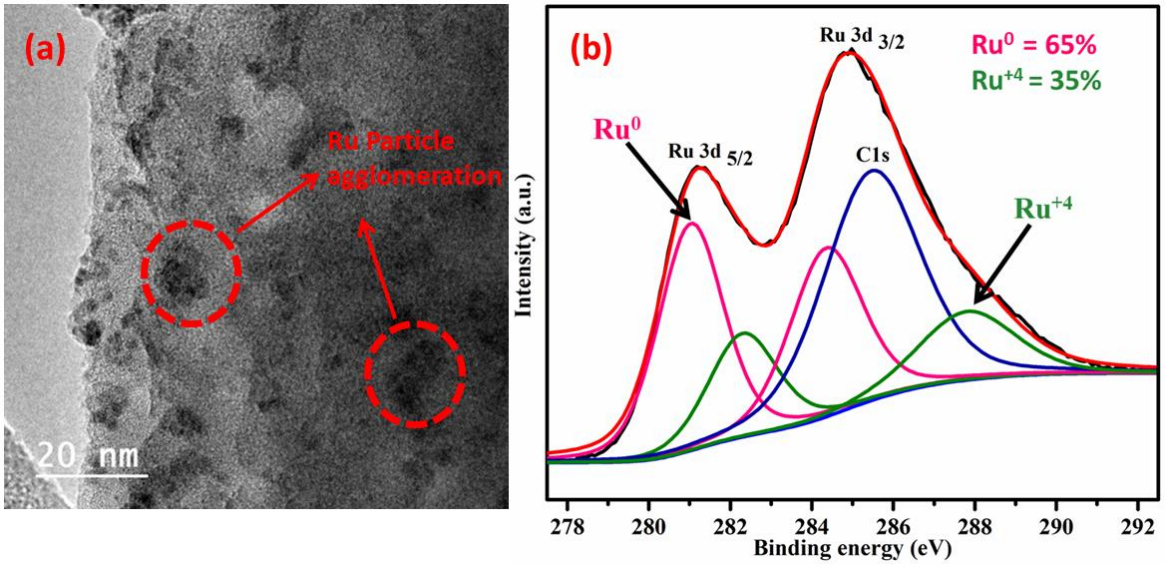

Fig. 5A.17 (a) HRTEM images and (b) XPS spectra of spent 3 wt % Ru-NaY catalyst.

5A.2. Conclusions

The oxidation of HMF to FDCA over Ru exchanged NaY catalysts was found to be an exciting reaction. The present study demonstrates the simple and straightforward synthesis method for the oxidation of HMF to FDCA. The extensive characterization techniques were employed at different stages, and the reaction results at different reaction conditions allow us to draw following conclusions.

1. All Ru supported NaY catalysts showed reasonably better HMF conversion and FDCA yield under the optimized reaction conditions. Among all, the 3 wt % Ru-NaY demonstrated excellent catalytic performance with complete HMF conversion and 94 % yield of FDCA, which is superior to many states of art catalysts.
2. The optimized 3 wt % Ru-NaY catalyst was highly recyclable even after the fourth cycle with a minor drop in the activity, pointing to the true potential of the catalyst for industrial applications.
3. The enhanced catalytic activity of 3 wt % Ru-NaY was attributed to the optimum metal loading, better metal dispersion, and appropriate acidic sites on the catalyst. Additionally, acidic -OH groups of the supercage and higher availability of metallic Ru (70 %) were found to play an important role in the HMF oxidation.

References

1. A.S. Nagpure, N. Lucas, S.V. Chilukuri, ACS Sustainable Chem. Eng. 3 (2015) 2909–2916.
2. D.K. Mishra, A.A. Dabbawala, J.S. Hwang, J. Mol. Catal. A Chem. 376 (2013) 63–70.
3. N. Chakroune, G. Viau, S. Ammar, L. Poul, D. Veautier, M.M. Chehimi, C. Mangeney, F. Villain, F. Fievet, Langmuir 21 (2005) 6788–6796.
4. J. Chen, X. Chen, Y. Zheng, Q. Li, RSC Adv. 5 (2015) 20248–20255.
5. A.M. Fonseca, S. Goncalves, P. Parpot, I.C. Neves, Phys. Chem. Chem. Phys. 11 (2009) 6308–6314.
6. Babaei, M. Zendehdel, B. Khalilzadeh, A. Taheri, Colloids Surf. B Biointerfaces 66 (2008) 226–232.
7. J. McCarthy, C.M.P. Marques, H. Trevino, W.M.H. Sachtler, Catal. Lett. 43 (1997) 11–18.
8. K.R. Reddy, K. Ramesh, K.S. Kothapalli, V.V. Rao, V.R.C. Komandur, Catal. Commun. 4 (2003) 112–117.
9. S.G. Nicholas, X. Bingjun, J. Catal. 358 (2018) 80–88.
10. W. Wang, H. Liu, T. Wu, P. Zhang, G. Ding, S. Liang, T. Jiang, B. Han, J. Mol. Catal. A Chem. 355 (2012) 174–179.
11. S.Y. Chin, O.S. Alexeev, M.D. Amiridis, Appl. Catal. A Gen. 286 (2005) 157.
12. X. Han, C. Li, X. Liu, Q. Xia, Y. Wang, Green Chem. 19 (2017) 996–1004.
13. D.K. Mishra, H.J. Lee, J. Kim, H.S. Lee, J.K. Cho, Y.W. Suh, Y. Yi, Yong J. Kim, Green Chem. 19 (2017) 1619–1623.
14. P. Gogoi, A.S. Nagpure, P. Kandasamy, C.V.V. Satyanarayana, T. Raja, Sustain. Energy Fuels 4 (2020) 678.
15. J. Cai, H. Ma, J. Zhang, Q. Song, Z. Du, Y. Huang, J. Xu, Chem. Eur. J. 19 (2013) 14215–14223.
16. Zhang, W. Yang, I.I. Roslan, S. Jaenicke, G.K. Chuah, J. Catal. 375 (2019) 56–67.
17. S. Albonetti, A. Lolli, V. Morandi, A. Migliori, C. Lucarelliand, F. Cavani, Appl. Catal. B 163 (2015) 520–530.
18. X. Tong, Y. Linhao, H. Chen, X. Zhuang, S. Liao, H. Cui, Catal. Commun. 90 (2017) 91–94.
19. Y.B. Wang, K. Yu, D. Lei, W. Si, Y.J. Feng, L.L. Lou, S.X. Liu, ACS Sustainable Chem.Eng. 4 (2016) 4752–4761.

20. M. Sajid, X. Zhao, D. Liu, Green Chem. 20 (2018) 5427–5453,

Chapter-5B

An enhanced Catalytic Performance of Ru Nanoparticles supported NMC Catalyst for the Oxidation of HMF to FDCA

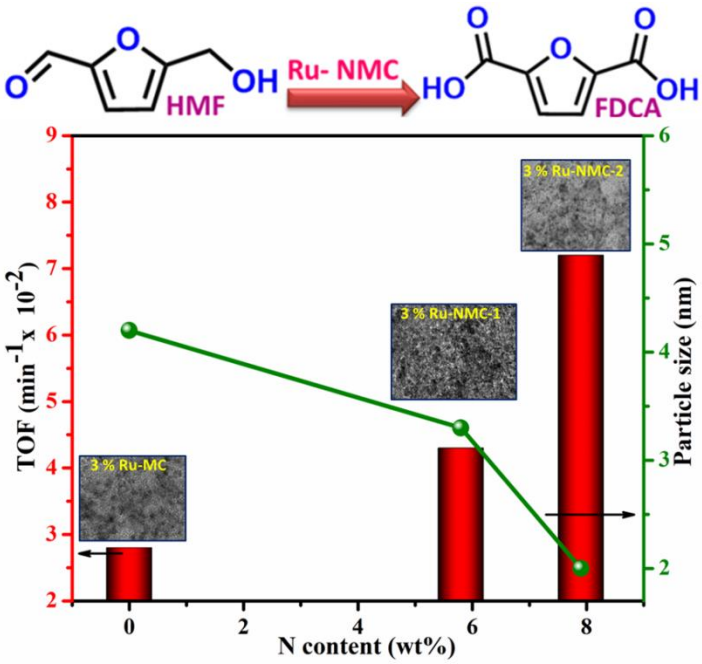

Synopsis

- Nitrogen-doped mesoporous carbons (NMCs) with varying N content were synthesized by silica assisted sol-gel process and incipient wetness impregnation method was adopted to incorporate Ru nanoparticles on the NMC support

- 3 wt % Ru-NMC-2 catalyst showed reasonably good yield of FDCA (83 %) under base free conditions

- The synergistic interactions between the nitrogen and smaller Ru nanoparticles play a crucial role in the overall catalytic performance of the catalysts

- Nitrogen content contributed to an increase in the percentage of Ru^0 in the catalysts, which increased the number of active catalytic sites in the catalysts for HMF conversion

5B.1. Results and discussion

5B.1.1. Catalyst characterization

5B.1.1.1. Powder X-ray diffraction

Powder X-day diffraction was performed to examine the crystal planes of pristine mesoporous carbon (MC), nitrogen-doped mesoporous carbon (NMCs) and Ru supported catalysts. The results are shown in **Fig. 5B.1**. Typically, two broad diffraction peaks were observed for all the catalysts at around 24.2° and 43.5° corresponds to the (002) and (100) planes of graphitic structure [1, 2]. The diffraction peak positions did not change even after Ru loading in the nitrogen-doped carbon framework. No additional peaks were observed for Ru oxides and metallic Ru in the samples, suggesting the uniform distribution of Ru nanoparticles on MC and NMCs supports.

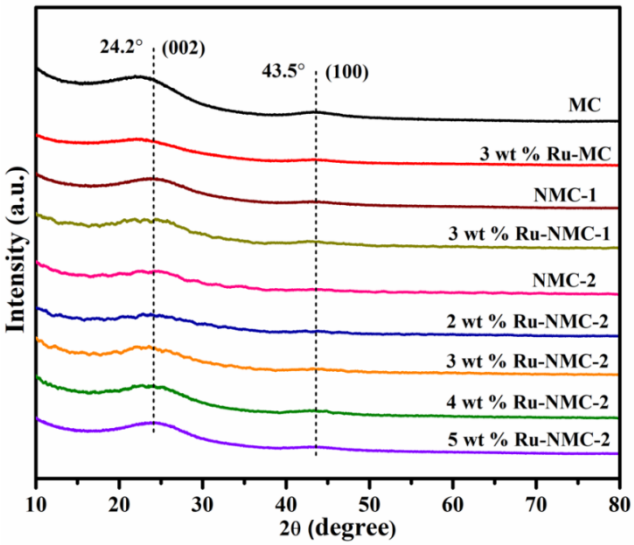

Fig. 5B.1 XRD pattern of NMCs and Ru supported NMC catalysts.

5B.1.1.2. Physicochemical properties

Surface textural properties and porous structure of the catalyst were analyzed by N_2-adsorption-desorption analysis. BET surface area and pore volume of the catalysts are given in **Table 5B.1**. The results showed that the surface area of MC, NMCs supports and catalysts falls in the range of 600-900 m^2/g. The surface area of pristine NMC-2 is 884 m^2/g, upon metal loading both surface area and pore volume of the catalysts decreased slightly. This decrease in surface area is due to the surface coverage and the partial blockage of the pore mouth by the Ru nanoparticles. The amount of Ru present in the catalysts was calculated from ICP-OES. The basicity of nitrogen-doped mesoporous carbon (NMCs) and Ru supported catalyst were estimated by CO_2–TPD. The doping of nitrogen into the carbon

framework imparts basicity to the catalyst, which is expected to play a key role in its conversion of HMF.

Table 5B.1 Physicochemical properties of the catalysts

Catalysts	BET Surface area (m^2/g)	Total pore volume[a] (cm^3/g)	Micropore volume[b] (cm^3/g)	Elemental analysis (wt %)				Ru Content[c] (wt %)	CO_2 desorbed[d] (mmol g^{-1})
				C	N	H	N/C		
MC	652	0.75	0.12	85.34	0	1.32	-	-	-
3 wt % Ru-MC	630	0.63	0.10	-	-	-	-	2.83	-
NMC-1 (M/P = 1)	831	1.04	0.09	80.44	5.8	0.64	0.07	-	0.18
3 wt % Ru-NMC-1	813	1.0	0.06	-	-	-	-	2.87	0.14
NMC-2 (M/P = 2)	884	1.18	0.08	75.62	7.9	0.82	0.10	-	0.32
2 wt % Ru-NMC-2	851	1.16	0.07	-	-	-	-	1.86	0.27
3 wt % Ru-NMC-2	832	1.10	0.07	-	-	-	-	2.92	0.24
4 wt % Ru-NMC-2	809	0.81	0.06	-	-	-	-	3.91	0.21
5 wt % Ru-NMC-2	776	0.64	0.05	-	-	-	-	4.68	0.20

(a) Total pore volume at $P/P_0 = 0.99$.

(b) Micropore volume calculated by t-plot method.

(c) Amount of Ru calculated from ICP-OES.

(d) Basicity obtained from CO_2-TPD.

M/P = Melamine-to-phenol ratio.

5B.1.1.3. Fourier transform infrared spectroscopy

The FTIR spectrum of NMCs and Ru supported catalysts were analyzed in the absorption band spanning from 500-3500 cm^{-1} region and are depicted in **Fig. 5B.2**. The band emerging at 1129 cm^{-1} could be due to C-N stretching vibrations [3]. The strong band that appeared at 1404 cm^{-1} is related to C=C backbone stretching vibration of the aromatic group [4]. The absorption band appearing at 1650 cm^{-1} is attributed to the vibration of phenylene conjugated C=C bonds [4]. The broad bands at 2997-3332 cm^{-1} can be assigned to N-H and O-H stretching vibrations [5].

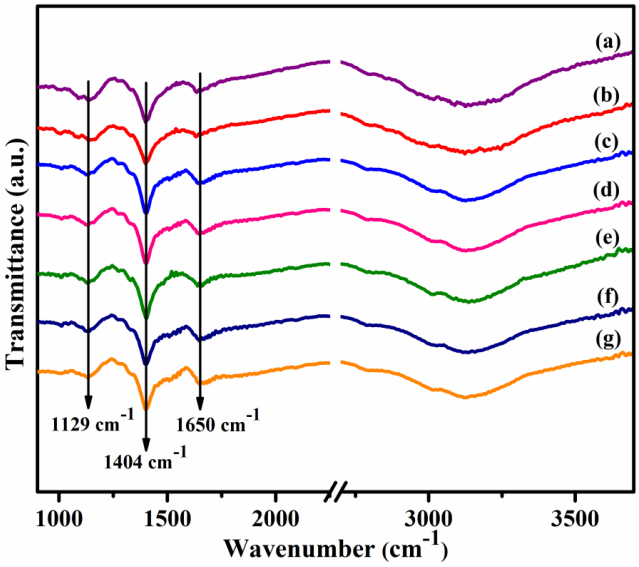

Fig. 5B.2 FTIR spectra of (a) NMC-1, (b) 3 wt % Ru-NMC-1, (c) NMC-2, (d) 2 wt % Ru-NMC-2, (e) 3 wt % Ru-NMC-2, (f) 4 wt % Ru-NMC-2 and (g) 5 wt % Ru-NMC-2.

5B.1.1.4. Raman spectroscopy

Further Raman spectroscopy was employed to understand the structural defects in the catalysts. As shown in **Fig. 5B.3**, the bands at 1330 and 1595 cm^{-1} are assigned to D-band (defect induced) and G-band (graphitic) bands of sp^2 hybridized carbon atoms in the NMC framework [2, 6-7]. No detectable change in the band shifts was observed upon increasing the metal loading which suggest that the framework structure of NMC remains intact after Ru loading. The intensity ratios of D-band to G-band (I_D/I_G) are 1.49, 1.71 and 2.12, for MC, NMC-1 and NMC-2, respectively. Notably, the peak intensity is increased upon increasing N content. A similar pattern was also observed for metal supported catalysts. This result implies that the doping nitrogen in the carbon framework induces more disorderliness in the catalysts.

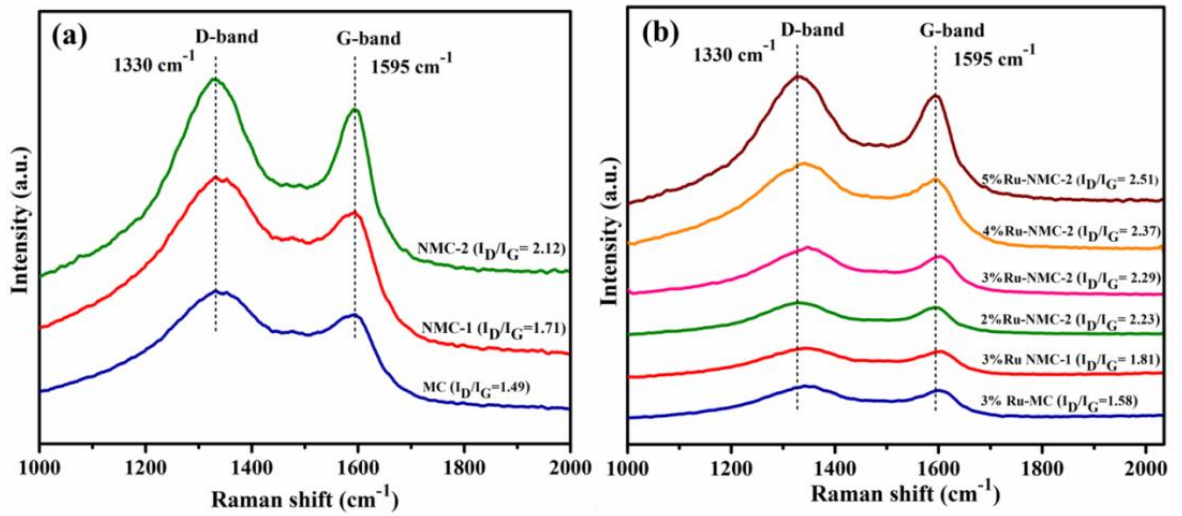

Fig. 5B.3 Raman spectra of (a) NMCs and (b) Ru supported NMCs catalysts.

5B.1.1.5. Transmission electron microscopy

Further to ascertain the structural morphology and distribution of Ru nanoparticles on the NMC supports, HRTEM of all the catalysts were carried out and depicted in **Fig.5B.4.** The TEM micrographs clearly show that the Ru nanoparticles are homogeneously distributed on the nitrogen doped mesoporous carbon support. The average particles size of Ru supported NMCs catalysts were 3.3, 2.4, 2.0, 3.0 and 3.8 nm for 3 wt % Ru-NMC-1, 2 wt % Ru-NMC-2, 3 wt % Ru-NMC-2, 4 wt % Ru-NMC-2, and 5 wt % Ru-NMC-2, respectively. A broad distribution of Ru nanoparticles size ranging from 1 to 5 nm was evident in the case of N-free counterpart (3 wt % Ru-MC) with an average nanoparticles size of 4.2 ± 1 nm, which is relatively larger among all the catalysts. This result explicitly proves that the N in the carbon matrix plays a vital role in stabilizing the small Ru nanoparticles in the catalysts. Notably, higher nitrogen content (7.9 wt %) in case NMC-2 promotes the better stabilization of Ru nanoparticles and helps to maintain a small size of Ru nanoparticles in the catalyst. Accordingly 3 wt % Ru-NMC-2 catalyst showed average Ru nanoparticle size of 2 nm and afforded highest Ru dispersion (66 %) among all the catalysts. Interestingly, 3 wt % Ru-NMC-2 exhibited higher yield of FDCA among all which might be due to the above attributes. Thus it is reasonable to believe that N content in the catalysts not only amplifies the metal dispersion and simultaneously boosts the catalytic performance of the catalysts.

The Ru metal dispersion for all the catalysts was calculated from HRTEM analysis, by assuming the spherical nature of Ru nanoparticles and using the following formula [8, 9].

$$\textbf{Dispersion (\%)} = (600.M_{Ru}) / (\rho.d_{nm}.\ a_{Ru}.N_a)$$

Where,

M- Atomic weight of the metal

ρ- Density of metal

d_{nm}- Particle size in nm obtained from TEM

a - Atomic surface area

N - Avogadro's number

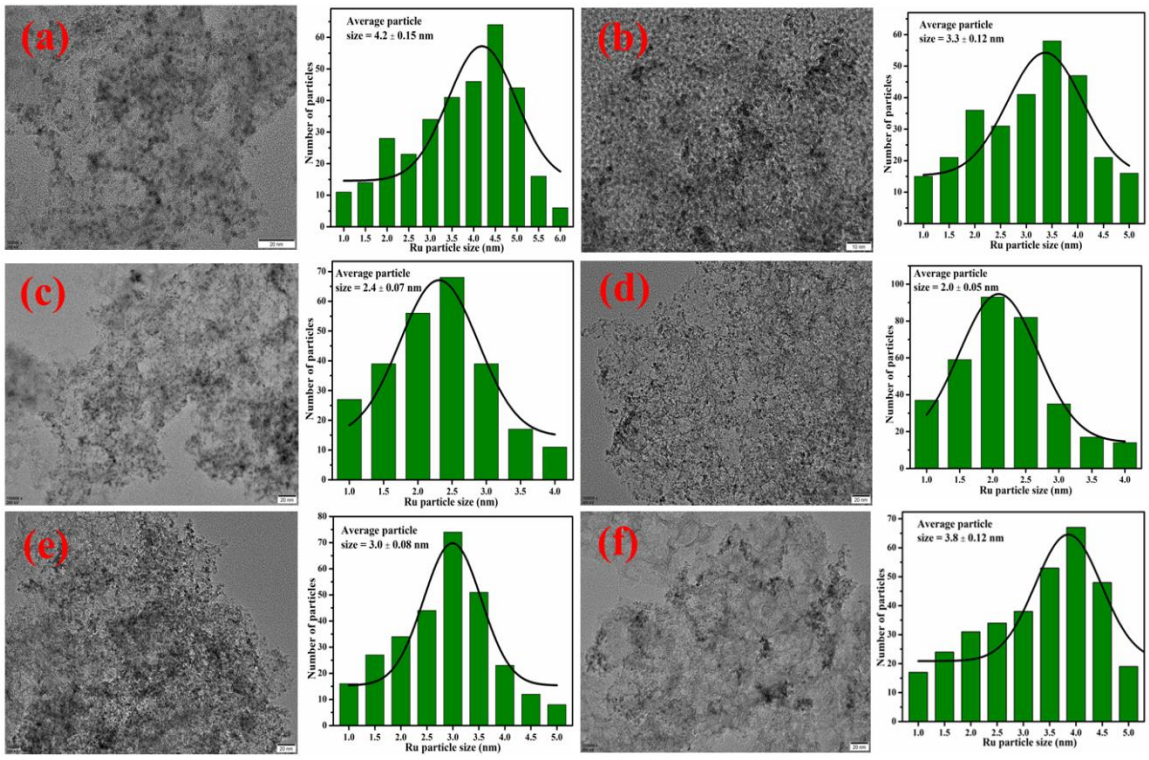

Fig.5B.4 HRTEM images of fresh catalysts (a) 3 wt % Ru-MC, (b) 3 wt % Ru-NMC-1, (c) 2 wt % Ru-NMC-2, (d) 3 wt % Ru-NMC-2, (e) 4 wt % Ru-NMC-2, and (f) 5 wt % Ru-NMC-2.

Table 5B.2 Ru particle size, dispersion and turnover frequency of the catalyst

Catalysts	**Average Ru particle size [a] (nm)**	**Ru metal dispersion [b] (%)**	**TOF [c] (min^{-1})**
3 wt % Ru-MC	4.2 ± 0.15	31	2.8×10^{-2}
3 wt % Ru-NMC-1	3.3 ± 0.12	40	4.3×10^{-2}
2 wt % Ru-NMC-2	2.4 ± 0.07	51	6.0×10^{-2}
3 wt % Ru-NMC-2	2.0 ± 0.05	66	7.2×10^{-2}
4 wt % Ru-NMC-2	3.0 ± 0.08	43	5.1×10^{-2}
5 wt % Ru-NMC-2	3.8 ± 0.12	34	4.0×10^{-2}
Spent 3 wt % Ru-MC	5.3 ± 0.11	22	-
Spent 3 wt % Ru-NMC-2	3.3 ± 0.16	44	-

(a) Calculated from TEM analysis.

(b) Estimated basis of the average Ru particle size using TEM analysis and using the equation described by Isaifan *et al.* in refs. [8, 9].

(c) TOF = Turnover frequency (moles of HMF converted per mole of active metal sites per hour)

5B.1.1.6. X-ray photoelectron spectroscopy

The XPS analysis was executed for NMCs and Ru-supported samples to study the elemental composition, nature of N species, and possible oxidation state of Ru nanoparticles. **Fig. 5B.5a** shows the XPS survey spectra of NMCs support. Three distinct peaks were observed at 284.7, 400.2, and 532.2 eV, which are related to C1s, N1s, and O1s core levels. The binding energy value at 284.7 eV corresponds to carbon 1s spectra, which is associated with graphitic carbon. These results indicated that most of the carbon atoms present in the samples were assembled on a conjugated honeycomb lattice [1, 10]. **Fig. 5B.5b** shows the N1s spectra which are deconvoluted into three different N species in the NMC support. The peaks located at 398.4, 400.5 and 401.7 eV are assigned to pyridinic N (N1), pyrrolic N (N2), and graphitic N (N3). It is worth mentioning that as the catalysts have been prepared through similar synthesis protocols, the percentage distribution of N for all the catalysts remains the same. The distribution confirms that most of the nitrogen atoms present at the edges of the carbon framework (N1, N2) and a minor fraction of N were incorporated into the sp^2 hybridized carbon atom [2, 11]. Research investigation suggests that the N present in the sp^2 hybridized carbon framework is not directly acting as an anchoring site for the Ru nanoparticles. The existence of pyridinic N and pyrrolic N in the carbon framework serves as acting sites for Ru nanoparticles and maximizes the disordered graphitic carbon structure, thus reflecting peak broadening in the Raman spectra. Let us note that since the distribution of N throughout all the catalysts remain the same, therefore N content in the catalyst may influence the catalytic activity.

The XPS spectra of Ru supported MC and NMCs catalyst in the Ru 3p region are shown in **Fig. 5B.5d-e** where 3p core-level spectra is deconvoluted into three different peaks [12]. The peak at 462.6 eV can be assigned to metallic Ru and the peak observed at 464.4 eV corresponds to anhydrous RuO_2 (Ru^{+4}) [2, 13]. In addition, a small peak at 466.7 eV is attributed to hydrous RuO_2, which is well matched with the previous report [14]. Among all 3 wt % Ru-NMC-2 catalyst manifested higher availability of metallic Ru^0 (57 %) in the catalyst, which have major role to attain high yield of FDCA. Whereas, nitrogen free catalyst 3 wt % Ru-MC exhibits the least metallic Ru^0 (31 %) due to which the catalyst displayed lowest catalytic performance among all. The above results clearly established the dominating catalysis of Ru nanoparticles in the reaction. Nonetheless, the N content in the carbon framework which is act as an anchoring site for the Ru nanoparticles also facilitates the

reduction of Ru nanoparticles in the catalysts. This is in good agreement with the H_2-TPR results of the catalysts, discussed in subsequent section.

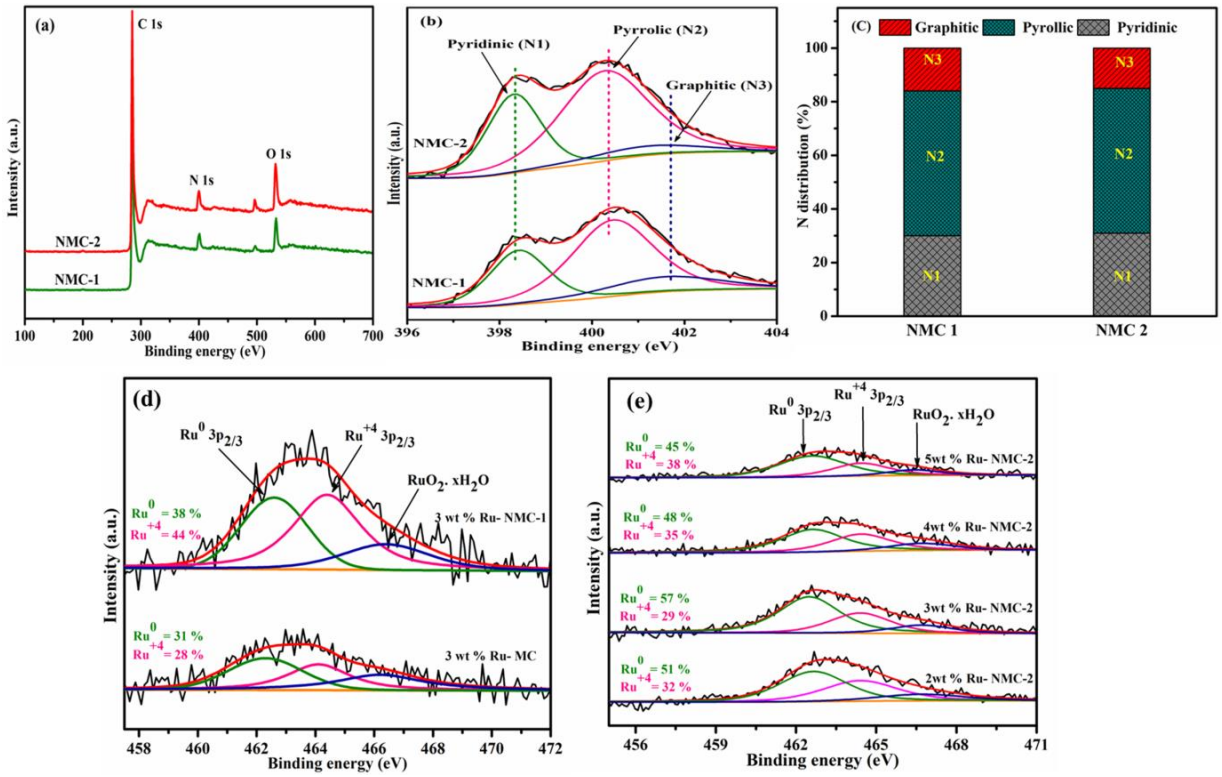

Fig. 5B.5 (a) XPS survey, (b) N1s spectra of NMCs, (c) The distribution of different N species in the NMCs support (d-e) Ru 3p core level spectra.

5B.1.1.7. Temperature programmed reduction

H_2-TPR analysis was performed to investigate the reducibility of Ru supported MC and NMCs catalysts and the interactions of Ru nanoparticles with the supports. The TPR reduction profiles are depicted in **Fig.5B.6** and it can be seen that all of the Ru supported MC and NMCs catalysts exhibit a single reduction peak in the range 70-180 °C temperature, which can be attributed mainly to the reduction of RuO_x species [15, 10]. Interestingly, the reduction peak for Ru nanoparticles was shifted to lower temperature in case of N doped mesoporous carbons as compared to N free counterparts. As reported previously [2], N on carbon framework imparts basicity to the catalysts which donate its electrons to the vacant d-orbitals of the Ru nanoparticles and facilitate reduction of Ru nanoparticles in the catalysts. Therefore, the shift in the reduction peaks lower temperatures is due to the N-promoted reduction of Ru nanoparticles in the catalysts. Thus, the TPR results clearly evident that the strong synergistic interaction between N and Ru nanoparticles in the catalysts.

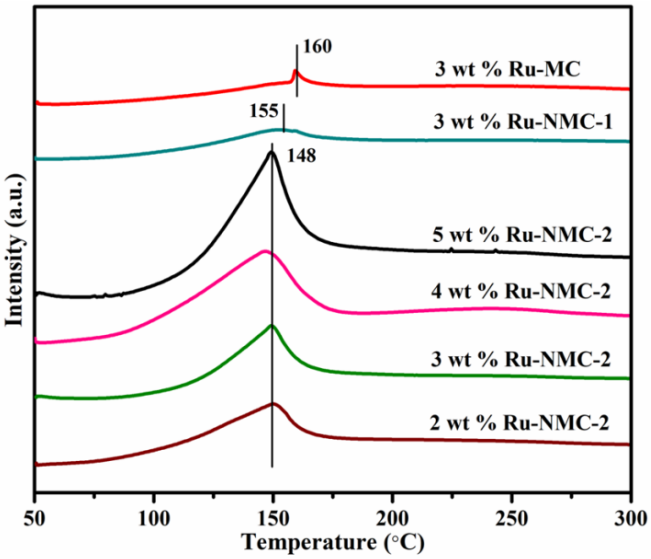

Fig. 5B.6 TPR profiles of Ru supported catalysts.

5B.1.2. Catalytic performance of HMF oxidation

5B.1.2.1. Aerobic oxidation of HMF to FDCA

The above synthesized catalysts were tested for the selective oxidation of HMF to FDCA using Parr autoclave reactor (refer **Section 2.4.13.**). The reaction was executed under the mild conditions: at 110 °C, 150 mg catalyst and 10 bar oxygen pressure. **Fig. 5B.7** shows the yield of FDCA with function of reaction time. It was observed that the catalytic performance of nitrogen free 3 wt % Ru-MC catalyst showed 22 % yield of FDCA after 10 h of reaction. Whereas, the nitrogen containing 3 wt % Ru-NMC-1 and 3 wt % Ru-NMC-2 catalysts demonstrated relatively better catalytic performance in terms of FDCA yield. Importantly, the 3 wt % Ru-NMC-2 catalyst poses higher N content (7.9 wt %) offered a complete HMF conversion and highest FDCA yield amongst all. Let us note that, the 3 wt % Ru-NMC-2 catalyst demonstrated a complete HMF conversion within 2 h of reaction time and further prolonging a maximum 83 % FDCA yield was achieved after 10 h of reaction time. This result implies that the nitrogen content in the NMC support plays a vital role in the reaction to achieve better yield of FDCA. Nitrogen on the carbon framework has dual role in the catalytic performance of the catalysts. It imparts basicity to the catalysts and simultaneously acts as anchoring sites for Ru nanoparticles in the catalysts which in turn helps to maintain better Ru dispersion in the catalysts. The superior catalytic performance in case of 3 wt % Ru-NMC-2 catalyst can be attributed to the higher availability of metallic Ru (57 %), small size Ru nanoparticles (2 nm), and strong synergistic interaction owing to the electronic

migration between nitrogen and vacant d-orbitals of Ru nanoparticles. Therefore, NMC-2 support was further investigated for the influence of Ru content on the catalyst.

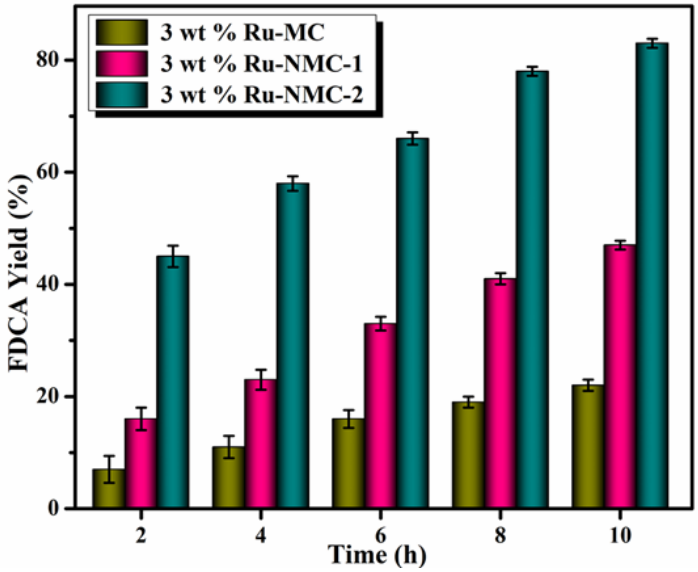

Fig. 5B.7 Oxidation of HMF over 3 wt % Ru supported MC, NMC-1 and NMC-2.

Reaction conditions: *HMF (0.5 mmol); Catalyst (150 mg); 30 mL H_2O; 10 bar O_2; 110 °C.*

Scheme 5B.1 Represents the tandem reaction pathways for HMF oxidation. In the first step HMF oxidized to DFF or HMFCA in the presence of oxygen. Further, both intermediates may be oxidized to FFCA. Finally, FFCA oxidized to value-added products FDCA.

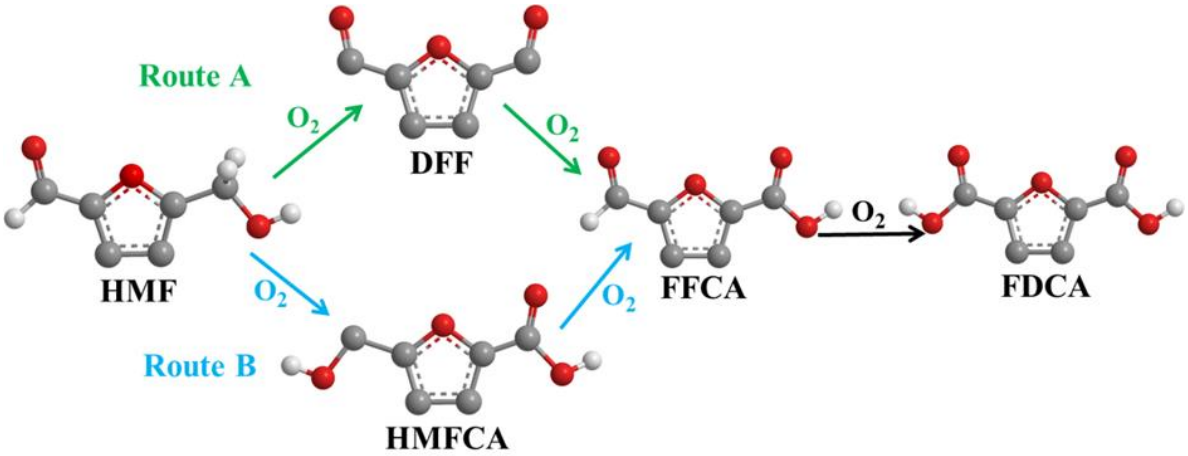

Scheme 5B.1 Typical reaction pathways for aerobic oxidation of HMF to FDCA.

5B.1.2.2. Influence of catalyst composition

In order to find the optimum Ru loading in the catalysts the reaction was carried out with catalysts having different Ru content. **Fig. 5B.8** depicted the catalytic performance of different Ru supported NMC catalysts for HMF oxidation to FDCA, under the similar

reaction conditions. A 2 wt % Ru-NMC-2 catalyst exhibited complete HMF conversion in 4 h of reaction. Meanwhile, the yield of FDCA increased progressively with the course of reaction time. However, only 53 % FDCA yield was achieved at the 10 h of the reaction. This observation indicates that the active sites available in 2 wt % Ru-NMC-2 are not sufficient to attain the high yield of FDCA as confirmed from the XPS result of the catalysts.

Further, Ru metal loading was increased to 4 and 5 wt % in NMC-2 support for HMF oxidation. Interestingly, both the catalysts showed a comparable yield of FDCA in the initial hours of reaction. Upon increasing the reaction time, the yield of FDCA decreased slowly. This could be due to the larger particle size of Ru nanoparticles (mean size of 4% Ru = 3 nm and 5% Ru = 3.8 nm), thereby decreasing Ru metal dispersion on the NMC support and relative percentage of metallic Ru present in the catalyst. **Table 5B.3** shows the catalytic behaviour of different catalysts in the selective oxidation of HMF to FDCA. Interestingly, optimized 3 wt % Ru-NMC-2 catalyst with N content (7.9 %) and average Ru nanoparticle size in the range of 2.0±0.05 nm showed comparably higher activity than nitrogen free MC and NMC-1 supports. This result firmly indicates that nitrogen content is essential part of the catalyst for HMF oxidation. The catalytic results also depict the size dependent catalytic activity of the synthesized catalysts. Moreover, nitrogen contributes to stabilizing the active Ru species and helps to achieve smaller particle size in the catalysts. Thus, nitrogen controls the Ru aggregation over the catalyst surface.

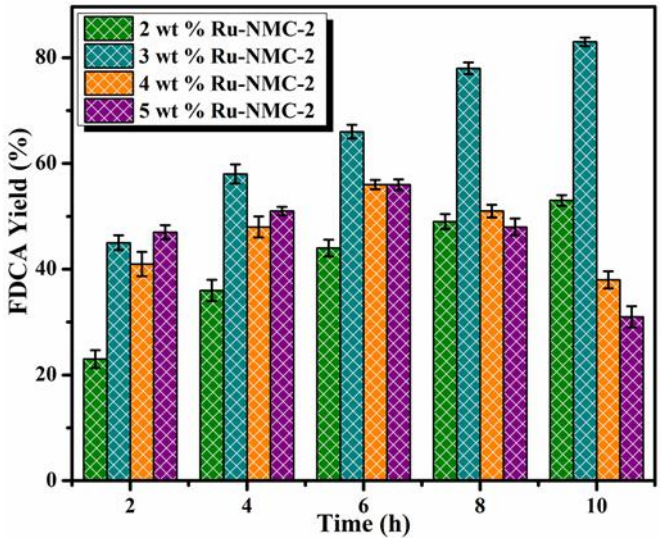

Fig. 5B.8 Effect of Ru loading on HMF oxidation.

Reaction conditions: *HMF (0.5 mmol); catalyst (150 mg); 30 mL H_2O; 10 bar O_2; 110 °C.*

Table 5B.3 Catalytic performance for base-free oxidation of HMF to FDCA over different catalysts

Entry	Catalysts	HMF Conversion (%)	Yield of DFF (%)	Yield of FFCA (%)	Yield of FDCA (%)
1	MC	7	4	0	0
2	3 wt % Ru-MC	33	57	8	22
3	NMC-1	15	14	0	0
4	3 wt % Ru-NMC-1	67	23	30	47
5	NMC-2	28	20	5	0
6	2 wt % Ru-NMC-2	100	11	36	53
7	3 wt % Ru-NMC-2	100	0	17	83
8	4 wt % Ru-NMC-2	100	5	57	38
9	5 wt % Ru-NMC-2	100	16	53	31

Reaction conditions: *HMF (0.5 mmol); catalyst (150 mg); 30 mL H_2O; 10 bar O_2; 110 °C.*

Fig. 5B.9 represents a clear relationship between the nitrogen content of the supports with catalytic activity results and Ru particle size. These results indicate that nitrogen content in the catalyst plays a significant role in anchoring smaller Ru nanoparticles, thereby increasing the turnover frequency (TOF) of the catalysts.

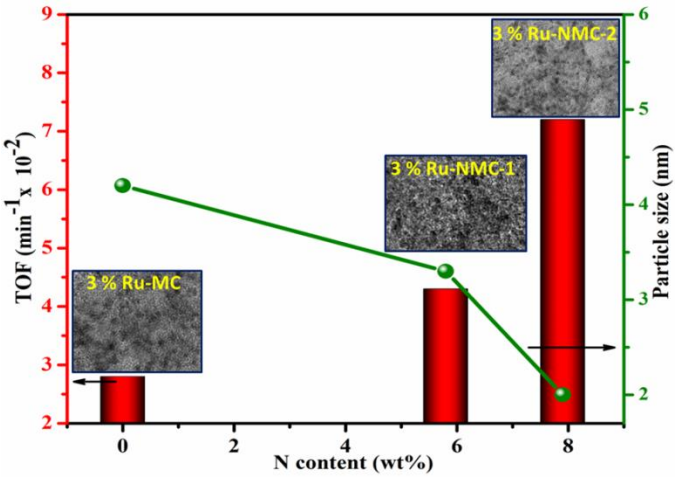

Fig. 5B.9 Correlation between the N content of the catalysts with turnover frequency (TOF) and Ru particle size.

5B.1.2.3. Effect of reaction temperature and pressure

To gain more insights into the catalytic performance of HMF oxidation, the influence of reaction temperature and pressure were studied on 3 wt % Ru-NMC-2 catalyst, and are depicted in **Fig. 5B.10**. The catalytic result clearly shows the activation of HMF at lower reaction temperature, while the FDCA yield was enhanced as the reaction prolonged to 10 h. However, at both 80 and 100 °C, the yield of FDCA was 38 and 68 % respectively. Upon

increasing the temperature to 110 °C; 83 % FDCA yield was achieved at 10 h. With further increase in the reaction temperature to 130 °C, the yield of FDCA decreased rapidly to 29 % at end of the reaction. At high temperature HMF was not stable and it degraded into humins [16, 17].

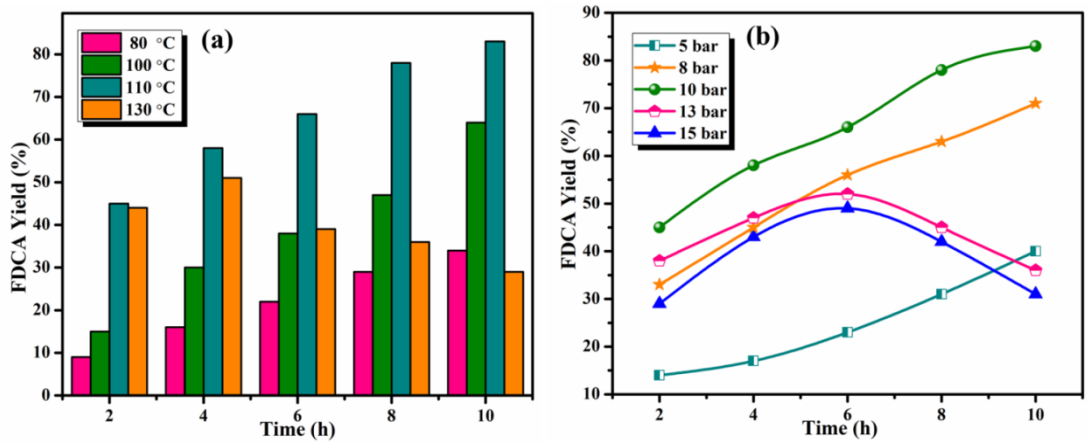

Fig. 5B.10 Effect of (a) Reaction temperature at 10 bar O_2 and (b) Pressure at 110 °C over 3 wt % Ru-NMC-2.

Reaction conditions: *HMF (0.5 mmol); catalyst (150 mg); 30 mL H_2O.*

The optimized 3 wt % Ru-NMC-2 catalyst for HMF oxidation was further studied for the influence of oxygen pressures and the results are depicted in **Fig.5B.10b**. Initially the reaction was performed at 5 and 8 bar O_2 pressure, which gave appreciable yield of FDCA. Upon increasing the pressure to 10 bar, complete HMF conversion was observed with 83 % yield of FDCA. With further increase in O_2 pressure to 13 and 15 bar gave a low yield of FDCA, which confirms that high oxygen pressure reduces HMF oxidation [16]. These observations matches well with reported literature suggesting that high pressure is not necessary to increase yield of FDCA [18-20].

5B.1.2.4. Catalytic recyclability test for 3 wt % Ru- NMC-2 catalyst

The stability and recyclability of the 3 wt % Ru-NMC-2 catalyst were investigated with the above optimal reaction conditions. After each reaction cycle, the catalyst was filtered and washed several times with distilled water and ethanol. Afterwards, the final residue was dried in an oven at 100 °C for overnight. The catalyst was reused for five consecutive runs and the results shown in **Fig.5B.11** clearly demonstrate the excellent recyclability and stability of the synthesized catalysts. A minor drop in the yield of FDCA was observed after the third cycle

which could be attributed to the aggregation of Ru nanoparticles or loss of active metallic Ru sites under the oxygen atmosphere.

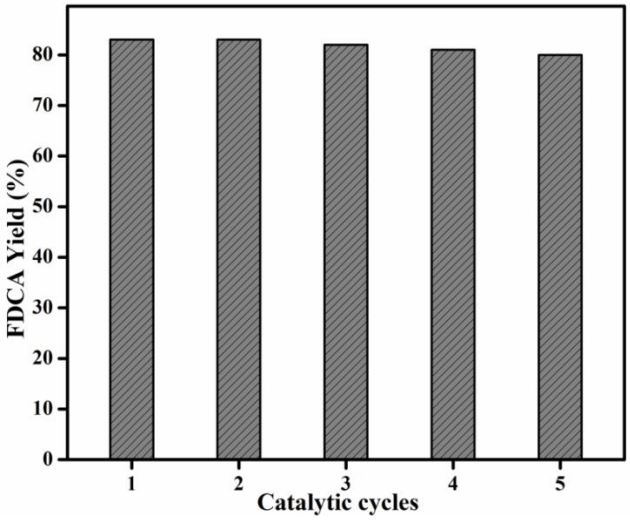

Fig. 5B.11 Recycling experiments for HMF oxidation over 3 wt % Ru-NMC-2.
Reaction conditions: *HMF (0.5 mmol); catalyst (150 mg); 30 mL H_2O; 10 bar O_2; 110 °C.*

Table 5B.4 shows various metal supported catalysts that have been investigated for conversion of HMF to FDCA. Whereas, our reaction conditions and the catalytic activity results are much more comparable to the reported catalyst for HMF oxidation.

Table 5B.4 Oxidation of HMF to FDCA over different catalysts reported in the literature

Catalyst	**Base**	**Oxidant (bar)**		**Time (h)**	**Temp. (°C)**	**FDCA Yield (%)**	**HMF Con. (%)**	**Ref.**
		O_2	**Air**					
Pt/C	2 equiv. Na_2CO_3	--	40	6	100	69	99	21
Pt/TiO_2	2 equiv. Na_2CO_3	--	40	6	100	84	90	22
Pt/CNT	base free	30	--	12	100	97	100	23
Pt-NP5	base free	1	--	6	80	60	100	24
Pd/CNF	2 equiv. K_2CO_3	5	--	5	160	70	100	25
Pd/CNT	2 equiv. K_2CO_3	5	--	5	160	60	100	23
Pd/C	2 equiv. NaOH	5	--	4	70	71	100	26
Au/C	2 equiv. NaOH	6.9	--	6	23	7	100	26
Au/CeO_2	5 equiv. NaOH	0.3	--	6	60	73	99	27
Au–Pd/CNT	base free	5	--	12	100	94	100	28

$Ru(OH)_x/La_2O_3$	base free	30	--	5	100	48	98	29
Ru/C	p^H = 13	10	--	4	50	6.4	98	30
Ru/C	1 equiv. NaOH	2	--	5	120	69	100	19
Ru/AC	4 equiv. $NaHCO_3$	--	40	2	100	75	100	31
$Ru/MnCo_2O_4$	base free	--	24	10	120	99	100	32
Ru/ZrO_2	base free	10		16	120	71	100	33
3 wt % Ru-NMC-2	base free	10	--	10	110	83	100	This work

5B.1.2.5. Spent catalyst analysis

Fig. 5B.12a represents the powder X-ray diffraction pattern of the spent 3 wt % Ru-NMC-2 catalyst after 5 catalytic cycles. The spent catalyst revealed no phase transformation; pointing out that the sp^2 hybridized graphitic structure remains intact even after 5th cycle. The elemental composition of the spent 3 wt % Ru-NMC-2 catalyst was investigated by XPS and the results are depicted in **Fig. 5B.12b**. No change in the binding energies of Ru was observed in the XPS spectrum. However, the relative percentage of active metallic Ru was decreased (38 %) after the 5th cycle, owing to the oxidation of metallic Ru under the reaction conditions. These results prove that smaller metallic Ru nanoparticles in the NMC support play major role to achieve high yield of FDCA and similar observation was observed in our previous study.

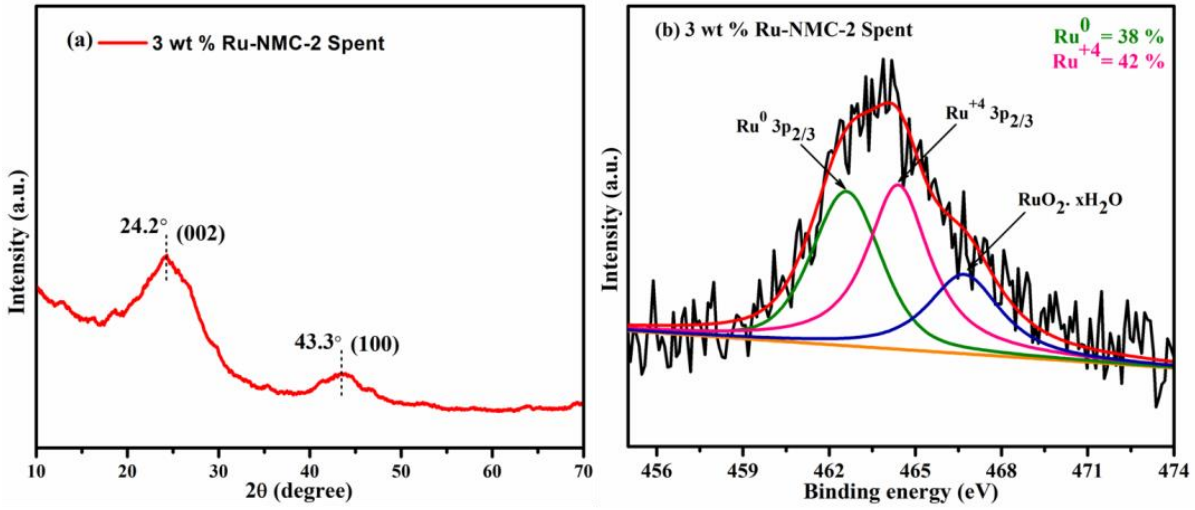

Fig. 5B.12 (a) PXRD and (b) Ru 3p core level XPS spectrum of spent 3 wt % Ru-NMC-2 catalyst.

The above catalytic activity results demonstrated that Ru particle size plays a vital role in the conversion of HMF to FDCA. **Fig.5B.13** depicts TEM images of spent 3 wt % Ru-MC and 3 wt % Ru-NMC-2 catalysts; it can be clearly evident that Ru nanoparticles were aggregated for both the catalysts after five consecutive runs under HMF oxidation reaction conditions. The particle size distribution of spent 3 wt % Ru-MC catalyst indicates the presence of larger Ru particle size 5.3 nm, hence decreasing Ru metal dispersion (22 %) on the MC support. Whereas, histogram of spent 3 wt % Ru-NMC-2 catalysts represents the less aggregation of Ru metal nanoparticles (mean size = 3.3 nm) than the nitrogen free catalyst. Therefore, a minor drop in the FDCA yield could be due to the aggregation of Ru metal nanoparticles and oxidation of some active catalytic sites in the catalyst.

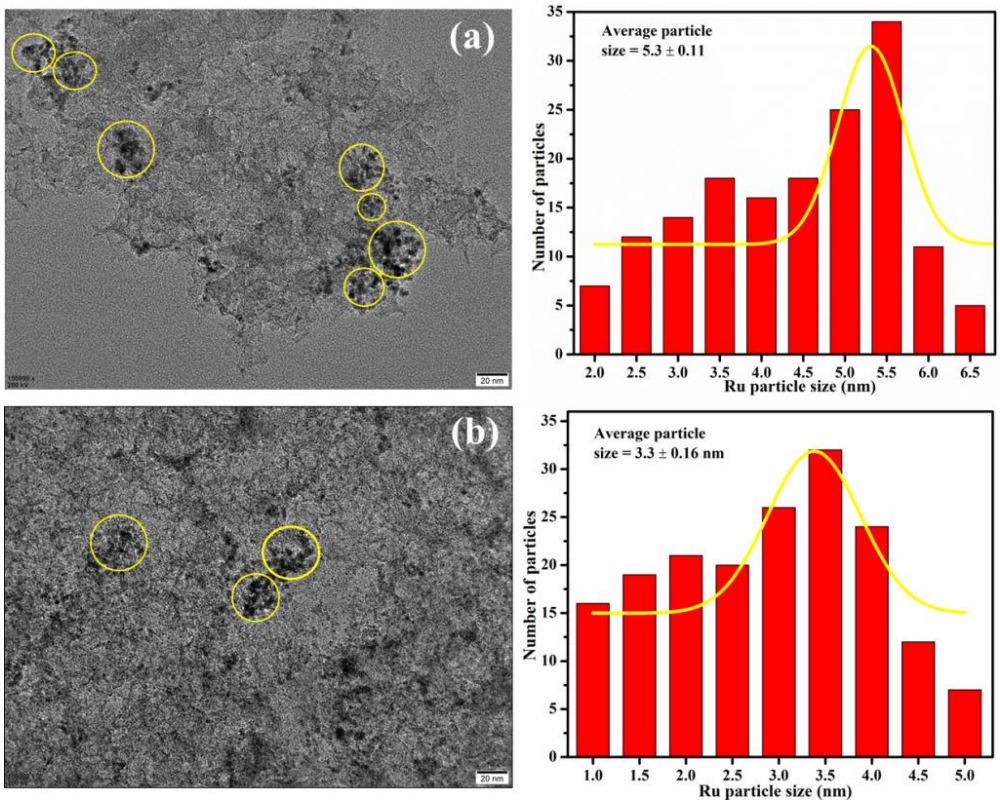

Fig.5B.13 HRTEM micrograph of spent catalysts (a) 3 wt % Ru-MC and 3 wt % Ru-NMC-2.

5B.2. Conclusions

Nitrogen-doped mesoporous carbon was synthesized via sol-gel process using Ludox-AS40 as silica source. The incorporated nitrogen in the highly porous mesoporous carbon supports contributes towards the stabilization of active Ru nanoparticles and consequently helps to maintain smaller particle size, surface basicity and high metal dispersion of the catalysts. The physio-chemical properties were characterized by XRD, FTIR, Raman spectroscopy, TEM,

CO_2-TPD, N_2- adsorption studies. XPS spectra of 3 wt % Ru-NMC-2 show higher metallic Ru on the catalyst, which leads to an increase in the yield (83 %) of FDCA. Furthermore, strong synergistic effect between N, Ru and metal supports enhanced the overall catalytic performance of the catalysts towards the HMF oxidation. The present study provides a new strategies to tailor Ru supported nitrogen doped mesoporous carbon for base free oxidation of HMF to FDCA.

References

1. H. Chen, F. Sun, J. Wang, W. Li, W. Qiao, L. Ling,D. Long, J. Phys. Chem. C 117 (2013) 8318−8328.
2. P. Gogoi, N. Kanna, P. Begum, R.C. Deka, C.V.V. Satyanarayana, T. Raja, ACS Catal. 10 (2020) 2489.
3. Z. Lei, M. Zhao, L. Dang, L. An, M. Lu, A. Ya. Lo, N. Yub, S.B. Liu, J. Mater. Chem. 19 (2009) 5985–5995.
4. M.K. Sahoo, P. Gogoi, G. Rajeshkhanna, S.V. Chilukuri, G.R. Rao, Applied Sur. Sci. 418 (2017) 40-48.
5. G.P. Hao, W.C. Li, D. Qian, A.H. Lu, Adv. Mater. 22 (2010) 853-857.
6. X. Xu, Y. Li, Y. Gong, P. Zhang, H. Li, Y. Wang, J. Am.Chem. Soc. 134 (2012) 16987−16990.
7. A. Sadezky, H. Muckenhuber, H. Grothe, R. Niessner, Poschl, Carbon 43 (8) (2005) 1731−1742.
8. R.J. Isaifan, S. Ntais, M. Couillard, E.A. Baranova, J. Catal. 324 (2015) 32−40.
9. R.J. Isaifan, H.A.E. Dole, E. Obeid, L. Lizarraga, P. Vernoux, E.A. Baranova, Electrochem. Solid-State Lett. 15 (2012) E14−E17.
10. A.S. Nagpure, P. Gogoi, N. Lucas, S.V. Chilukuri, Sustainable Energy Fuels 4(2020) 3654-3667.
11. W. Guan, Y. Zhang,Y. Wei, B. Li, Y. Feng, C. Yan, P. Huo, Y. Yan, Fuel 278 (2020) 118362.
12. D.R.M. Godoi, J. Perez, H.M. Villullas, J. Phys. Chem. C 113 (2009) 8518−8525.
13. P.A. Velazquez, E. Brillas, C. Arias, F. Centellas, J.M. Garrido, R.M. Rodriguez, P.L. Cabot, J. Phys. Chem. C 116 (2012) 18469−18478.
14. R. Chetty, W. Xia, S. Kundu, M. Bron, T. Reinecke, W. Schuhmann, M. Muhler, Langmuir 25 (2009) 3853−3860.
15. J. Jae, W. Zheng, R.F. Lobo, D.G. Vlachos, ChemSusChem, 6 (2013) 1158
16. X. Han, C. Li, X. Liu, Q. Xia, Y. Wang, Green Chem. 19 (2017) 996–1004.
17. D. Yan, J. Xin, Q. Zhao, K. Gao, X. Lu, G. Wang, S. Zhang, Catal. Sci. Technol. 8 (2018) 164.
18. M. Ventura, F. Nocito, E.D. Giglio, S. Cometa, A. Altomare, A. Dibenedetto, Green Chem. 20 (2018) 3921-3926.
19. G. Yi, S.P. Teong, Y. Zhang, Green Chem. 18 (2016) 979-983.

20. S. E. Davis, B. N. Zope, R. J. Davis, Green Chem. 14 (2012) 143-147.
21. H.A. Rass, N. Essayem, M. Besson, Green Chem.15 (2013) 2240.
22. H.A. Rass, N. Essayem, M. Besson, ChemSusChem 8 (2015) 1206–1217
23. P. Sharma, M. Solanki, R.K. Sharma, New J. Chem. 43 (2019) 10601-10609.
24. S. Siankevich, S. Mozzettini, F. Bobbink, S. Ding, Z. Fei, N. Yan, P.J. Dyson, ChemPlusChem, 83 (2018) 19–23.
25. C. Espinosa, R.C. Contreras, S. Navalon, C.R. Carcamo, M. Alvaro, B.F. Machado, P. Serp, H. Garcia, Eur. J.Inorg. Chem. 2019 (2019) 1979-1987.
26. S.E. Davis, L.R. Houk, E.C. Tamargo, A.K. Datye, R.J. Davis, Catal. Today, 160 (2011) 55-60.
27. J. Cai, H. Ma, J. Zhang, Q. Song, Z. Du, Y. Huang, J. Xu, Chem. Eur. J.19 (2013) 14215–14223.
28. X. Wan, C. Zhou, J. Chen, W. Deng, Q. Zhang, Y. Yang, Y. Wang, ACS Catal. 4 (2014) 2175–2185.
29. T. Stahlberg, E. Eyjolfsdottir, Y.Y. Gorbanev, I. Sadaba, A. Riisager, Catal. Lett. 142 (2012),1089-1097.
30. K.R. Vuyyuru, P. Strasser, Catal. Today, 195 (2012) 144–154.
31. F. Kerdi, H.A. Rass, C. Pinel, M. Besson, G. Peru, B. Leger, S. Rio, E. Monflier, A. Ponchel, Appl. Catal. A 506 (2015) 206–219.
32. D.K. Mishra, H.J. Lee, J. Kim, H.S. Lee, J.K. Cho, Y.W. Suh, Y. Yi, Y.J. Kim, Green Chem. 19 (2017) 1619–1623.
33. C.M. Pichler, M.G.A. Shaal, D. Gu, H. Joshi, W. Ciptonugroho, F. Schuth, ChemSusChem 11 (2018) 2083–2090.

Chapter-6

Summary and Conclusions

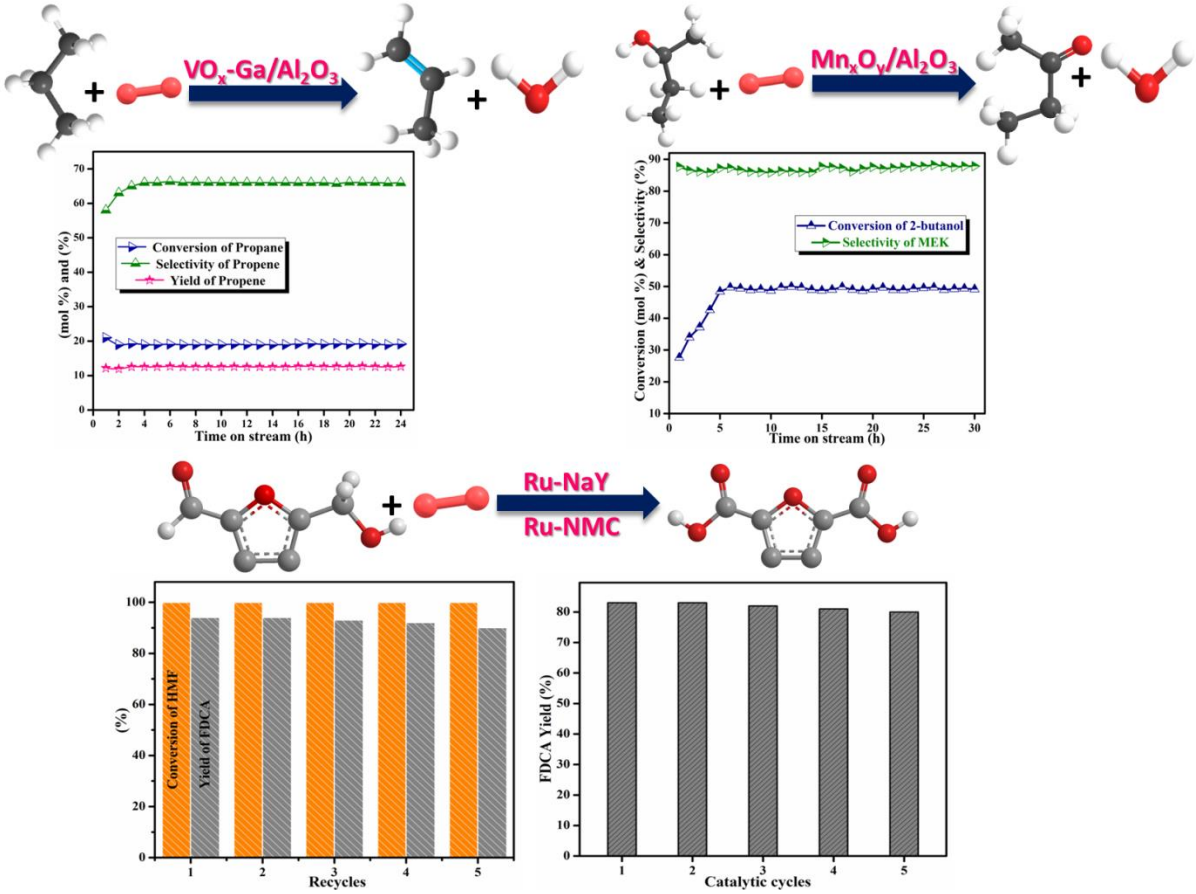

This chapter emphasizes the recent advances and importance of selective oxidation catalysis present in this dissertation. On the other hand, existing industrial technology processes and their significant drawbacks have been briefly explained. Various characterization studies were performed to understand the physicochemical properties of the tailored catalysts. This thesis deals with three different oxidation reactions: selective oxidation of propane, 2-Butanol, and 5-HMF oxidation to specialty chemicals. The summarization of the current process and catalyst development is briefly discussed.

Chapter 1: Introduction

This chapter addresses a brief introduction to catalysis and heterogeneous catalysis. The importance of selective oxidation catalysis and their advantages over the traditional process for the production of propene, MEK, and FDCA. A literature background for the ODH of propane and biomass utilization was extensively discussed.

Chapter 2: Synthesis methodology and characterization techniques

This chapter furnished the catalyst design and characterization technique used to appraise their surface properties. The synthesized catalysts are (VO_x-Ga) supported γ-Al_2O_3, Mn_xO_y with different oxide supports (ZrO_2, Al_2O_3, CeO_2 and SiO_2) Ru-NaY and Ru-NMC are widely described in this chapter. The designed catalysts were characterized by using powder X-ray diffraction. BET analysis, FTIR, TEM, XPS, TPR, etc. The instrument, theory, and configuration description are briefly discussed.

Chapter 3: New insights into the composition and catalytic performance of VO_x-Ga/γ-Al_2O_3 for the oxidative dehydrogenation of propane to propene

In the present work, ODH of propane to propene was studied over vanadium, and gallium oxide supported on γ-Al_2O_3 and optimized the catalyst composition. The VGA-2 catalyst showed excellent catalytic activity, and the catalyst was exhibited for long-term stability (24 h of reaction) with stable activity. TPR and UV-visible spectra showed highly dispersed monomeric VO_x species with tetrahedral coordination geometries influencing the product selectivity. The redox nature of vanadium ($V^{5+}$and V^{4+}) oxide and higher V^{5+} surface in VGA-2 catalyst is more favorable for C-H activation. In addition, Lewis acid sites and four coordinated $Ga^{3+}O_x$ species are highly active for ODHP. The spent catalysts were analyzed by thermogravimetric analysis, where the optimized catalyst showed the least coke deposition.

Chapter 4: Effective and selective oxidation of 2-Butanol over Mn supported catalyst systems

Oxidation of 2-Butanol to MEK is an important reaction due to its wide range of applications. Various catalysts were synthesized via co-precipitation, and the sol-gel method and structure-selectivity-surface properties were characterized by different physicochemical properties. It was found that the presence of Mn_3O_4 species in Mn_xO_y-Al_2O_3 (MA) catalysts is responsible for maximum catalytic activity towards 2-Butanol oxidation. MA catalyst conferred a maximum 2-Butanol conversion of 51 % and 88 % selectivity towards MEK. XPS analysis revealed that Mn in MA catalyst exists in +2, +3, and +4 oxidation states and is responsible for 2-Butanol oxidation. Moreover, it was found that the acidity of the catalyst also plays an important role in catalytic activity. Synergetic effect of appropriate acidity along with active Mn species is responsible for this reaction, and MA catalyst was demonstrated for long-term stability for 30 h of continuous reaction under optimized reaction conditions.

Chapter 5: Selective oxidation of 5-Hydroxymethylfurfural to 2,5-Furandicarboxylic acid

This chapter provides a brief introduction to a synthesis of HMF, a background of the work, and an important reaction for the production of recyclable bio-based polymers. This chapter is divided into two parts.

A. A highly efficient and reusable Ru-NaY catalyst for the base free oxidation of 5-Hydroxymethylfurfural to 2,5-Furandicarboxylic acid

Selective oxidation of HMF to FDCA is an important reaction for the production of recyclable bio-based polymers. Herein, reported series of Ru nanoparticles supported on NaY zeolites catalysts for the oxidation of HMF to FDCA. The catalysts were prepared by the ion-exchanged method. Among all the compositions prepared, the optimized 3 wt % Ru-NaY catalyst showed fairly excellent catalytic activity under base-free conditions with a shorter period of reaction time. The complete conversion of HMF with 94 % FDCA yield was achieved. The catalyst was reused for four cycles, with an insignificant decrease in the yield of FDCA. Furthermore, the acidic hydroxyl groups of the supercage, as well as a higher amount of metallic Ru^0, are also responsible for the high yield of FDCA.

B. An enhanced catalytic performance of Ru nanoparticles supported NMC catalyst for the oxidation of HMF to FDCA

In this chapter, we investigated the effect of nitrogen content, Ru particle size, and Ru^0 on their catalytic performance. Nitrogen-doped mesoporous carbon (NMCs) and mesoporous carbon (MC) were synthesized via the silica-assisted sol-gel method. The catalyst was demonstrated for base-free oxidation of HMF to FDCA. The catalyst with 3 wt % Ru-NMC-2 exhibits an admirable yield to FDCA (83 %), compared to all other Ru compositions impregnated on NMC-2. Higher nitrogen content NMC-2 (7.9 wt %) support facilitates the high metal dispersion, higher abundance of metallic Ru, and stabilization of Ru nanoparticles. In addition, surface basicity and strong synergistic effect between the N and Ru are responsible for the higher yield of FDCA. The turnover frequency (TOF) for 3 wt % Ru-NMC-2 catalyst was 7.2×10^{-2} min^{-1}, which is found to be reasonably better than the other catalysts.

Summary and future perspective

Selective oxidation catalysis plays a crucial role in the petrochemical industry to produce platform chemicals and intermediates. The conventional and existing industrial processes are direct dehydrogenation, steam cracking, and homogeneous catalytic methods for propene and methyl ethyl ketone production. However, these processes have several disadvantages to overcome this ODH/selective oxidation, which is a promising alternative to conventional technology. The reaction takes place at a lower reaction temperature in the presence of oxygen as an oxidant.

Despite, employing oxygen as an oxidant in propane and 2-Butanol activation at high temperature leads to undesirable deep-oxidation. A substantial effort has been steadfast to designing an efficient catalyst, and reactor engineering is key elements for future implementation in large-scale production. In contrast, using CO_2 as a mild oxidant to avoid the hot spots and deep-oxidation. In addition, employing a CO_2 oxidant is relevant to utilizing greenhouse gas to reduce net CO_2 emissions. Numerous catalysts have been reported for FDCA monomer for the production of renewable polymer polyethylene furanoate (PEF), which is a substitute for conventional fossil-based polyethylene terephthalate (PET). However, this process has not yet been implemented for market scale, owing to the high cost of the noble metals, instability, using external base, and degradation of HMF at high temperature. Therefore, strategies for the rational design of catalysts and develop stability remain a key challenge.

Abstract

Name of the Student: Prabu K **Registration No. : 10CCl7J26022**

Faculty of Study: Chemical Sciences **Year of Submission: 2021**

AcSIR academic centre/CSIR Lab: CSIR-NCL **Name of the Supervisor: Dr. T. Raja**

Title of the thesis: Selective catalytic oxidation over metal oxides for the valorization of biomass derived feedstocks and Propane.

Heterogeneous catalysis plays a key role in the petrochemical industry, oil refining, polymeric materials and environmental remediation. Selective oxidation technology is the most important process for manufacturing of propene, methyl ethyl ketone and 2,5-furandicarboxylic acids; which are prominent processes in the chemical industry for the production of fine and specialty chemicals. Traditionally, olefins are produced through steam cracking, fluid catalytic cracking (FCC) and catalytic dehydrogenation (DH) of alkanes. However, steam, FCC and dehydrogenation process need more energy and have many other drawbacks. Conventionally, methyl ethyl ketone and 2,5-furandicarboxylic acids are produced by homogeneous catalytic methods using oxidizing agents such as permanganates, chromates and bromates. However, these stoichiometric oxidants are more expensive and toxic, due to the huge metal wastes that cause severe environmental impacts. In this aspect, selective oxidation/oxidative dehydrogenation is considered to be a more viable alternative method of producing ketones, carboxylic acids and lower olefins. This is highly exothermic in nature and the reaction runs at a lower temperature, which minimizes the formation of coke deposits on the catalyst surface, ensuring the catalyst's robustness. This study systematically investigates designing a catalyst to obtain highly stable and selective catalyst VO_x-Ga/γ-Al_2O_3 for the oxidative dehydrogenation of propane. The optimized catalyst was stable even after 24 h of reaction through 19 % conversion achieved at 400 ºC with 66 % selectivity. Selective oxidation of 2-Butanol to methyl ethyl ketone (MEK) is an important reaction due to its wide range of applications. The present work explores the selective oxidation of 2-Butanol to MEK over Mn supported on different oxide supports. The oxidation of 5-hydroxymethylfurfural (HMF) to 2,5-furandicarboxylic acid (FDCA) plays an important role in the production of recyclable green polymers. The present work reported a series of Ru nanoparticles supported on NaY zeolites and nitrogen-doped mesoporous carbon (NMC) catalysts showed superior catalytic activity under base free oxidation of HMF to FDCA.

List of publication(s) emanating from the thesis work:

- **Prabu. K**, Prabu. M, Ashok Kumar. V, Aswathy T.V, W.V.Y.S. Sandilya, C.S. Gopinath, T. Raja, Effective and selective oxidation of 2-Butanol over Mn supported catalyst systems. ***Appl. Catal. A Gen.*, 2016**, 525, 237–246.
- **Prabu. K**, Pranjal Gogoi, Aswathy T.V, T. Raja, A highly efficient and reusable Ru-NaY catalyst for base free oxidation of 5-Hydroxymethylfurfural to 2,5-Furandicarboxylic acid. ***Catalysis Today, 2021****, 375, 145-154.*
- **Prabu. K**, Aswathy T.V, Eeswar U, Siva Prasad M, T. Raja, New insights intothe composition and catalytic performance of VO_x-Ga/γ-Al_2O_3 for the oxidative dehydrogenation of propane to propene (To be communicated).
- **Prabu. K**, Pranjal Gogoi, Aswathy T.V, T. Raja, An Enhanced catalytic performance of Ru nanoparticles supported NMC catalyst for the oxidation of HMF to FDCA (Manuscript under preparation).

List of publication(s) not emanating from the thesis:

- M. Manikandan, Ashok Kumar. V, **Prabu. K**, R.K. Jha, T. Raja, Role of surface synergistic effect on the performance of Ni-based hydrotalcite catalyst for highly efficient hydrogenation of furfural, ***J. of Mol. Catal. A Chemi., 2016****, 417, 153–162.*
- M. Prabu, M. Manikandan, **Prabu. K**, P.R. Kalaivani, N. Rajendiran, T. Raja, Synthesis of biodiesel using the Mg/Al/Zn hydrotalcite/SBA-15 nanocomposite catalyst, ***ACS Omega, 2019****, 4, 3500-3507.*
- P. Gogoi, A.S. Nagpure, **Prabu. K**, C.V.V. Satyanarayana, T. Raja, Insights into the catalytic activity of Ru/NaY catalysts for efficient H_2 production through aqueous phase reforming, ***RSC Sustainable Energy Fuels, 2020****, 4, 678.*
- Aswathy T.V, **Prabu. K**, N.N. Gupta, T. Raja, Promoted mesoporous Fe-alumina catalysts for the non-oxidative dehydrogenation of isobutane, ***Catalysis Communications, 2021****, 150, 106263.*
- Aswathy T.V, **Prabu. K**, P. Gogoi, R.K. Jha, T. Raja, Utilizing the oxygen carrier property of cerium iron oxide for the low-temperature synthesis of 1,3-butadiene from 1-butene, ***Catalysis Letters, 2021, 151, 3057-3066.***

- Lakshmiprasad Gurrala, M.M. Kumar, Attada Yerrayya, **Prabu. K**, Pedro Castaño, T. Raja, Giovanni Pilloni, Changyub Paek, R. Vinu, Unraveling the reaction Mechanism of selective C9 monomeric phenol formation from lignin using Pd-Al_2O_3-activated biochar catalyst, ***Bioresource Technology, 2022,*** *344, 126204.*

Conferences

- Participant, **CATSYMP**, CSIR- CSMCRI, Bhavnagar, Gujarat, 2015.
- Poster presenter, "A highly efficient and reusable Ru-NaY catalyst for the base free oxidation of 5-hydroxymethylfurfural to 2,5-furandicarboxylic acid", **The 8th Asia-Pacific Congress on Catalysis (APCAT-8)**, Bangkok, Thailand, 2019.
- Poster presenter, "New insights into the composition and catalytic performance of VO_x-Ga/γ-Al_2O_3 for the oxidative dehydrogenation of propane to propene", **National Science Day**, CSIR-NCL, Pune, 2020.
- Poster presenter, "A highly efficient and reusable Ru-NaY catalyst for the base free oxidation of 5-hydroxymethylfurfural to 2,5-furandicarboxylic acid", **International Conference on Recent Trends in Catalysis (RTC 2020)**, NIT Calicut, Kerala, 2020.

Applied Catalysis A: General 525 (2016) 237–246

Contents lists available at ScienceDirect

Applied Catalysis A: General

journal homepage: www.elsevier.com/locate/apcata

Effective and selective oxidation of 2-butanol over Mn supported catalyst systems

Kandasamy Prabu, Marimuthu Prabu, Ashok Kumar Venugopal, Aswathy Thareparambil Venugopalan, W.V.Y. Sai Sandilya, Chinnakonda S. Gopinath, Thirumalaiswamy Raja*

Catalysis Division and PSE division, CSIR-National Chemical Laboratory, Dr. Homi Bhabha Road, Pune- 411 008, India

ARTICLE INFO

Article history:
Received 9 June 2016
Received in revised form 28 July 2016
Accepted 3 August 2016
Available online 4 August 2016

Keywords:
Selective oxidation
2-Butanol
Methyl ethyl ketone
Mn based catalysts

ABSTRACT

Oxidation of alcohols to their corresponding aldehydes/ketones is an important reaction in industries as well as in academic perspective. Selective oxidation (Selox) of alcohols like methanol, ethanol and propanol are well studied in literature; however, alcohols like butanol, pentanol, octanol is a challenging task. Selective oxidation of 2-butanol to methyl ethyl ketone (MEK) is an important reaction due to its wide range of applications. Herein, we demonstrated the selective oxidation of 2-butanol to MEK over Mn supported on different oxide supports. A series of Mn_xO_y-Al_2O_3 (MA), Mn_xO_y-CeO_2 (MC), Mn_xO_y-ZrO_2 (MZ) and Mn_xO_y-SiO_2 (MS) catalysts were prepared by co-precipitation followed by hydrothermal method. As synthesised catalysts were characterised by various physico-chemical characterisation techniques. It was found that the presence of Mn_3O_4 species in MA and MZ catalysts is responsible for maximum catalytic activity towards 2-butanol oxidation. MA catalyst conferred a maximum 2-butanol conversion of 51% and 88% selectivity towards MEK. XPS analysis revealed that Mn in MA catalyst exists in +2 and +3 oxidation states and responsible for 2-butanol oxidation. Moreover it was found that the acidity of the catalyst also plays an important role in catalytic activity.

1. Introduction

Oxidation of alcohols to their corresponding aldehydes/ketones is one of the important processes in chemical industries, as well as in academia, for the production of value added chemicals. Conventionally, aldehydes/ketones were prepared by the oxidation of alcohols using stoichiometric amount of oxidants, such as salts of permanganates [1], chromates [2,3] and bromates [4]. Due to the generation of enormous quantity of metal wastes, conventional methods are replaced by catalytic method for the production of aldehydes/ketones. In homogeneous catalytic method, high catalytic activity towards desired product was achieved; however, it has a major drawback in separation and reuse of the catalysts. To overcome these difficulties, heterogeneous catalytic method was used. It plays a vital role in separation and reuse of the catalysts; but the challenging task was the synthesis of catalysts with high selectivity towards desired products. Preparing high active catalysts and selective towards desired products with sustainability is an interesting area of research in heterogeneous catalysis. Hence, it provides further details about the physical and chemical properties of the catalysts.

Alcohols such as methanol, ethanol, propanol and butanol are the raw materials for the production of renewable and sustainable energy sources [5]. Compared to lower carbon chain alcohols such as methanol, ethanol and propanol, butanol shows less hygroscopic, high energy density, low vapor pressure, and low affinity to water [6–9]. *n*-Butanol is one of the promising biofuels, which has received much attention due to its renewability over other biofuels [5]. Methyl ethyl ketone (2-butanone) (MEK) is one of the important products, which has wide spectrum of applications in industries. Commercially, MEK is produced by dehydrogenation of 2-butanol using copper, zinc catalysts but it requires harsh reaction conditions [10,11]. There are some other processes examined for the production of MEK such as oxidation of 2-butene [12] and oxidation of isobutyl benzene [13]; however, these processes are not commercialized. Owing to its less impact to environment and mild reaction conditions, oxidation of 2-butanol using an oxidant is an alternative method for production of MEK. In such a process alternative oxi-

* Corresponding author at: Catalysis Division, CSIR-National Chemical Laboratory, Dr. Homi Bhabha Road, Pune- 411 008, Maharashtra, India.
** Corresponding author.
E-mail addresses: t.raja@ncl.res.in, traja58@gmail.com (T. Raja).

http://dx.doi.org/10.1016/j.apcata.2016.08.005
0926-860X/

dant gases are like air, CO_2, O_2 and N_2O is co-fed to oxidize butanol to 2-butanone. There are seldom a few reports for the production of MEK using above said oxidants. Mistry et al. reported that catalytic activity of 2-butanol oxidation depends upon the morphology of 'Pt' nanoparticles supported on γ-Al_2O_3 [13]. Mapa et al. employed a solid solution of ZnO and InN for selective oxidation of 2-butanol to MEK, but at high temperatures between 350 and 450 °C [14]. Hou et al. reported that liquid phase oxidation of 2-butanol using oxygen as oxidant over Au:Pd bimetallic nanoparticles shows higher selectivity towards 2-butanone at 60 °C [15]. Several d-block metals like Pt, Ru, Rh, Au, Co, Ni, Ag and Ir [16,17] were tested as catalysts for oxidation of alcohols in liquid [17] as well as in gas phase [16] reactions.

In many oxidation reactions metals like V, Cr, and Mn were used due to their redox properties, oxygen storage capacity, etc. [18–20]. Apart from redox properties, certain ratio of different oxidation states in such metals can alter the catalytic activity. Mn supported catalysts were used in many field of research due to its redox properties. Controlling an active oxidation state in Mn-based materials is a challenging task in heterogeneous catalysis. In this paper we stabilized and maintained the oxidation states of Mn during the selective oxidation of 2-butanol. In eletrocatalytic [21]. and photocatalytic [22] reactions, Mn-based mixed oxide catalysts showed better catalytic activity with suitable supports in many reactions. In this work, manganese oxide on Al_2O_3, CeO_2, ZrO_2 and SiO_2 mixed oxide catalysts were prepared by co-precipitation and sol-gel methods. Catalysts which has certain ratio of Mn^{+2}/Mn^{+3} shows better catalytic activity towards oxidation of 2-butanol. This reaction was performed in fixed bed reactor (FBR) system and characterized by several techniques. Powder X-ray diffraction (PXRD), Raman spectroscopy, N_2 adsorption desorption, temperature programmed desorption (NH_3-TPD), transmission electron microscopy (TEM) confirmed the structural and textural properties. Presence of different oxidation states in the active catalyst was confirmed by X-ray photoelectron spectroscopy (XPS). Maximum conversion of 51% and 88% selectivity towards MEK was achieved by Mn_xO_y-Al_2O_3 catalyst over 12 h. By using surface characterization techniques, surface species on the catalysts were confirmed.

2. Experimental

2.1. Catalyst synthesis

All the chemicals used to synthesize catalyst were of reagent grade. Manganese (II) nitrate ($Mn(NO_3)_2{\cdot}4H_2O$, 98%), aluminium (III) nitrate ($Al(NO_3)_3{\cdot}9H_2O$, ≥95%), cerium (III) nitrate ($Ce(NO_3)_3{\cdot}6H_2O$, 99.5%), zirconyl (IV) nitrate ($ZrO(NO_3)_2{\cdot}H_2O$), TEOS ($Si(OC_2H_5)_2$, 98%), sodium hydroxide (NaOH, 98%), ethanol (C_2H_5OH) and hydrochloric acid (HCl) were used as precursors for catalyst synthesis. All the chemicals were purchased from Alfa Aesar and Merck.

2.2. Hydrothermal method

Mn supported catalysts were synthesized by co-precipitation followed by hydrothermal method [23].The procedure is as follows: Metal nitrates precursors (Mn^{2+}, Al^{3+}, Ce^{3+}, Zr^{4+}) were dissolved in water and precipitating agent (NaOH) were added simultaneously drop wise at constant pH (9.5 ± 0.2). The solution was transferred into a teflon lined autoclave for hydrothermal synthesis kept at 150 °C for 12 h. Then the solid was filtered, washed and dried at 110 °C for overnight followed by calcination at 450 °C for 6 h in air. As-synthesized Mn_xO_y-Al_2O_3, Mn_xO_y-CeO_2 and Mn_xO_y-ZrO_2 catalyst were labelled as MA, MC and MZ, respectively.

2.3. Sol-gel method

Mn supported SiO_2 catalyst was synthesized by sol-gel method [24]. Mn $(NO_3)_2{\cdot}4H_2O$ and TEOS was diluted using ethanol and the solution was stirred at room temperature to get homogeneous clear solution. Half of the alcohol was used for this and another half was used to dilute the water and acid. The mixed solution of EtOH-H_2O-HCl was added drop wise to the above Mn-TEOS-EtOH solution with constant stirring. After complete addition, the solution was stirred at 40 °C for 12 h. Then the solution was dried at 110 °C for overnight and calcined at 450 °C for 6 h in presence of air. Finally, Mn_xO_y-SiO_2 catalyst was labelled as MS.

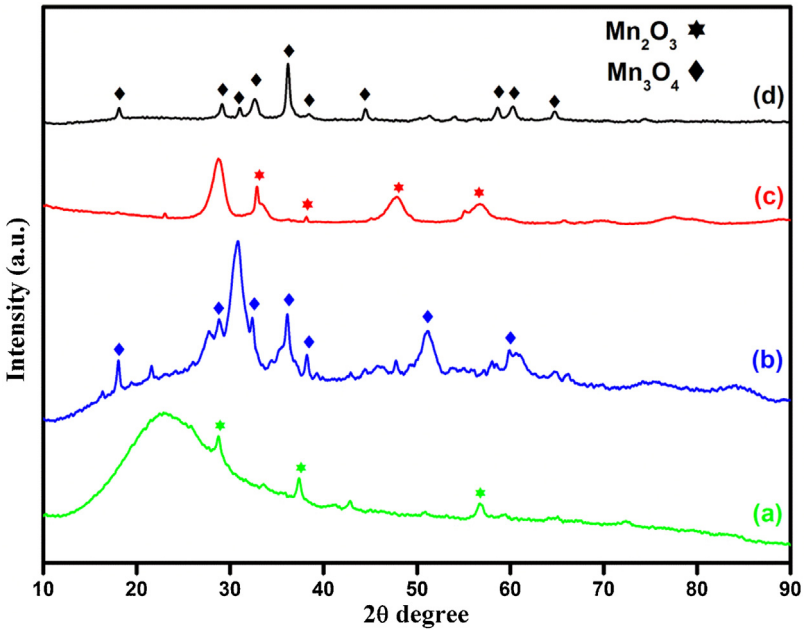

Fig. 1. Powder X-ray diffraction pattern of as-calcined Mn containing mixed oxide catalysts (a) Mn_xO_y-SiO_2, (b) Mn_xO_y-ZrO_2, (c) Mn_xO_y-CeO_2, and (d) Mn_xO_y-Al_2O_3.

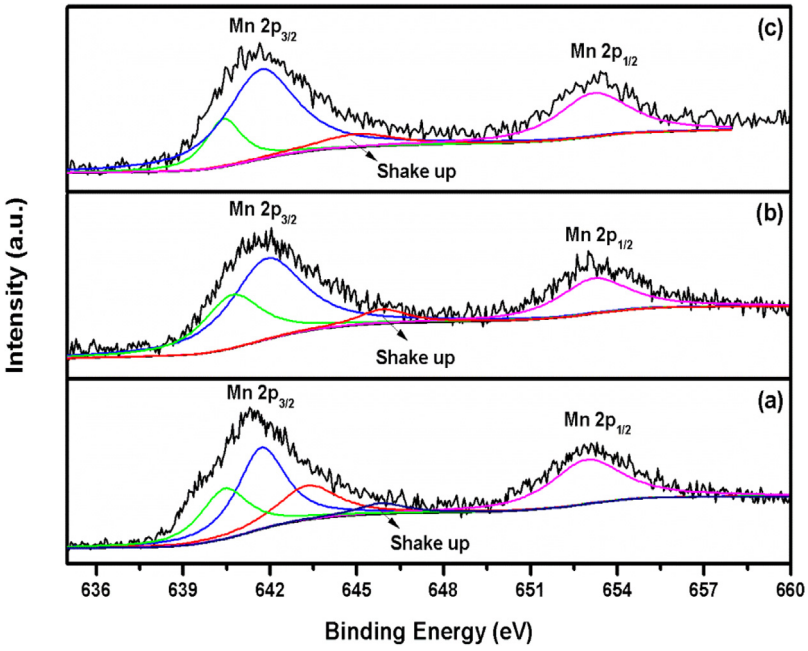

Fig. 2. XPS spectra of Mn 2p core levels for (a) manganese oxide, (b) fresh-Mn_xO_y-Al_2O_3 and (c) used-Mn_xO_y-Al_2O_3.

Table 1
Textural properties of as-synthesised catalysts calcined in air at 450 °C.

S.No	Catalysts	Surface area (m^2/g)[a]	Total pore volume (cc/g)[b]	Crystallite size (nm)[c]
1	Mn_xO_y-Al_2O_3	84	0.32	24.7 ± 1.0
2	Mn_xO_y-CeO_2	89	0.18	5.5 ± 1.0
3	Mn_xO_y-ZrO_2	103	0.20	4.6 ± 1.0
4	Mn_xO_y-SiO_2	339	0.25	19.8 ± 1.0

[a] Calculated from BET surface area analysis.
[b] Obtain from BJH analysis.
[c] Calculated from PXRD by using Scherer formula.

2.4. Characterization

PXRD pattern of synthesized catalysts were collected by PANanalyticalX'pert Pro dual goniometer diffractometer at a step size of 0.008° and a scan rate of 0.5° min^{-1}. X-ray was generated by using Cu Kα (1.5418 Å) with Ni filter and the flat holder in Bragg–Brentango geometry used for data collection. Autosorb 1C Quantachrome USA was used to collect Nitrogen adsorption/desorption isotherms for the catalysts. The surface area from the adsorption branch was calculated by using Brunauer–Emmett–Teller (BET) equation. High resolution transmission electron microscopy (HRTEM) of all catalysts was recorded by FEI TECNAI F30 electron microscope operating at 300 kV. Samples were prepared by dispersion powder catalysts in isopropanol before depositing onto a holey carbon grid. Raman spectra were recorded on a Horiba JY LabRAMHR800 Raman spectrometer coupled with microscope in reflectance mode with 514 nm excitation laser sources and a spectral resolution of 0.3 cm^{-1}. Oxidation states of manganese and aluminium was studied by ambient pressure photoelectron spectrometer (APPES) [25]. X-ray was produced by using Mg Kα with the energy of 1253.6 eV.

2.5. Catalytic activity

The activity of the catalyst was performed in fixed bed continuous down flow reactor (FBR) over a temperature range of 200–350 °C atmospheric pressure. 1 ml catalyst was loaded at the centre of Inconel reactor (13 mm × 510 mm), packed with ceramic beads on either sides of the catalyst bed. Temperatures of the catalyst bed were measured by k-type thermocouple. 2-Butanol and oxygen feed flow were monitored by using isocratic pump (Lab Alliance series II) and Brook's Mass flow controllers (5850 series) respectively. The volume of the gaseous products was measured by a wet gas flow meter (Ritter Drum-Type Gas Meter). The reaction liquid products were condensed and analysed by Agilent 6890N gas chromatography (FID) with HP-5 (5.5% phenyl methyl siloxane) column and gaseous products were analysed by customised Thermo Fisher 1110 GC with (Molecular Sieve) TCD detectors.

3. Results and discussion

3.1. Powder x-ray diffraction

PXRD is one of the primary techniques which offer the detailed information about catalyst nature and structure. Fig. 1 shows the PXRD pattern of as-calcined MA, MZ, MC and MS catalysts. It is clearly seen from Fig. 1(a), MS mixed oxide catalyst shows the presence of SiO_2 phase at 21° and manganese oxide in the form of Mn_2O_3 phase which matches with JCPDS No.78-0390. MZ mixed oxide catalyst shows peaks at 18°, 28°, 32°, 36°, 38°, 50° and 60° correspond to Mn_3O_4 (JCPDS No.24-0734). In MC mixed oxide catalyst, a high intensity peak at around 28° corresponds to ceria (JCPDS No. 75-0151) and the other peaks correspond to Mn_2O_3 phase (JCPDS No.78-0390) which reveals that manganese is well dispersed in ceria. Fig. 1(d) shows MA mixed oxide catalyst, which offer information about presence of Mn_3O_4 phase. The presence of active

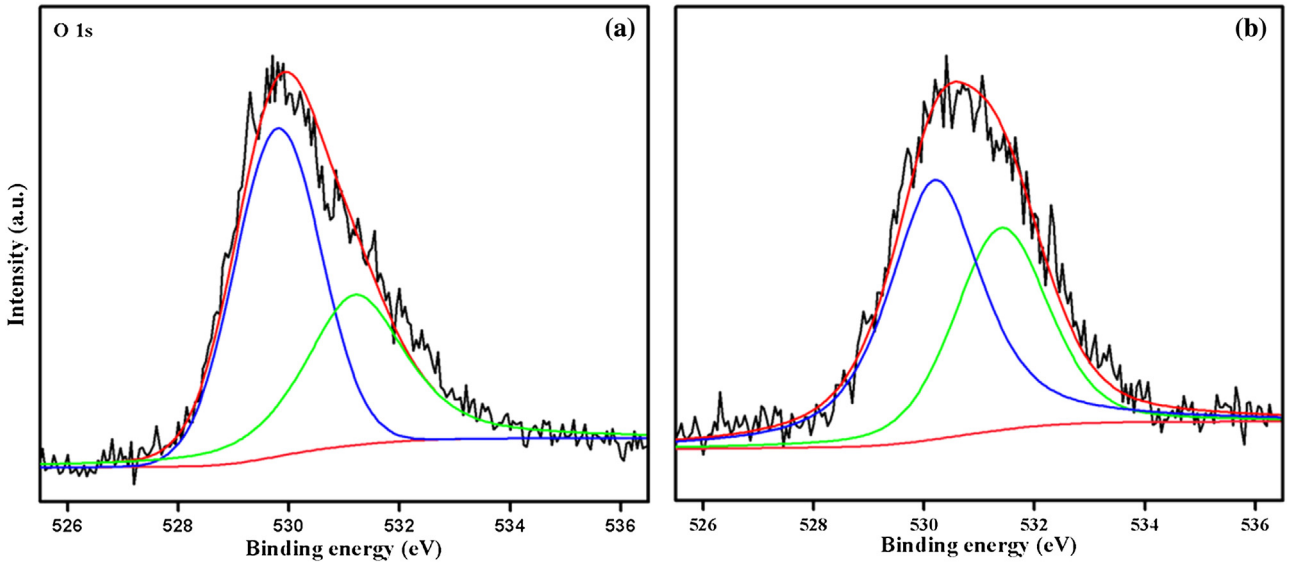

Fig. 3. XPS spectra of O 1s (a) fresh-Mn_xO_y-Al_2O_3 and (b) used-Mn_xO_y-Al_2O_3.

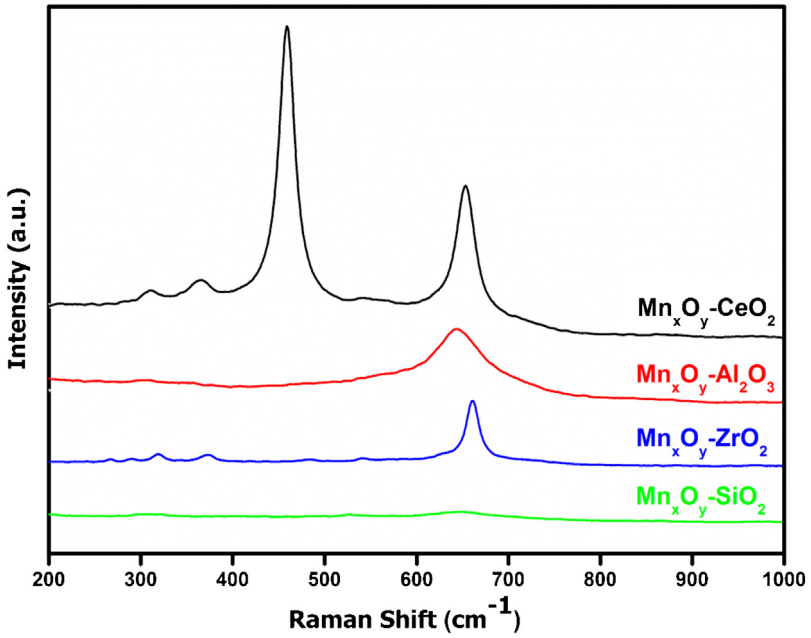

Fig. 4. Raman spectrum of all as-synthesized catalysts calcined in air at 450 °C.

sites in MA mixed oxide catalyst reveals that dispersion of manganese oxide in alumina is very well than other catalysts. Presence of Mn_3O_4 phase was further confirmed by JCPDS data -24-0734.

3.2. Surface area

Catalytic activity of the reaction depends upon different parameters, one of important parameter is BET surface area. All the as-synthesized catalysts were analysed by N_2-adsorption desorption isotherms. Table 1. provides the details about textural properties of as-synthesized catalysts. Surface area of manganese containing mixed oxide catalysts increased in the order, MnxOy-Al_2O_3 < Mn_xO_y-CeO_2 < Mn_xO_y-ZrO_2 < Mn_xO_y-SiO_2 respectively. Mn_xO_y-Al_2O_3 mixed oxide catalyst shows the lowest surface area (84 m^2/g) compared to other catalysts due to be bigger crystallite size [26]. Mn_xO_y-SiO_2 mixed oxide catalyst exhibit the highest surface area in comparison with other catalysts (339 m^2/g). High surface area of Mn_xO_y-SiO_2 catalyst is due to SiO_2 support, where SiO_2 support shows 369 m^2/g surface area which decreases to 339 m^2/g after Mn was incorporated.

Mn_xO_y-CeO_2 and Mn_xO_y-ZrO_2 catalysts showed 89 and 103 m^2/g surface area respectively. Both catalysts showed near 5 ± 1.0 nm crystallite size. Compared to other catalysts, Mn_xO_y-Al_2O_3 showed high pore volume (0.32 cc/g) and this may be the one of the reasons for the maximum catalytic activity of 2-butanol.

3.3. X-ray photoelectron spectroscopy (XPS)

To explore the chemical composition of the catalyst surface and the oxidation state of the elements, XPS was used. Fig. 2 shows XPS spectra of Mn 2p core level of pure manganese oxide, fresh and used Mn_xO_y-Al_2O_3 catalysts. XPS spectra of Mn containing mixed

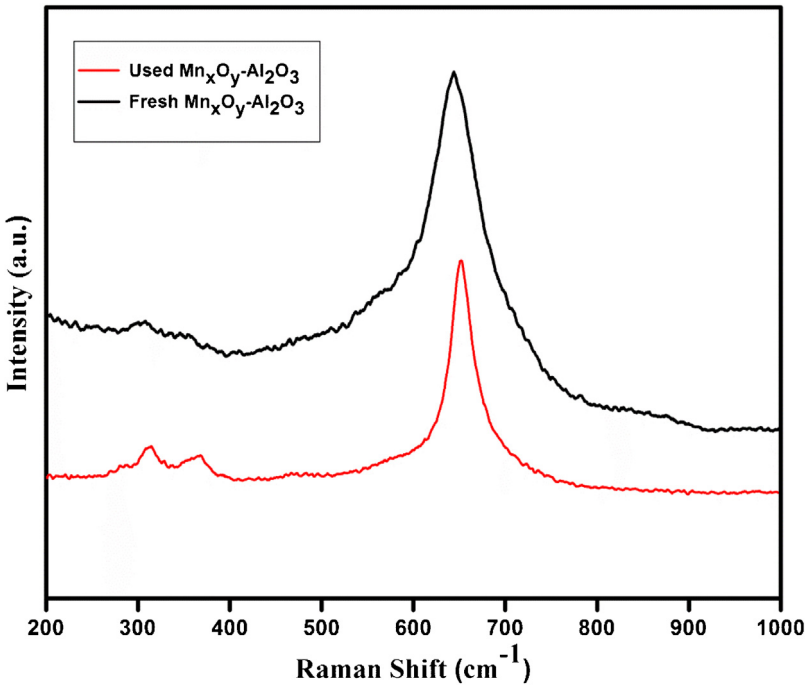

Fig. 5. Raman spectrum of fresh and used Mn_xO_y-Al_2O_3 catalysts.

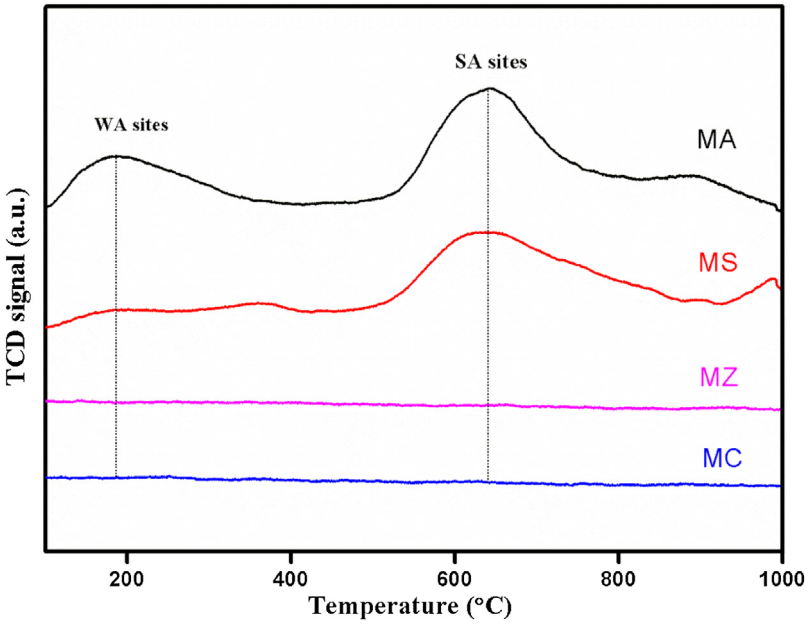

Fig. 6. NH_3-temperature programmed desorption profile of as-synthesised catalysts calcined in air at 450 °C.

oxide and pure manganese oxide catalysts reveal the information about active species on the surface and oxidation states of manganese oxide. XPS was recorded to know about surface chemical composition of manganese oxide in Mn containing mixed oxide catalysts. Multiple peaks corresponding to Mn^{+2}, Mn^{+3} and Mn^{+4} were observed which was deconvoluted by peak fitting method with Shirley background removal in Mn 2p core level spectrum. Mn $2p_{3/2}$ deconvolution shows three peaks at 640.4, 641.7 and 643.3 eV binding energy which corresponds to Mn(II), Mn(III) and Mn(IV) respectively [27]. It clearly shows that manganese in pure manganese oxide has multiple oxidation states. Fig. 2(b) shows the XPS spectra of Mn $2p_{3/2}$ core level for fresh Mn_xO_y-Al_2O_3 catalyst at 641.7 eV [27,28]. The peaks at 640.4 and 641.7 eV clearly indicate the presence of Mn in Mn^{+2} and Mn^{+3}oxidation states. This satellite structure, noticeable on the higher binding energy of Mn $2p_{3/2}$ core-level in the XPS spectrum of the manganese compounds originates from the charge transfer from oxygen ligand to unfilled 3d orbital of Mn during the final state of photoelectron emission process [29]. It is further confirmed that fresh Mn_xO_y-Al_2O_3 catalyst shows both Mn^{+2} and Mn^{+3}oxidation states. The catalytic activity of M_xO_y-Al_2O_3 catalyst was evaluated for 2-butanol oxidation, and it shows maximum conversion (51%) and selectivity (88%) than other tested catalysts. To study the surface chemical composition of the catalyst, the spent Mn_xO_y-Al_2O_3 catalyst was analysed by XPS measurement. Spent catalyst analysis reveals the presence of peaks at

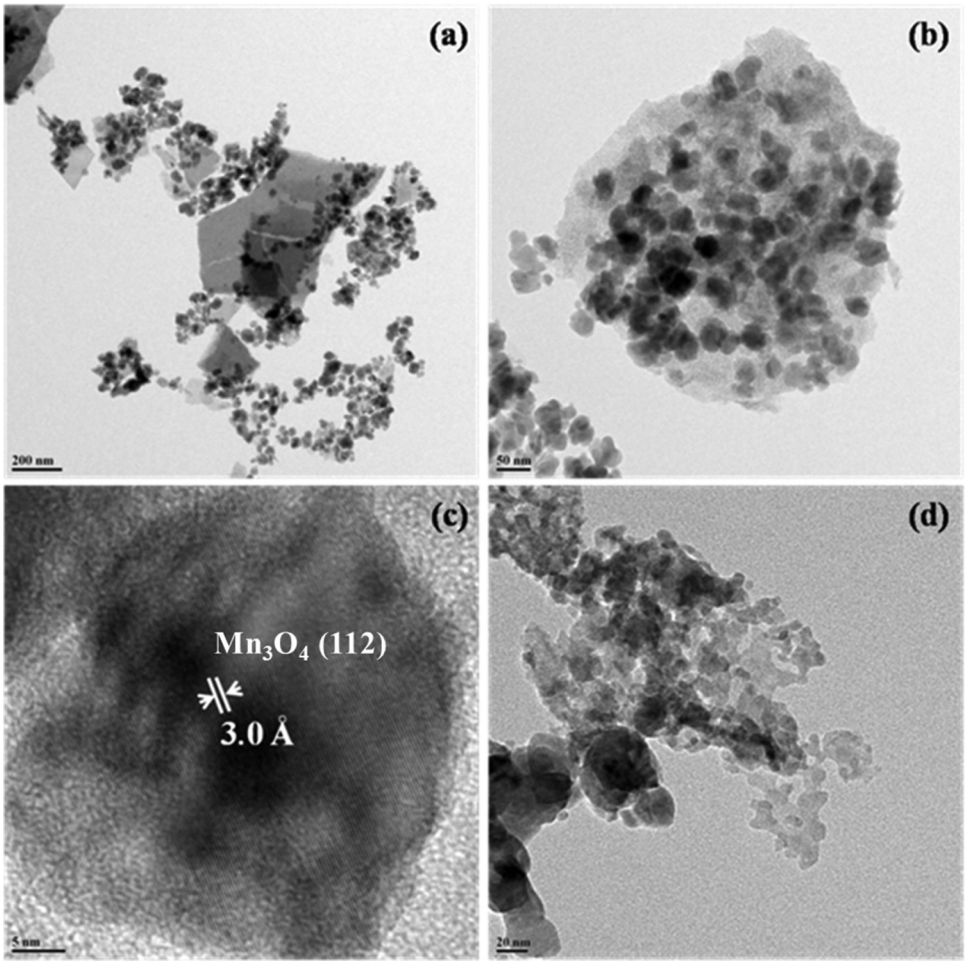

Fig. 7. TEM images of Mn_xO_y-Al_2O_3 fresh and spent catalyst (a–c) fresh Mn_xO_y-Al_2O_3 and (d) spent Mn_xO_y-Al_2O_3.

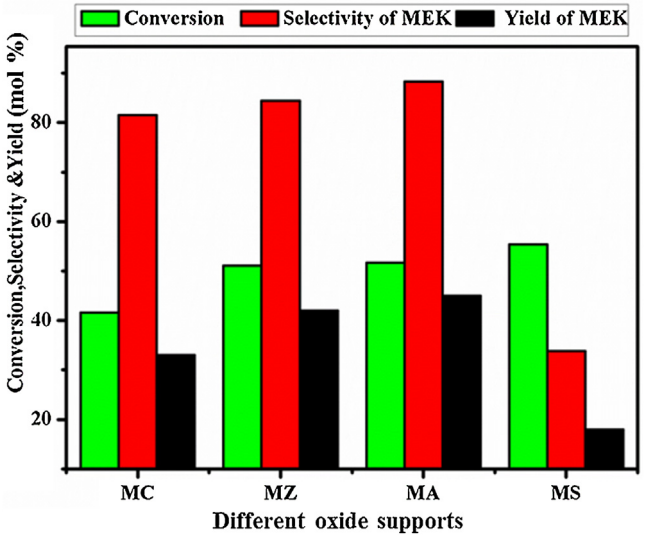

Fig. 8. Conversion of 2-butanol and selectivity of MEK at different Mn supported catalysts reaction conditions: 300 °C, LHSV 1.8 h^{-1} with respect to 2-butanol and GHSV 1200 h^{-1} with respect to oxygen at atmosphere pressure.

640.4 and 641.7 eV proving that there is no significant change in the catalyst after reaction. It is also confirmed that the catalyst possess stable oxidation state even after 12 h on time on stream under optimum reaction conditions (Fig. 3).

O 1s spectra of all fresh and used MA catalyst were recorded. Fresh Mn_xO_y-Al_2O_3 catalyst showed peaks around 530, and 531.5 eV corresponds to lattice oxygen, surface hydroxyl species [30,31]. On the surface of spent catalyst, presence of lattice oxygen and surface hydroxyl species was confirmed by peaks at 530 and 531.5 eV respectively. Catalytic activity of Mn_xO_y-Al_2O_3 catalyst showed maximum yield due to surface oxygen species which favours selective oxidation of 2-butanol. In spent catalyst O 1s spectrum, it is clear that the intensity of surface oxygen species is more which confirms the role of these species.

3.4. Raman spectroscopy

Fig. 4 shows the Raman spectral data of Mn_xO_y-Al_2O_3, Mn_xO_y-CeO_2, Mn_xO_y-ZrO_2 and Mn_xO_y-SiO_2 catalysts. Raman spectroscopy provides detailed information about vibration modes of catalysts/materials. Characteristic peaks for Mn_xO_y-ZrO_2 catalyst is in the range of 300–700 cm^{-1}. High intensity peak is at 660 cm^{-1} and two small intensity peaks at 317 and 372 cm^{-1}corresponds to Mn_3O_4. These characteristic Raman bands support the results obtained in PXRD. In Mn_xO_y-Al_2O_3 catalyst presence of broad peak at 645 cm^{-1} corresponds to Mn_3O_4 [32].The characteristic Raman band at 630 and 680 cm^{-1} is not seen which confirms that there is no formation of Mn_2O_3. There was no characteristic peaks observed for Mn_xO_y-SiO_2 catalyst. Mn_xO_y-CeO_2 catalyst showed four characteristic peaks in the range of 300–700 cm^{-1}. The high intensity peak at 457 cm^{-1} corresponds to vibration mode of cubic fluorite

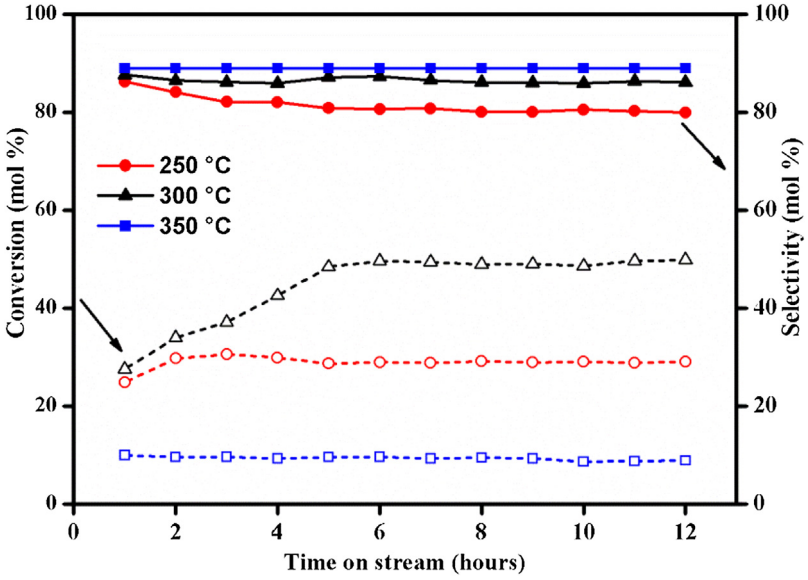

Fig. 9. Conversion of 2-butanol and selectivity of MEK at various reaction temperatures over MA. Reaction conditions: LHSV 1.8 h^{-1} with respect to 2-butanol and GHSV 1200 h^{-1} with respect to oxygen at atmosphere pressure.

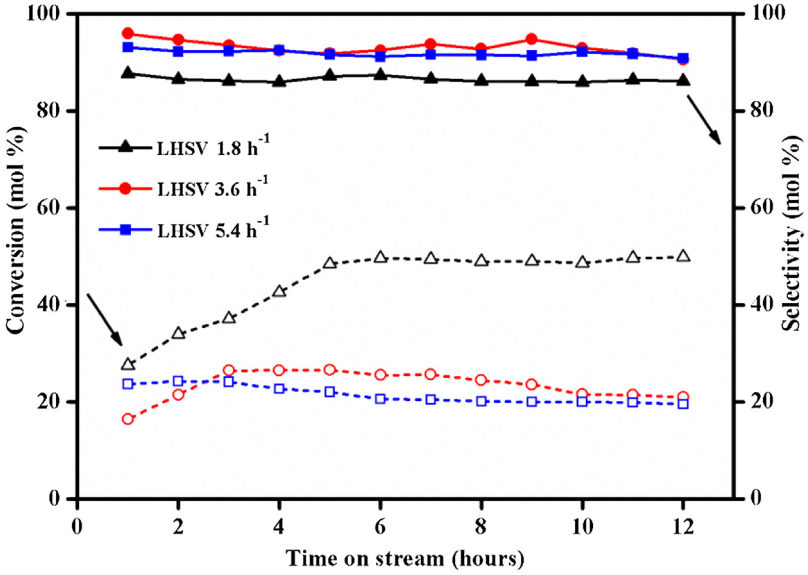

Fig. 10. Conversion of 2-butanol and selectivity of MEK at various 2-butanol flow rates over MA. Reaction conditions: 300 °C, GHSV 1200 h^{-1} with respect to oxygen at atmosphere pressure.

(F_{2g}) CeO_2 lattice [33,34] and other peaks corresponds to Mn(III)-O and Mn(IV)-O bonds (Fig. 5).

Used Mn_xO_y-Al_2O_3 was analysed to observe the nature of catalyst after reaction and to see what type of coke is formed during reaction. The Raman characteristic peaks of used-Mn_xO_y-Al_2O_3 catalyst was compared with fresh Mn_xO_y-Al_2O_3 catalyst, noticeably strong vibration band at 650 cm^{-1} which corresponds to Mn_3O_4 and smaller band at 313 and 367 cm^{-1} corresponds to high surface area manganese oxide were observed [35]. No peaks corresponding to D and G bands [36] were observed which suggests that there is no graphitic coke formation after long time on stream (12 and 30 h) reaction conditions.

3.5. Temperature programmed desorption (NH_3-TPD)

Acidity is one of the parameter which plays an important role in the catalytic activity of 2-butanol oxidation. To find the acidity of the catalysts, NH_3-temperature programmed desorption was carried out for all calcined catalysts and the results are given in Fig. 6. Mn_xO_y-CeO_2 and Mn_xO_y-ZrO_2 catalysts showed no peaks which confirmed that both the catalysts has no acidity. In Mn_xO_y-SiO_2 catalyst the peak at 650 °C corresponds to strong acidic centres and very little amount of weak acid sites (200–300 °C) from the SiO_2 were also observed. Mn_xO_y-Al_2O_3 catalyst showed two major peaks in which the peak observed at lower temperature (~200 °C) is due to weak acidic centres present in the catalyst and peak observed at a higher temperature (~650 °C) is due to strong acid site. MA exhibits more number of weak as well as strong acid sites in comparison to MS emphasizes that the former possess more acidic centres. This important feature associated with MA helps in enhancing the catalytic activity of MA catalyst, which showed maximum and stable catalytic activity over a period of 30 h.

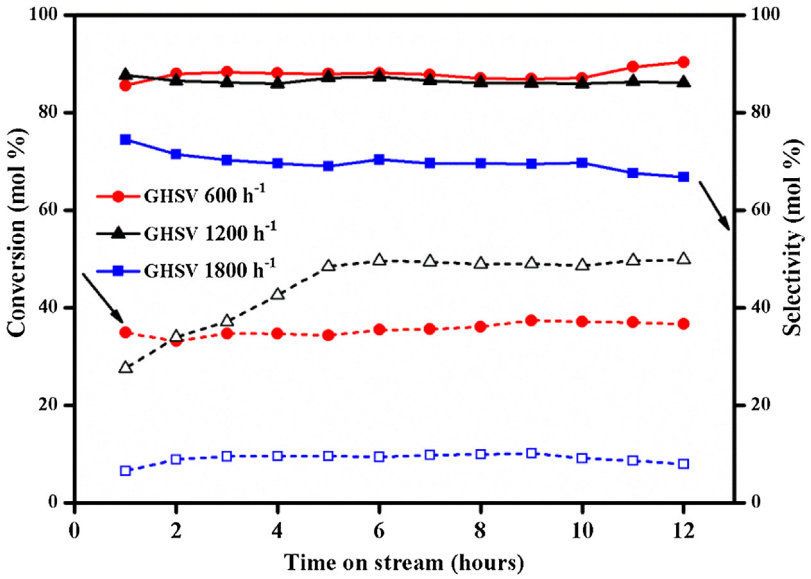

Fig. 11. Conversion of 2-butanol and selectivity of MEK at different oxygen flow rates over MA. Reaction conditions: 300 °C, LHSV 1.8 h^{-1} with respect to 2-butanol at atmosphere pressure.

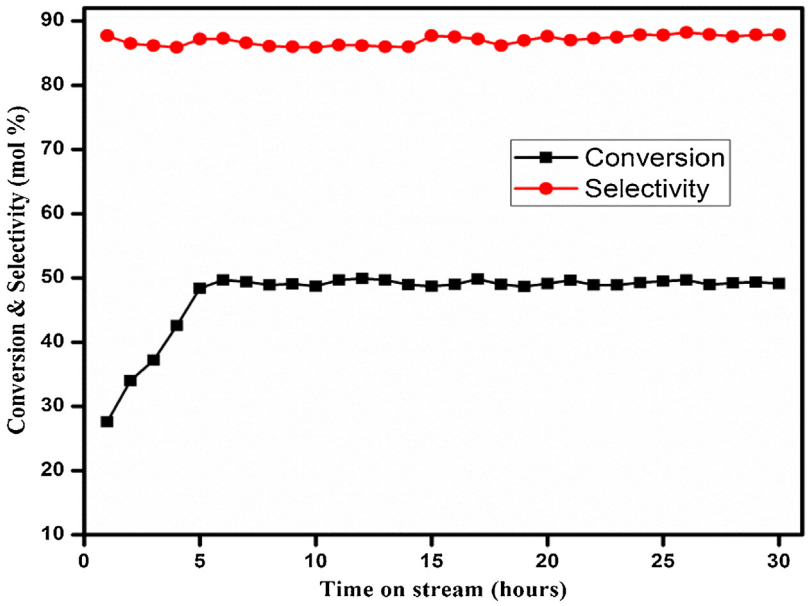

Fig. 12. 30 h TOS study using MA catalyst. Reaction conditions: 300 °C, LHSV 1.8 h^{-1} with respect to 2-butanol and GHSV 1200 h^{-1} with respect to oxygen at atmosphere pressure.

Table 2
Catalytic activity of Mn_xO_y loaded on different supports.

S. No.	Catalysts	Conversion of 2-butanol (mol%)[a]	Selectivity (mol%)				Yield of MEK (mol%)
			MEK	Acetone	CH_3OH	CO_x[b]	
1	Mn_xO_y/CeO_2	41	81	12	02	05	35
2	Mn_xO_y/ZrO_2	51	84	08	07	01	42
3	Mn_xO_y/Al_2O_3	51	88	05	05	02	45
4	Mn_xO_y/SiO_2	55	33	17	14	36	18

[a] Conversion at steady state. Reaction conditions: 300 °C, LHSV 1.8 h^{-1} with respect to 2-butanol and GHSV 1200 h^{-1} with respect to oxygen at atmosphere pressure.
[b] CO and CO_2.

3.6. Transmission electron microscopy (TEM)

Fig. 7. shows the TEM images of fresh and used Mn_xO_y-Al_2O_3 catalyst. TEM images reveal the information about the morphology and lattice of the catalysts. Fig. 7(a)–(c) displays TEM images of fresh Mn_xO_y-Al_2O_3 catalyst in low and high resolutions, respectively. Fig. 7(a) and (b) TEM images clearly confirmed the dispersion of manganese oxide on Al_2O_3. Indeed, a nice decoration of alu-

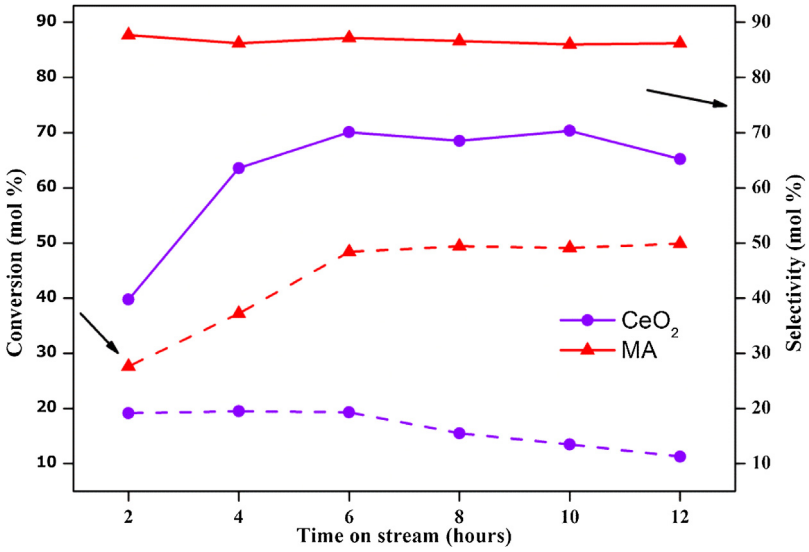

Fig. 13. Conversion of 2-butanol and selectivity of MEK for (i) MA (ii) CeO_2. Reaction conditions: 300 °C, LHSV 1.8 h^{-1} with respect to 2-butanol and GHSV 1200 h^{-1} with respect to oxygen at atmosphere pressure.

mina by nano Mn_xO_y has been directly demonstrated from the TEM results. The d-spacing value of Mn_xO_y-Al_2O_3 catalyst is 3.0 Å which is in agreement with the value obtained from PXRD results. Used Mn_xO_y-Al_2O_3 catalysts TEM image (Fig. 7(d)) shows a thin layer of coke deposited on the surface of the catalyst and there was no other changes in the morphology of the catalyst. Highly dispersed manganese oxide on Al_2O_3 showed maximum yield on 2-butanol oxidation using molecular oxygen.

3.7. Effect of supports

Support has an important role in any catalytic activity of a reaction. Choosing a suitable support is a critical part in heterogeneous catalysis. To study the influence of the support for 2-butanol to MEK reaction, manganese oxide catalyst was loaded on four different supports. Manganese oxide on Al_2O_3, CeO_2, ZrO_2 and SiO_2 mixed oxide catalysts were subjected to oxidation of 2-butanol at optimized reaction conditions and the results are given in Fig. 8 and Table 2. MC catalyst shows maximum 2-butanol conversion and MEK selectivity of 41 and 81%, respectively. MS catalyst shows better conversion (54%), but selectivity towards MEK is very low due to complete oxidation of 2-butanol to undesired products. Minimum selectivity (33%) towards MEK was observed with MS catalyst. MA and MZ catalysts shows about 50% conversion and 88% selectivity towards MEK. MA and MZ catalysts show similar pattern up to certain time on stream. However after certain time on stream, MA catalyst shows slight increase in catalytic activity but in MZ the catalyst activity decreases at the end of 12 h. This decrease in catalytic activity may be due to coke formation which might block the catalytic active centres. MA catalysts shows better activity than other tested catalysts. There is no conversion of 2-butanol to MEK was observed over alumina, which confirms that bare alumina is not active for 2-butanol oxidation. 2-butanol conversion on MA increases dramatically to 51%. MA shows high conversion as well as yield of MEK, which is attributed to synergistic effect of manganese and alumina. Conversion of 2-butanol and yield towards MEK is stable up to 30 h. Catalytic activity of 2-butanol is further carried out using MA catalyst for optimization of different parameters.

3.8. Effect of temperature

Temperature is one of the main important factors which affect the catalytic activity. To examine the influence of temperature, oxidation of 2-butanol was carried out at three different temperatures ranging from 250, 300–350 °C in FBR and the results are shown in Fig. 9. Oxidation of 2-butanol was carried out at LHSV = 1.8 h^{-1} with respect to 2-butanol, and GHSV = 1200 h^{-1} with respect to oxygen at atmospheric pressure. At low temperature (250 °C), conversion towards 2-butanol and selectivity towards MEK was observed to be 30 and 80%, respectively. Further increase in temperature to 300 °C, conversion and selectivity increased to 51 and 88% respectively and remains constant for 30 h time on stream. At the high temperature (350 °C), very less conversion but high selectivity (90%) towards MEK was observed, which is higher than other two temperatures. Decrease in conversion and yield may be due to complete oxidation of 2-butanol to undesired products like CO_x, methanol, acetone and water at higher temperature. An appropriate and suitable reaction condition was always required for partial oxidation. At 300 °C maximum conversion and selectivity was observed due to appropriate temperature and active centres to activate the reactants. Maximum catalytic activity was observed at 300 °C and it is optimised for oxidation of 2-butanol.

3.9. Effect of 2-butanol flow

To study the effect of contact time between reactants and catalytic active centres, reaction was performed at different 2-butanol flow and the results are shown in Fig. 10. Oxidation was carried out at three different 2-butanol flow (LHSV 1.8, 3.6 and 5.4 h^{-1} with respect to 2-butanol), at 300 °C, GHSV = 1200 h^{-1} respect to oxygen at atmospheric pressure. At LHSV 1.8 h^{-1}, 51% conversion of 2-butanol was observed with maximum selectivity (88%) of MEK. At this flow, 2-butanol has optimum contact time to react with adsorbed oxygen on the surface of the catalyst. While increasing the 2-butanol flow to LHSV 3.6 h^{-1} conversion of 2-butanol was decreased to 26% but the selectivity of MEK was increased to 90%. At LHSV 5.4 h^{-1} conversion as well as selectivity decreased to 20 and 89%, respectively. Due to decreasing contact time between reactants and active centres a decrease in yield was observed at higher LHSV of 2-butanol viz. 3.6 and 5.4 h^{-1}. The maximum conversion of 2-butanol (51%) and selectivity towards MEK (88%) was obtained at appropriate flow rate (LHSV 1.8 h^{-1}), which favours selective oxidation.

3.10. Effect of oxygen flow

To understand the effect of oxidant on catalytic activity, this reaction was carried out at three different molecular oxygen flows and the results are shown in Fig. 11. In any oxidation reaction, the change in catalytic activity depends upon the flow of oxidants. In this work, reaction was carried with three different oxygen flow rates (GHSV 600, 1200 and 1800 h^{-1}). At GHSV = 600 h^{-1} the conversion towards 2-butanol was 35%, and 70% MEK selectivity was observed. Further increase in oxidant flow to GHSV = 1200 h^{-1} conversion attained the maximum (51%) and selectivity (88%) which favours the partial oxidation of 2-butanol to MEK. Further increase in GHSV to 1800 h^{-1} relatively low conversion and selectivity was obtained which may be due to complete oxidation of 2-butanol to CO_x and undesired side products. Based on the above results GHSV 1200 h^{-1} (O_2) was optimized for oxidation of 2-butanol.

3.11. Catalyst stability and reaction sustainability

To understand the stability and durability of the MA catalyst, the optimization study was carried out with long time on stream (TOS) with optimised reaction parameters. The reaction conditions are GHSV 1.8 h^{-1} with respect to 2-butanol and GHSV 1200 h^{-1} with respect to molecular oxygen at 300 °C .The activity of the catalyst remains same for longer duration (30 h) the result shown in Fig. 12.Gradual increase in catalyst activity in the first few hours under wide variety of reaction conditions demonstrated a change in the nature of the catalyst under reaction conditions towards higher active form for this particular selective oxidation. Both conversion and selectivity linearly increases, till the reaction reaches a steady state. When comparing the oxidation ability of CeO_2 alone as catalyst for this reaction, it gives very less conversion and selectivity (Fig. 13).

4. Conclusion

MA, MC, and MZ catalysts were prepared by co-precipitation followed by hydrothermal method; however, MS was prepared by sol-gel method. All the catalysts were characterized by various analytical techniques like Raman spectroscopy, N_2-adsorption, XPS, TEM and NH_3-TPD. Presence of Mn_3O_4 and Mn_2O_3 phases was revealed by PXRD. Presence of different oxidation states were confirmed by XPS spectra which shows that MA catalyst has Mn^{+2} and Mn^{+3}oxidation states. All the catalysts were subjected to 2-butanol oxidation using molecular oxygen in continuous flow fixed bed reactor. MA catalyst shows maximum catalytic activity of 51% conversion of 2-butanol and 88% selectivity towards MEK. Active centres in the catalysts were confirmed by XPS and Raman spectroscopy. Raman spectroscopy shows the presence of Mn_3O_4 which was correlated with PXRD. Nature of acidity was confirmed by NH_3-TPD. When CeO_2 alone is used as catalyst for this reaction it is less active and deactivates fast. Synergetic effect of appropriate acidity along with active Mn species is responsible for this reaction. Using oxidants like air in oxidation reaction leads to environmental friendly and green reaction. More work is in progress with CO_2 as oxidant for this reaction.

Acknowledgment

TR thanks CSC0125 12 FYP- Network project for funding and KP thanks industry funded SSP294726 project for his fellowship.

References

[1] F.M. Menger, C. Lee, Tetrahedron Lett. 22 (1981) 1655–1656.
[2] K.P.C. Vollhardt, N.E. Schore, Organic Chemistry: Structure and Function, Freeman, New York, 1999, pp. 300.
[3] D.G. Lee, U.A. Spitzer, J. Org. Chem. 35 (1970) 3589–3590.
[4] C.K. Lee, B.-S. Koo, Y.S. Lee, H.K. Cho, K.-J. Lee, Bull. Korean Chem. Soc. 23 (2002) 1667–1670.
[5] J. Zhang, Liangjie Wei, Xingjia Man, Xue Jiang, Yingjia Zhang, Erjiang Hu, Zuohu Huang, Energy Fuels 26 (2012) 3368–3380.
[6] G.A. Nahar, S.S. Madhani, Int. J. Hydrogen Energy 35 (2010) 98–109.
[7] W. Wang, Y. Cao, Int. J. Hydrogen Energy 36 (2011) 2887–2895.
[8] W.J. Wang, Y.Y. Cao, Int. J. Hydrogen Energy 35 (2010) 13280–13289.
[9] P.S. Nigam, A. Singh, Prog. Energy Combust. Sci. 37 (1) (2011) 52–68.
[10] L. Zhenhua, H.U.O. Wenzhou, M.A. Hao, Qiaokai, Chem. Eng. 14 (5) (2006) 676–684.
[11] G. Ertl, H. Knözinger, J. Weitkamp, Handbook of Heterogeneous Catalysis, vol. 5, VCH, Weinheim, Germany, 1997, pp. p2140.
[12] W. Neier, GuenterStrehlke 2-Butanone InUllmann's Encyclopedia of Industrial Chemistry, Wiley-VCH, Weinheim, 2002.
[13] H. Mistry, F. Behafarid, E. Zhou, L.K. Ono, L. Zhang, B. RoldanCuenya, ACS Catal. 4 (1) (2013) 109–115.
[14] M. Maitri, S. Kumarsrinivasan, D.S. Bhange, B. Saha, P. Chakraborty, A.K. Viswanath, C.S. Gopinath, Chem. Mater. 22 (2010) 565–578.
[15] W.B. Hou, N.A. Dehm, R.W.J. Scott, J. Catal. 253 (2008) 22–27.
[16] P. Papaefthimiou, T. Ioannides, X.E. Verykios, Appl. Catal. B 13 (1997) 175–184.
[17] T. Wang, H. Shou, Y. Kou, H.C. Liu, Green Chem. 11 (2009) 562–568.
[18] G. Deo, E. Israel, Wachs J. Catal. 146 (1994) 323–334.
[19] A. Heidarnezhada, Farzad Zamani, Catal. Commun. 60 (2014) 105–109.
[20] A.J. Dubey, S.K. Kolekar, C.S. Gopinath, ChemCatChem 8 (2016) 2296–2306.
[21] Fabio H.B. Lima, Marcelo L. Calegaro, Edson A. Ticianelli, Electrochim. Acta 52 (2007) 3732–3738.
[22] Yan Ma, Yuanzhi Li, Ming yang Mao, Jingtao Hou, Min Zeng, Xiujian Zhao, J. Mater. Chem. A 3 (2015) 5509.
[23] A.K. Venugopal, A.T. Venugopalan, P. Kaliyappan, T. Raja, Green Chem. 15 (2013) 3259–3267.
[24] Kanichikamiya, Toshinobu Yoko, J. Mater. Sci. 21 (1986) 842–848.
[25] K. Roy, C.P. Vinod, C.S. Gopinath, J. Phys. Chem. C 117 (2013) 4717–4726.
[26] P. Kaliyappan, A.T. Venugopalan, A.K. Venugopal, M. Marimuthu, R. Shukla, A.K. Tyagi, T. Raja, RSC Adv. 5 (2015) 3619.
[27] S. Bag, K. Roy, C.S. Gopinath, C. Retna Raj, ACS Appl. Mater. Interfaces 6 (2014) 2692–2699.
[28] J. Pal, C. Mondal, A.K. Sasmal, M. Ganguly, Y. Negishi, T. Pal, ACS Appl. Mater. Interfaces 6 (2014) 9173–9184.
[29] B. Murugan, D. Srinivas, C.S. Gopinath, V. Ramaswamy, A.V. Ramaswamy, Chem. Mater. 17 (2005) 3983–3993.
[30] A.E. Nelson, K.H. Schulz, Appl. Surf. Sci. 210 (2003) 206–221.
[31] C.S. Gopinath, S.G. Hedge, A.V. Ramasamy, S. Mahapatra, Mater. Res. Bull. 37 (2002) 1323–1332.
[32] L. Li, Z. Go, A. Du, H. Liu, J. Mater. Chem. 22 (2012) 3600–3605.
[33] E.S. Gnanakumar, C.J. Jino, T. Raja, C.S. Gopinath, J. Nanosci. Nanotechnol. 13 (2013) 2682–2688.
[34] E.S. Gnanakumar, J. Madhusudhan Naik, M. Manikandan, T. Raja, C.S. Gopinath, ChemCatChem 6 (2014) 3116–3124.
[35] F. Kapteijn, A.D. Vanlangeveld, J.A. Moulijn, A. Andreini, M.A. Vuurman, A.M. Turek, J.M. Jehng, I.E. Wachs, J. Catal. 150 (1994) 94–104.
[36] P.A. Bharad, K. Sivaranjani, C.S. Gopinath, Nanoscale 7 (2015) 11206–11215.

Catalysis Today 375 (2021) 145–154

Contents lists available at ScienceDirect

Catalysis Today

journal homepage: www.elsevier.com/locate/cattod

A highly efficient and reusable Ru-NaY catalyst for the base free oxidation of 5-Hydroxymethylfurfural to 2,5-Furandicarboxylic acid

Prabu Kandasamy [a,b], Pranjal Gogoi [a,b], Aswathy Thareparambil Venugopalan [a,b], Thirumalaiswamy Raja [a,b,*,1]

[a] Catalysis and Inorganic Chemistry Division, CSIR-National Chemical Laboratory, Dr. Homi Bhabha Road, Pune 411 008, India
[b] Academy of Scientific and Innovative Research (AcSIR), Ghaziabad, Uttar Pradesh 201 002, India

ARTICLE INFO

Keywords:
Biomass utilization
HMF conversion
Base free oxidation
Ru nanoparticles
NaY zeolite
2,5-Furandicarboxylic acid

ABSTRACT

Oxidation of 5-hydroxymethylfurfural (HMF) to 2,5-furandicarboxylic acid (FDCA) is an important reaction for the production of recyclable bio-based polymers. Herein, we report a series of Ru nanoparticles supported on NaY zeolites catalysts for the oxidation of HMF to FDCA. The catalysts were prepared by simple ion exchanged method. Among all the catalysts, the optimized 3 wt % Ru-NaY catalyst showed superior catalytic activity under base free conditions with a shorter period of reaction time. The conversion of HMF was 100 % with 94 % FDCA yield. This catalyst was reused for fourth cycles, with an insignificant decrease in the yield of FDCA. H_2-chemisorption and HRTEM studies confirmed that high metal dispersion and small size of Ru nanoparticles play vital roles for the HMF oxidation. In addition, the acidic hydroxyl groups of the supercage as well as higher amount of metallic Ru° are also responsible for the high yield and productivity of FDCA.

1. Introduction

Identifying renewable energy resources for clean energy fuels and chemicals is one of the major challenges that humankind is confronting [1]. Currently, more than 90 percent of energy and chemicals are produced from petroleum derived feedstocks (natural gas, coal, and crude oil). However, the burning of fossil fuels is neither secure nor sustainable in the long run, produces 21.3 billion tonnes of CO_2 per year there by increasing global warming which is one of the serious environmental issues humanity is witnessing [2–4]. These environmental issues triggered the use of renewable resources for the production of chemicals and fuels [5]. 5- hydroxymethylfurfural (HMF) is one of the most important biomass-based chemicals, draws significant attention in these days owing to its full application in industries for various value added chemicals and fuels [6–9]. HMF can undergo a variety of chemical transformations such as hydrogenation, oxidation, and esterification, etc. The catalytic oxidation of HMF can produce several value added products such as 2,5-diformylfuran (DFF), 5-hydroxymethyl-2-furancarboxylic acid (HMFCA), and 2,5-Furandicarboxylic acid. Recently Zhang and co-workers are reported aerobic oxidation of HMF to DFF using Cs doped MnO_x and nitrogen doped carbon material with high yield of DFF [10,11]. A smaller Ag nanoparticle stabilized by poly(vinylpyrrolidone) supported ZrO_2 shows excellent catalytic activity with 98 % yield of HMFCA and 100 % conversion of HMF at 20 °C for 2 h [12]. Among the oxidation product, the most important commodity chemical 2,5-furandicarboxylic acid (FDCA) serves as a substitution for terephthalic acid in the polymer industries. It is also a monomer for the production of bio-based polyethylene furanote (PEF) [13] and has huge potential to replace conventional fossil based polyethylene terephthalate (PET) [14–16].

In the past decades, homogeneous catalytic processes were investigated using molecular oxygen as an oxidant for the catalytic oxidation of HMF using Co/Mn/Zr/Br catalysts with acetic acid as solvent [17]. However, the major drawback of this process is the separation and reusability of the catalysts. To overcome these difficulties, researchers have been started exploring heterogeneous noble metals such as Au, Pt, Pd and Ru based catalysts for the higher and excellent catalytic activity of the reaction [18]. Recently, supported gold catalysts like Au/Al_2O_3 [19], Au/CeO_2 [20], and Au on carbon was found to be active for the oxidation of HMF to FDCA using external base [21], where the reaction proceeds through the oxidation of aldehyde group which is the rate-limiting step. Other active catalysts for oxidation of HMF to FDCA

* Corresponding author.
E-mail address: t.raja@ncl.res.in (T. Raja).
[1] Present address: Catalysis and Inorganic Chemistry Division, CSIR-National Chemical Laboratory, Dr.Homi Bhabha Road, Pune- 411008, Maharashtra, India.

https://doi.org/10.1016/j.cattod.2020.05.009
Received 13 October 2019; Received in revised form 1 April 2020; Accepted 3 May 2020
Available online 6 May 2020

are Pt/TiO_2 and Pt supported on carbon using basic aqueous solution at high pressure [22,23]. HMF oxidation into FDCA using Pd nanoparticles supported on carbon and Pd/PVP catalyst also gives a similar yield of FDCA as with Pt [24,25]. However, in alkaline medium the Pd/PVP catalyst suffers from difficulty in separation and recyclability issues. Another strategy used by researchers to improve productivity of FDCA is the designing of bimetallic catalysts such as Pd-Au [26,27] and Au-Cu [28], which can lead to a more efficient and stable production of FDCA.

Very importantly, in most of the cases, the catalyst stability remains a significant issue because of excess usage of external bases like NaOH and Na_2CO_3 in the reaction medium. There is an interesting observation for the base free oxidation of HMF to FDCA using Au supported hydrotalcite catalyst using O_2 as oxidant, where the yield of FDCA was 92 %. However, this value was not stable [29]. Recently, Gao et al. reported the bimetallic Au-Pd nanoparticles over La doped LDH catalyst which gave 100 % yield of FDCA within 6 h of reaction time [30]. Haian et al. reported that reconstructed hydrotalcite supported Pd-Au bimetallic catalyst achieved a high yield of FDCA (90 %) at 60 °C over 6 h [31]. However, the commercial implementation of HMF conversion to FDCA will require the new catalytic material and approaches which minimize precious metal content in the catalyst. Therefore, from the commercial and economic viewpoint, using noble metals (Au, Pt and Pd) based catalysts are not a cost effective process. Also, this catalyst needs an external base, which is not environmentally benign.

Very recently, Han et al., reported MnO_X-CeO_2 composite for the production of FDCA and it showed high activity at 20 bar oxygen pressure in the presence of a higher concentration of inorganic bases $KHCO_3$ and $NaHCO_3$ [32]. Rao et al., achieved high FDCA yield; around 95 % over Co-Mn based catalysts using $NaHCO_3$ as an external base [33]. The enhanced catalytic activity of the catalyst was attributed to the high lattice oxygen mobility and redox properties Mn^{4+} and Mn^{3+}. Moreover, strong bases would accelerate the degradation of HMF and lead to the formation of undetectable products as observed by previous reports [32]. Yan and co-workers synthesized Fe-Zr-O catalyst using ionic liquids [Bmim]Cl as a solvent, which showed a maximum yield of FDCA (60 %) at 160 °C and 20 bar pressure [34]. According to the earlier reports, at high temperature HMF is degraded into insoluble humins and hence even though the conversion of HMF is high, the desired product FDCA yield will be low. Another recently published work from Chen et al., proposed the use of ionic liquids-heteropoly acids as catalyst for HMF oxidation using different solvents and additives, among that [Bmim]Cl is active for FDCA production [35]. Shuai et al. reported a photocatalyst composed of cobalt thioporphyrazine dispersed on g-C_3N_4, which shown outstanding selectivity towards FDCA (yield = 96 %) at room temperature under pressurized air [36]. However, most of the non-noble metals based catalysts need a high concentration of base operated at high temperature and pressure.

Presently, Ru based catalyst is found to be highly active for HMF oxidation into FDCA without using any base. Guangshun et al., reported Ru/C catalyst under base free conditions with 88 % yield of FDCA which may be further improved. [37]. Mishra and co-workers developed an efficient Ru supported on $MnCO_2O_4$ spinel catalyst with tunable bronsted and lewis acidic sites which plays an important role in the production of FDCA. The yield achieved was 99.1 % at 24 bar pressure [38]. However, the catalyst demonstrated activity at high pressure and the role of acidic sites were not explained thoroughly. Pichler et al., synthesized Ru supported ZrO_2 with high surface area using surface casting method and the selectivity of FDCA achieved was 97 % after 16 h of reaction [39]. Nevertheless, maintaining the surface area and synthesizing Ru/ZrO_2 support prepared by using silanol–rich SiO_2 aerogel as template in the surface casting process is quite complicated. In perspective of the above reported work, Ru metal catalyst may recruits for the production of FDCA which can impose technical limitation like lack of recyclability and as a result, high metal loading as well as lower reaction temperature could be utilized.

To alleviate the above problems, we have developed a highly efficient, cost-effective, and reusable Ru based catalyst for the catalytic oxidation of HMF to FDCA. Herein, we are reporting Ru nanoparticles supported on NaY zeolites catalyst for the selective oxidation of HMF to FDCA for the first time. A simple ion exchange method was adopted for the synthesis of Ru/NaY catalysts. These materials were extensively characterized by various notable physicochemical characterization techniques to get more insights into the catalytic activity. We observed that 3 wt % Ru-NaY catalyst demonstrated highest yield of FDCA (94 %) within a short period of time, at low pressure under base free condition. Notably, the catalyst was highly recyclable, with insignificant drop in the yield of FDCA even after the fourth cycle. In a nutshell, Ru exchanged NaY catalysts were found to be highly active and selective for the production of FDCA, and their catalytic activity results are superior compared to many catalysts reported so far.

2. Experimental section

2.1. Materials

The NaY zeolite (CBV-100, Si/Al ratio = 2.5) was purchased from Zeolite international, USA. Ruthenium chloride ($RuCl_3.H_2O$), HMF, FFCA, HMFCA, DFF, and FDCA were provided by Sigma-Aldrich and sodium borohydride ($NaBH_4$) was obtained from Loba chemicals, Mumbai.

2.2. Material synthesis

The synthesis of Ru nanoparticles by ion- exchange method has been described in Scheme 2. Briefly, an appropriate amount of NaY zeolite was suspended in 30 mL of deionized water. The above solution was sonicated for 0.5 h at room temperature to get well dispersion of the NaY zeolite. To this 12 mL of $RuCl_3$ solution was added dropwise (for 3 wt % Ru-NaY) and the resulting mixture was stirred at 80 °C for 3 h. Then, the solution was cooled down to room temperature, and then, an aqueous solution of $NaBH_4$ (Ru/$NaBH_4$, 1:4) was added dropwise to the resulting mixture in a closed system with constant stirring to obtain metallic Ru. The resulting mixture was filtered and washed thoroughly with 2-litre deionized water. Finally, the filtered sample was dried at 110 °C for 10 h and denoted as 3 %. A similar synthesis procedure was followed for 1 %, 2 % and 5 wt % Ru-NaY catalysts with calculated amount of Ru precursor.

2.3. Catalyst characterization

Powder X-ray diffraction (XRD) measurement of as synthesized samples were executed using PANanalytical X pert pro dual goniometer with Ni as the filter and Cu Kα (λ =1.5406 Å) source with step size 0.008° using a flat holder Bragg-Brentano geometry. The Nitrogen sorption measurement was measured by (Quantachrome Autosorb IQ, USA) at -196 °C. The specific surface areas of the catalysts were determined by Brunauer-Emmett- Teller (BET) equation. Acidity of the catalyst was examined by NH_3- temperature programmed desorption using Micromertics Autochem-2920 instrument (USA). Around 50 mg of the sample was taken and pre-treated under helium atmosphere at 300 °C with constant flow rate (20 mL.min^{-1}) for 30 min which was controlled by mass flow controller (Brooks). Then, temperature was brought down to 50 °C and NH_3 was adsorbed to sample surface using 10 % NH_3 in He (20 mL.min^{-1}). Pure He (20 mL.min^{-1}) was flushed for 30 min at 100 °C to remove any physisorbed NH_3 from the sample surface. The desorption of NH_3 was performed in He flow (20 mL.min^{-1}) by raising the temperature 100−700 °C at 5 °C min^{-1} and desorbed NH_3 was monitored by thermal conductivity detector (TCD). The metal dispersion and Ru crystallite size were calculated by (Quantachrome Autosorb IQ, USA) using H_2 as a probe molecule. Initially, the catalyst was reduced under H_2 flow at 250 °C, before chemisorption at 40 °C. FESEM images of the catalysts were recorded on JEOL-JSM-5200

systems. ICP-OES (Spectro Arcos, FHS-12) was used to find the metal percentage in the sample. TPR analysis was performed using (Micromertics Autochem-2920, USA) instrument. Before TPR study, the catalyst was pretreated at 250 °C for 60 min using 5 % O_2 in He gas mixture. Later reduction was performed under 5 % H_2 in Ar in the temperature range 50−600 °C at 5 °C/ min^{-1}. H_2 consumption was measured quantitatively by a thermal conductivity detector (TCD). The infrared spectra of the samples were recorded in the range of 500−4000 cm^{-1} using Nicolet iS50 FT-IR (Thermo Scientific) coupled with MCTB detector and KBR window.The Bronsted and Lewis acidity were measured through pyridine adsorption experiment. Before the analysis, sample was preheated under N_2 atmosphere at 250 deg for 1 h. Further, the pretreated samples were cooled down to room temperature. Finally, pyridine vapors were (25 °C–200 °C) introduced into the samples and FT-IR spectra were collected in absorbance mode after pyridine treatment. High resolution transmission electron microscopy (HR-TEM) and high angle annular dark-field scanning TEM (HAADF-STEM) were collected on a FEI Technai TF-30 instrument operating at 300 k V. X-ray photoelectron spectroscopy (XPS) were carried out on ThermoKalpha$^+$ spectrometer using monochromated Al Kα radiation with energy (1486.6 eV). The in situ CO- FTIR spectra were collected using an FTIR spectrometer (Nicolet, iS50- Thermo Scientific) equipped with an MCT detector (cooled by liquid N_2) at a resolution of 8 cm^{-1} and 200 scans. Firstly, the sample was flushed with N_2 50 mL/$min^{-1}$for 20 min^{-1} and was reduced at 250 °C for 1 h in 5 % H_2/Ar (20 mL/min^{-1}). Afterwards, the sample was cooled to 50 °C and background spectrum was collected under N_2 atmosphere. Eventually, the CO gas mixture (1 vol %/CO/N_2) was passed through MFC into the reaction chamber and IR spectra were collected at from room temperature to 250 °C.

2.4. Catalytic tests

Catalytic tests were evaluated using Parr autoclave USA (4848 reactor) controllers with 5500 series compact reactor. In a 50 mL reactor vessel, catalyst (50−175 mg), water (30 mL), and HMF (0.5 mmol) were added and pressurized using O_2 gas. Subsequently, the reaction temperature (100−140 °C) was brought to the desired value and the solution was stirred at 650 rpm. To maintain constant pressure (5−15 bar O_2 pressure), the reactor was connected to the O_2 cylinder with proper safety precautionary measurements. Sample was collected in 2 h of time interval during the course of the reaction. The sample mixture was filtered using 0.22 μm nylon filter and was analyzed by Agilent HPLC, equipped with RI detector using Rezex-organic acid H^+ column (300 mm × 7.8 mm). H_2SO_4 (5 mM), was used as a mobile phase and the yield of 2,5-furandicarboxylic acid (FDCA) and conversion of 5-hydroxymethylfurfural (HMF) were confirmed by HPLC using external standard calibration method. Recyclability of the catalyst (3 wt % Ru-NaY) was performed for five cycle and, the spent 3 wt % Ru-NaY catalyst was characterized by XRD, HRTEM and XPS analysis to understand any morphological change of the catalyst after reaction.

3. Results and discussion

3.1. Powder X-ray diffraction

To understand the structural features of the materials, PXRD analysis was conducted and Fig. 1shows the diffraction patterns of bare NaY zeolite compared with different ruthenium metal loaded NaY. The PXRD pattern of pure NaY zeolite exhibits highly crystalline nature of the zeolite framework (JCPDS No.00−043-0168) whose intensities did get not changed even after Ru exchange. No peak pertaining to metallic Ru or its oxides were observed, pointing the homogeneous distribution of Ru nanoparticle on the zeolite support. The absence of any peak corresponds to Ru may also be due to the higher intensities of NaY zeolite support [40,41].

The textural properties of the catalysts were analyzed by N_2 adsorption-desorption study. Table 1 shows BET surface area of NaY zeolite as 866 m^2/g, and the pore volume is 0.37 cm^3/g. However, with increasing the metal loading, surface area and pore volume of the catalyst is decreasing gradually. This decrease in the surface area was due to pore blockage by Ru nanoparticles in the cavities of zeolite. Most of the Ru particles were well dispersed on the surface of NaY support, which was confirmed by H_2 chemisorption study. It was noticed that at higher Ru loading the crystallite size of Ru were large, leading to the lower dispersion of those nanoparticles on the support. At lowest metal loading the catalyst demonstrated highest dispersion. Ru metal surface area was also calculated from H_2-chemisorption study and it was observed that 5 % Ru loaded catalyst has least active surface area reflecting in the lowest activity of the catalyst. The actual Ru content was obtained by ICP-OES analysis.

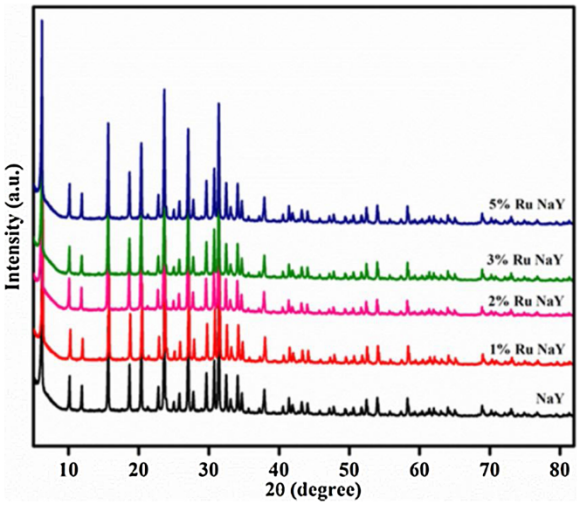

Fig. 1. Powder XRD pattern of pristine NaY and Ru supported NaY catalysts.

3.2. Field emission scanning Electron microscopy

The surface morphology of the catalyst was investigated by FE-SEM. Fig. 2 (a) shows pure NaY zeolite having a porous structure and crystalline nature. SEM micrographs clearly reveals that the morphology of the catalysts did not change after exchanging Ru in the zeolite framework. This observation is in good agreement with the XRD results of the catalysts.

3.3. Transmission Electron microscopy

The dispersion of Ru and their particle size on 3 wt % Ru-NaY catalyst were further confirmed by HRTEM analysis. It was observed that the Ru metal nanoparticles were uniformly distributed over the surface of the NaY zeolites with a broad distribution Ru particles ranging from 1−12 nm. The diffraction pattern shows uniform interplanar spacing of 0.2 nm corresponding to 101 plane of Ru nanoparticles and interplanar spacing of 0.23 nm matches well with 100 plane. Ru particle size distribution was derived by TEM analysis, which is represented in Fig. 3. The average particle size of Ru nanoparticles were 4 nm which is in accordance with the H_2 chemisorption results. However, Ru particle size (4 nm) is bigger than the pore size of NaY zeolite, therefore, the majority of Ru particles are present on the external surface of the NaY zeolite. Fig. 4 shows HAADF-STEM and elemental mapping of 3 wt % Ru-NaY catalyst which confirmed that Ru nanoparticles are homogeneously distributed over the NaY support.

3.4. Insitu CO-FTIR

Insitu CO-FTIR was carried out to understand the possible oxidation

Table 1
The textural properties of Ru-NaY catalysts.

Samples	BET Surface area[a] (m^2/g)	Total pore volume[a] (cm^3/g)	BJH pore size (Å)	Ru content[b] (wt %)	Ru metal dispersion [c] (%)	Ru metal surface area[c] (m^2/g)	Average Ru crystallite[c] size (nm)
NaY	866	0.37	19.0	–	–	–	–
1 wt % Ru-NaY	842	0.36	18.7	0.91	53.2	4.7	1.8
2 wt % Ru-NaY	833	0.36	18.4	1.82	32.4	3.4	3.2
3 wt % Ru-NaY	820	0.34	18.1	2.91	22.6	3.2	3.4
5 wt % Ru-NaY	786	0.31	17.6	4.70	12.3	2.4	6.4

(a) Calculated from BET (b) Amount of Ru calculated from ICP-OES (c) Obtained by H_2-Chemisorption.

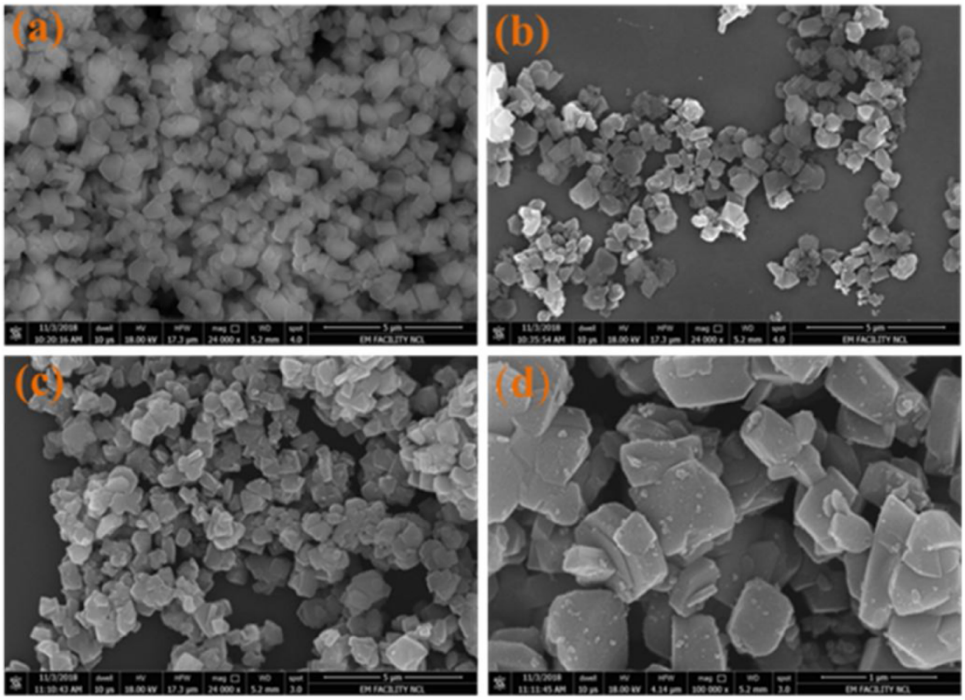

Fig. 2. FE-SEM images of (a) NaY, (b) 2 wt % Ru-NaY and (c, d) 3 wt % Ru-NaY.

state of Ru in the prepared catalysts. The spectra was collected at 120 °C and given in Fig. 5. It was observed that IR bands appears in the range 2000−2500 cm^{-1} for all catalysts can be attributed to the vibrational stretching mode of CO bound to different types of Ru present on the support. The bands emerging at 2117 and 2175 cm^{-1} region assigned to two different multicarbonyl species adsorbed on partially oxidized Ru species (Ru^{+n}) (CO)x, x >1) [42]. However, still debates are going on about the precise oxidation of Ru (n) and the number of carbonyl group adsorbed on Ru species. Whereas, the IR band observed at 2053 cm^{-1} region can correlated with the linearly bound CO with the metallic Ru species. Interestingly the intensity of this peak was more among all, which implies the higher abundancy of metallic Ru in the catalysts. The CO-FTIR results are in good agreement with the chemisorption and XPS results.

3.5. X-ray photoelectron spectroscopy

In order to investigate the oxidation state of active Ru species on the NaY supports XPS analysis was performed. Fig. 6 depicts the Ru 3d core-level spectra of 3 wt % Ru-NaY which was deconvoluted by peak fitting method into three major peaks (Ru $3d_{5/2}$, Ru $3d_{3/2}$ and C 1s). The peak at 284.7 eV corresponds to carbon contamination on the surface. The electronic structure of 3 wt % Ru-NaY catalyst confirms Ru exist in two different oxidation states. The metallic ruthenium was observed at 280.6 and 284.5 eV were allocated to Ru° $3d_{5/2}$ and Ru° $3d_{3/2}$ peaks and the peak at 281.7 and 286.6 eV were assigned to +4 oxidation state of Ru in RuO_2 [43]. According to XPS data, the surface atomic composition of metallic ruthenium and ruthenium oxide were 70 % and 30 % respectively.

3.6. Fourier transform infrared spectroscopy

Fig. 7 shows the FTIR spectrum of bare NaY and Ru supported NaY. The broad peak at 3428 cm^{-1} corresponds to the stretching vibration of hydroxyl group T—OH from the surface of NaY zeolites or in supercages, which was confirmed for all the samples [44]. The IR band appears at 1021 cm^{-1} related to asymmetric stretching of $(Si/Al\text{-}O)_4$ and the bending vibration of water molecule appears at 1638 cm^{-1} [45,46]. Therefore, proton abstraction is considered as the first step for the conversion of HMF to FDCA. The acidic OH groups in sodalite cage and high frequency acidic OH groups located at supercage play an important role in the HMF conversion. However, internal hydroxyl groups within the supercage are bronsted acids and these can be detected by in situ pyridine FTIR.

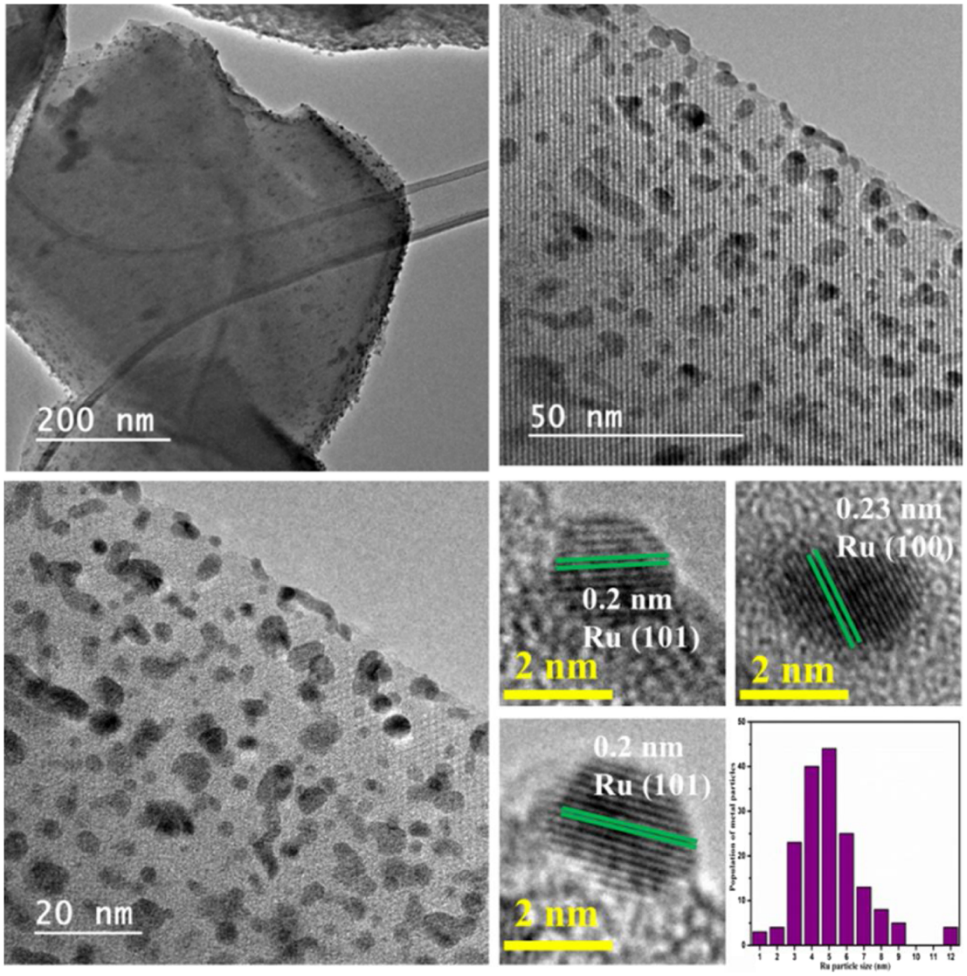

Fig. 3. HRTEM images and Ru particle size distribution of 3 wt % Ru-NaY.

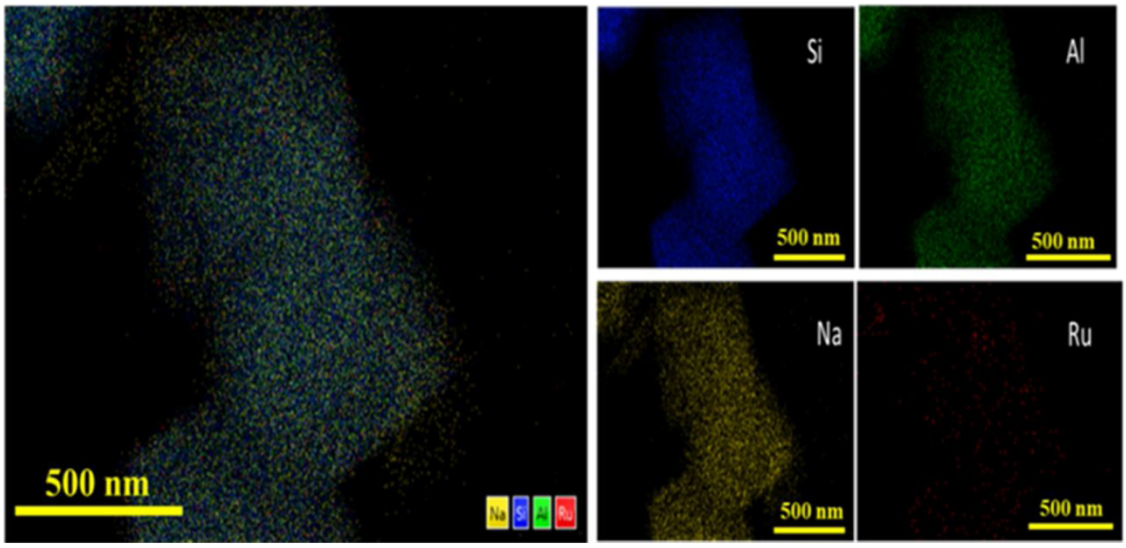

Fig. 4. HAADF-STEM elemental mapping of 3 wt % Ru-NaY.

3.7. Temperature programmed reduction

The reducibility of Ru supported NaY samples was investigated by H_2-TPR as shown in Fig. 8. The main peak at 70–150 °C temperature region can be ascribed to the reduction of RuO_x species. However, with increasing metal loading from 1 % to 5 % the intensity of TPR peak is gradually increased [47]. Implying that hydrogen consumption is increased with the increase in Ru content of the catalysts.

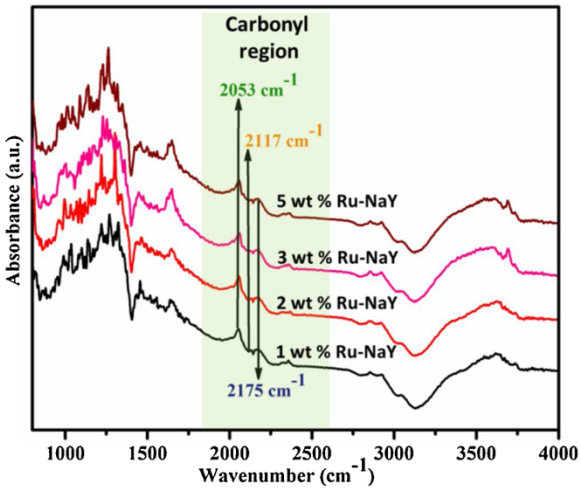

Fig. 5. CO-FTIR spectra of Ru exchanged NaY catalysts.

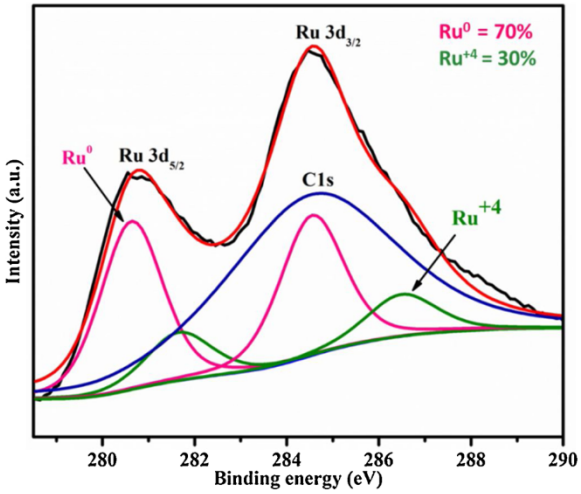

Fig. 6. XPS spectra of 3 wt % Ru-NaY catalyst.

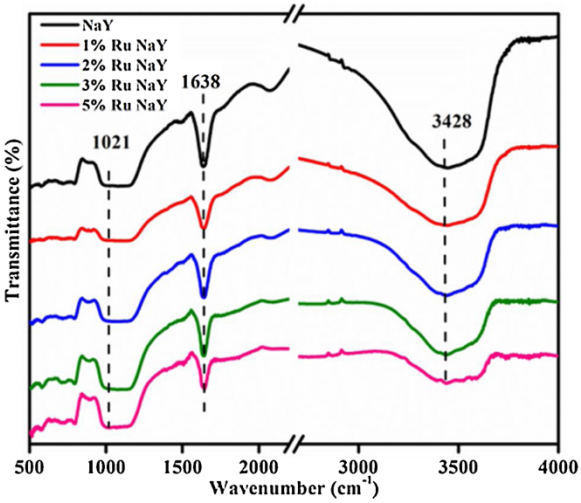

Fig. 7. FTIR Spectrum of Ru supported NaY catalysts.

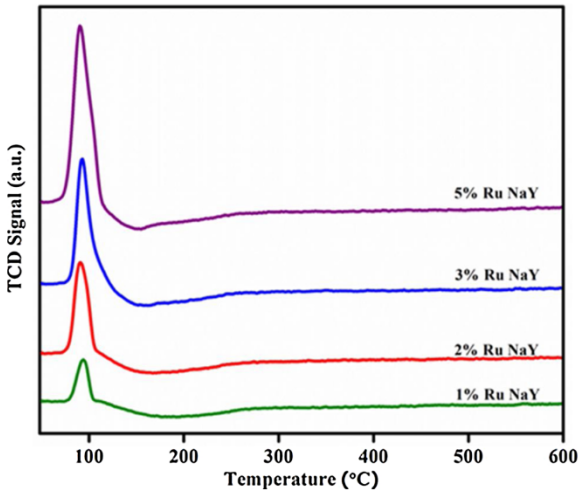

Fig. 8. H_2-TPR profiles of the Ru supported NaY catalysts.

3.8. NH_3-temperature programmed desorption

It is well known that the bronsted and lewis acid sites of catalyst play an important role in the conversion of HMF to furandicarboxylic acid, therefore the synthesized catalysts were subjected to NH_3-TPD to find out exact quantity of the acidic sites in the catalysts. The results are shown in the Fig. 9. NH_3-TPD profiles clearly indicated that a single peak was observed for ammonia desorbed around 240−300 °C corresponding to moderate acidity of the surface [48]. On increasing ruthenium loading the acidity of the materials was also increased (5 wt % Ru-NaY: 1.43 mmol/g). However, activity of the catalysts were not proportionally increased with the increase in the acid strength. In fact, 5 wt % Ru-NaY demonstrated lowest yield of FDCA among all the catalysts. This abnormal catalytic trend may be due to the formation of intermediate FFCA products. 3 wt % Ru-NaY shows the highest yield of FDCA. The role of bronsted and lewis acidity on the catalytic activity will be discussed in In-situ pyridine FTIR.

3.9. Insitu-Pyridine FTIR

To study the function of bronsted, and lewis acidity for NaY zeolite, metal ion exchanged zeolites were subjected to insitu- FTIR spectroscopy of adsorbed pyridine. Fig. 10 shows absorption bands at 1507 cm^{-1} and 1540 cm^{-1} corresponds to pyridine adsorbed at bronsted acidic sites [49]. The bands at 1455 and 1558 cm^{-1} specify the existence of coordinatively bonded pyridine from lewis acid sites [50]. The peak at 1489

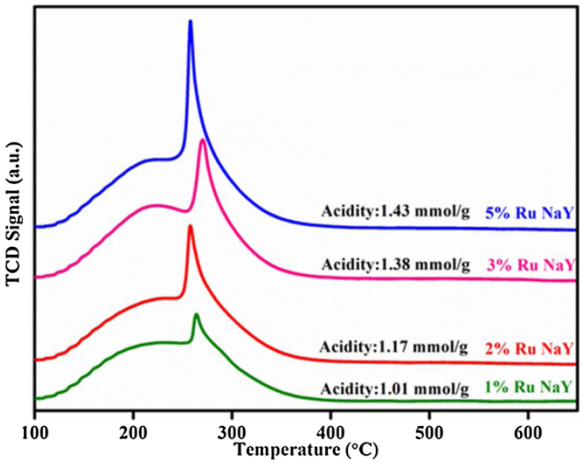

Fig. 9. NH_3-TPD profiles of Ru supported NaY catalysts.

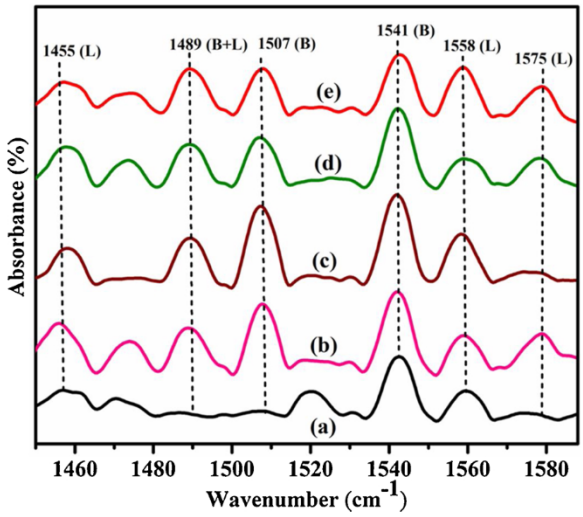

Fig. 10. Insitu Pyridine FT-IR spectra of (a) NaY zeolite (b) 1 wt % Ru-NaY (c) 2 wt % Ru-NaY (d) 3 wt % Ru-NaY and (e) 5 wt % Ru-NaY.

cm^{-1} attributed to both bronsted and lewis acidity. The band at 1575 cm^{-1} could also be considered as quantification for lewis acidic sites, but these bands are typically less intense than 1558 cm^{-1} band and have some degree of overlap. The pyridine FTIR spectra indicate that NaY and metal loaded NaY have both lewis and bronsted acidic sites while pure NaY shows less intense peak than the metal loaded samples. It implies that Ru also plays an important role in improving the acidic strength of the samples, which could perform an important role for the oxidation of HMF to attain maximum yield of FDCA. The L/B ratio for each catalyst were calculated by peak deconvolution the amount of pyridine adsorbed on each type of sites [50].

4. Catalytic tests

4.1. Base free oxidation of HMF to FDCA

Fig. 11 represents the catalytic tests of HMF to FDCA over 3 wt % Ru-NaY catalyst. The reaction was performed at 120 °C and 10 bar initial oxygen pressure under base free condition. The catalyst demonstrated complete HMF conversion in 2 h with a yield of 58 % towards FDCA. Interestingly,the yield of FDCA increased gradually with the increase of the reaction time and at the end of 8th h the yield of FDCA and FFCA

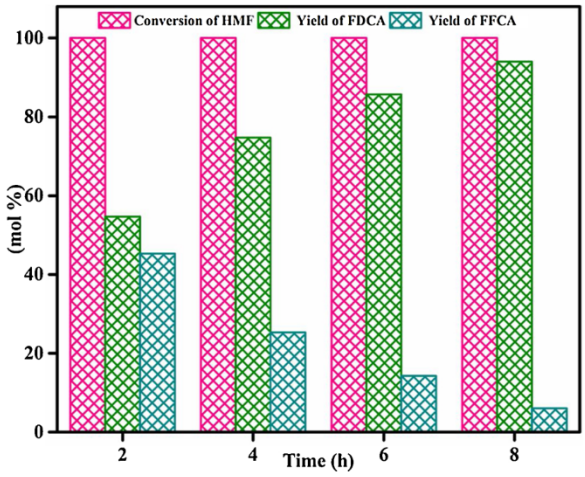

Fig. 11. HMF conversion and the yield of FDCA with time over 3 wt%Ru-NaY. **Reaction Conditions:** 3 wt % Ru-NaY catalyst (150 mg), HMF (0.5 mmol), Water (30 mL), O_2 (10 bar), 120 °C, 8 h.

were 94 % and 6 %, respectively. Further studies on the relationship of the catalytic activity with Ru particle size and amount of acidic −OH groups inside the supercage have proved that they possess a crucial role in achieving the high yield of FDCA [51,52].

Scheme 1 exhibits a general reaction pathways for the selective oxidation of HMF to FDCA. Initially, HMF may be oxidized to 2,5-diformylfuran (DFF) or 5-hydroxymethyl-2-furancarboxylic acid (HMFCA), important intermediates of this reaction while using molecular oxygen as an oxidant. These two intermediates further could be oxidized to 5-formyl -2-furancarboxylic acid (FFCA). Finally, FFCA will be oxidized to furandicarboxylic acid (FDCA).

4.2. Product distribution of HMF oxidation over Ru-NaY catalysts

To determine the optimal catalyst composition for the production of FDCA from HMF a series of Ru exchange NaY catalysts with different metal loading were prepared by the ion-exchange method and their activity are shown in Fig. 12. The catalytic performance of 3 wt % Ru-NaY catalyst was already discussed in the above section. Although, a complete HMF conversion was observed for 3 wt % Ru-NaYcatalysts within 2 h, the maximum yield of FDCA was achieved after 8 h. Therefore reaction time also hold a crucial role for this reaction. The higher catalytic activity of this catalyst could be assigned to the optimum metal loading, better metal dispersion, higher availability of catalytic active sites and desired acidic sites of the catalyst. Despite the higher metal dispersion, 1 wt % Ru-NaY shows only 31.04 % yield of FDCA after 8 h. This could be due to the lower metal loading and less acidic sites (1.01 mmol /g) of this material as confirmed by NH_3-TPD analysis. Recently Mishra et al. reported bronsted and lewis acidic sites have a major role in achieving higher yield of FDCA [38]. Upon increasing the metal loading up to 2 wt %, the yield of FDCA was further increased to 75.66 %. However, the catalytic activity was still inferior to 3 wt % Ru-NaY. On the other hand, 5 wt % Ru-NaY catalyst showed a decrease in FDCA yield (32.8 %) with simultaneous increase in FFCA yield (67.2 %). This may be due to the larger crystallite size of Ru (6.4 nm) which reduces metal dispersion on the NaY support as confirmed from H_2-chemisorption results. A similar reaction was also performed over metal free NaY zeolite support under the optimized reaction conditions which showed 26 % of HMF conversion with DFF yield of 5.3 %. No FDCA formation was noticed during the reaction, proving the dominating catalysis of Ru nanoparticles over NaY support. The above results confirmed superior catalytic activity of 3 wt % Ru on NaY support as a whole catalyst.

4.3. Effect of reaction temperature

Since 3 wt % Ru-NaY catalyst was found to be the best catalyst among all, this catalyst was further subjected to temperature study for the best catalytic activity results. Temperature is a vital parameter, which can influence catalytic activity of 3 wt % Ru-NaY catalyst. Fig. 13 represents the catalytic activity of 3 wt % Ru-NaY at different temperatures. Table 2 shows the product distribution and no HMFCA was observed under these reaction conditions. The oxidation of HMF mainly produced DFF, FFCA and FDCA. Initially, reaction was performed at 100 °C where the conversion of HMF was 100 % with the yield of FDCA approximately equal to 47 %. Further, with increasing temperature upto 120 °C; 94 % yield of FDCA was obtained with complete HMF conversion at 8 h. When the reaction was performed at 140 °C, initially yield of FDCA was higher than the reaction performed at 120 °C. However with the increase in the reaction time, activity was decreased gradually to 70 % at 8 h. This might be due to degradation of HMF at high temperature [53]. Thus, 120 °C is observed as the optimized temperature for HMF oxidation to FDCA.

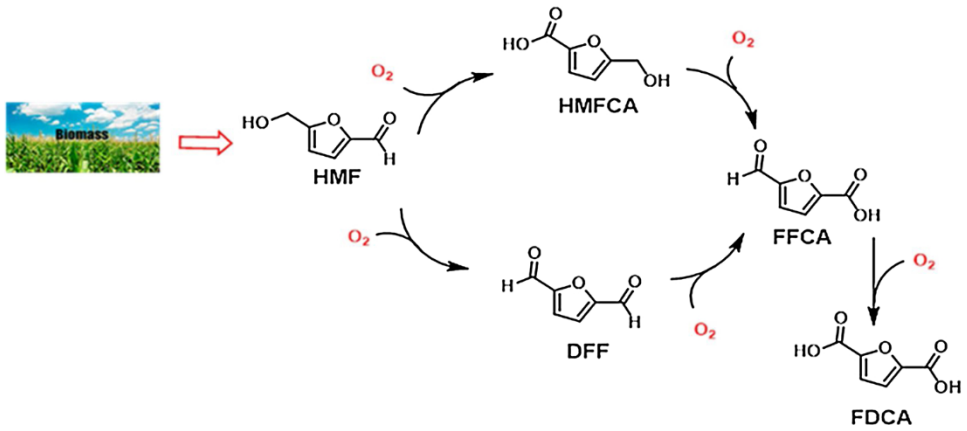

Scheme 1. Possible reaction pathway for selective oxidation of HMF to FDCA.

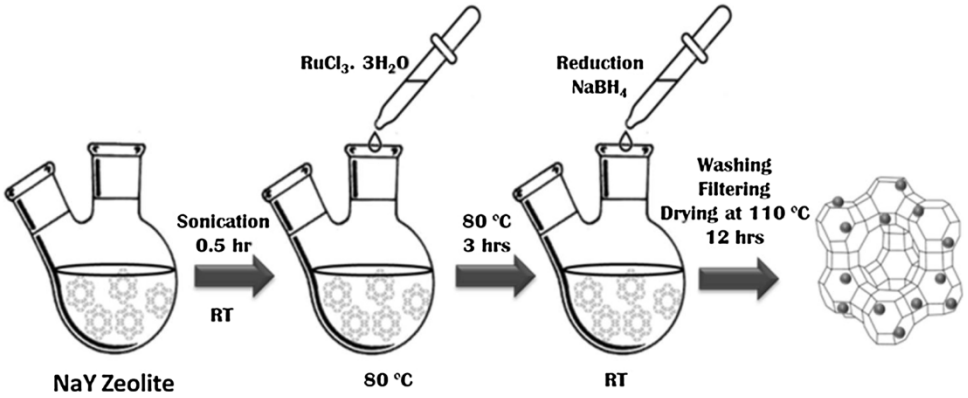

Scheme 2. Graphical representation of the synthesis technique for Ru exchanged NaY zeolite.

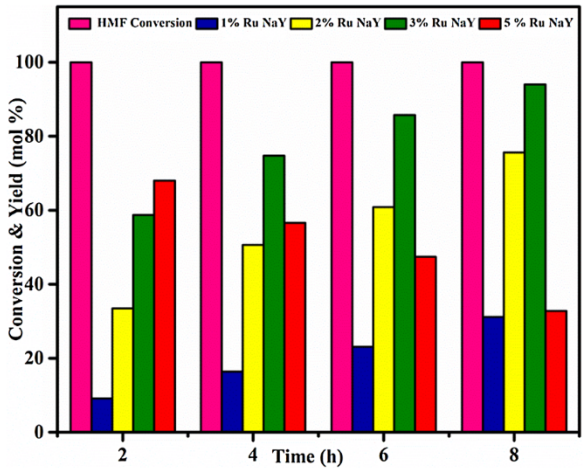

Fig. 12. Effect of Ru loading on HMF conversion and FDCA yield with time. **Reaction conditions**: HMF (0.5 mmol), catalyst (150 mg), 120 °C, Water (30 mL), O_2 (10 bar), 8 h.

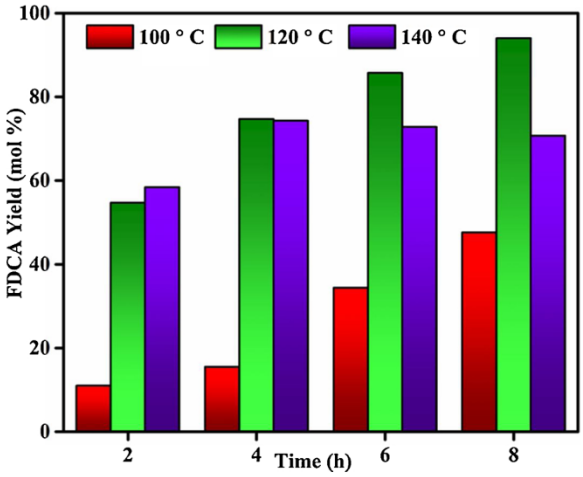

Fig. 13. Effect of reaction temperature on FDCA yield over 3 wt % Ru-NaY. **Reaction conditions:** 3 wt % Ru-NaY catalyst (150 mg), HMF (0.5 mmol), Water (30 mL), O_2 (10 bar), 8 h.

4.4. Effects of pressure and catalyst loading

The effect of oxygen pressure was examined over 3 wt % Ru-NaY catalyst for HMF oxidation. The oxygen pressure was varied from 5–15 bar at a stable reaction temperature viz. 120 °C. The results are shown in Fig. 14(a) wherein 5 bar oxygen pressure leads to increasing FDCA yield with the reaction time and the maximum yield achieved was 83 % with complete conversion of HMF at 8 h. On further increasing the pressure upto 8 bar, the yield of FDCA was gradually increased as reaction time prolonged. However, these pressures are still need to be increased to achieve maximum yield. Further increasing the oxygen pressure to 10 bar, higher yield of FDCA (94 %) was achieved with 100 % conversion of HMF whereas high pressure did not fetch appreciable increasing the yield.

Later, we have investigated the influence of catalyst amount for selective oxidation of HMF to FDCA. Fig. 14(b) shows the yield of FDCA at

Table 2
Catalytic tests of HMF oxidation over various Ru supported catalysts.

Entry	Catalysts	HMF Conversion (%)	Yield of FFCA (%)	Yield of DFF (%)	Yield of FDCA (%)	TOF [a] (h^{-1})	L/B [b] ratio
1	1 wt % Ru-NaY	100	68.8	0	31.14	4.1×10^{-2}	0.93
2	2 wt % Ru-NaY	100	24.34	0	75.66	5.8×10^{-2}	1.06
3	3 wt % Ru-NaY	100	6.0	0	94.0	7.6×10^{-2}	1.04
4	5 wt % Ru-NaY	100	67.2	0	32.8	4.3×10^{-2}	0.98
5	NaY	26	0	5.3	0	0	0.76

Reaction conditions: catalyst (150 mg), HMF (0.5 mmol), Water (30 mL), O_2 (10 bar), 120 °C 8 h, (a)TOF = turnover frequency (moles of HMF converted per mole of metal per hour), (b) L/B = Lewis and Bronsted acid sites (L/B) ration was calculated from pyridine FT-IR.

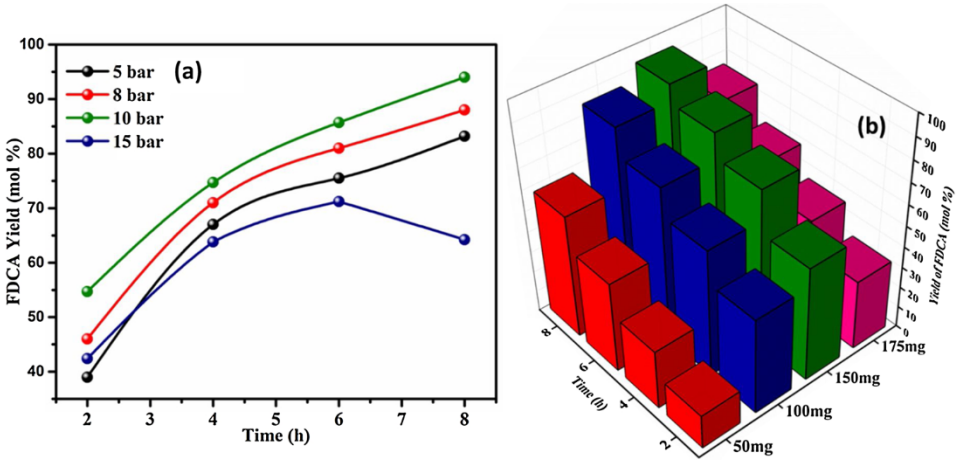

Fig. 14. (a) Effect of reaction pressure and **(b)** catalysts amount on FDCA yield over 3 wt Ru-NaY catalysts. **Reaction conditions:** 120 °C, HMF (0.5 mmol), Water (30 mL).

varying catalyst quantity. The study was started using 50 mg of 3 wt % Ru-NaY at optimized pressure and temperature. The yield of furandicarboxylic acid increases as reaction time prolonged to 8 h and a low yield of FDCA was observed as 59 %. It confirms that the number of Ru active sites is not sufficient for the oxidation of HMF to FDCA. We attempted to enhance the catalytic activity by using 100 mg and 150 mg of the catalyst and the yield of FDCA obtained was 86 % and 94 % respectively. Furthermore, increasing catalyst amount up to 175 mg, a decrease in the yield of FDCA (75.8 %) was observed which may be due to the formation of other side products [54]. Finally, we optimized the catalyst amount as 150 mg which gave superior catalytic performance of HMF to FDCA.

4.5. Reaction pathway for base free oxidation of HMF to FDCA

The base free oxidation of HMF using 3 wt % Ru-NaY catalyst shows higher catalytic activity and productivity of FDCA. Based on the above results on HMF oxidation, the reaction mechanism follows an aldehyde group through DFF and FFCA by identifying the reaction profile of the products. A 100 % HMF conversion was attained in a shorter reaction time (2 h). Especially, complete conversion of DFF was observed at 2 h, for the yield of FFCA (45.3 %) and FDCA (54.7 %). When the reaction was prolonged to 8 h, 94 % yield of FDCA was achieved while FFCA yield was 6 %. According to the catalyst characterizations and experimental part for HMF oxidation, acidic sites can favor the adsorption of an aldehyde group on the catalyst surface [55]. In addition, a high concentration of basic sites produces HMFCA via hemiacetal [56,57].

4.6. Recyclability test

Catalysts recyclability is one of the essential factors in industrial and economic viewpoint. As 3 wt % Ru-NaY catalyst was found to be the best catalyst among all, it was further tested for recyclability study to understand the true performance of the catalyst. Initially 3 wt % Ru-NaY catalyst was filtered, washed several times with distilled water and finally washed with ethanol, dried at 110 °C for 10 h. The resulting catalyst was reused for HMF oxidation and it was observed that 3 wt % Ru-NaY catalyst was truly recyclable even after 5th cycle with a minor drop in the FDCA yield was observed after 4th cycle and the results are depicted in Fig. 15. This drop in the product yield may be due to the loss of some of the active catalytic sites during reaction or post reaction process.

Fig. S1 represents XRD pattern of spent 3 wt % Ru-NaY catalyst which clearly indicating that the morphology of the catalyst did not get changed even after oxidation reaction. The absence of any Ru peak or its oxides pointing that these metal nanoparticles are well dispersed on the

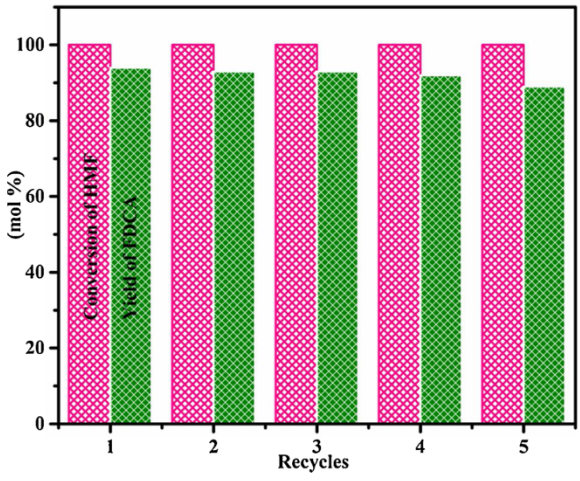

Fig. 15. Recyclability of 3 wt % Ru-NaY catalyst. **Reaction conditions:** 3 wt % Ru-NaY (150 mg), HMF (0.5 mmol), O_2 (10 bar), water (30 mL), 120 °C.

NaY support. Morphology of the catalyst was measured by TEM (Fig. S2, a) where it is clearly indicating that some of the Ru nanoparticles were agglomerated under the reaction conditions and the XPS (Fig. S2,b) spectra of spent 3 wt % Ru-NaY catalyst indicated that the some active metallic ruthenium was oxidized into Ru oxide under the reaction conditions. Hence the slight drop in the FDCA yield may be due to loss of catalytic active sites and agglomeration of Ru nanoparticles after reaction.

5. Conclusions

The oxidation of HMF to FDCA over Ru exchange NaY catalysts was found to be an exciting reaction. In the present work, we have shown a simple and straight forward synthesis method for the oxidation of HMF to FDCA. The extensive characterization techniques employed at different stages and the reaction results at different reaction conditions allow us to draw following conclusions.

1 All the Ru supported NaY catalysts showed reasonably bettter HMF conversion and FDCA yield under the optimized reaction conditions. Among all, the 3 wt % Ru-NaY demonstrated excellent catalytic performance with complete HMF conversion and 94 % yield of FDCA, which is superior to many states of an art catalyst.
2 The optimized 3 wt % Ru-NaY catalyst was highly recyclable even after fourth cycle with minor drop in the activity, pointing the true potential of the catalyst for industrial applications.
3 The enhanced catalytic activity of 3 wt % Ru-NaY was attributed to the optimum metal loading, better metal dispersion and appropriate acidic sites on the catalyst. Additionally, acidic −OH groups of the supercage and higher availability metallic Ru (70 %) were found to play an important role in the HMF oxidation.

Declaration of conflicting interests

The authors declare that they have no known competing financial interests or personal relationships that could have appeared to influence the work reported in this paper.

Acknowledgments

P.K. acknowledges CSIR, New Delhi, India, for the Senior Research Fellowship and financial support from CSIR-Mission Mode Project HCP-0009.

Appendix A. Supplementary data

Supplementary material related to this article can be found, in the online version, at doi:https://doi.org/10.1016/j.cattod.2020.05.009.

References

[1] J.H. Clark, F.E.I. Deswarte, T.J. Farmer, Biofuels, Bioprod. Biorefin 3 (2009) 72.
[2] B. Kahn, Earth's CO_2 passes the 400 PPM threshold —maybe permanently, Climate Central. (2016).
[3] R.D. Perlack, L.L. Wright, A.F. Turhollow, R.L. Graham, B.J. Stokes, D.C. Erbach, Agriculture (2005). DOE/GO-102, 78.
[4] S. Roy Goswami, M.J. Dumont, V. Raghavan, Starch 68 (2016) 274–286.
[5] P. Gallezot, Chem. Soc. Rev. 41 (2012) 1538–1558.
[6] A.A. Rosatella, S.P. Simeonov, R.F.M. Frade, C.A.M. Afonso, Green Chem. 13 (2011) 754–793.
[7] S.G. Wettstein, D.M. Alonso, E.I. Gürbüz, J.A. Dumesic, Curr. Opin. Chem. Eng. 1 (2012) 218–224.
[8] C. Rasrendra, J. Soetedjo, I. Makertihartha, S. Adisasmito, H. Heeres, Top. Catal. 55 (2012) 543–549.
[9] Z. Zhang, G.W. Huber, Chem. Soc. Rev. 47 (2018) 1351–1390.
[10] Z. Yuan, B. Liu, P. Zhou, Z. Zhang, Q. Chi, Catal. Sci. Technol. 8 (2018) 4430–4439.
[11] Y. Ren, Z. Yuan, K. Lv, J. Sun, Z. Zhang, Q. Chi, Green Chem. 20 (2018) 4946–4956.
[12] A. Jiahuan, S. Guohan, X. Haian, ACS Sustainable Chem. Eng. 7 (2019) 6696–6706.
[13] https://www.avantium.com/renewable-polymers, Amsterdam, The Netherlands.
[14] A.R.C. Morais, A.M. da Costa Lopes, R.B. Lukasik, Chem. Rev. 115 (2015) 3–27.
[15] C.S. Lancefield, L.W. Teunissen, B.M. Weckhuysen, P.C.A. Bruijnincx, Green Chem. 20 (2018) 3214–3221.
[16] Rogerio A.F. Toma s, Joao C.M. Bordado, Joao F.P. Gomes, Chem. Rev. 113 (2013) 7421–7469.
[17] W. Partenheimer, V.V. Grushin, Adv. Synth. Catal. 343 (2001) 102–111.
[18] Z. Zhang, K. Deng, ACS Catal. 5 (2015) 6529–6544.
[19] C. Megias-Sayago, A. Lolli, S. Ivanova, S. Albonetti, F. Cavani, J.A. Odriozola, Catal. Today 333 (2019) 169–175.
[20] Onofre Casanova, Sara Iborra, Avelino Corma, ChemSusChem. 2 (2009) 1138–1144.
[21] Baira Donoeva, Nazila Masoud, Petra E. de Jongh, ACS Catal. 7 (2017) 4581–4591.
[22] H. Ait Rass, N. Essayem, M. Besson, ChemSusChem. 8 (2015) 1206–1217.
[23] H.A. Rass, N. Essayem, M. Besson, Green Chem. 15 (2013) 2240–2251.
[24] S.E. Davis, L.R. Houk, E.C. Tamargo, A.K. Datye, R.J. Davis, Catal. Today 160 (2011) 55–60.
[25] B. Siyo, M. Schneider, M.M. Pohl, P. Langer, N. Steinfeldt, Catal. Lett 144 (2014) 498–506.
[26] Villa, A. Schiavoni, M. Campisi, S. Veith, G.M. Prati, ChemSusChem. 6 (2013) 609–612.
[27] X. Wan, C. Zhou, J. Chen, W. Deng, Q. Zhang, Y. Yang, Y. Wang, ACS Catal. 4 (2014) 2175–2185.
[28] T. Pasini, M. Piccinini, M. Blosi, R. Bonelli, S. Albonetti, N. Dimitratos, Jose A. L. Sanchez, M. Sankar, Q. He, C.J. Kiely, G.J. Hutchings, F. Cavani, Green Chem. 13 (2011) 2091–2099.
[29] N.K. Gupta, S. Nishimura, A. Takagaki, K. Ebitani, Green Chem. 13 (2011) 824.
[30] Zhi Gao, X. Renfeng, G. Fan, L. Yang, F. Li, ACS Sustainable Chem. Eng. 5 (2017) 5852–5861.
[31] X. Haian, A. Jiahuan, H. Mei, X. Siquan, L. Zhang, Z. Cailin, Catal. Today 319 (2019) 113–120.
[32] X. Han, C. Li, X. Liu, Q. Xia, Y. Wang, Green Chem. 19 (2017) 996–1004.
[33] K.T.V. Rao, J.L. Rogers, S. Souzanchi, L. Dessbesell, M.B. Ray, C. Charles Xu, ChemSusChem 11 (2018) 3323–3334.
[34] D. Yan, J. Xin, Q. Zhao, K. Gao, X. Lu, G. Wang, S. Zhang, Catal. Sci. Technol. 8 (2018) 164.
[35] R. Chen, J. Xin, D. Yan, H. Dong, X. Lu, S. Zhang, ChemSusChem. 12 (2019) 2715–2724.
[36] X. Shuai, Z. Peng, Z. Zehui, Y. Changjun, Z. Bingguang, D. Kejian, B. Steven, Z. Huaiyong, J. Am. Chem. Soc. 139 (2017) 14775–14782.
[37] Guangshun Yi, Siew Ping Teong, Yugen Zhang, Green Chem. 18 (2016) 979–983.
[38] D.K. Mishra, H.J. Lee, J. Kim, H.S. Lee, Jin Ku Cho, Y.W. Suh, Yongjin Yi, Yong Jin Kim, Green Chem. 19 (2017) 1619–1623.
[39] C.M. Pichler, M.G.A. Shaal, H. Joshi, W. Ciptonugroho, F. Schuth, ChemSusChem 11 (2018) 2083–2090.
[40] Atul S. Nagpure, Nishita Lucas, S.V. Chilukuri, ACS Sustainable Chem. Eng. 3 (2015) 2909–2916.
[41] D.K. Mishra, A.A. Dabbawala, J.S. Hwang, J. Mol. Catal. A Chem. 376 (2013) 63–70.
[42] S.Y. Chin, O.S. Alexeev, M.D. Amiridis, Appl. Catal. A Gen. 286 (2005) 157.
[43] W. Wang, H. Liu, T. Wu, P. Zhang, G. Ding, S. Liang, T. Jiang, B. Han, J. Mol. Catal. A Chem. 355 (2012) 174–179.
[44] N. Chakroune, G. Viau, S. Ammar, L. Poul, D. Veautier, M.M. Chehimi, C. Mangeney, F. Villain, F. Fievet, Langmuir 21 (2005) 6788–6796.
[45] Jiebo Chen, Xinxiang Chen, Ying Zheng, Qinglu Li, RSC Adv. 5 (2015) 20248–20255.
[46] A.M. Fonseca, S. Gonçalves, P. Parpot, I.C. Neves, Phys. Chem. Chem. Phys. 11 (2009) 6308–6314.
[47] Ali Babaei, M. Zendehdel, B. Khalilzadeh, Alireza Taheri, Colloids Surf. B Biointerfaces 66 (2008) 226–232.
[48] T.J. McCarthy, C.M.P. Marques, H. Trevino, W.M.H. Sachtler, Catal. Lett. 43 (1997) 11–18.
[49] K.R. Reddy, K. Ramesh, K.S. Kothapalli, V.V. Rao, V.R.Chary Komandur, Catal. Commun. 4 (2003) 112–117.
[50] Nicholas S. Gould, Bingjun Xu, J. Catal. 358 (2018) 80–88.
[51] P. Gogoi, A.S. Nagpure, P. Kandasamy, C.V.V. Satyanarayana, T. Raja, Sustain. Energy Fuels (2020).
[52] J. Cai, H. Ma, J. Zhang, Q. Song, Z. Du, Y. Huang, J. Xu, Chem. Eur. J. 19 (2013) 14215–14223.
[53] Zhang, W. Yang, I.I. Roslan, S. Jaenicke, G.K. Chuah, J. Catal. 375 (2019) 56–67.
[54] S. Albonetti, A. Lolli, V. Morandi, A. Migliori, C. Lucarelliand, F. Cavani, Appl. Catal. B 163 (2015) 520–530.
[55] X. Tong, Y. Linhao, H. Chen, X. Zhuang, S. Liao, H. Cui, Catal. Commun. 90 (2017) 91–94.
[56] Y.B. Wang, K. Yu, D. Lei, W. Si, Y.J. Feng, L.L. Lou, S.X. Liu, ACS Sustainable Chem. Eng. 4 (2016) 4752–4761.
[57] F.Z. Su, J. Ni, H. Sun, Y. Cao, H.Y. He, K.N. Fan, Chem. – Eur. J. 14 (2008) 7131–7135.

About the author

Mr. Prabu. K, son of Kandasamy and Ranjitham, was born in Surrapatti, a village of Dharmapuri district, Tamil Nadu, India, in 1990. He completed his Bachelor's degree in Chemistry from Sri Ramakrishna Mission Vidyalaya College of Arts and Science, Bharathiar University Coimbatore (2007-2010). He obtained his Master's degree in Chemistry from the same institute in 2012. He joined the Ph.D. program under the supervision of Dr. T. Raja, Senior Principal Scientist in Catalysis and Inorganic Chemistry Division, CSIR- National Chemical Laboratory, Pune, after qualifying CSIR- SRF. During his stay at CSIR-NCL, he published eight research articles in international peer-reviewed journals. His work was based on the synthesis of mixed metal oxides and metal nanoparticles supported catalysts for selective oxidation catalysis.